
Conceptual Design of a Laser-Plasma Accelerator Driven Free-Electron Laser Demonstration Experiment

Thorben Seggebrock



Ludwig-Maximilians-Universität München

2015

Thorben Seggebrock

Conceptual Design of a Laser-Plasma Accelerator Driven Free-Electron Laser Demonstration Experiment

Thorben Seggebrock

Dissertation

zur Erlangung des Doktorgrades
der Fakultät für Physik
der Ludwig-Maximilians-Universität München

vorgelegt von
Thorben Seggebrock
aus München

München
2015

Erstgutachter: Prof. Dr. F. Grüner

Zweitgutachter: Prof. Dr. J. Schreiber

Tag der mündlichen Prüfung: 8. Juli 2015

Zusammenfassung

Freie-Elektronen-Laser (FEL) zur Erzeugung kurzwelliger Strahlung sind bisher Anlagen mit einer Größe von Hunderten Metern bis hin zu mehreren Kilometern. Aufgrund von Fortschritten in der Laser-Plasma-Beschleunigung innerhalb der letzten Jahren ist diese Art von Beschleunigern eine vielversprechende Alternative zum Betreiben einer Synchrotronstrahlungsquelle der fünften Generation geworden – eines Freie-Elektronen-Lasers auf Laborgröße.

Bisher war es, wegen der für diese Art von Beschleuniger typischen breiten Energieverteilung, nicht möglich, ein Demonstrationsexperiment umzusetzen. Diese Arbeit behandelt mit analytischen Methoden und Simulationen die wichtigsten Herausforderungen des Konzeptdesigns für eine erste Demonstration eines Freie-Elektronen-Lasers auf Laborgröße.

Die breite Energieverteilung der Elektronen beeinträchtigt die FEL-Leistung direkt durch eine Verringerung des Microbunching und indirekt durch einen, vom Fokussiersystem verursachten, chromatischen Emittanzzuwachs. Beide Effekte können durch eine Dekompression des Elektronenpulses in einer magnetischen Schikane reduziert werden, wobei die Elektronen nach Energien sortiert werden. Dies verringert sowohl die lokale Breite der Energieverteilung, als auch den lokalen chromatischen Emittanzzuwachs und reduziert Leistungsverluste, die durch die kurze Elektronenpulsdauer verursacht werden. Des Weiteren sorgt die energieabhängige Fokusposition für eine Bewegung der Strahltaile durch den Elektronenpuls, welche mit dem Lichtpuls synchronisiert werden kann und somit zu einer Erhöhung der Stromdichte im Wechselwirkungsbereich führt. Dieses Konzept wird als chromatische Fokusanpassung (chromatic focus matching) bezeichnet. Die Vorteile der longitudinalen Dekompression gegenüber dem alternativen Ansatz der transversalen Dispersion werden in einem Vergleich aufgezeigt.

Bei Elektronenpulsen, wie sie typischerweise von einem Laser-Plasma-Beschleuniger erzeugt werden, tragen kohärente Synchrotronstrahlung und Raumladung gleichermaßen zum Emittanzzuwachs während der Dekompression bei. Es wird gezeigt, dass daher eine mittlere Schikanenlänge erforderlich ist und die Schikane somit nicht so schwach und lang wie möglich sein darf um ausschließlich Synchrotronstrahlung zu unterdrücken.

Ferner wird das Zusammenspiel der einzelnen Konzepte und Komponenten mit einer Simulation des vollständigen Systems untersucht und damit die generelle Machbarkeit bestätigt. Zusätzlich werden Toleranzen für ein erstes Demonstrationsexperiment ermittelt,

um die Praxistauglichkeit sicherzustellen. Die aufgezeigten Herausforderungen, jenseits der Breite der Energieverteilung, betreffen vor allem die Stabilität des Beschleunigers und die Präzision der Elektronenoptik.

Abstract

Up to now, short-wavelength free-electron lasers (FEL) have been systems on the scale of hundreds of meters up to multiple kilometers. Due to the advancements in laser-plasma acceleration in the recent years, these accelerators have become a promising candidate for driving a fifth-generation synchrotron light source – a lab-scale free-electron laser.

So far, demonstration experiments have been hindered by the broad energy spread typical for this type of accelerator. This thesis addresses the most important challenges of the conceptual design for a first lab-scale FEL demonstration experiment using analytical considerations as well as simulations.

The broad energy spread reduces the FEL performance directly by weakening the microbunching and indirectly via chromatic emittance growth, caused by the focusing system. Both issues can be mitigated by decompressing the electron bunch in a magnetic chicane, resulting in a sorting by energies. This reduces the local energy spread as well as the local chromatic emittance growth and also lowers performance degradations caused by the short bunch length. Moreover, the energy dependent focus position leads to a focus motion within the bunch, which can be synchronized with the radiation pulse, maximizing the current density in the interaction region. This concept is termed chromatic focus matching. A comparison shows the advantages of the longitudinal decompression concept compared to the alternative approach of transverse dispersion.

When using typical laser-plasma based electron bunches, coherent synchrotron radiation and space-charge contribute in equal measure to the emittance growth during decompression. It is shown that a chicane for this purpose must not be as weak and long as affordable to reduce coherent synchrotron radiation, but that an intermediate length is required.

Furthermore, the interplay of the individual concepts and components is assessed in a start-to-end simulation, confirming the feasibility of the envisioned experiment. Moreover, the setup tolerances for a first demonstration experiment are determined, confirming the general practicability. The revealed challenges, besides the energy spread, especially concern the source stability and the precision of the beam optics setup.

Contents

Zusammenfassung	v
Abstract	vii
1 Introduction	1
2 FEL Theory	3
2.1 Electron Motion in the Undulator	4
2.2 Spontaneous Undulator Radiation	8
2.3 High-Gain Theory	9
2.4 Degrading Effects	23
2.5 Ming Xie's Fit	33
2.6 Summary	35
3 Concepts for a Laser-Plasma Driven FEL	37
3.1 Laser-Wakefield Acceleration	38
3.2 Parameter Choice	42
3.3 Decompression Concept	47
3.4 TGU Concept	63
3.5 Conclusion	70
4 FEL Tolerances	73
4.1 Tolerance Budget	73
4.2 Sensitivities and Tolerances	75
4.3 Conclusion	91
5 Bunch Decompression	93
5.1 (De)compression in Chicanes	94
5.2 Energy Spread Generation	101
5.3 Emittance Growth	110
5.4 Compression vs. Decompression	116
5.5 Conclusion	118
6 Decompressor Optimization	119
6.1 Simulation	119

6.2	Twiss Optimization	120
6.3	Layout Optimization	126
6.4	Scalability	133
6.5	Conclusion	136
7	Electron Optics	139
7.1	Electron Optics Theory	139
7.2	Error Sources	145
7.3	Chromatic Focus Matching	151
7.4	Layout Concept	159
7.5	Conclusion	169
8	Start-to-End Simulation	171
8.1	Beam Transport	171
8.2	Undulator – FEL	177
8.3	Conclusion	184
9	Conclusion and Outlook	187
	Bibliography	191
	Publications	201
	Acknowledgements	203

1 Introduction

Since its first observation in 1947 [1], synchrotron radiation has become an invaluable tool for many different research areas ranging from solid-state physics to medical applications.

Over the years, different synchrotron radiation sources have been developed and built. In the early days, during the first generation of synchrotron radiation sources, the emission of radiation was a by-product of bending magnets in circular accelerator structures built for high-energy physics. The second generation still relied on simple bending magnets as radiation sources; however, these facilities were built with the focus on radiation production and not on particle physics.

Later generations of synchrotron radiation facilities used dedicated insertion devices, undulators and wigglers, in addition to bending magnets. Undulators and wigglers provide a periodic magnetic field, leading to a sinusoidal electron motion. This allows for interference of waves emitted in the individual periods, resulting in an increase of flux and brightness when compared to bending magnets.

Advancements of accelerator technology over the years further increased the electron beam quality in terms of the emittance and therefore also improved the photon beam quality, leading to the latest, fourth generation of synchrotron radiation sources. One type of these sources are short-wavelength free-electron lasers (FEL) operating in the ultraviolet and X-ray range.

Free-electron lasers not only produce spontaneous radiation as the other sources do but have undulators or wigglers long enough to allow for an interaction of electrons and previously emitted radiation. This interaction causes the build-up of an energy modulation on the scale of the light wavelength that gets converted to a density modulation by the dispersive character of the magnetic field. The rising amplitude of this density modulation allows for more and more coherent emission to occur, increasing the brightness by several orders of magnitude.

The major limitation of such sources today is the large size, as they consist of a kilometer-scale accelerator as well as beam transport sections and undulators on the order of tens to a hundred meters. The large size and the resulting high costs on the order of a billion euros restrict the availability of such sources to a few world wide. Operational are the UV and soft-X-ray systems TTF-FEL (FLASH) [2] and FERMI@Elettra [3], as well as

the hard-X-ray sources LCLS [4] and SACLA [5]. Several other sources like the European XFEL [6] and SwissFEL [7] are currently under construction, but the number of these sources is and will be very limited.

In order to increase their availability, new ways have to be followed. One such path has been provided by the invention of laser-plasma acceleration by Tajima and Dawson in 1979 [8]. This concept harnesses the power of intense laser pulses to accelerate electrons with fields three orders of magnitude stronger than those of conventional accelerators. With this technique compact accelerators delivering peak energies comparable to large scale systems used for driving FELs became feasible. A major breakthrough was achieved in 2004 by the groups of Geddes, Mangles, and Faure providing high-quality electrons from laser-plasma accelerators for the first time [9–11].

The availability of the new acceleration technique triggered the idea of a free-electron laser driven by such an accelerator [12], which would be a first source of the fifth generation. The basic feasibility of a soft-X-ray synchrotron radiation source driven by this new type of accelerator was demonstrated by Fuchs [13] and Maier [14]. The major challenge on the path to a first laser-plasma accelerator driven free-electron laser is, up to now, the high energy spread of the electrons. Over the recent years the design parameters required for a first demonstration experiment have advanced from the optimistic, initial parameters [12] closer to the results of state-of-the-art laser-plasma accelerator experiments [15–17].

In this thesis the current design concept for a laser-plasma accelerator driven free-electron laser to be built at the Centre for Advanced Laser Applications (CALA) is discussed in detail including the individual challenges and optimization concepts. Chapter 2 provides an overview over the basic FEL physics as a foundation for the later optimization considerations. In Chap. 3 the electron parameter set currently envisioned is introduced, and two optimization concepts reducing the performance degradation due to a broad energy spread (longitudinal decompression and transverse dispersion) are compared. Based on the design parameters and the chosen optimization concept, longitudinal decompression, the tolerances of the FEL with respect to different error sources, like field errors and alignment errors, are evaluated in Chap. 4. Chapter 5 introduces the basics of longitudinal phase space manipulation and the degrading effects leading to emittance growth. Based on the most important degrading effects, the decompressor layout is optimized in Chap. 6. The fundamentals of electron optics as well as setup tolerances that are based on the FEL tolerance study and an optimization concept for high energy spread scenarios are discussed in Chap. 7. Finally the full setup performance and the interplay of the individual components and effects is assessed using a start-to-end simulation discussed in Chap. 8.

2 FEL Theory

The basic physics of a free-electron laser completely differ from the concepts of a conventional laser. The radiation generation mechanism does not rely on bound electrons in a gain medium but uses freely propagating electrons from a particle accelerator. This allows to avoid one of the biggest limitations of conventional lasers, the availability of suited gain media for the desired wavelength range. FELs can operate in all spectral regions from the far-infrared down to hard X-rays. This advantage is complemented by the possibility to avoid the need for any mirrors potentially restricting the system in its spectral properties due to limited reflectivity.

In an FEL highly relativistic electrons propagate through the periodic magnetic field of an undulator. The magnetic field forces the electrons onto a sinusoidal path, leading to the emission of synchrotron radiation. The radiation wavelength depends on the period length of the magnetic structure as well as the energy of the electrons, and is therefore tunable, leading to a further advantage when compared to conventional lasers. The electron motion causes a Doppler frequency up-shift of the emitted radiation, making FELs perfectly suited for the generation of short-wavelength radiation like X-rays.

Due to the high velocity close to the speed of light, the electrons propagate within the radiation field and interact with it due to their transverse motion. This leads to an energy exchange and therefore an energy modulation of the electrons on the scale of the radiation wavelength. Since the trajectory of a charged particle in a magnetic field is energy dependent, the energy modulation gets converted to a density modulation called microbunching, again on the scale of the wavelength of the emitted radiation. This can change the emission process from incoherent to coherent during the propagation through the undulator, given a long enough interaction distance. The radiation power rises exponentially along the undulator and reaches a maximum before the microbunching gets smeared out due to the energy dependent trajectories and an overshooting of the electrons over their ideal positions within the bunch.

This mechanism enables free-electron lasers to produce coherent X-ray pulses with a duration of a few femtoseconds and multi-gigawatt peak power, making them the brightest currently available source of synchrotron radiation [18]. Due to these radiation characteristics, FELs are a key-member of the fourth generation light sources and will in combination with advanced accelerator concepts also be the basis for the fifth generation.

In this chapter, the basic theory of a high-gain FEL in the 1D approximation as well as degrading effects, including 3D effects, are reviewed. These basic scalings are the basis for the design considerations of the laser-plasma accelerator driven FEL demonstration experiment discussed subsequently.

Several resources are the basis for this chapter and are recommended for further reading [18–23]. The major part of this chapter follows the reasoning of [19, 20].

2.1 Electron Motion in the Undulator

The heart of every FEL is the undulator. It provides a periodic magnetic field forcing the electrons onto an oscillatory trajectory, leading to the emission of synchrotron radiation. In its simplest form, the undulator consist of a series of dipole pairs separated by a small gap. If the plane of the dipole field is fixed, the device is called a planar undulator. Systems with a field plane rotating along the setup are termed helical. In this thesis all discussions will be restricted to planar layouts, although the basic physics are also applicable for helical structures.

In order to increase the field strength in the undulator, often hybrid devices are used. In this case each undulator half does not consist of a series of dipoles with a field pointing in the direction of the gap, but the magnets are placed with the field parallel to the undulator axis. Poles consisting of iron or other high permeability materials are used to guide the flux into the gap increasing the density of the field lines with respect to a pure permanent magnet design. Many more undulator concepts [23] like electromagnet based systems and all-optical setups [24, 25] exist. The construction details, however, have no impact on the basic FEL theory.

The coordinate system used in the FEL discussion is shown in Fig. 2.1. The undulator axis and therefore the main propagation direction of the electrons defines the s -axis. The dipole field points along the y -axis, and the electron deflection occurs in the x -direction.

2.1.1 Magnetic Field

Within the undulator gap the field has to fulfill Maxwell's equations for a static magnetic field $\nabla \times \mathbf{B} = 0$ and $\nabla \cdot \mathbf{B} = 0$. Consequently, the field can be expressed as the gradient of a scalar potential $\mathbf{B} = -\nabla\phi$ which has to fulfill Laplace's equation $\nabla^2\phi = 0$. A reasonable ansatz for the potential is given by [20, 26]

$$\phi = \frac{B_0}{k_y} \cos(k_x x) \sinh(k_y y) \sin(k_u s), \quad (2.1)$$

using the wave numbers k_x , k_y , $k_u = 2\pi/\lambda_u$ with the period length of the undulator λ_u , and the peak field B_0 . To fulfill Laplace's equation, the relation

$$k_u^2 = k_y^2 - k_x^2, \quad (2.2)$$

has to hold. This implies that the focusing strength of an undulator in both transverse directions is conserved. For many cases it is sufficient to assume the poles to be infinitely broad, resulting in $k_x = 0$ and $k_y = k_u$, i.e. a pure vertical focusing. Outward bent pole surfaces, leading to a defocusing in the x -direction, can be modeled by a real value of k_x . This can also be used to imitate the effect of finite, flat poles which result in a defocusing effect in the horizontal plane, too. The case of inward bent poles, leading to a focusing effect in the x -direction, is described by an imaginary value of k_x reducing the focusing strength in the y -direction.

The peak field of the undulator is material and geometry dependent. An approximation taking both dependencies into account has been found by Elleaume et al. [27]

$$B_0 = a_1 \exp \left(a_2 \frac{g}{\lambda_u} + a_3 \left(\frac{g}{\lambda_u} \right)^2 \right). \quad (2.3)$$

The material characteristics are included by means of the coefficients a_i , the geometry dependence is described by the gap g and the undulator period λ_u . Typical hybrid undulators using NdFeB permanent magnets and vanadium permendur poles can be described with $a_1 = 3.694$, $a_2 = -5.068$, and $a_3 = 1.520$. The approximation is valid for the parameter range $0.1 < g/\lambda_u < 1$.

Using the potential above, the magnetic field is given by

$$\begin{aligned} \mathbf{B} &= -\nabla\phi \\ &= -\frac{B_0}{k_y} \begin{pmatrix} -k_x \sin(k_x x) \sinh(k_y y) \sin(k_u s) \\ k_y \cos(k_x x) \cosh(k_y y) \sin(k_u s) \\ k_u \cos(k_x x) \sinh(k_y y) \cos(k_u s) \end{pmatrix}. \end{aligned} \quad (2.4)$$

Since typical transverse particle offsets are small when compared to the undulator period, i.e. sub-mm-scale offsets compared to cm-scale period lengths, the transverse dependencies can be expanded up to the second order yielding

$$\mathbf{B} = -B_0 \begin{pmatrix} -k_x^2 x y \sin(k_u s) \\ \left(1 - \frac{(k_x x)^2}{2} + \frac{(k_y y)^2}{2} \right) \sin(k_u s) \\ k_u y \cos(k_u s) \end{pmatrix}. \quad (2.5)$$

All basic properties of an FEL can be described by using the on-axis magnetic field $B_y = -B_0 \sin(k_u s)$ only. However, to describe the more detailed particle motion within the undulator, including focusing effects, the general expression is required.

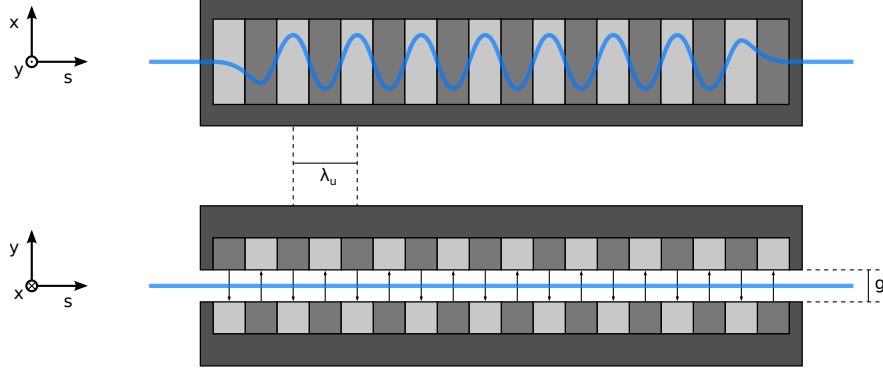


Figure 2.1: Schematic drawing of a planar undulator and the corresponding, ideal electron trajectory (blue) shown from a top-down view (top) and a side view (bottom). The coordinate system is chosen so that the undulator axis and the mean electron trajectory coincide with the s -axis. The magnetic field is oriented in the y -direction, resulting in an electron deflection in the x -direction.

2.1.2 Electron Motion

The exact particle motion in the undulator distracts from the dominant and important features. To get a better insight into the different effects, it is useful to separate the motion in a fast component describing the oscillatory motion on the scale of the undulator period and a slow component resembling a slow drift of the whole beam and focusing effects influencing the beam envelope with a typical scale of several undulator periods [20]. The complete particle motion can then be expressed as the sum of both contributions

$$\mathbf{r}_{\text{tot}}(t) = \mathbf{r}(t) + \mathbf{r}_{\text{slow}}(t). \quad (2.6)$$

The particle trajectory due to the fast motion is given by [19]

$$x(t) = \frac{K}{\gamma k_u} \sin(\omega_u t), \quad (2.7)$$

$$y(t) = 0, \quad (2.8)$$

$$s(t) = c\bar{\beta}_s t - \frac{K^2}{8\gamma^2 k_u} \sin(2\omega_u t), \quad (2.9)$$

using the oscillation frequency $\omega_u = k_u \bar{\beta}_s c$, the normalized, average longitudinal velocity $\bar{\beta}_s = 1 - (1 + K^2/2)/2\gamma^2$, the normalized energy γ , and the undulator parameter defined as

$$K = \frac{eB_0}{mck_u}, \quad (2.10)$$

using the electron mass m and the elementary charge e . For a typical undulator with a period length of a centimeter and a peak field of one tesla the parameter is on the order of unity. The oscillation of the forward velocity can be neglected for many practical cases as its amplitude is proportional to γ^{-2} . A sketch of the fast electron motion in the undulator is shown in Fig. 2.1.

Assuming k_x and k_y to be real numbers, i.e. modeling a planar undulator with finite pole width, the slow electron motion is given by [20]

$$x_{\text{slow}}(t) = x_{\text{slow},0} \cosh(\kappa_x \bar{\beta}_s ct) + \frac{x'_{\text{slow},0}}{\kappa_x} \sinh(\kappa_x \bar{\beta}_s ct), \quad (2.11)$$

$$y_{\text{slow}}(t) = y_{\text{slow},0} \cos(\kappa_y \bar{\beta}_s ct) + \frac{y'_{\text{slow},0}}{\kappa_y} \sin(\kappa_y \bar{\beta}_s ct), \quad (2.12)$$

using the wave numbers $\kappa_{x,y} = Kk_{x,y}/\sqrt{2}\gamma$ characterizing the scale of each motion. The types of motion correspond to the (de)focusing properties of the undulator. Assuming k_x and k_y to be real leads to a defocusing effect in the horizontal direction, resulting in a hyperbolic motion. The vertically increasing field, however, has a focusing effect giving rise to an oscillatory motion in the vertical plane.

The focusing force can be used to maintain a constant vertical beam size along the undulator. Requiring $\langle y \rangle = \langle y' \rangle = 0$, i.e. a beam propagating along the undulator axis, and using the definition of the beam emittance* measuring the area occupied by the particles in the transverse phase space $\epsilon_y^2 = \langle y^2 \rangle \langle y'^2 \rangle - \langle yy' \rangle^2$ the vertical beam envelope is given by

$$\sigma_y(s) = \sqrt{\sigma_{y_0}^2 \cos^2(\kappa_y s) \pm \frac{\sqrt{\sigma_{y_0}^2 \sigma_{y'_0}^2 - \epsilon_y^2}}{\kappa_y} \sin(2\kappa_y s) + \left(\frac{\sigma_{y'_0}}{\kappa_y}\right)^2 \sin^2(\kappa_y s)}. \quad (2.13)$$

Here σ_{y_0} is the initial vertical beam size and $\sigma_{y'_0}$ the initial vertical divergence. The “+” indicates an initially diverging beam, whereas the “−” holds for a converging beam. A constant beam size along the undulator is reached for a beam waist at the undulator entrance, i.e. $\sigma_{y_0}^2 \sigma_{y'_0}^2 = \epsilon_y^2$, with a beam size of $\sigma_{y_0} = \sqrt{\epsilon_y/\kappa_y}$. In the case of inward bent poles, i.e. an imaginary k_x , the same reasoning holds for the horizontal component. If planar or even outward bent poles are used, a constant horizontal beam size along the undulator is not possible and the beam envelope is usually controlled by the means of additional electron optics. This can also be necessary in order to reach an acceptable beam size in the vertical component if the focusing strength of the undulator is not sufficient. This is usually the case at high electron energies due to the energy dependence of the wavenumbers $\kappa_{x,y}$.

*For more details about the emittance definition see Sect. 7.1.

2.2 Spontaneous Undulator Radiation

The source of the spontaneous undulator radiation is the fast oscillation of the electrons. In an intuitive picture an electron can be seen as a relativistic, oscillating dipole. Due to the relativistic speed, the radiation is Doppler frequency up-shifted and concentrated into a narrow cone with opening angle $\theta = 1/\gamma$ around the longitudinal direction of flight. Although undulator radiation is a kind of synchrotron radiation, its spectral and spatial characteristics are significantly different.

The probably most interesting property of any radiation is its wavelength. The exact radiation characteristics could be derived by starting with the Liénard-Wiechert potentials, but as in the case of the electron motion in the undulator this distracts from the most relevant, basic characteristics.

An intuitive approach is to see the undulator as a series of emitters [23], i.e. each undulator period is the source of a plane wave. These waves interfere with one another and, depending on the setup characteristics, only allow for certain wavelengths to be found

$$\lambda_l \approx \frac{\lambda_u}{2n\gamma^2} \left(1 + \frac{K^2}{2} + \gamma^2\theta^2 \right), \quad (2.14)$$

which depend on the angle of observation θ . Here it can easily be seen why undulator based sources like FELs are suited for the production of short-wavelength radiation. The γ^{-2} -scaling allows to produce few-nm-radiation with an undulator period length on the order of a centimeter and electron energies of only a few hundred MeV. Furthermore, the equation shows why these sources can provide an easily tunable wavelength. There are multiple knobs to turn on:

- **Electron energy** – Depending on the accelerator, the electron energy can be adjusted within a certain range to yield the desired wavelength. This is limited by the maximum acceleration gradient and the tuning range of the electron optics controlling the beam size.
- **Field amplitude** – Most undulators are designed such that the magnetic field amplitude can be varied. In the case of electromagnets this can be done by changing the applied current, but it is also possible for permanent magnet based devices by changing the gap. It is interesting to note that the wavelength increases with the undulator parameter and therefore the magnetic field. This is in contrast to the properties of synchrotron radiation in simple bending magnets where the achievable wavelength decreases with the field strength.
- **Period length** – Usually the undulator period can only be chosen prior to the construction since a fixed period length allows the best control over the field quality. However, undulator designs with a variable period length exist [28].

In addition to the fundamental wavelength also higher harmonics, caused by the anharmonic motion due to the longitudinal velocity oscillations, are produced. On the undulator axis only odd harmonics are detectable, whereas even harmonics are found off-axis. These extend the usable wavelength range significantly if the source is designed appropriately.

The bandwidth of the radiation is limited due to the interference of the individual waves and is given by [23]

$$\frac{\Delta\lambda}{\lambda_l} = \frac{1}{1 + N_u n}, \quad (2.15)$$

with N_u being the number of undulator periods. Since the number of undulator periods is high in most cases, the bandwidth is approximately inversely proportional to it. Assuming a typical undulator period of one centimeter and a length of one meter results in a bandwidth of 1%. This is an important difference when compared to the continuous spectrum of synchrotron radiation from bending magnets, ensuring the high brightness of fourth- and fifth-generation synchrotron radiation sources.

The high brightness is further supported by the narrow opening angle [23]

$$|\theta| = \sqrt{\frac{2\lambda_l}{N_u \lambda_u}} = \frac{1}{\gamma} \sqrt{\frac{1 + \frac{K^2}{2}}{N_u}}, \quad (2.16)$$

which is again a result of interference. The opening angle drops slower with the undulator length than the bandwidth, nevertheless, a reduction of an order of magnitude when compared to the opening angle of radiation from a bending magnet can easily be reached for $N_u = 100$.

The total emitted power integrated over all angles and frequencies is [29]

$$P_{\text{int,tot}} = \frac{I e \gamma^2 K^2 k_u N_u}{6\epsilon_0}, \quad (2.17)$$

using the current of the electron beam I . It rises linearly along the undulator and can reach high values; however, it is still based on an incoherent process – the spontaneous emission of photons by randomly distributed electrons. It is not to be confused with the power that can be reached with an FEL where the electrons can emit coherently.

2.3 High-Gain Theory

In this section the mechanism of a high-gain FEL is reviewed. When compared to the previous section discussing the spontaneous undulator radiation, now the interaction between electrons and radiation plays a major role. The term “high-gain” refers to systems where the power growth per pass through the undulator is not negligible. Ideally even

the full radiation power is reached during a single pass through the undulator. A “low-gain” theory also exists but is only applicable for systems with a negligible amplification per pass and relying on multiple passes through the undulator. Since resonators are not yet available with a sufficient quality in the X-ray range, this theory will not be covered in this thesis. It can, however, be derived based on the high-gain theory in the limit of small gain.

2.3.1 Resonance

In any undulator based radiation source the electrons co-propagate with their own emitted radiation. Due to the oscillating motion of the electrons in the radiation field, each electron is subject to energy changes depending on its position relative to the phase of the field. The energy change can be expressed as [19]

$$\frac{dW}{dt} = -\frac{ec\hat{K}E_x(s)}{2\gamma}(\cos\Psi + \cos\chi), \quad (2.18)$$

using the position dependent radiation field amplitude $E_x(s)$, the modified undulator parameter \hat{K}^* , and the phases

$$\Psi = (k_u + k_l)s - \omega_l t + \phi_0 \quad \text{and} \quad \chi = (k_u - k_l)s - \omega_l t + \phi_0. \quad (2.19)$$

Here ω_l is the radiation frequency, k_l the corresponding wave number, and ϕ_0 an arbitrary phase offset. The first phase Ψ is called **ponderomotive phase** and plays an important role in the whole FEL theory. It can be interpreted as a longitudinal position of an electron within the bunch and also characterizes the electrons position with respect to the radiation field.

Depending on its position with respect to the light wave a particle will either gain or lose energy. For an FEL a constant energy transfer is desired to ensure an amplification of the light wave. Therefore, the ponderomotive phase should ideally remain constant during the pass through the undulator

$$\frac{d\Psi}{dt} = (k_u + k_l)\bar{\beta}_s c - \omega_l \stackrel{!}{=} 0. \quad (2.20)$$

Solving for the light wavelength leads to the **resonance condition** of the free-electron laser

$$\lambda_l = \frac{\lambda_u}{2\gamma^2} \left(1 + \frac{K^2}{2} \right). \quad (2.21)$$

*The modified undulator parameter takes the longitudinal velocity oscillations of the electrons into account and is given by $\hat{K} = K \left(J_0 \left(\frac{K^2}{4+2K^2} \right) - J_1 \left(\frac{K^2}{4+2K^2} \right) \right)$.

This is exactly the wavelength of the spontaneous undulator radiation for $\theta = 0$, i.e. on-axis. This allows an FEL to work in a self seeding mode, i.e. amplifying the spontaneous emission produced in the first few undulator periods.

The energy exchange between the electrons and the radiation field results in an energy modulation of the electrons on the scale of the radiation wavelength. Due to the energy dependence of the electron motion, the energy modulation will translate into a current density modulation called **microbunching**. Since this modulation is periodic on the scale of the light wavelength, the radiation gets more and more coherent, resulting in an exponential growth of the field amplitude. A sketch of the process is shown in Fig. 2.2.

The exact behavior of an FEL can either be described using first-order equations, which describe the whole phase space dynamics but do not allow for an analytical solution of the field evolution, or by an analytically solvable third-order differential equation characterizing the evolution of the field amplitude. Both approaches are covered in the following two sections.

2.3.2 First-Order Equations

The dynamics of the individual electrons caused by the electron-radiation interaction as well as the evolution of the field amplitude can be described by the **first-order equations** [19]

$$\frac{d\Psi_n(s)}{ds} = 2k_u\eta_n, \quad (2.22)$$

$$\frac{d\eta_n(s)}{ds} = -\frac{e}{\gamma_r mc^2} \Re \left(\left(\frac{\widehat{K} \tilde{E}_x(s)}{2\gamma_r} - \frac{ic^2 \mu_0 \tilde{j}_1(s)}{\omega_l} \right) \exp(i\Psi_n) \right), \quad (2.23)$$

$$\frac{d\tilde{E}_x(s)}{ds} = -\frac{\mu_0 c \widehat{K}}{4\gamma_r} \tilde{j}_1(s), \quad (2.24)$$

$$\tilde{j}_1(s) = 2j_0 \frac{1}{N} \sum_{n=1}^N \exp(-i\Psi_n), \quad (2.25)$$

with $n = 1 \dots N$ identifying the individual particle within one radiation wavelength*, $\eta_n = \Delta\gamma_n/\gamma_r$ characterizing the energy **detuning** of an electron with respect to the resonance energy γ_r , and $\tilde{j}_1(s)$ being the position dependent amplitude of the current density modulation in addition to the unperturbed current density j_0 . Complex quantities are indicated by a tilde and are used to simplify the mathematics.

This set of $2N+1$ coupled differential equations and one algebraic equation includes all important features of the 1D FEL theory for infinitely long, periodic bunches. The

*Here other parts of the bunch are assumed to be identical copies of the described region, however, the model can be extended to nonperiodic cases [19].

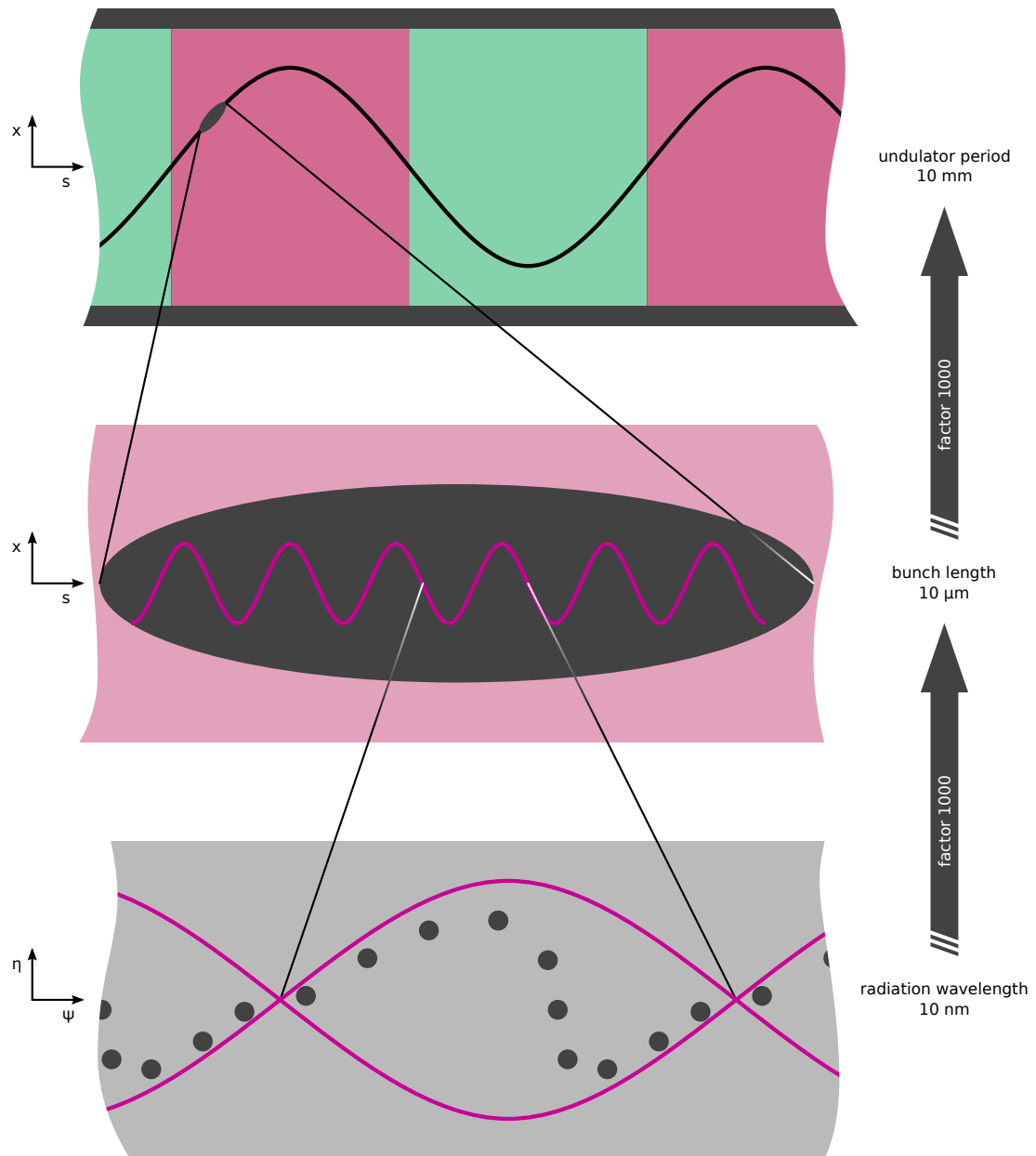


Figure 2.2: Sketch of the FEL process and typical orders of magnitude. The electron bunch oscillates during its propagation through the undulator (top). Due to the high electron velocity, it co-propagates with the radiation produced by itself and interacts with it (middle). The oscillation of the electrons in the radiation field causes an energy modulation on the scale of the light wavelength that gets converted into a density modulation due to the dispersive character of the undulator (bottom). The build-up of this density modulation results in an increase of coherent emission, leading to an exponential power rise.

equations can be solved numerically for a suited set of initial conditions and are the foundation of 1D FEL codes; however, due to the large number of electrons per slice no analytical solution is possible. Nevertheless, the individual equations can provide a deeper understanding of the underlying mechanisms.

The amplitude of the current density modulation can be cast into a new form

$$\tilde{j}_1(s) = 2j_0 \cdot |\langle \exp(-i\Psi_n) \rangle| \cdot \exp(-i\Phi_{j_1}). \quad (2.26)$$

Here the **bunching factor** [20] $|\langle \exp(-i\Psi_n) \rangle|$, with $\langle \dots \rangle$ indicating an average over all particles, and the bunching phase Φ_{j_1} were used. The bunching factor resembles the root-mean-square distance to the origin of a random walk in the complex plane. For a uniform random distribution, e.g. the electron distribution at the undulator entrance, it scales as $1/\sqrt{N}$. In simulations this property is of special interest since usually not single electrons but macro particles, replacing a large number of electrons each, are used to model the FEL process. This several orders of magnitude smaller number of macro particles has to have the same statistical properties as the simulated bunch. Consequently, no simple random distribution can be used, but special care has to be taken to reduce the initial noise [20, 30]. During the propagation through the undulator the microbunching builds up and the bunching factor rises. For realistic cases the bunching factor at saturation of the FEL process is on the order of 10^{-2} [20].

Using the bunching factor, the change of the field amplitude can be expressed as

$$\frac{d\tilde{E}_x(s)}{ds} = -\frac{\mu_0 c \hat{K}}{4\gamma_r} \tilde{j}_1(s) \propto |\langle \exp(-i\Psi_n) \rangle| \cdot \exp(-i\Phi_{j_1}). \quad (2.27)$$

The growth rate of the field amplitude is directly proportional to the bunching factor. Whether the field is amplified or reduced, however, crucially depends on the phase of the current density modulation with respect to the phase of the complex field amplitude. The absolute value of the field amplitude change $|\Delta\tilde{E}_x(s)|$ per integration step Δs is small compared to the existing field amplitude. Using the phase of the complex field amplitude $\Phi_{\tilde{E}_x}$, this leads to the requirement $|\Phi_{j_1} - \Phi_{\tilde{E}_x}| < \pi/2$ according to the law of cosines. In the phase space picture this is equivalent to requiring the majority of the electrons in a bucket to be located in the right half where they will lose energy, leading to field amplitude growth.

The rate of energy change of an electron neglecting space-charge effects is proportional to

$$\frac{d\eta_n(s)}{ds} = -\frac{e}{\gamma_r m c^2} \Re \left(\left(\frac{\hat{K} \tilde{E}_x(s)}{2\gamma_r} \exp(i\Psi_n) \right) \right) \propto -|\tilde{E}_x(s)| \cos(\Phi_{\tilde{E}_x}(s) + \Psi_n(s)). \quad (2.28)$$

The rate of energy change therefore depends on the position dependent amplitude of the radiation field and the phase relation between field amplitude and electron. For field

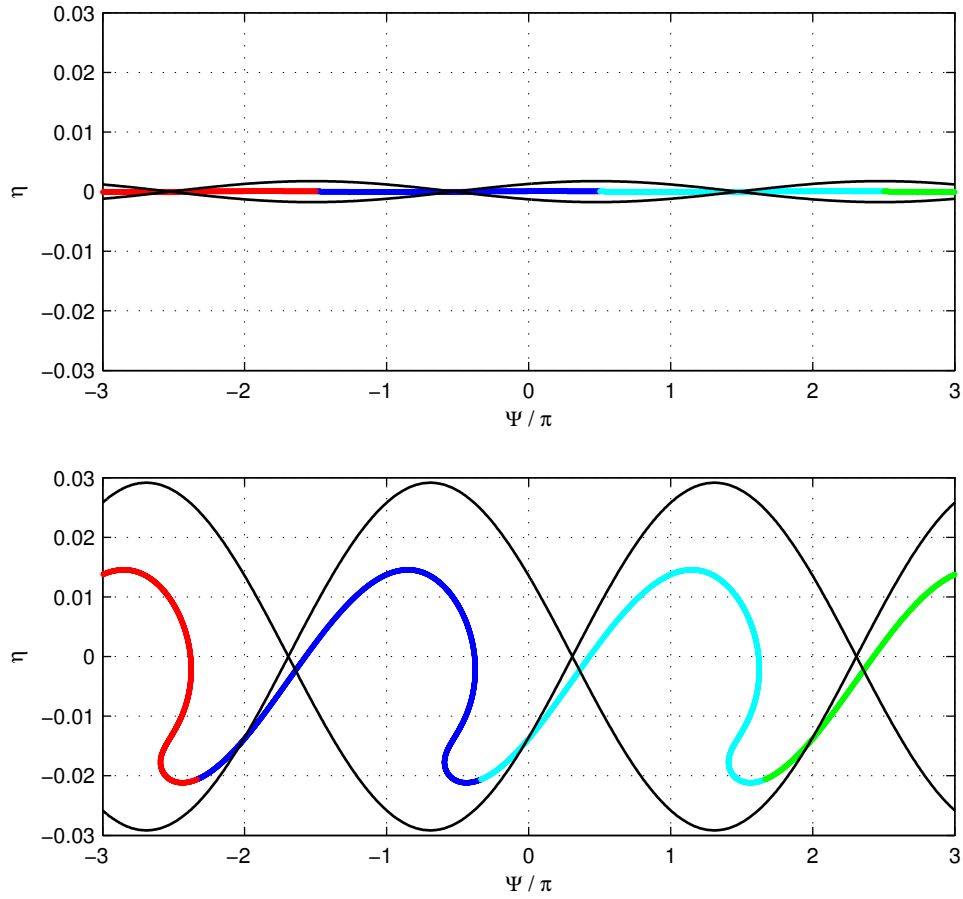


Figure 2.3: Phase space close to the undulator center (top) and exit (bottom) assuming a system that reaches a maximum of field amplification at the undulator exit. Initially the electrons were homogeneously distributed in Ψ (the color code represents the starting bucket) with all electrons starting on resonance $\eta_0 = 0$. During the interaction the quasi-separatrix (black) surrounding the buckets grows and moves towards lower phases Ψ . The electron distribution becomes asymmetrically distributed in each bucket, allowing for field amplification.

amplification the condition $|\Phi_{\tilde{E}_x}(s) + \Psi_n(s)| < \pi/2$ has to hold. So far this is equivalent to the requirement for the phase of the current modulation above. However, a closer look reveals two important characteristics of the phase space: First, field amplification will also lead to a growth of the energy change rate, changing the phase space structure over time and resulting in a growth of the quasi-separatrix height. Second, any change of the phase of the complex field amplitude $\Phi_{\tilde{E}_x}(s)$ will shift the phase space structure, moving the regions of energy loss and gain. It can be shown that during the amplification process the phase velocity of the radiation field is reduced (see Sect. 2.3.4) what is equivalent to growth of $\Phi_{\tilde{E}_x}(s)$, resulting in a bucket motion towards lower phases. The combination of these two effects allows a high-gain FEL to operate with on-resonance electrons. Two steps of the phase space evolution close to the start and end of the amplification process are shown in Fig. 2.3.

2.3.3 Third-Order Equation – Analytical Solution

In order to obtain an analytical solution of the field amplification in an FEL, one has to switch from the description of individual particles to an ansatz using a phase space density [19]

$$\tilde{f}(s, \eta, \Psi) = f_0(\eta) + \left(\tilde{f}_1(s, \eta) \exp(i\Psi) \right). \quad (2.29)$$

The first summand $f_0(\eta)$ is the energy distribution of the electron bunch and does not depend on the propagation distance. The second summand resembles the density modulation periodic in Ψ with a position dependent amplitude. To allow for an analytical solution, the additional assumption of **small density modulations** is necessary $|\tilde{f}_1(s, \eta)| \ll |f_0(\eta)|$.

An advantage of the collective description of the particles using a density is that it has to follow a continuity equation, in this case the Vlasov equation

$$\frac{df}{ds} = \frac{\partial f}{\partial s} + \frac{\partial f}{\partial \Psi} \frac{d\Psi}{ds} + \frac{\partial f}{\partial \eta} \frac{d\eta}{ds} = 0. \quad (2.30)$$

This allows to express the change of the field amplitude as [19]

$$\begin{aligned} \frac{d\tilde{E}_x(s)}{ds} &= i \frac{k_u \mu_0 \hat{K} n_e e^2}{2m\gamma_r^2} \int_0^s \left(\frac{\hat{K} \tilde{E}_x(\sigma)}{2\gamma_r} + 4i \frac{c\gamma_r}{\omega_l \hat{K}} \frac{d\tilde{E}_x(\sigma)}{d\sigma} \right) \dots \\ &\quad \times \int_{-\delta}^{+\delta} f_0(\eta)(s - \sigma) \exp(-2ik_u\eta(s - \sigma)) d\eta d\sigma, \end{aligned} \quad (2.31)$$

with the electron density n_e . This **integro-differential equation** is valid for all energy distributions fulfilling $f_0(|\eta| \geq \delta) = 0$ with $\delta \ll 1$. To continue with a scenario that is as general as possible, it would be desirable to approximate the energy distribution by a Gaussian; however, no analytical solution exists for this case [22].

Assuming a monoenergetic energy distribution $f_0(\eta) = \delta(\eta - \eta_0)$ centered at an arbitrary detuning η_0^* and introducing new variables characterizing the FEL properties allows to recast the integro-differential equation to [19]

$$\frac{\tilde{E}_x'''}{\Gamma^3} + 2i\frac{\eta}{\rho}\frac{\tilde{E}_x''}{\Gamma^2} + \left(\left(\frac{k_p}{\Gamma} \right)^2 - \left(\frac{\eta}{\rho} \right)^2 \right) \frac{\tilde{E}_x'}{\Gamma} - i\tilde{E}_x = 0. \quad (2.32)$$

This is the **third-order differential equation** characterizing the field amplitude evolution in a high-gain free-electron laser in the one-dimensional approximation including space-charge and detuning as degrading effects. The new parameters used are the **gain parameter** Γ , the **space-charge parameter** k_p , and the **Pierce parameter** ρ [31] They are defined as:

- **Gain parameter**

$$\Gamma = \left(\frac{\mu_0 \hat{K}^2 e^2 k_u n_e}{4\gamma_r^3 m} \right)^{1/3}. \quad (2.33)$$

As the name already indicates the gain parameter is a measure for the FEL gain, i.e. the growth rate of the field amplitude, and therefore the achievable radiation power.

- **Space-charge parameter**

$$k_p = \left(\frac{2k_u \mu_0 n_e e^2 c}{\gamma_r m \omega_l} \right)^{1/2}. \quad (2.34)$$

The space-charge parameter measures the impact of local space-charge effects caused by the microbunching. Due to the scaling $k_p \propto (\gamma_r \omega_l)^{-1/2} \propto \gamma_r^{-3/2}$, space-charge effects are often negligible for short-wavelength FELs.

- **Pierce parameter**

$$\rho = \frac{\Gamma}{2k_u} = \frac{1}{2\gamma_r} \left[\frac{I_{\text{peak}}}{I_A} \left(\frac{\hat{K} \lambda_u}{\sqrt{2} 2\pi \sigma_r} \right)^2 \right]^{1/3}. \quad (2.35)$$

Here the Alfvén current $I_A = 4\pi mc/\mu_0 e \approx 17 \text{ kA}$ is used. I_{peak} is the peak current of a finite electron pulse and σ_r its rms radius. The Pierce parameter is the probably most important parameter in the FEL theory. Due to its proportionality to the gain parameter, it is also related to the rate of field amplification. In addition, it is a measure for the efficiency of the FEL in terms of its capability to transfer power stored in the electron beam to the radiation field. The typical range for linear accelerator based FELs is $\rho = 10^{-3} - 10^{-4}$. Furthermore, it characterizes the

*To simplify the further notation η_0 will be replaced by η .

bandwidth (see Sect. 2.3.4) and consequently is a measure for the sensitivity of the setup to errors and degrading effects (see Sect. 2.4).

Due to these relations, it is of high importance to ensure a high Pierce parameter. This is limited by the short design wavelengths of ultraviolet and X-ray systems due to the competing scalings of both. The only wavelength independent parameters are the current I_{peak} and the beam size σ_r ; however, these are limited by the capabilities of the accelerator and the focusing system.

The general solution of the third-order differential equation has the form

$$\tilde{E}_x(s) = \sum_{i=1}^3 c_i(\eta, k_p) \exp(\alpha_i(\eta, k_p)s), \quad (2.36)$$

with the coefficients c_i depending on both, the initial conditions and the degrading effects, whereas the exponents depend on the degrading effects only.

For an ideal system the third-order equation can be simplified by assuming:

- The beam to be on resonance, i.e. the detuning to be negligible $\eta = 0$. This approximation is well justified for self seeding systems since the on-axis undulator radiation wavelength fulfills the resonance condition.
- That space-charge effects are negligible $k_p = 0$, which is reasonable for a short-wavelength system due to the high energy.

Neglecting these effects leads to the simple equation

$$\frac{\alpha^3}{\Gamma^3} - i = 0, \quad (2.37)$$

which is solved by

$$\alpha_1 = \frac{(i + \sqrt{3})\Gamma}{2}, \quad \alpha_2 = \frac{(i - \sqrt{3})\Gamma}{2}, \quad \alpha_3 = -i\Gamma. \quad (2.38)$$

All three solutions contain an oscillatory behavior with the first providing an additional exponential growth due to the positive real part, whereas the second shows an additional exponential decay. Consequently, the first solution will dominate the field amplitude evolution for sufficiently long systems, i.e. $s \gg \Gamma^{-1}$, and will result in the power scaling

$$P(s) \propto |\tilde{E}_x(s)|^2 \approx |c_1|^2 \exp\left(\sqrt{3}\Gamma s\right). \quad (2.39)$$

Here not only the meaning of the gain parameter becomes obvious but also one of the major deficits of the simplified theory – it predicts an infinite, exponential power growth. This is owed to the assumption of small density modulations $|\tilde{f}_1| \ll |f_0|$ used in the

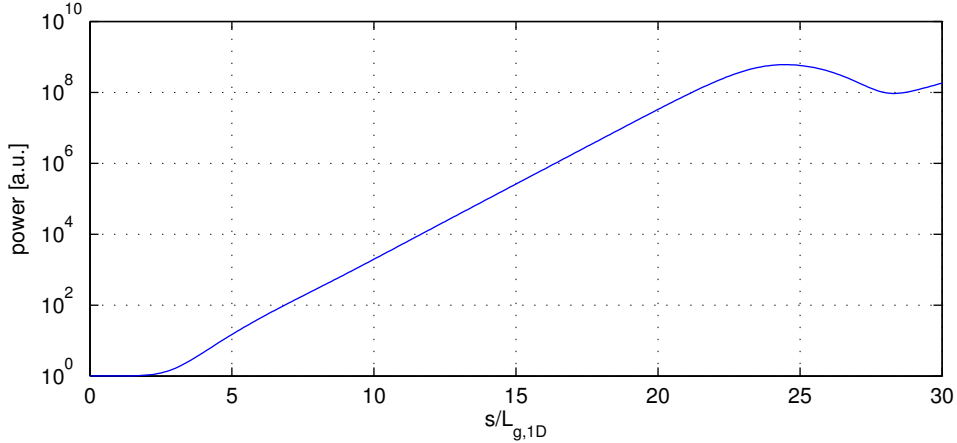


Figure 2.4: Power as a function of the longitudinal position for a seeded FEL based on the first-order equations (2.22)–(2.25) neglecting all degrading effects. The power curve can be divided into three sections: $s \leq 3L_{g,1D}$, here no significant amplification is found due to the competing solutions (exponential growth and decay). In the range $3L_{g,1D} < s \leq 23L_{g,1D}$ the power rises exponentially until saturation is reached for $s > 23L_{g,1D}$ and the power starts to oscillate.

derivation which does not hold when strong bunching and, therefore, the highest field amplification is reached.

Although the gain parameter is well suited to characterize the amplification process, the more often used quantity characterizing the power gain is the e-folding length of the system, the one-dimensional **power gain length** (or just gain length*) defined as

$$L_{g,1D} = \frac{1}{\sqrt{3}\Gamma} = \frac{\lambda_u}{4\pi\sqrt{3}\rho}. \quad (2.40)$$

The coefficients c_i used in the exponential ansatz solving the general third-order differential equation depend on the initial conditions. In general, two major classes of high-gain FELs can be distinguished in terms of their initial conditions:

- **Seeded FELs** – In these systems the initial radiation field is provided by an external source. In terms of initial conditions this corresponds to a nonvanishing initial field amplitude while all derivatives of the field amplitude are zero. In experiments the major challenge for the case of short-wavelength FELs is to provide a strong enough seed pulse at the resonant wavelength that is synchronized with the electron bunch.

*In the literature different definitions of the gain length are used. In some cases the term refers to the field gain length $L_{g,1D,\text{field}} = 2L_{g,1D}$, and in other manuscripts the gain length is defined as the inverse of the gain parameter $L_{g,1D,\text{alt.}} = \Gamma^{-1} = \sqrt{3}L_{g,1D}$.

- **SASE FELs** – Here self amplification of spontaneous emission (SASE) is used to drive the FEL, i.e. the spontaneous undulator radiation produced on the first few undulator periods gets amplified by the interaction process. The initial conditions here only contain the first and second field amplitude derivatives since they are related to the current modulation driving the spontaneous emission, and the initial field amplitude is zero. This is the most common way of operation for short-wavelength FELs up to now.

Although the initial conditions differ significantly, the gain mechanism is not influenced by them and, therefore, the gain lengths are identical.

2.3.4 Properties

Besides the scale of amplification, there are further important properties of free-electron lasers and their radiation.

Saturation

An important effect not included in the third-order differential equation is saturation. The linearization of the theory introduced by the assumption of small modulations $|\tilde{j}_1| \ll |j_0|$ eliminated this feature from the theory. It is, however, included in the first-order equations.

The linearized theory only allows for an estimate of the saturation properties. Due to the exponential growth of the field amplitude, the bulk of the power is generated on the last few gain lengths. In addition, the highest possible growth rate is reached at the maximum of microbunching. The saturation power can consequently be estimated by assuming maximum current density modulation $|\tilde{j}_1| = |j_0|$ and integrating the field amplitude growth over one field gain length, i.e. two power gain lengths.

The resulting estimate for the saturation power is [19]

$$P_{\text{sat}} \approx \rho P_{\text{beam}}, \quad (2.41)$$

using the power of the electron beam given by $P_{\text{beam}} = \gamma mc^2 I_{\text{peak}}/e$. This shows that the Pierce parameter is a measure for the efficiency of an FEL.

The undulator length needed to reach the maximum power, i.e. the saturation length, can be approximated by [18]

$$L_{\text{sat}} \approx \frac{\lambda_u}{\rho}. \quad (2.42)$$

If the setup length exceeds this length, the power growth is not only stopped, but electrons start to regain energy from the radiation field, leading to a reduction of the radiation

power. Consequently, care has to be taken in the setup design – a longer undulator does not necessarily result in a better performance.

Bandwidth

A further interesting characteristic of FEL radiation is its bandwidth. This is not to be confused with the bandwidth of the undulator radiation depending on interference only. In order to characterize the bandwidth of a free-electron laser its capability to amplify detuned radiation has to be taken into account. In general the power growth is given by

$$P(s, \eta) \propto \exp(\Re(2\alpha_1(\eta))s), \quad (2.43)$$

with $\alpha_1(\eta)$ characterizing the detuning dependent solution of the third-order equation leading to exponential growth (see Sect. 2.4.1). The growth rate can be approximated by [19]

$$\Re(2\alpha_1(\eta)) \approx \left(1 - \frac{\eta^2}{9\rho^2}\right) \frac{1}{L_{g,1D}}. \quad (2.44)$$

This allows to express the power growth as

$$P(s, \eta) \propto \exp\left(\frac{s}{L_{g,1D}}\right) \exp\left(-\frac{(\omega - \omega_l)^2}{2\sigma_\omega^2(s)}\right), \quad (2.45)$$

using the radiation bandwidth

$$\sigma_\omega(s) = 3\sqrt{2}\omega_l\rho\sqrt{\frac{L_{g,1D}}{s}}. \quad (2.46)$$

Similar to the spontaneous undulator radiation, the FEL bandwidth drops with the setup length; however, it is proportional to $1/\sqrt{s}$. Assuming a system operating in saturation, the relative bandwidth can be approximated by the Pierce parameter

$$\frac{\sigma_{\omega,\text{sat}}}{\omega_l} \approx \rho. \quad (2.47)$$

This is not only a characteristic of the radiation but also sets limits to the tolerances the setup has to fulfill (see Sect. 2.4).

Cooperation Length

An important characteristic of an FEL is the cooperation length. It is defined as the distance slipped by a photon with respect to the electrons during the bunch propagation over one gain length [32]

$$l_{\text{co}} = \frac{L_{g,1D}}{\lambda_u} \lambda_l. \quad (2.48)$$

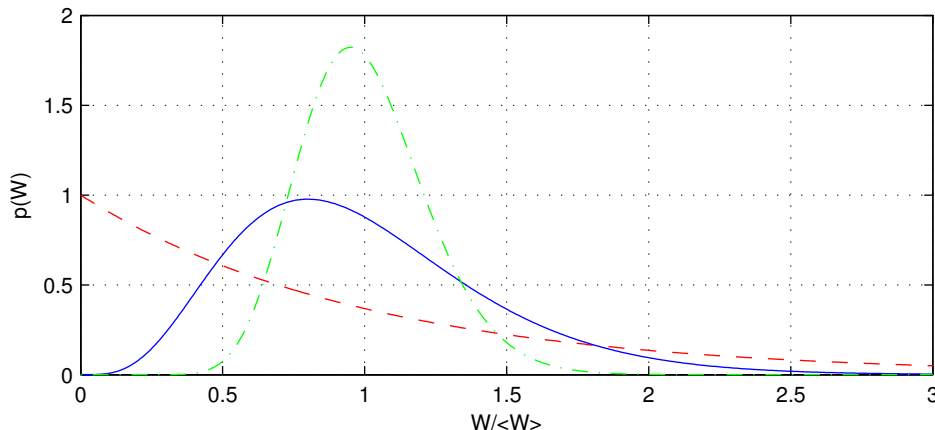


Figure 2.5: Probability density functions for $M = 1$ (dashed red), $M = 5$ (solid blue), and $M = 20$ (dash-dotted green) based on Eq. (2.50). In the limiting case of short bunches, i.e. low number of modes, the distribution becomes a negative exponential distribution, whereas for long bunches, i.e. high numbers of modes, the distribution converges against a Gaussian distribution.

This sets the scale over that communication in the bunch can occur during one gain length and consequently limits correlations to this range. It is, therefore, also a measure for the coherence length. The corresponding coherence time can be approximated by $t_{\text{co}} \approx l_{\text{co}}/c$. The gain length is used as scale since it is the characteristic length of the FEL process, defining features of the final radiation pulse.

Since SASE FELs start from the shot-noise of the initial electron distribution, the produced radiation has the properties of chaotic polarized radiation [33]. Depending on the ratio of bunch duration to coherence time

$$M = \frac{t_{\text{bunch}}}{t_{\text{co}}}, \quad (2.49)$$

on average M independent modes will exist in the time and frequency domain [33]. In the extreme case of $t_{\text{bunch}} \leq t_{\text{co}}$ only one single mode will exist, resulting in $M = 1$; however, in this regime also the FEL performance will significantly be affected [32, 34, 35]. This will be discussed in Sect. 2.4.6.

A further characteristic feature of an FEL pulse depending on the number of modes is the fluctuation of the radiation energy W . For completely chaotic polarized light, the probability density distribution of the radiation energy $p(W)$ in the exponential gain regime $s \gg \Gamma^{-1}$ is given by [33]

$$p(W) = \frac{M^M}{\Gamma(M)} \left(\frac{W}{\langle W \rangle} \right)^{M-1} \frac{1}{\langle W \rangle} \exp \left(-M \frac{W}{\langle W \rangle} \right), \quad (2.50)$$

here $\langle W \rangle$ is the average of the radiation energy over many pulses, Γ is the gamma function, and M is the number of modes defined above. Different examples are shown in Fig. 2.5. Two extreme cases can be distinguished:

- $M = 1$ – resulting in a negative exponential distribution
- $M \gg 1$ – allowing to approximate the distribution by a Gaussian

Independent of the extreme cases, the distribution shows that significant shot-to-shot energy fluctuations can be expected in the exponential gain regime. This is a characteristic feature of an FEL, and can be used as evidence for an FEL process in first demonstration experiments.

Velocities

Slippage of the light wave with respect to the electrons is a fundamental characteristic of an FEL. The right amount of slippage ensures a constant field amplification and is the key to a resonant behavior. Up to now, all calculations assumed the phase velocity to be the vacuum speed of light $v_{\text{ph}} = c$. However, this cannot hold since the radiation field is not propagating in vacuum but in an electron bunch with an increasing density modulation, i.e. a medium; hence, a modification of the phase velocity is to be expected.

In the exponential gain regime $s \gg \Gamma^{-1}$ the radiation field can be approximated by [19]

$$\tilde{E}_x(s, t) = c_1 \exp(\Re(\alpha_1)s) \exp(i(k_{l,\text{eff}}s - \omega_l t)), \quad (2.51)$$

with the effective wave number $k_{l,\text{eff}} = \Im(\alpha_1) + k_l$. Using the solution of the third-order differential equation $\alpha_1 = (i + \sqrt{3})\Gamma/2$ the phase velocity can be approximated by

$$v_{\text{ph}} = \frac{\omega_l}{k_{l,\text{eff}}} \approx c \left(1 - \frac{\lambda_l}{L_{\text{sat}}} \right), \quad (2.52)$$

using the approximation $L_{\text{sat}} \approx \lambda_u/\rho$. This relation shows that a light wave slips by one light wavelength with respect to a wave propagating with the vacuum speed of light over the saturation length. This characteristic is the reason for the bucket motion in the phase space mentioned earlier (see Sect. 2.3.2) and, therefore, essential for the on-resonance operation of a high-gain free-electron laser.

Using the same approximation of the radiation field as above, also the group velocity can be approximated [19]

$$v_g = \frac{d\omega_l}{dk_{l,\text{eff}}} \approx c \left(1 - \frac{1}{3\gamma_r^2} \left(1 + \frac{K^2}{2} \right) \right). \quad (2.53)$$

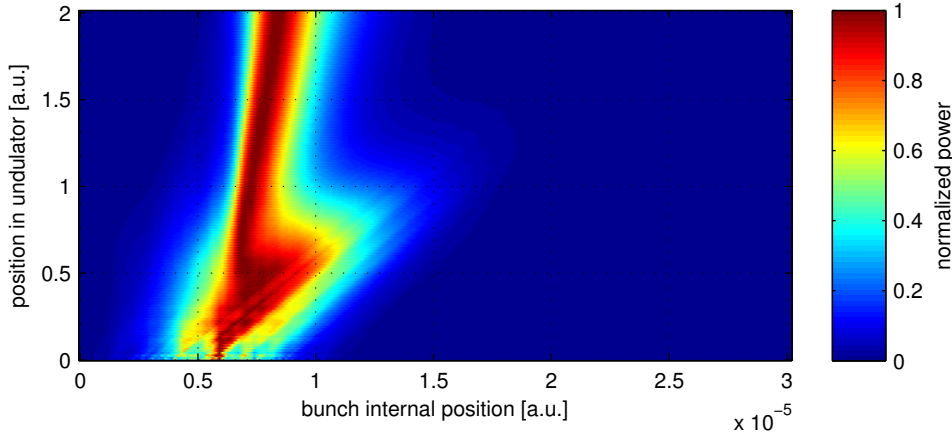


Figure 2.6: Power normalized to the peak power P/P_{peak} for each position in the undulator as a function of the bunch internal position obtained with GENESIS [36]. At the beginning of the FEL process (lower half of the figure) the major part of the power is caused by spontaneous emission that slips through the bunch, i.e. to the right, with one light wavelength per undulator period. As soon as the FEL amplification reaches the exponential gain regime the slippage gets reduced as explained by the reduced group velocity in Eq. (2.54).

To get a more instructive picture, the resulting slippage of a wave packet with respect to the electron bunch can be compared to the corresponding slippage occurring in vacuum [22]

$$\frac{v_g - \bar{\beta}_s c}{c - \bar{\beta}_s c} = \frac{c \frac{1}{6\gamma_r^2} \left(1 + \frac{K^2}{2}\right)}{c - c \left(1 - \frac{1}{2\gamma_r^2} \left(1 + \frac{K^2}{2}\right)\right)} = \frac{1}{3}. \quad (2.54)$$

This relation shows that, although a wave packet is still faster than the electron bunch, the velocity difference between wave packet and electron bunch is significantly reduced during the exponential growth regime. The data obtained with a time-dependent GENESIS [36] simulation shown in Fig. 2.6 clearly shows the difference in slippage velocities for the startup and exponential growth regime. This effect is of importance when optimizing a system with respect to slippage effects (see Sect. 7.3).

2.4 Degrading Effects

The theory discussed so far did not only use several assumptions but also neglected all degrading effects. The goal of this section is to discuss the most important degrading effects. Some effects are already included in the third-order differential equation (2.32) or

the more general integro-differential equation (2.31) and an exact discussion is possible. Other effects not included in the theory can only be estimated in this frame.

2.4.1 Detuning

An effect included in the third order-equation is the detuning characterized by the parameter η . Detuning has been introduced in terms of an energy deviation of the electrons from resonance. It can, however, also be used to characterize a frequency deviation of the light wave from the resonant frequency

$$\eta = -\frac{\omega - \omega_r}{2\omega_r}. \quad (2.55)$$

The minus sign takes into account that a too high frequency corresponds to a too low electron energy and the factor two in the denominator is caused by the γ_r^2 dependence of the frequency on the electron energy.

Using the ansatz $\tilde{E}_x(s) = \sum_{i=1}^3 c_i(\eta) \exp(\alpha_i(\eta)s)$ and the third-order equation (2.32) neglecting space-charge effects yields the eigenvalue equation

$$\frac{\alpha^3}{\Gamma^3} + 2i\frac{\eta}{\rho}\frac{\alpha^2}{\Gamma^2} - \left(\frac{\eta}{\rho}\right)^2 \frac{\alpha}{\Gamma} - i = 0, \quad (2.56)$$

in the case of detuning. From this equation it can already be seen that the Pierce parameters is a scale for the detuning. This equation can be solved analytically, resulting in the eigenvalue leading to exponential growth

$$\alpha_1 = \frac{1}{6} \left(u - \frac{4}{u} \left(\frac{\eta}{\rho} \right)^2 - 4i \frac{\eta}{\rho} \right) \Gamma, \quad (2.57)$$

with the helper function

$$u = \left(108i - 8i \left(\frac{\eta}{\rho} \right)^3 + 12 \sqrt{12 \left(\frac{\eta}{\rho} \right)^3 - 81} \right)^{1/3}. \quad (2.58)$$

The comparison of the growth rate in the case of detuning and the ideal growth rate shown in Fig. 2.7 shows important characteristics: First, the dependence of the growth rate on the detuning is not symmetric. This can be understood as a result of the bucket motion in the phase space, leading to different relative velocities between bucket and electron depending on the sign of detuning. Second, a threshold exists at $\eta \approx 1.88\rho$. Any higher detuning will result in a breakdown of the amplification process. In the phase space this can be understood as the consequence of the high rate of phase change leading to a vanishing net energy change.

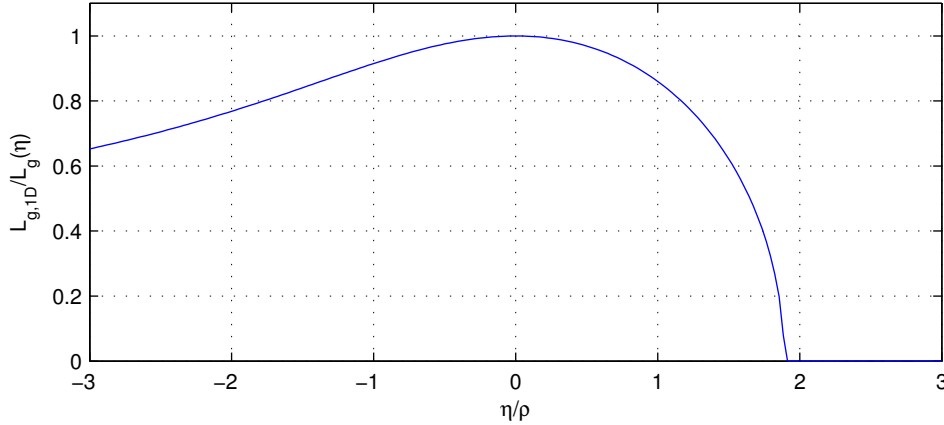


Figure 2.7: Normalized growth rate of the FEL power $L_{g,1D}/L_g(\eta)$ as a function of the relative detuning η/ρ . A threshold is found at $\eta \approx 1.88\rho$. Consequently, too high electron energies or too low photon frequencies cause a complete breakdown of the amplification process. In these cases the location and relative motion of separatrix and electrons differ so much that no resonant interaction is possible. This sets tight limits to the acceptable errors of seeded FELs.

It is in the nature of things that detuning is of high importance for seeded systems. Here the energy jitter of the accelerator as well as the the frequency jitter of the seed source are limited by the requirement $\eta \approx 1.88\rho$. With typical Pierce parameters in the range $\rho = 10^{-3}$ – 10^{-4} this is a challenging requirement.

Detuning can also become important for SASE FELs when other degrading effects are taken into account, e.g. in the presence of a Gaussian energy spread the highest gain does not occur on resonance but for an energy spread dependent detuning (see below).

2.4.2 Energy Spread

Energy spread* is of importance for every system since a perfectly monoenergetic beam cannot be created at any accelerator, although, very low energy spreads are possible with state-of-the-art linear accelerators. Consequently, energy spread is of high importance for all free-electron lasers. The effect is not included in the third-order differential equation due to the assumption of a monoenergetic beam. Therefore, the integro-differential equation (2.31) has to be used to obtain an analytical solution.

*In this section the width and center of the energy distribution are assumed to be constant along the bunch. If the mean energy or the energy spread vary along the bunch, the effective energy spread integrated over one cooperation length has to be used as long as no further correction mechanisms in the setup, like a taper of the undulator, are used.

For an arbitrary energy distribution the eigenvalue equation can be shown to be [19]

$$\alpha = (i\Gamma^3 - k_p^2\alpha) \int \frac{f_0(\eta)}{(\alpha + 2ik_u\eta)^2} d\eta. \quad (2.59)$$

This relation can only be solved analytically for a few distributions not including the typical Gaussian distribution [20]. A Lorentz distribution

$$f_0(\eta) = \frac{1}{\pi} \frac{\Delta}{\eta^2 + \Delta^2}, \quad (2.60)$$

with the half-width at half maximum $\Delta = \sigma_\eta/\rho$ can be used as an approximation of a Gaussian with width $\sigma_\eta = \sigma_\gamma/\gamma$. The normalization using the Pierce parameter already introduces a scale for the energy spread. The resulting eigenvalue equation neglecting space-charge effects and detuning reads [20]

$$\frac{\alpha^3}{\Gamma^3} + 2\Delta \frac{\alpha^2}{\Gamma^2} + \Delta^2 \frac{\alpha}{\Gamma} - i = 0. \quad (2.61)$$

This relation has the same structure as in the case of detuning (2.56) and again allows for an analytical solution. The eigenvalue leading to an exponential amplification is given by

$$\alpha_1 = \left(\frac{u}{6} + \frac{2}{3u} \Delta^2 - \frac{2}{3} \Delta \right) \Gamma, \quad (2.62)$$

using the helper function

$$u = \left(108i + 8\Delta^3 + 12\sqrt{12i\Delta^3 - 81} \right)^{1/3}. \quad (2.63)$$

The resulting growth rate in comparison to the ideal case is shown in Fig. 2.8. Already an energy spread of $\sigma_\eta \approx 0.75\rho$ result in a doubling of the gain length. This range is usually seen as not acceptable due to the larger setup size and higher costs.

As stated above, the more realistic case of a Gaussian energy distribution given by

$$f_0(\eta) = \frac{1}{\sqrt{2\pi}\sigma_\eta} \exp\left(-\frac{1}{2} \left(\frac{\eta - \eta_0}{\sigma_\eta}\right)^2\right), \quad (2.64)$$

with the relative energy spread σ_η and the mean energy detuning η_0 cannot be solved analytically; however, asymptotic expressions for the case of small and large energy spreads in combination with detuning can be derived [22]. Assuming a small energy spread, i.e. $\Delta \ll 1$, and optimizing the detuning for maximum amplification yields the eigenvalue

$$\Re(\alpha_1) \approx \frac{\sqrt{3}}{2} (1 - \Delta^2) \Gamma. \quad (2.65)$$

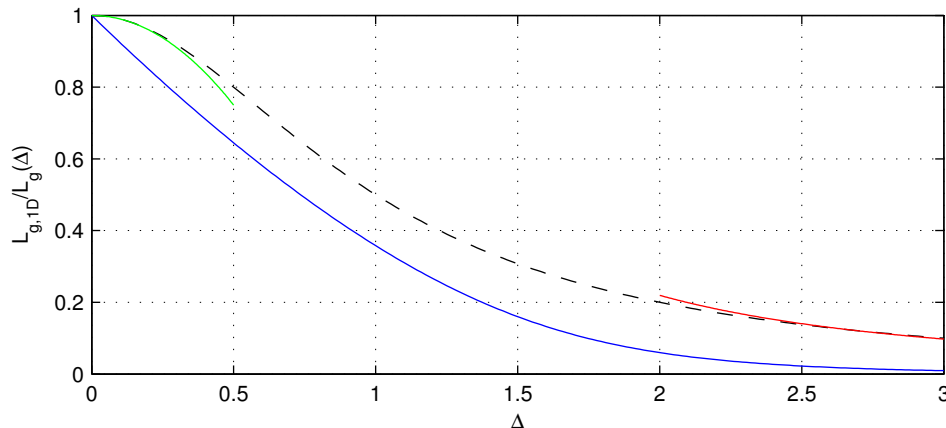


Figure 2.8: Normalized growth rate of the FEL power $L_{g,1D}/L_g(\Delta)$ as a function of the normalized energy spread $\Delta = \sigma_\eta/\rho$. The dependence for a Lorentzian energy distribution is shown in solid blue, solid green and red show the asymptotic dependence for a Gaussian energy distribution based on Eqs. (2.65) and (2.66). The dashed black line uses the approximation (2.67) and results in a good approximation for the shown Δ -range.

The detuning maximizing the growth rate is given by $\eta_{\text{opt}} \approx 3\Delta^2\rho$. For the case of a broad energy spread, i.e. $\Delta \gg 1$, the maximum growth rate is given by

$$\Re(\alpha_1) \approx \frac{0.76}{\Delta^2}\Gamma, \quad (2.66)$$

for an optimum detuning of $\eta_{\text{opt}} \approx \Delta\rho$. An approximation connecting both asymptotic cases is [37]

$$\Re(\alpha_1) \approx \frac{\sqrt{3}}{2} \frac{1}{1 + \Delta^2}\Gamma. \quad (2.67)$$

Comparing the resulting growth rate to the ideal case shows a quick drop already for $\Delta = 0.5$. This leads to the typical requirement

$$\sigma_\eta < \frac{\rho}{2}. \quad (2.68)$$

The impact of energy spread in general, as well as this limit, can also be motivated in the phase space. In general energy spread will smear out the microbunching due to the population of a larger phase space region, reducing the current modulation, leading to a gain reduction. The limit can be motivated as follows: In an undisturbed FEL the quasi-separatrix moves with the rate $d\Psi/dt \approx -ck_u\rho$ in the exponential growth regime as can be shown using the reduced phase velocity and the first-order equations. In terms of the electron motion this rate corresponds to a detuning of $\eta = -\rho/2$ [16]. Electrons with an initial detuning of $\eta \leq -\rho/2$ will therefore on average end up in the left half of a bucket where their net energy change is positive, resulting in a reduction of the field

amplitude. Requiring $\sigma_\eta < \rho/2$ consequently prevents these phase space regions from being populated.

As in the case of detuning, the energy spread requirement is challenging due to the typically small Pierce parameter and pushes the limits of accelerator technology. Consequently, free-electron lasers can be seen as a benchmark for accelerator performance.

2.4.3 Space-Charge

So far all discussions assumed a vanishing impact of space-charge on the FEL performance. This might be justified in many cases; however, space-charge effects will always be present, although they may be small.

In general, space-charge effects can be grouped in two categories: local space-charge effects that are included in the theory derived so far and are based on microbunching and the corresponding charge density modulation on the scale of the light wavelength, and global space-charge effects caused by the finite extension of a real electron bunch. The later will cause an energy chirp within the whole bunch, finally leading to a Coulomb explosion.

Local Effects

To study the impact of local space-charge effects, the third-order differential equation can be solved by using the exponential ansatz. The resulting eigenvalue equation including space-charge effects but neglecting detuning reads

$$\frac{\alpha^3}{\Gamma^3} + \left(\frac{k_p}{\Gamma}\right)^2 \frac{\alpha}{\Gamma} - i = 0. \quad (2.69)$$

The structure of the equation already indicates that the scale for local space-charge effects is given by the gain parameter Γ instead of the Pierce parameter as in the case of energy detuning and spread.

The eigenvalue leading to exponential growth can be determined analytically yielding

$$\alpha_1 = \left(\frac{u}{6} - \frac{2}{u} \left(\frac{k_p}{\Gamma} \right)^2 \right), \quad (2.70)$$

using the function

$$u = \left(108i + 12\sqrt{12 \left(\frac{k_p}{\Gamma} \right)^6 - 81} \right)^{1/3}. \quad (2.71)$$

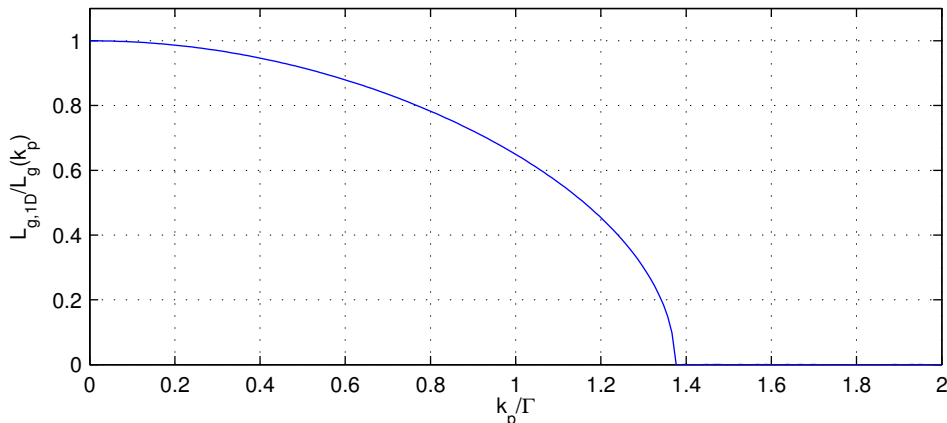


Figure 2.9: Normalized growth rate of the FEL power $L_{g,1D}/L_g(k_p)$ as a function of the normalized space-charge parameter k_p/Γ . A threshold is found at $k_p \approx 1.38\Gamma$. At this point the space-charge forces prevent a build-up of microbunching and therefore prevent the FEL process.

Comparing the so obtained growth rate $\Re(2\alpha_1)$ to the ideal case, as shown in Fig. 2.9, reveals a fast drop, leading to vanishing gain at approximately $k_p \approx 1.38\Gamma$. In this case the space-charge driven debunching counteracting the microbunching prevents it completely and therefore suppresses the FEL process. For short-wavelength FELs this effect is usually negligible due to the high energies and the different energy scalings of the space-charge parameter $k_p \propto \gamma^{-3/2}$ and the gain parameter $\Gamma \propto \gamma^{-1}$.

Global Effects

Global space-charge effects are not included in the theory discussed so far, neither in the first-order equations nor in the third-order or integro-differential equation. Even most numerical codes are not capable of taking this effect into account; however, the impact on the FEL performance can be estimated analytically.

The major space-charge induced effect on the bunch scale is the buildup of a longitudinal energy chirp. Electrons at the bunch head get accelerated while electrons at the bunch tail get decelerated. This energy modulation can reduce the efficiency of the FEL process. To maintain the FEL performance the width of the detuning range traversed by a photon during one gain length has to be smaller than the Pierce parameter [12]. Since a photon slips by one cooperation length per gain length with respect to the electrons, this is equivalent to the requirement

$$l_{\text{co}} \frac{d\eta}{dz} < \rho, \quad (2.72)$$

with $d\eta/dz$ being the relative energy chirp along along the internal bunch coordinate z . The energy modulation will also lead to a longitudinal bunch expansion reducing the peak current and the slope of the induced chirp [38].

For most short-wavelength systems global space-charge effects are negligible due to the energy scaling discussed above, but they can become important for systems as they are discussed in this thesis due to moderate energies and extremely high peak currents [38,39].

2.4.4 Emittance

The beam emittance is a parameter characterizing the transverse beam phase space and is therefore not included in the one-dimensional theory. Any real electron beam will have a finite transverse size and also a transverse momentum spread, leading to changes of the beam envelope along the setup. The beam emittance characterizes the area occupied by the beam in the transverse phase space and is defined as

$$\epsilon_x = \sqrt{\langle x^2 \rangle \langle x'^2 \rangle - \langle x x' \rangle^2}, \quad (2.73)$$

using the transverse particle offset x with respect to the ideal trajectory and the slope of the particle trajectories $x' = dx/dz$. For this definition to hold the condition $\langle x \rangle = \langle x' \rangle = 0$ has to be fulfilled. The same formalism can be applied to the y component. As long as acceleration and degrading effects are neglected the emittance is a conserved quantity.

A finite emittance is always linked to a finite beam divergence, which is equivalent to a transverse velocity spread. This transverse velocity spread gives rise to a longitudinal velocity spread

$$\sigma_{s_\epsilon} = c \frac{\epsilon}{\beta_{\text{av}}}, \quad (2.74)$$

using the average β -function along the setup β_{av} (for more details see Chap. 7). This velocity spread causes any structures in the phase space to be smeared out reducing the microbunching in the same way as an energy spread does. The corresponding effective energy spread is given by

$$\sigma_{\gamma,\epsilon} = \frac{1}{c} \left(\frac{d\bar{\beta}_s}{d\gamma} \right)^{-1} \sigma_{s_\epsilon} \approx \frac{\gamma^3 \epsilon}{\beta_{\text{av}}}. \quad (2.75)$$

Applying the energy spread limit derived above (2.68) leads to an emittance limit

$$\epsilon < \frac{\beta_{\text{av}} \rho}{2\sqrt{2}\gamma^2}, \quad (2.76)$$

that has to be fulfilled to ensure a minimal degradation of the FEL performance due to emittance. This can be rewritten using the more convenient normalized emittance

$\epsilon_n = \gamma\epsilon$, which is conserved during acceleration and holds for any position inside an accelerator as long as degrading effects are neglected. The normalized emittance has to fulfill

$$\epsilon_n < \frac{\beta_{\text{av}}\rho}{2\sqrt{2}\gamma}. \quad (2.77)$$

Assuming an average β -function of $\beta_{\text{av}} \approx 10$ m, a Pierce parameter of $\rho = 10^{-3}$, and an energy of $\gamma = 10^3$ as typical parameters for linear accelerator based free-electron lasers requires a normalized emittance on the order of $\epsilon_n < 4 \cdot 10^{-7}$ m rad. This requirement is pushing the beam quality limits of state-of-the-art linear accelerators.

2.4.5 Diffraction

An assumption implicitly included so far is the perfect overlap of electrons and radiation field. However, even in cases with a constant electron beam size the radiation field will undergo diffractive widening. The radiation produced by an FEL can be described using Gaussian modes as in the case of conventional lasers. Using this formalism the beam widening can be characterized by means of the Rayleigh length

$$s_R = \frac{4\pi\sigma_r^2}{\lambda_l}, \quad (2.78)$$

defined as the length over which the beam cross section doubles. Here the transverse electron beam size σ_r is used since the electrons are the source of the radiation.

An effect counteracting the diffractive losses is the amplification of the radiation in the electron beam leading to so-called gain guiding [19]. For this effect to compensate the diffractive losses, however, a gain length sufficiently short when compared to the Rayleigh length has to be ensured. Due to the opposing requirements on the gain length $L_{g,1D} \propto \sigma_r^{2/3}$, which should be as short as possible, and the Rayleigh length $s_R \propto \sigma_r^2$, which should be as long as possible, a compromise is needed. A typical requirement is a Rayleigh length equaling the field gain length [19]

$$s_R = 2L_{g,1D}. \quad (2.79)$$

Using the corresponding definitions (2.40) and (2.78), the emittance requirement (2.76), and the relation $\lambda_u/2\gamma^2 < \lambda_l$ leads to an alternative version of the emittance requirement based on the radiation wavelength

$$\epsilon \leq \frac{\lambda_l}{4\pi}. \quad (2.80)$$

This relation emphasizes the special challenge in terms of the emittance when aiming for short-wavelength systems.

2.4.6 Bunch Length

Besides the 3D effects also the impact of a finite bunch length has been neglected. For short-wavelength FELs this assumption is usually well justified due to bunch lengths on the order of tens of micrometers and radiation wavelengths on the angstrom scale. For such systems the bunch length σ_z is much longer than the total slippage of the radiation until saturation $\sigma_z \gg 20l_{co}$. In the case of laser-plasma accelerator based systems, however, this assumption is not always justified. Due to the extremely short bunches on the order of a micrometer and less in combination with radiation wavelengths reaching up to the 100-nm-range, light can slip out of the bunch well before saturation is reached. This parameter range is called the superradiant regime [34,35] with characteristics significantly differing from the steady-state regime [32]. One major issue in this regime is the gain reduction, i.e. the increase of the gain length. An analytical solution of the power growth for flat-top current profiles has been derived by Bonifacio et al. [32] for the two extreme cases of a:

- **Long bunch** with $l_b \gg 2\pi l_c$, resulting in the normalized emitted power $E_L = P/(\rho P_{\text{beam}})$ to grow like

$$E_L(\bar{s}) = \frac{1}{3\sqrt{4\pi\sqrt{3}\bar{s}N_{l_c}}} \exp\left(\sqrt{3}\bar{s}\right), \quad (2.81)$$

using the normalized position along the undulator $\bar{s} = s/L_g$, with the gain length defined as $L_g = \lambda_u/4\pi\rho$, and the number of electrons within a cooperation length $N_{l_c} = N_\lambda l_c/\lambda_l$ using the cooperation length $l_c = \lambda_l/4\pi\rho$ and the number of electrons within on radiation wavelength N_λ .

- **Short bunch** with $l_b \leq 2\pi l_c$ with the normalized power scaling as

$$E_L(\bar{s}) = \frac{\sqrt{\bar{l}_b}}{12\pi\sqrt{3}N_\lambda} \frac{\exp\left(3\sqrt{3}(y/2)^{2/3}\right)}{(y/2)^{5/3}}, \quad (2.82)$$

with the normalized bunch length $\bar{l}_b = l_b/l_c$ and $y = \sqrt{\bar{l}_b}\bar{s}$. The scaling of short bunches does not show a typical exponential growth any more but a more complex dependence. Consequently, it is not possible to define a gain length in the sense used so far.

These scalings provide a deeper insight in the FEL physics but are limited by the assumption of a flat-top current profile that is far from the structure of realistic bunches.

An empirical scaling of the gain length and saturation power for short bunches and Gaussian current profiles has been found by S. Bajlekov based on one-dimensional non-period-averaged FEL simulations [35]. The correction of the gain length has been chosen

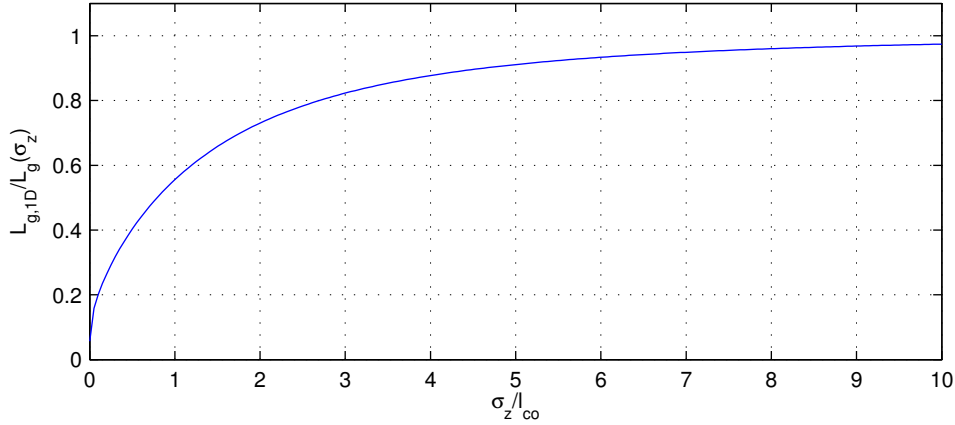


Figure 2.10: Normalized growth rate of the FEL power $L_{g,1D}/L_g(\sigma_z)$ as a function of the normalized bunch length σ_z/l_{co} . If the bunch length is on the order of the cooperation length or even shorter, the growth rate drops due to the reduced interaction time of electrons and light wave.

so that a scaling converging to the ideal behavior in the case of long bunches is ensured. According to the simulations for different parameter ranges, the gain length is well approximate by

$$L_g = L_{g,1D} (1 + \eta_z), \quad (2.83)$$

with the bunch length dependent degradation parameter η_z defined as

$$\eta_z = b_1 \exp \left(b_2 \left(\frac{\sigma_z}{l_{co}} \right)^{b_3} \right), \quad (2.84)$$

and the fit coefficients

$$b_1 = 16.7512, \quad b_2 = -3.0420, \quad b_3 = 0.3267. \quad (2.85)$$

The resulting gain length scaling is shown in Fig. 2.10. As can be expected from theory the scale for slippage effects is given by the cooperation length. A bunch length on the order of the cooperation length leads to a significant increase of the gain length due to the reduced interaction time.

2.5 Ming Xie's Fit

So far all degrading effects have been discussed independently. One widely used scaling combining multiple degrading effects of importance for short-wavelength free-electron

$\alpha_1 = 0.45$	$\alpha_2 = 0.57$	$\alpha_3 = 0.55$	$\alpha_4 = 1.6$
$\alpha_5 = 3$	$\alpha_6 = 2$	$\alpha_7 = 0.25$	$\alpha_8 = 2.9$
$\alpha_9 = 2.4$	$\alpha_{10} = 51$	$\alpha_{11} = 0.95$	$\alpha_{12} = 3$
$\alpha_{13} = 5.4$	$\alpha_{14} = 0.7$	$\alpha_{15} = 1.9$	$\alpha_{16} = 1140$
$\alpha_{17} = 2.2$	$\alpha_{18} = 2.9$	$\alpha_{19} = 3.2$	

Table 2.1: Fit parameters derived by Xie for the gain length scaling (2.86).

lasers has been derived by Xie [37]. The scaling is based on an interpolation of a variational approximation of the evolution of the fundamental mode. The scaling assumes space-charge to be negligible, as is usually justified for short-wavelength systems, and the detuning is optimized for the highest growth rate. For these conditions the gain length can be approximate by

$$L_{g,3D} = L_{g,1D} (1 + \Lambda), \quad (2.86)$$

using the degradation factor Λ . The degradation factor is a function of the three scaled parameters characterizing the impact of:

- **Diffraction** via the ratio of ideal gain length and Rayleigh length

$$\eta_d = \frac{L_{g,1D}}{s_R}. \quad (2.87)$$

- **Emittance** assuming a constant β -function β_{av} along the undulator

$$\eta_\epsilon = \frac{L_{g,1D}}{\lambda_l} \frac{4\pi\epsilon}{\beta_{av}}. \quad (2.88)$$

- **Energy spread** via the ratio of relative energy spread and the Pierce parameter

$$\eta_\gamma = 4\pi \frac{L_{g,1D}}{\lambda_u} \sigma_\eta = \frac{1}{\sqrt{3}\rho} \sigma_\eta. \quad (2.89)$$

Using these parameters the degradation factor is given by

$$\begin{aligned} \Lambda = & \alpha_1 \eta_d^{\alpha_2} + \alpha_3 \eta_\epsilon^{\alpha_4} + \alpha_5 \eta_\gamma^{\alpha_6} \\ & + \alpha_7 \eta_\epsilon^{\alpha_8} \eta_\gamma^{\alpha_9} + \alpha_{10} \eta_d^{\alpha_{11}} \eta_\gamma^{\alpha_{12}} + \alpha_{13} \eta_d^{\alpha_{14}} \eta_\epsilon^{\alpha_{15}} \\ & + \alpha_{16} \eta_d^{\alpha_{17}} \eta_\epsilon^{\alpha_{18}} \eta_\gamma^{\alpha_{19}}. \end{aligned} \quad (2.90)$$

The saturation power for a specific parameter set can be approximated by

$$P_{\text{sat}} \approx 1.6\rho \left(\frac{L_{g,1D}}{L_{g,3D}} \right)^2 P_{\text{beam}}, \quad (2.91)$$

using the electron beam power P_{beam} .

This formalism allows to obtain quick performance estimates for short-wavelength FELs without the need for simulations. It is therefore an invaluable tool for parameter scans and preliminary setup optimizations.

The original scaling can be extended to include the gain length correction for a finite bunch length. The extended scaling is given by [35]

$$L_{g,3D,\sigma_z} = L_{g,1D} (1 + \Lambda) (1 + \eta_z), \quad (2.92)$$

using the modified bunch length correction

$$\eta_z = b_1 \exp \left(b_2 \left(\frac{\sigma_z}{l_{\text{co},3D}} \right)^{b_3} \right). \quad (2.93)$$

Here the cooperation length including 3D effects, i.e. based on the 3D power gain length,

$$l_{\text{co},3D} = \frac{L_{g,3D}}{\lambda_u} \lambda_l, \quad (2.94)$$

has to be used.

This extended scaling is of special interest for laser-plasma based setups operating in, or close to, the bunch length limited regime.

2.6 Summary

In this chapter the physics of a high-gain free-electron laser in the 1D approximation has been reviewed.

The discussion started with the electron motion within the undulator and the generation of spontaneous undulator radiation. It was followed by an overview of the one-dimensional high-gain FEL theory. Subsequent, extensions of the ideal theory taking different degrading effects into account were discussed.

The basic scalings presented in this chapter are the foundation for the design of every high-gain free-electron laser and allow to find a suited parameter range depending on the setup requirements. They will be used in the following chapter in order to motivate a reasonable parameter set allowing for a first FEL demonstration experiment driven by a state-of-the-art laser-wakefield accelerator.

In addition to the ideal FEL characteristics also the inclusion of degrading effects in the design considerations is crucial to assess the feasibility. The effect of energy spread on the FEL performance takes center stage in the design of laser-plasma accelerator

driven systems due to typical energy spreads on the multi-percent-level that exceed the acceptance limits of typical FEL designs by about one order of magnitude. Besides the energy spread also space-charge and diffraction play an important role in the design concept due to the extreme parameter combinations typical for laser-wakefield accelerator based setups.

The setup optimization discussed in the next chapter will rely on the here discussed scalings especially on the extended version of Xie's scaling law taking energy spread, diffraction, emittance, and bunch length effects into account.

3 Concepts for a Laser-Plasma Driven FEL

State-of-the-art X-ray free-electron lasers like the Linac Coherent Light Source (LCLS) are all driven by conventional, radio-frequency (RF) based linear accelerators. They allow to provide high quality electron beams with currents on the kA-level and energies of multiple GeV. In these accelerators the electron bunch is usually generated using a photocathode electron source [6, 40, 41]. Here an ultraviolet (UV) laser illuminates the cathode and extracts the electrons from the surface. The laser properties in combination with the surface geometry define the initial bunch properties. Therefore, this part of the accelerator is crucial for the successful operation of an FEL. Due to the low initial energies, the maximum charge is limited to about 1 nC for state-of-the-art systems [6, 40, 41]. Otherwise, space-charge forces lead to a Coulomb explosion of the bunch and a degradation of the emittance. The resulting currents are on the order of tens of ampere. Afterwards, the bunch is accelerated using RF cavities providing accelerating electrical fields on the order of 10 MV/m. To reach the high electron energies on the order of 10 GeV needed for the operation of a hard-X-ray FEL in the angstrom wavelength range, an accelerator length of about 1 km is needed.

In order to reach short gain lengths, high currents are needed. To increase the current from the few-ampere-level to the kA-range, bunch compressors are used at linear accelerator based facilities. First, an approximately linear, longitudinal energy-position correlation is introduced by off-crest acceleration, resulting in the bunch head to have a lower energy than the bunch tail. Due to the vanishing velocity differences, a dispersive section, a magnetic chicane, is used to introduce energy dependent trajectories. The path length differences lead to a compression of the electron distribution. The maximum achievable compression is, amongst others, limited by the following two points: First, the maximum allowed energy chirp leading to path length differences is limited by the maximum acceptable energy spread of the FEL. Second, emission of synchrotron radiation in the magnetic chicane results in a degradation of the bunch in terms of emittance, and consequently limits the strength of the chicane. The achievable peak currents are on the order of a few kA [6, 41], and allow to reach Pierce parameters on the order of $\rho \approx 5 \cdot 10^{-4}$. In combination with undulator periods of a few centimeters, this leads to a typical saturation length on the order of 100 m (see Eq. (2.42)). Parameter sets of LCLS and the European XFEL are shown in Table 3.1.

	LCLS	XFEL
Peak current [kA]	3.4	5
Energy [GeV]	14.4	17.5
Slice energy spread	$6 \cdot 10^{-5}$	$9 \cdot 10^{-5}$
Undulator period [mm]	30	35.6
Undulator parameter	3.7	3.3
Radiation wavelength [\AA]	1.5	1.0
Pierce parameter	$5 \cdot 10^{-4}$	$5 \cdot 10^{-4}$
Saturation length [m]	86	133
Saturation power [GW]	8	20

Table 3.1: Parameters of LCLS [40] in the high energy mode and the SASE-1 beamline of the European XFEL [6].

These typical numbers show that short-wavelength free-electron lasers are large facilities, leading to high cost and space requirements. Due to these requirements, only few systems of this kind exist and/or are under construction, significantly limiting the availability of their unique radiation.

In order to increase the availability of such sources, drastic changes to the setup have to be made in order to reduce the size as well as the costs. Further improvements of the currently used technology do not allow for significant changes since the systems are already working close to physical limitations, e.g. breakdown effects in the case of the accelerator. To reduce the size of the biggest part of the system, the accelerator, a completely different technology has to be used. A promising candidate is laser-wakefield acceleration [8, 42].

In this chapter the basics of laser-wakefield acceleration, motivating the most important scalings, are reviewed. Based on the parameters of state-of-the-art laser-wakefield accelerators a design parameter set for a first FEL demonstration experiment based on such accelerators is discussed. For the basic parameter set two optimization concepts, longitudinal decompression and transverse dispersion, are compared.

3.1 Laser-Wakefield Acceleration

Laser-wakefield acceleration relies on the intense power of short-pulse lasers allowing to excite plasma waves of high amplitude in gas. These waves, i.e. the charge separation, gives rise to electrical fields three orders of magnitude higher than in conventional, RF-based, linear accelerators, allowing to reduce the acceleration distance by the same factor. Wavebreaking and other injection mechanisms can be used to place electrons in the

accelerating field. The concept of laser-wakefield acceleration has been proposed by Tajima and Dawson in 1979 [8], but only with the availability of high power lasers it has been possible to realize the idea. Since 2004 electron bunches of high quality, charge, and energy have become available [9–11].

3.1.1 Basic Principles

When an intense laser pulse propagates through a plasma, electrons are expelled from the high intensity region of the pulse due to the ponderomotive force [42]

$$\mathbf{F}_p = -mc^2 \nabla \left(\frac{\mathbf{a}_0^2}{2} \right). \quad (3.1)$$

Here $\mathbf{a}_0 = e\mathbf{A}/mc$ is the normalized vector potential of the laser. The positive ions will remain at rest due to their greater mass and result in a restoring force, leading to an oscillation of the electrons around their initial position with the relativistic plasma frequency

$$\omega_p = \sqrt{\frac{e^2 n_e}{\gamma m \epsilon_0}}, \quad (3.2)$$

with n_e being the electron density of the plasma and γ the normalized energy of the oscillating electrons. A plasma wave with the wavelength approximately given by [42]

$$\lambda_p [\mu\text{m}] \approx 3.3 \cdot 10^{10} \sqrt{n_e [\text{cm}^{-3}]^{-1}}, \quad (3.3)$$

is set up behind the laser pulse – a so-called wakefield is created. Assuming a density of $n_e = 10^{18} \text{ cm}^{-3}$ yields $\lambda_p = 33 \mu\text{m}$. This length not only characterizes the wave but also limits the bunch length that can get accelerated*. Since this wave is directly linked to the laser pulse, it propagates with its group velocity. A schematic representation of the process is shown in Fig. 3.1.

The electrons contributing to the wave will not get accelerated themselves but set up an intense longitudinal field [42]

$$E_0 [\text{V/m}] = 96 \sqrt{n_e [\text{cm}^{-3}]}. \quad (3.4)$$

Assuming the same plasma density as above yields a field of $E_0 = 96 \text{ GV/m}$. This exceeds fields achievable in RF-based linear accelerators by approximately three orders of magnitude. This field can be used for the acceleration of electrons on ultra-short length scales, however, a suited injection mechanism for the electron to be accelerated is required.

*The actual bunch length will be a fraction of the plasma wavelength since only one fourth of the wave provides an accelerating and focusing field [42], and the bunch slips with respect to the wave during acceleration.

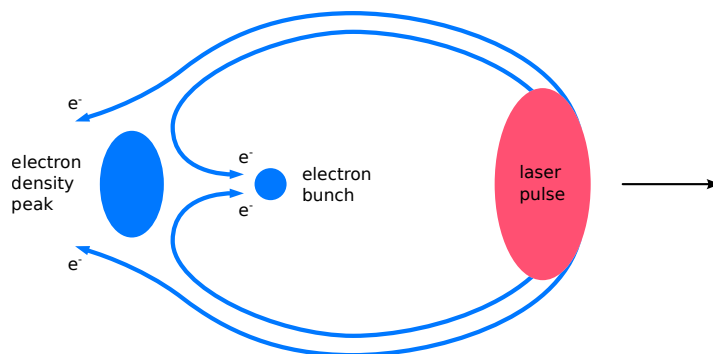


Figure 3.1: Schematic representation of the acceleration process. Electrons of the plasma (blue) get expelled from the high intensity region of the laser pulse (red) that propagates to the right. A plasma wave is created, resulting in an electron density peak trailing the laser pulse. If the laser is intense enough for the given electron density, wave breaking occurs and electrons get trapped in the accelerating region behind the laser pulse.

As in the case of a surfer on a water wave, an electron that is to be accelerated has to have a high enough initial velocity/energy to catch the wave. If the laser intensity is too low, the electrons of the plasma do not have sufficient energy to get trapped and an additional injection mechanism or an external electron source are needed. Schemes for controlled injection are inter alia based on the combination of multiple laser pulses [43,44], ionization-injection [45–47], and plasma density variations [48,49].

Another possibility to reach injection is to use an intense enough driver laser to set up a nonlinear wakefield and ultimately reach wave breaking that causes electrons originally contributing to the plasma wave to get trapped and accelerated. This is the case in the so-called bubble regime [50]. Given enough laser intensity, this approach is easier to realize than controlled injection since no fs-timing and/or μm -position-control are required; however, it also results in less control over the trapping. This is an important point since the trapping mechanism ultimately determines the energy spread that can be achieved.

The achievable energy is limited by several effects [42]:

- **Depletion** – The laser pulse will over time transfer its energy to the plasma wave and the accelerating electrons. Consequently, the distance over that the wakefield can be sustained is limited by the available pulse energy.
- **Dephasing** – Due to the acceleration, the trapped electrons overtake the accelerating wave and reach the decelerating part of the wave after a propagation distance

dominantly depending on the plasma wavelength.

- **Diffraction** – If no optical guiding is used, the laser pulse will widen during the propagation and, after some distance on the order of the Rayleigh length, drop below the intensity required to drive the wakefield.
- **Beam loading** – The trapped electrons reduce the accelerating field due to their own Coulomb field and can even cancel it completely.

The combination of injection mechanism and acceleration distance determines the final energy distribution. Typically, a local energy spread as well as an energy-position correlation, an energy chirp, are to be expected.

3.1.2 State-of-the-Art

Since the first demonstration of high quality electron beams with a well defined energy distribution in 2004 [9–11], huge steps in the direction of a source with beam parameters comparable to large scale linear accelerators have been made.

Over the years, the achievable energy has been increased from about hundred MeV to the multi-GeV-range. The latest published energy record is 4.2 GeV [51], achieved with a laser power of 300 TW within an acceleration distance of nine centimeters. This is only a factor of four below the energy-range used at linear accelerator driven free-electron lasers operating in the hard-X-ray regime and therefore more than sufficient for driving a lab-scale FEL in the UV and X-ray range. With the increased availability of high-power lasers in the PW-range even higher energies are to be expected in the near future.

The energy spread of the produced beams has been reduced from tens of percents down to one percent [52]. New beam diagnostics even indicate a slice energy spread of less than 0.5% [53]. This progress brings a laser-plasma based free-electron laser within grasp.

In addition to the improvements regarding the achievable energy spectra also the beam quality in terms of the normalized emittance has been improved from the multi-mm-mrad-range down 0.1 mm mrad [54]. Here laser wakefield accelerators can even outperform state-of-the-art linear accelerators.

The achievable bunch charges reach up to hundreds of pC [9] and allow in combination with ultra-short bunches on the order 0.5 μm [55, 56] peak currents of multiple kA. At linear accelerators such high currents are – if at all – only available after bunch compression.

This combination of high peak currents, high beam quality, and reasonable energy spread, achievable within ultra-short acceleration distances on the order of a few centimeters makes laser-plasma accelerators a promising candidate for driving compact free-electron lasers. The high currents exceeding the peak currents of conventional linear accelerators

by up to an order of magnitude further lead to a short gain length, allowing for a reduction of the total undulator length. Hence, this technology can be seen as the key to lab-scale free-electron lasers, i.e. fifth-generation synchrotron light sources.

3.2 Parameter Choice

The goal of the parameter set discussed in this section is to allow for a first FEL demonstration experiment using electron bunches produced by a state-of-the-art laser-wakefield accelerator and a compact undulator in the spirit of a lab-scale system. The radiation wavelength is required to be in the ultraviolet or even X-ray range. All electron parameters are chosen so that they are within reach for current generation laser-wakefield accelerators. The undulator and optics parameters are based on existing and recently developed technology. The whole parameter set is chosen to allow for an demonstration of amplification, i.e. the FEL power should exceed the power of the spontaneous undulator radiation by at least an order of magnitude, but it is explicitly not required to reach saturation.

3.2.1 Electrons

Based on experimental results obtained at state-of-the-art laser-wakefield accelerators, several similar parameter sets suited for the operation of a free-electron laser have recently been discussed [17, 57, 58]. The parameters used in this thesis are based on the scheme by Maier et al. [17], and have already been achieved individually, but the combination of all has still to be demonstrated.

The major limiting factor of bunches produced by laser-wakefield accelerators from an FEL point of view is the large relative energy spread typical for these accelerators. A relative projected and slice energy spread of $\sigma_\eta = 1\%$ has been set as a requirement for a first FEL demonstration experiment, and has already been achieved by Wiggins et al. [52]. This value is still challenging for the further FEL design due to the typical requirement $\sigma_\eta < \rho/2$ consequently requiring a Pierce parameter on the percent-level (see Sect. 2.4.2). Any initial energy chirp has been neglected although it is predicted by the laser-plasma accelerator theory and indications for its existence have been obtained in first experiments [53]. Neglecting the initial chirp and assuming the slice energy spread to be as broad as the projected energy spread resembles a worst case scenario in terms of the expected FEL performance and, therefore, results in conservative performance estimates [17]. Assuming an initial chirp in combination with the same projected energy spread leads to a lower slice energy spread and better FEL performance. All concepts discussed in this thesis are also applicable in this case.

The normalized electron energy has been chosen to be $\gamma = 600$. This energy level has already been achieved and even exceeded in multiple experiments [51, 59–62] and is no challenge for the acceleration. It is motivated not only by the availability of such beams but also by the compromise between a short radiation wavelength $\lambda_l \propto \gamma^{-2}$ and a high Pierce parameter $\rho \propto \gamma^{-1}$.

The current profile is assumed to be a Gaussian with an rms length of $\sigma_z = 0.5 \mu\text{m}$ in agreement with recent measurements [55, 56, 59]. While this allows for high peak currents with already moderate amounts of charge, which is beneficial for the FEL process, the short bunch also results in a challenge for a first FEL demonstration experiment due to the requirement $l_{co} \ll \sigma_z$ for negligible degrading effects due to the finite bunch length (see Sect. 2.4.6).

The bunch charge for the subsequent study is set to $Q = 15 \text{ pC}$ and is a compromise between the different cases discussed in [17]. There either a charge of $Q = 20 \text{ pC}$ and an initially uncorrelated energy spread was required, or a charge of $Q = 5 \text{ pC}$ in combination with an initial chirp and a reduced initial slice energy spread with all cases having a projected energy spread of $\sigma_\eta = 1\%$. The amount of charge is not a challenge itself and has already been achieved [59–61]; however, the combination with a small energy spread is challenging for current laser-wakefield accelerators. In combination with the short Gaussian bunch this leads to a peak current of $I = 3.6 \text{ kA}$, comparable with linear accelerator based systems after compression [6, 40].

Based on recent measurements at the accelerator to be used for the experiments the normalized emittance is set to $\epsilon_n = 0.2 \text{ mm mrad}$ [63]. This rather low value, even when compared to RF-based linear accelerators, allows for a small beam size $\sigma_{x,y} \propto \epsilon_n^{1/2}$ and conversely a high current density and Pierce parameter $\rho \propto (\sigma_x \sigma_y)^{-1/3}$ in agreement with the energy spread requirement.

3.2.2 Undulator

The undulator is the heart of every FEL and its parametrization is crucial for the FEL performance. For a first demonstration of a laser-plasma based free-electron laser three aspects are of major importance: First, as mentioned above, the FEL design has to accommodate for the broad energy spread and consequently maximize the Pierce parameter. Second, the gain length should be as short as possible to allow for a demonstration of the FEL process using a short undulator. Third, the cooperation length and hence the radiation wavelength should be in a reasonable range to minimize the performance degradation by slippage effects.

The Pierce parameter scales as $\rho \propto (\lambda_u K)^{2/3}$. This suggests to increase both, the period length as well as the undulator parameter, which is itself proportional to the period length, to increase the energy spread acceptance.

The power gain length, however, scales as $L_{g,1D} \propto \lambda_u^{1/3} K^{-2/3}$. To allow for a gain demonstration within a reasonable undulator length; therefore, the period length should be minimized while keeping the undulator parameter as high as possible.

The cooperation length is proportional to $l_{co} \propto \lambda_l/\rho$. Assuming $K^2 \gg 1$, as required by the previous two scalings, leads to the approximate proportionality $l_{co} \propto \lambda_u^{1/3} K^{4/3}$ favoring a small period length and undulator parameter.

The gain length scaling of Xie [37] taking energy spread into account combined with the bunch length scaling suggested by Bajlekov [35] can be used to estimate the interplay of the various effects. Figure 3.2 shows the resulting gain length scaling based on the electron parameters discussed above. Indeed the combination of a short period length and a high undulator parameter is favorable. However, both are coupled via

$$K = \frac{e}{2\pi mc} \lambda_u B_0 = \frac{e}{2\pi mc} \lambda_u a_1 \exp\left(a_2 \frac{g}{\lambda_u} + a_3 \left(\frac{g}{\lambda_u}\right)^2\right), \quad (3.5)$$

using the definition of the undulator parameter and Elleaume's model for the on-axis field [27]. The parameter range accessible for a conventional hybrid undulator using NdFeB permanent magnets and vanadium permendur poles ($a_1 = 3.694$, $a_2 = -5.068$, and $a_3 = 1.520$) is indicated by the dashed line in Fig. 3.2. For the first demonstration of laser-plasma driven free-electron laser it has been suggested to use a cryogenic undulator to maximize the undulator parameter for a given undulator period and gap [17]. Recently developed cryogenic undulator designs using praseodymium based magnets and vanadium permendur poles, developed by the Helmholtz-Zentrum Berlin [64, 65], can reach an undulator parameter of $K = 3.3$ at a temperature of $T = 50$ K, with a period length of $\lambda_u = 15$ mm and an undulator gap of $g = 3.0$ mm [65]. The fit parameters for the peak field estimate are $a_1 = 4.023$, $a_2 = -3.117$, and $a_3 = 2.012$ [17]. This parameter set has been chosen for the FEL design by Maier et al. [17] with a similar parameter choice made by Couprie et al. [57]. The in general possible parameter combinations accessible by using a cryogenic undulator are indicated by the solid line in Fig. 3.2 clearly showing the advantage of a cryogenic system over conventional designs. The figure also shows that a further increase of the undulator period would only result in small reductions of the gain length while the radiation wavelength would be increased significantly due to the impact of $\lambda_l \propto K^2$. Consequently, the combination of $\lambda_u = 15$ mm and $K = 3.3$ is a good compromise.

The undulator length has been set to $L_u = 2$ m in the spirit of a lab-scale device. The short length allows to avoid any additional electron optics within the undulator or between multiple undulator modules and consequently reduces the number of error sources.

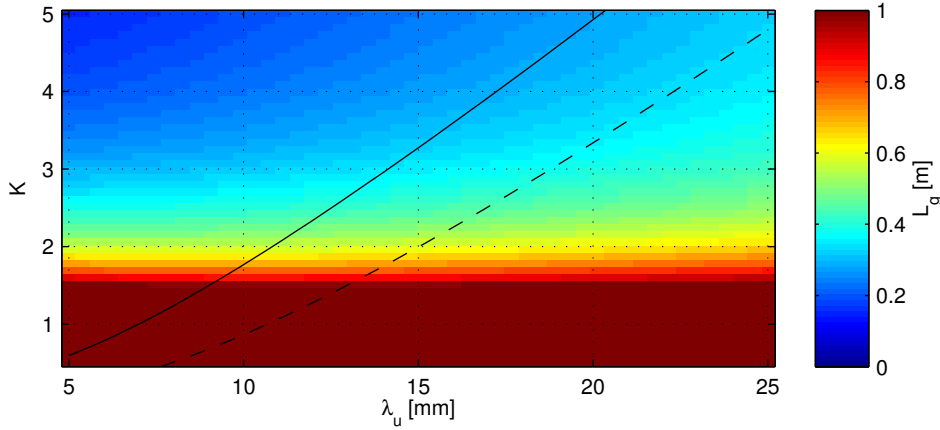


Figure 3.2: Gain length as a function of the undulator period length and undulator parameter for the electron parameters discussed above obtained with the gain length scaling by Xie [37] and the additional bunch length correction by Bajlekov [35] (see Sect. 2.5). The solid line represent parameter combinations accessible by recent cryogenic undulator designs, whereas the dashed line represents the parameter range of conventional NdFeB based undulators.

3.2.3 Optics

The electron optics controlling the beam size have to be designed such that the average beam size along the undulator is minimized, conversely maximizing the Pierce parameter $\rho \propto (\sigma_x \sigma_y)^{-1/3}$.

For the horizontal beam size the undulator can be treated as a free drift having no impact on the beam evolution. To minimize the average beam size along the undulator given by $\bar{\sigma}_x \approx \sqrt{\bar{\beta}_x \epsilon_x}$ it is convenient to minimize the average β -function along the undulator

$$\bar{\beta}_x = \beta_{x,0} - \alpha_{x,0} L_u + \frac{(1 + \alpha_{x,0}^2) L_u^2}{3\beta_{x,0}}, \quad (3.6)$$

using the initial Twiss parameters (for more details see Sect. 7.1 and [66]) $\alpha_{x,0}$, $\beta_{x,0}$, and the undulator length L_u . For a 2-meter-long undulator a minimum of the average β -function is reached for the initial values $\beta_{x,0} = \sqrt{4/3} L_u \approx 2.31$ m and $\alpha_{x,0} = \sqrt{3}$. The corresponding beam size is $\bar{\sigma}_x \approx 20$ μ m.

In the vertical direction the smallest average beam size can be reached by using the focusing properties of the undulator (see Sect. 2.1). The Twiss parameters of a matched beam are $\beta_{y,0} = \sqrt{2}\gamma/(Kk_y) \approx \sqrt{2}\gamma/(Kk_u) \approx 0.61$ m and $\alpha_{y,0} = 0$ for the discussed setup, resulting in a matched beam size of $\sigma_y \approx 14$ μ m. The comparison of horizontal and vertical beam size shows the advantage of using the focusing properties of the undulator.

This parametrization of the beam optics is well accessible with appropriate beam optics but only holds for the design energy of $\gamma = 600$ and neglects chromatic effects that are to be expected due to the broad energy spread. The resulting degradations and corresponding optimization concepts are discussed in Chaps. 7 and 8 and are neglected for the basic concept considerations in order to be independent of a specific optics design.

3.2.4 Summary

Summed up, the chosen parameter set is reasonable in terms of each individual parameter; however, the combination of all electron parameters has not yet been achieved. The derived FEL parameters (see Table 3.2) are reasonable for a first demonstration experiment requiring a few gain lengths only. Regarding the design wavelength and the electron energy the demonstration case is pretty close to the parameters of the first lasing of the TTF-FEL [67]. The comparison with the parameters of the first experiment at the TTF-FEL and the design parameters of LCLS (see Table 3.2), however, shows some noteworthy differences regarding the FEL performance. They are the:

- Ratio of energy spread to the Pierce parameter. In the case of the lab-scale FEL the chosen parameters lead to a ratio on the order of unity, which is close to the energy spread limit $\sigma_\eta < \rho/2$, leading to a significant gain reduction. For the TTF-FEL and LCLS the ratio is up to an order of magnitude smaller, resulting in negligible limitations of the FEL performance due to energy spread.
- Ratio of cooperation length to bunch length. The parameter set of the lab-scale FEL clearly violates the criterion $l_{co} \ll \sigma_z$, which is conversely fully satisfied in both other cases. This relation leads to significant limitations due to slippage effects.
- Ratio of Rayleigh length to gain length. For the lab-scale FEL the typical requirement of $s_R \geq 2L_g$ is not fulfilled at all, resulting in significant diffractive losses reducing the interaction between radiation and electrons. In the case of the TTF-FEL the criterion is also not fulfilled, but it is a near miss, whereas in the case of LCLS the Rayleigh length is an order of magnitude longer than the gain length due to the extremely short wavelength.

All three limitations could be mitigated by increasing the required charge, leading to a higher Pierce parameter and a shorter gain and cooperation length. However, this would result in a more challenging requirement for the accelerator, bringing a first demonstration experiment further away from currently available beams. An alternative to the increase of the required charge is a redistribution of the electrons in the phase space, which will be beneficial in terms of the first two points and is discussed in the next section.

	Lab-Scale FEL	TTF-FEL	LCLS
Electrons			
Peak current [kA]	3.6	0.4	3.4
Energy [GeV]	0.306	0.233	14.4
Energy spread	$1 \cdot 10^{-2}$	$1.3 \cdot 10^{-3}$	$6 \cdot 10^{-5}$
norm. Emittance [mm mrad]	0.2	6	1.2
Bunch length [μm]	0.5	240	23
Undulator			
Undulator period [cm]	1.5	2.73	3
Undulator parameter	3.3	1.17	3.7
FEL			
Radiation wavelength [nm]	135	109	0.15
Pierce parameter	$1.7 \cdot 10^{-2}$	$2.8 \cdot 10^{-3}$	$5 \cdot 10^{-4}$
Rayleigh length [m]	0.037	1.72	32
Cooperation length [μm]	3.7	5.4	0.048
Gain length [m]	0.41	1.35	4.7
Saturation length [m]	6.4	27	86
Saturation power [GW]	2.2	0.05	8

Table 3.2: Parameters of a lab-scale FEL estimated with the formalism of Xie [37] including the bunch length correction of Bajlekov [35] in comparison with the parameters of the first TTF-FEL experiments [67] and the design parameters of LCLS in the high energy mode [40].

The third limitation, the ratio of Rayleigh length to gain length can be optimized by increasing the beam size if a fixed electron parameter set and undulator are assumed. Any increase of the beam size, however, reduces the current density and, therefore, worsens energy spread and slippage effects via an increased 1D gain length and a reduced Pierce parameter. For the given parameter set, minimizing the transverse beam size is the way to go to ensure the best overall performance.

3.3 Decompression Concept

The decompression concept [17, 57, 68, 69] originally intended as a countermeasure for broad energy spreads actually addresses two of the major limitations of the discussed parameter set for a first laser-plasma driven FEL demonstration experiment: the broad energy spread and the short bunch length. The impact of both effects can be significantly reduced using this concept [69]. The idea is to make use of the high phase space density

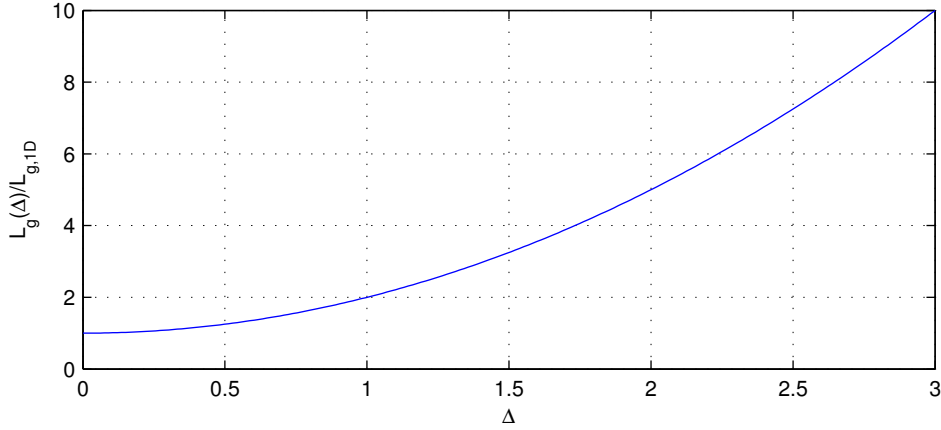


Figure 3.3: Gain length as a function of the normalized energy spread assuming a Gaussian energy distribution based on Eq. (3.7). For an energy spread on the order of the Pierce parameter, i.e. $\Delta = 1$ the gain length gets doubled.

of laser-wakefield accelerator based bunches, and optimize the electron distribution in the longitudinal phase space. Using a dispersive section the bunch can be stretched and effectively sorted by energies, resulting in a reduction of the local energy spread at the cost of a reduced peak current. The interplay of both effects can be optimized. Furthermore, the increased bunch length in combination with the optimized FEL performance minimizes the performance degradation due to slippage effects. This section is completely based on the corresponding publication [69].

3.3.1 Energy Spread Scaling

As discussed in Sect. 2.4.2, the normalized gain length, i.e. the ratio of the gain length taking energy spread into account to the ideal gain length, in the case of a Gaussian energy spread can be approximated by

$$\frac{L_g(\Delta)}{L_{g,1D}} \approx (1 + \Delta^2), \quad (3.7)$$

using the normalized energy spread $\Delta = \sigma_\eta/\rho$ and the ideal, one-dimensional gain length $L_{g,1D}$. This fast increase of the gain length with the normalized energy spread, shown in Fig. 3.3, is one of the major limiting aspects of the parameter set suggested for the laser-plasma driven FEL demonstration experiment.

Assuming an uncorrelated energy spread on the order of the Pierce parameter, as it is the case for the discussed parameter set, allows to reduce the gain length by decompressing

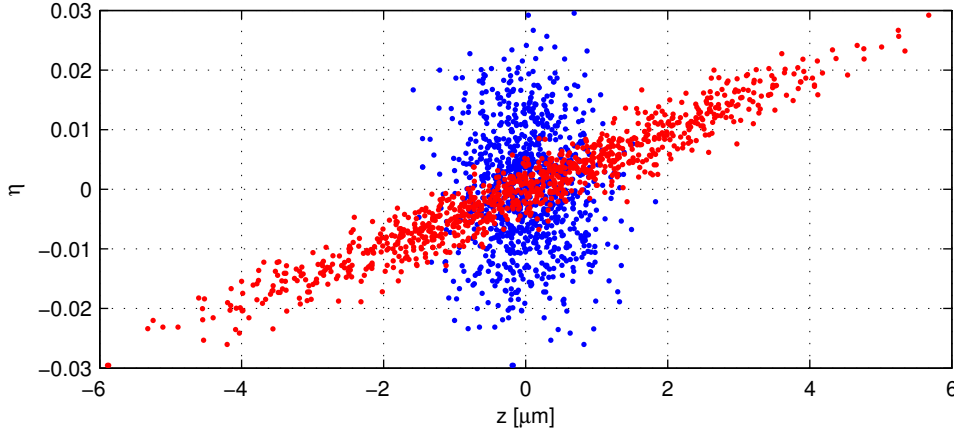


Figure 3.4: Longitudinal phase space of a bunch before (blue) and after (red) decompression. The decompression reduces the local energy spread and the peak current and introduces an energy chirp. To make use of the reduced local energy spread in an FEL, the chirp has to be compensated by a matching taper of the undulator.

the bunch using a dispersive beam transport section like a magnetic chicane. Elongating the bunch by a factor n

$$\sigma_z(n) = n\sigma_{z,0}, \quad (3.8)$$

in a dispersive beam transport section (see Chap. 5 for more details) leads to a reduction of the local energy spread at every longitudinal position along the bunch as well as the current proportional to n^{-1}

$$\sigma_\eta(n) = \frac{\sigma_{\eta,0}}{n}, \quad (3.9)$$

$$I(n) = \frac{I_0}{n}. \quad (3.10)$$

The projected energy spread of the whole bunch is conserved as long as degrading effects in the dispersive section are neglected, but an energy chirp along the bunch is introduced

$$\frac{d\eta}{dz}(n) \approx \frac{\sigma_{\eta,0}}{n\sigma_{z,0}}. \quad (3.11)$$

Figure 3.4 shows the longitudinal phase space of a bunch with an initially uncorrelated energy spread before and after decompression.

The chirp can be compensated by a matching taper of the undulator, i.e. a linear, longitudinal variation of the undulator parameter [70]

$$\frac{dK}{ds} = \frac{\left(1 + \frac{K_0^2}{2}\right)^2}{K_0\gamma^2} \frac{d\eta}{dz}, \quad (3.12)$$

with K_0 being the mean undulator parameter. Due to the taper, the resonance energy for a given wavelength changes along the undulator and allows to maintain resonance for photons propagating through the chirped bunch during the whole interaction time.

The reduced current after the decompression leads to an increase of the ideal gain length $L_{g,1D} \propto \rho^{-1} \propto I^{-1/3} \propto n^{1/3}$. However, at the same time the normalized, local energy spread is decreased $\Delta \propto n^{-2/3}$. The different proportionalities allow to find an optimum of the gain length by balancing the performance gain due to the reduced energy spread with the performance loss caused by the reduced current. The normalized gain length for an initial, normalized energy spread Δ including the decompression factor n reads

$$\frac{L_g(n, \Delta)}{L_{g,1D}} = \left(1 + \frac{\Delta^2}{n^{4/3}}\right) n^{1/3}. \quad (3.13)$$

The resulting scaling of the normalized gain length as a function of the initial normalized energy spread and the decompression factor is shown in Fig. 3.5 in combination with the ideal decompression factor minimizing the gain length for each energy spread given by

$$n_{\text{opt}} = 3^{3/4} \Delta^{3/2}. \quad (3.14)$$

A reduction of the gain length via bunch decompression is consequently possible for cases of $\Delta > 0.6$. For the case of an initial, normalized energy spread of unity $\Delta = 1$ the normalized gain length is minimized for a decompression factor of $n \approx 2.3$ and results in a decrease of the gain length by 13% when compared to the initial gain length. For cases with a small, initial, normalized energy spread $\Delta < 0.6$ the well known bunch compression is favored, which is the case for most linear accelerator based free-electron lasers.

The lab-scale parameter set has a normalized energy spread of $\Delta \approx 0.57$, so in the one-dimensional theory neglecting all further degrading effects no gain length reduction using decompression is possible. For a more realistic estimate of the usability of decompression the second major degrading effect, the bunch length on the order of the cooperation length, has to be taken into account.

3.3.2 Bunch Length Scaling

As discussed in Sect. 2.4.6, the FEL performance can be significantly reduced for bunch lengths on the order of the cooperation length since the radiation slips out of the bunch before being fully amplified. The normalized gain length as a function of bunch length is given by [35]

$$\frac{L_g(\sigma_z)}{L_{g,1D}} = (1 + \eta_z), \quad (3.15)$$

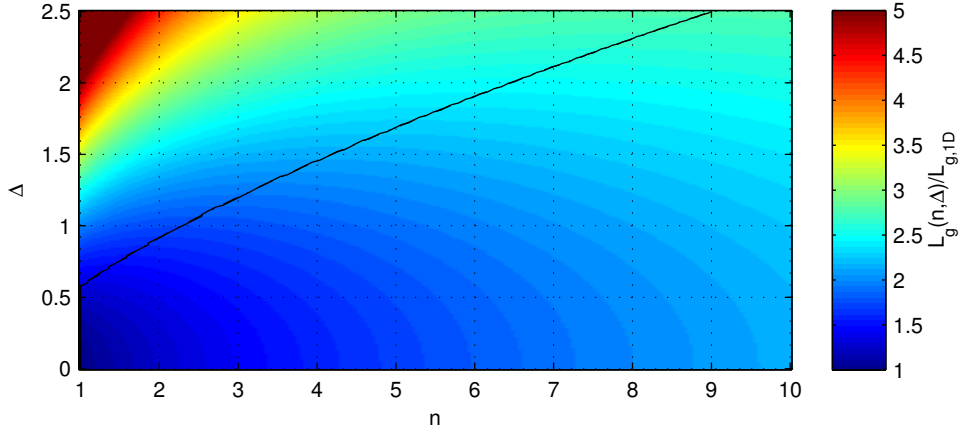


Figure 3.5: Normalized gain length as a function of the initial, normalized energy spread and the decomposition factor based on the energy spread scaling (3.13). The solid black line indicates the ideal decomposition factor for each initial energy spread minimizing the gain length. A gain length reduction is only possible for cases with an initial normalized energy spread of $\Delta > 0.6$.

using the correction parameter

$$\eta_z = b_1 \exp \left(b_2 \left(\frac{\sigma_z}{l_{\text{co},1D}} \right)^{b_3} \right), \quad (3.16)$$

with the bunch length σ_z , the cooperation length $l_{\text{co},1D} = \lambda_l L_{g,1D} / \lambda_u$, and the fit parameters

$$b_1 = 16.7512, \quad b_2 = -3.0420, \quad b_3 = 0.3267. \quad (3.17)$$

As in the energy spread scaling, a decompression affects the relevant quantities, the normalized bunch length $\sigma_z / l_{\text{co},1D}$ and the gain length, in different ways. The gain length increases as $L_{g,1D} \propto n^{1/3}$, whereas the normalized bunch length increases proportional to $\sigma_z / l_{\text{co},1D} \propto n^{2/3}$. This again suggests the possibility of an optimization of the gain length for cases limited by the bunch length using decompression. The normalized gain length is given by

$$\frac{L_g(n, \sigma_z)}{L_{g,1D}} = \left(1 + b_1 \exp \left(b_2 \left(\frac{\sigma_z}{l_{\text{co},1D}} n^{2/3} \right)^{b_3} \right) \right) n^{1/3}, \quad (3.18)$$

using the initial bunch length σ_z and the decomposition factor n . Evaluating this relation shows that for all values of $\sigma_z > 0$ and $n \geq 1$ this is a monotonically increasing function of n (see Fig. 3.6); consequently, decompression cannot be used to optimize the FEL performance of bunch length limited cases as long as other degrading effects are neglected.

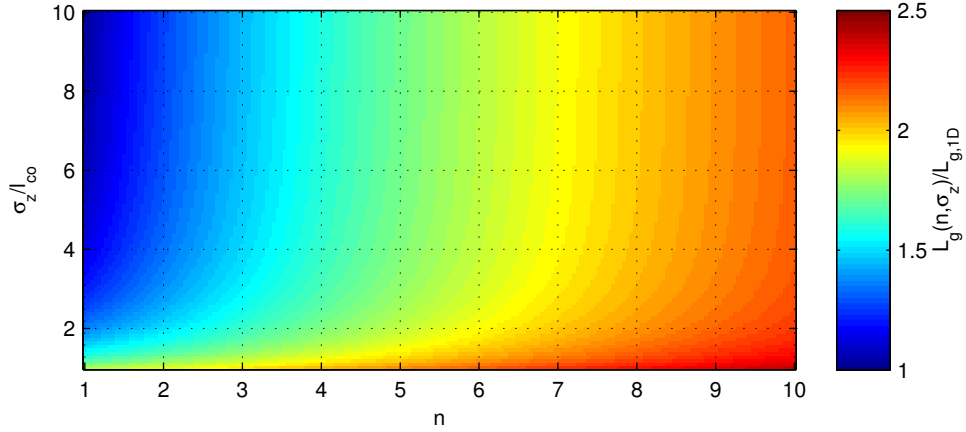


Figure 3.6: Normalized gain length as a function of the initial, normalized bunch length and the decomposition factor based on the bunch length scaling Eq. (3.18). The gain length rises significantly for $\sigma_z/l_{co} \sim 1$. It can clearly be seen that no gain length reduction by decompression is possible independent of the initial normalized bunch length.

3.3.3 Combined Scaling

Both effects discussed above, energy spread and slippage in combination with the short bunch, are of high importance for the lab-scale FEL demonstration experiment. Consequently, a combined scaling taking both effects into account is necessary. This can be achieved by applying the energy spread scaling first and using the corrected gain length for the bunch length scaling

$$L_g(n, \Delta, \sigma_z) = \left(1 + b_1 \exp \left(b_2 \left(\frac{n\sigma_z}{l_{co}(n, \Delta)} \right)^{b_3} \right) \right) \left(1 + \frac{\Delta^2}{n^{4/3}} \right) n^{1/3} L_{g,1D}, \quad (3.19)$$

using the initial bunch length σ_z , the initial energy spread Δ , the decompression factor n , and the cooperation length for the case of energy spread and decompression $l_{co}(n, \Delta) = \lambda_l L_g(n, \Delta) / \lambda_u$. The combined scaling shows that decompression can be even more efficient than indicated by the individual scalings. For cases that are limited by both effects, even the bunch length scaling can be improved using decompression. The reduction of the gain length in the case of energy spread and decompression $L_g(n, \Delta)$ leads to a decrease of the associated cooperation length $l_{co}(n, \Delta)$ in contrast to the simple bunch length scaling where a decompression leads to an increase. The combination of the reduction of the cooperation length and the increase of the bunch length allows for a further reduction of the final gain length in the combined scaling. Figure 3.7 shows the combined scaling as a function of the energy spread and the decompression factor for different ideal ratios of bunch length to cooperation length $\sigma_z/l_{co,1D}$.

For an initial energy spread of $\Delta = 1$ and a normalized bunch length of $\sigma_z/l_{co,1D} = 1$

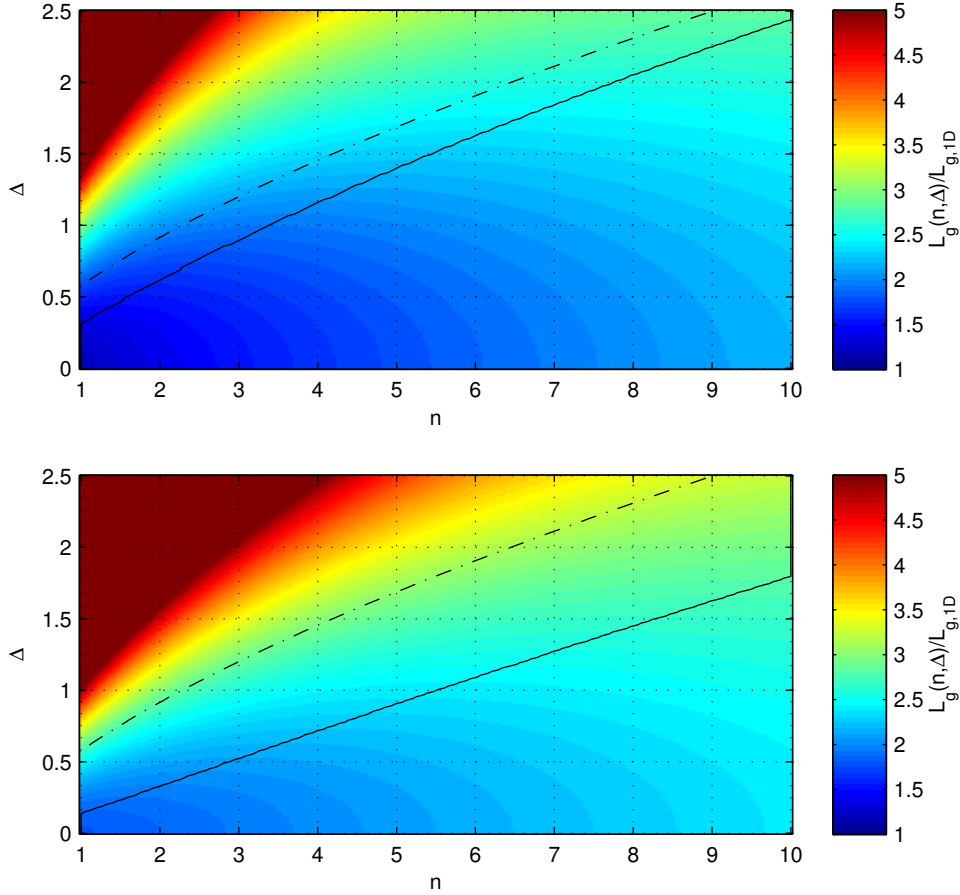


Figure 3.7: Normalized gain length as a function of the normalized energy spread Δ and the decomposition factor n calculated with the combined scaling Eq. (3.19) for a normalized bunch length of $\sigma_z/l_{co,1D} = 3$ (top) and $\sigma_z/l_{co,1D} = 1$ (bottom). The solid black line indicates the ideal decomposition factor for a given initial energy spread, and the dash-dotted black line indicates the ideal decomposition factor obtained with the simple energy spread scaling Eq. (3.7). The comparison of both cases shows a significant increase of the gain length for short normalized bunch lengths as well as an increase of the ideal decomposition factor.

the ideal decompression factor increases to $n \approx 5.5$, allowing for a gain length reduction by 52%. Comparing this to the scaling taking only energy spread into account where a reduction of 13% was possible shows the importance of including the bunch length scaling.

The lab-scale scenario has a ratio of bunch length to cooperation length of $\sigma_z/l_{\text{co},1D} = 1.4$. Taking the energy spread of $\Delta \approx 0.57$ into account it decreases to $\sigma_z/l_{\text{co}}(\Delta) = 1.1$. The individual scalings allowed for no reduction of the gain length with these parameters. However, the combined scaling shows a reduction of the gain length of approximately 17% for an optimized decompression factor of $n_{\text{opt}} \approx 2.7$. This can be understood as follows: the normalized energy spread, although it is not high enough to allow for optimization via decompression in the individual scaling, leads to a slower increase of the energy spread affected gain length $L_g(n, \Delta)$ during decompression when compared to a case neglecting energy spread. This translates into a slower growth of the corresponding cooperation length $l_{\text{co}}(n, \Delta)$, altering the bunch length scaling so that it is not monotonously growing anymore, leading to the afore mentioned optimum.

3.3.4 3D Scaling and Simulation

The combined scaling has been tested with a period-averaged 1D code [71] and the period-averaged 3D code GENESIS [36]. Both test were based on the parameter set for the FEL demonstration experiment discussed above (Table 3.2). The decompression has been modeled using Eqs. (3.9)–(3.11). In both simulations the undulator has been tapered according to Eq. (3.12) to compensate the energy chirp.

The resulting gain length scaling as a function of the decompression factor n is shown in Fig. 3.8. For both simulations 10 independent runs have been performed for each decompression factor, and the results have been averaged. The combined scaling and the result of the 1D simulation are in good agreement indicating the possibility of a gain length reduction with an optimum decompression factor in the range $n_{\text{opt}} \approx 2\text{--}3$. A slight deviation in the absolute numbers is found for small decompression factors which can be attributed to the fact that the bunch length scaling has been obtain with a non-period-averaged code [35, 72] in contrast to the here used period-averaged code since this type of simulation has been shown to underestimate the FEL performance for short bunches [73]. The simple energy spread scaling (3.7), in contrast to the combined scaling (3.19), shows a monotonous growth of the gain length with the decompression factor as expected. This confirms the importance of the bunch length correction for the here discussed case.

The significantly higher gain lengths obtained with GENESIS are the result of the additional degrading effects like diffraction, space-charge, emittance, and the evolution of the beam envelope taken into account. Without decompression $n = 1$ the emitted power was dominated by the spontaneous emission, leading to a linear power growth only, allowing

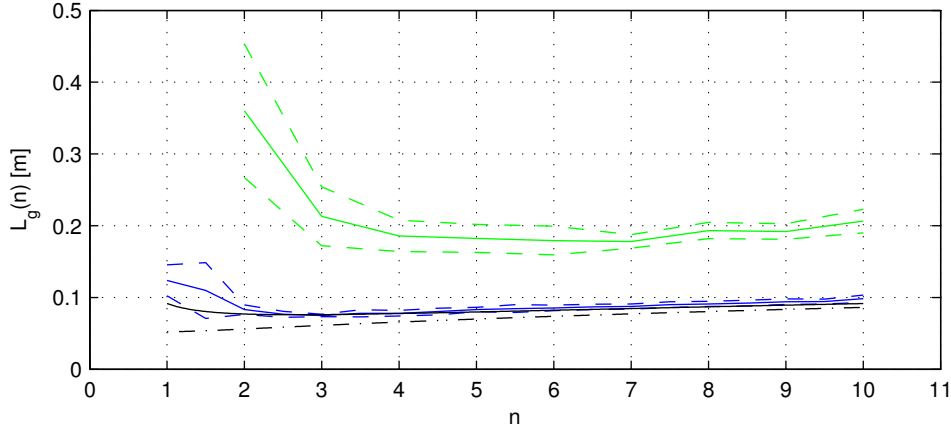


Figure 3.8: Gain length $L_g(n)$ as function of the decomposition factor obtained with the energy spread scaling (dash-dotted black) and the combined scaling including the bunch length correction (solid black). For the verification of the analytical scaling a 1D simulation with 10 runs per decomposition setting has been used, resulting in the mean gain length shown by the solid blue line, the standard deviation of the runs is indicated by dashed blue line. The result of a 3D scan obtained with GENESIS is shown in green, again the mean of 10 runs is indicated by the solid line, the standard deviation is shown by the dashed line.

no gain length to be estimated. In general, the 3D scaling confirms the applicability of the decompression concept. The effect is even more pronounced than in the 1D case making decompression essential to obtain an FEL signal at all. Besides the general increase of the gain length when compared to the 1D simulations also the optimum decompression factor increases to $n_{\text{opt}} \approx 4$.

The more pronounced decompression factor dependence in the three-dimensional simulations can be motivated using Xie's analytical model [37] in combination with the bunch length scaling (see Sect. 2.5). Figure 3.9 shows the individual degradation coefficients of Xie's formula including the fit parameters as a function of the decompression factor. The four most important degradation factors are related to the bunch length, energy spread, diffraction, and the combined effect of diffraction and energy spread. All other factors are at least two orders of magnitude smaller in the nondecompressed case $n = 1$. The significant impact of diffraction has been neglected so far and explains the higher gain lengths obtained in 3D simulations in comparison to the 1D values. The additional degradation factors, especially the diffraction related contributions, lead to a shift of the ideal decompression factor to $n_{\text{opt}} \approx 4$. For the lab-scale parameter set, decompression consequently leads to a reduction of the bunch length correction as well as all energy spread related terms, overcompensating the growth of the diffraction contribution and the further, smaller degradation factors for the discussed parameter range.

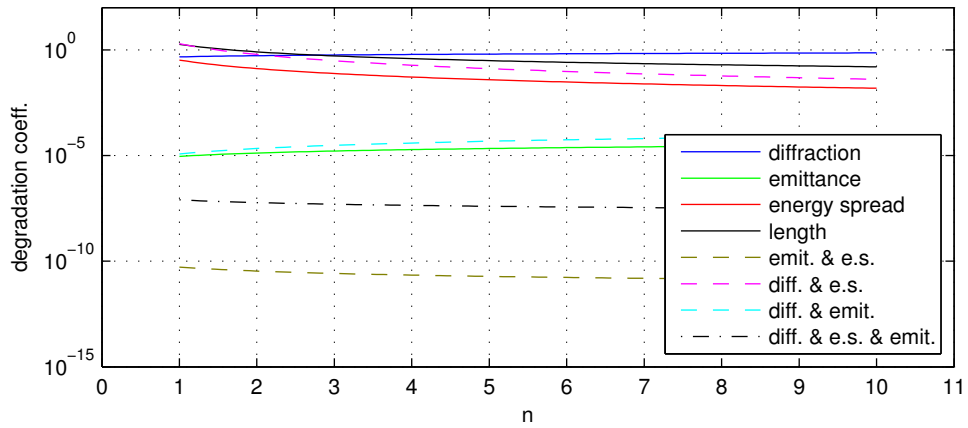


Figure 3.9: Degradation coefficients of Xie’s formula with bunch length correction (see Sect. 2.5) including fit parameters, i.e. the diffraction coefficient corresponds to $\alpha_1 \eta_d^{\alpha_2}$ etc., as a function of the decompression factor for the lab-scale parameter set. Solid lines characterize individual contributions, whereas dashed lines refer to the combinations of two degrading effects. The most important degrading effects are the already discussed energy spread and bunch length limitation, but also diffraction plays an important role. The combined coefficient of diffraction and energy spread even overcomes both individual coefficients in the nondecompressed case $n = 1$. All other correction factors are at least one order of magnitude smaller. Decompression reduces the bunch length correction as well as all energy spread related coefficients. This reduction overcompensates the growth of the diffraction term.

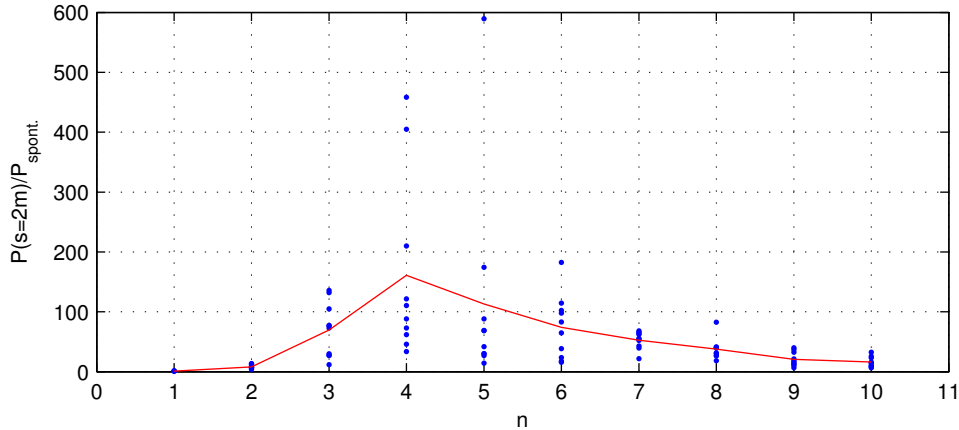


Figure 3.10: Ratio of power at the end of the undulator to spontaneous emission simulated with GENESIS. The power is evaluated within 100% bandwidth around the fundamental. Blue dots represent individual runs with different shot-noise seeds for the same general configuration. The solid red line is the mean value of the independent runs for each scenario. As in the gain length scaling in Fig. 3.8 an optimum decomposition factor of $n_{\text{opt}} \approx 4$ is found.

The figure of merit for a first lab-scale FEL demonstration experiment is the demonstration of gain, i.e. a significantly higher output power than in the case of spontaneous emission. As a design goal a ratio of $P_{\text{total}}/P_{\text{spont.}} \geq 10$ at the end of the undulator has been suggested [17]. Figure 3.10 shows this ratio at the end of the undulator obtained with GENESIS as a function of the decomposition factor. The power is evaluated within 100% bandwidth around the fundamental. As in the gain length scaling above (see Fig. 3.8) an optimum decomposition factor of $n_{\text{opt}} \approx 4$ is found maximizing the power ratio. The design goal of a ratio of at least an order of magnitude is fulfilled over a wide range of decomposition factors $n = 3$ –10. Since the design goal is exceeded by an order of magnitude for the ideal decomposition factor, one could relax the requirements on the initial bunch, but the excess will be kept as a safety margin since all degrading effects in the beam transport system, consisting of the electron optics and the dispersive section, have been neglected so far.

In the discussion of the energy spread scaling (Sect. 3.3.1) it has been stated that the electron energy chirp can – and has to – be compensated by a matching taper. For the parameter set of the lab-scale system with a decomposition factor of $n = 4$ the energy chirp is $d\gamma/dz = 3 \mu\text{m}^{-1}$ requiring a relative taper of $dK/(K_0 ds) \approx 5.3\%/m$ according to Eq. (3.12). Figure 3.11 shows the power ratio of total power to spontaneous emission at the undulator exit for a decomposition factor of $n = 4$ as a function of the relative taper. The power scaling confirms the theoretical model and shows that a matching taper is crucial for the decomposition concept. Without taper the power ratio drops by

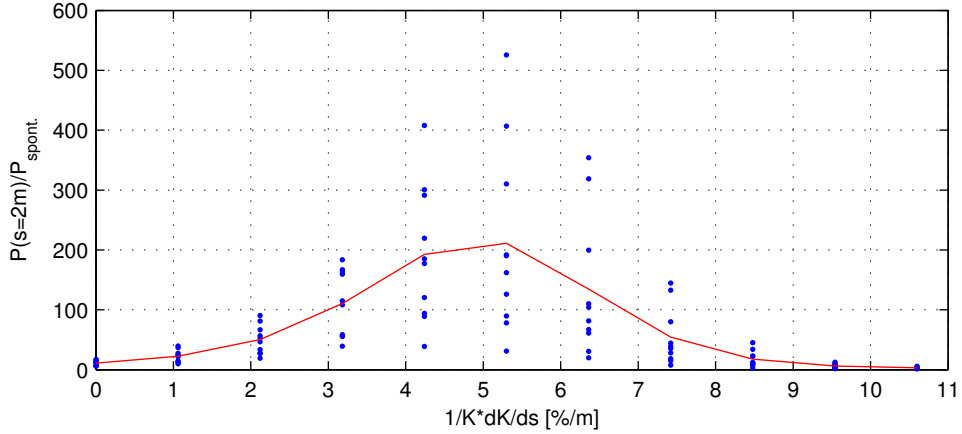


Figure 3.11: Ratio of total power to spontaneous emission at the end of the undulator as a function of the relative taper simulated with GENESIS. The blue dots represent independent runs with different shot-noise seeds for each undulator configuration. The red line indicates the average for each setup. As expected from the analytical calculation Eq. (3.12), the power is maximized for $dK/(K_0 ds) \approx 5.3\%/m$. The simulation result demonstrates that a correct taper of the undulator is essential for the decompression concept and the demonstration of radiation amplification.

more than one order of magnitude to $P(s = 2 \text{ m})/P_{\text{spont.}} \approx 11$ just above the desired limit.

The required gap variation for a given taper can be approximated based on Elleaume's formula (2.3) and is given by

$$\Delta g = \exp\left(\frac{a_2}{\lambda_u} + 2a_3 \frac{g_0}{\lambda_u^2}\right)^{-1} \frac{\Delta B}{B_0}. \quad (3.20)$$

For the case of a cryogenic undulator with the coefficients $a_1 = 4.023$, $a_2 = -3.117$, and $a_3 = 2.012$ [17], and a nominal gap $g_0 = 3 \text{ mm}$ the desired taper along a 2-meter-long undulator leads to a gap variation of $690 \mu\text{m}$. The required taper is feasible for the discussed setup [74] but also limits the maximum undulator length. Longer undulators can only support slower variations of K along the undulator which either requires a stronger decompression leading to a reduction of the chirp or an operation at a higher energy, with both approaches reducing the slippage and the required taper for a given chirp.

Figure 3.12 shows the growth of the power normalized to the spontaneous emission along the undulator for the unstretched case, a decompressed case without taper, and a decompressed case with taper. The unstretched case leads to spontaneous emission only, whereas both decompressed cases show a significant power growth due to the FEL process. The correct taper significantly reduces the gain length as previously shown

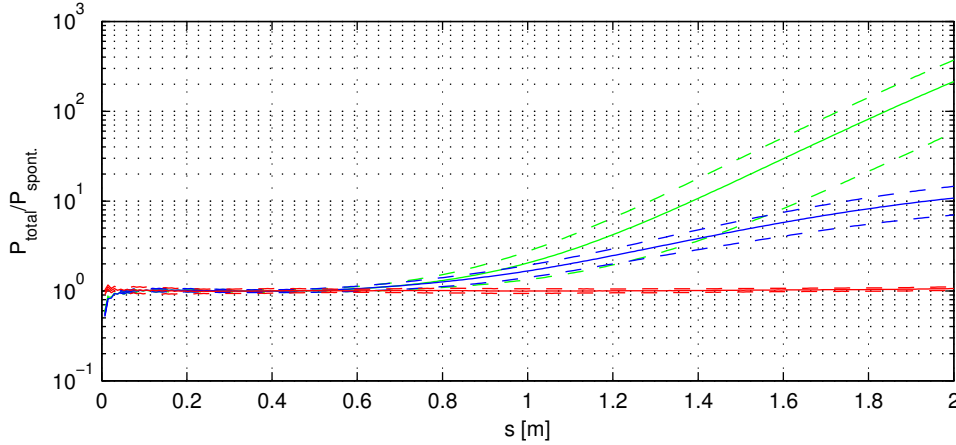


Figure 3.12: Total power normalized to the spontaneous emission as a function of the position along the undulator simulated with GENESIS for an unstretched bunch (red), a stretched bunch with $n = 4$ and an untapered undulator (blue), and a stretched bunch with a tapered undulator (green). Solid curves show the mean of ten independent runs, dashed lines indicate the standard deviation of the runs. Only in the stretched and tapered case an exponential power growth can be ensured along the whole undulator.

and also ensures an exponential power growth along the whole undulator, whereas the untapered case shows a reduction of the power growth from $s \approx 1.5$ m on. This can be understood as a loss of resonance between radiation and electrons due to the missing taper.

The decompressed case stretched by a factor of $n = 4$ and the corresponding tapered undulator will from now on be used as the reference case for all further discussions. A comparison of the initially suggested parameter set and the modified, decompressed version is shown in Table 3.3. So far, all degrading effects occurring during the beam transport and especially the decompression have been neglected. A detailed discussion of the decompression itself including degrading effects like coherent synchrotron radiation is presented in Chaps. 5 and 6. The influence of the optics, especially the chromaticity, is assessed in Chap. 7, and the interplay of the various setup parts and degrading effects is discussed in Chap. 8.

3.3.5 Coherent Spontaneous Emission

A characteristic of laser-plasma based bunches is the short bunch length on the micrometer or even sub-micrometer scale. Depending on the radiation wavelength and the current profile this can lead to coherent spontaneous emission (CSE) of radiation in the undulator without any microbunching [75, 76]. The so produced high output power could be

	Lab-Scale FEL (basic)	Lab-Scale FEL (decomp.)
Electrons		
Peak current [kA]	3.6	0.9
Energy [MeV]		306
Energy spread (relative)	$1 \cdot 10^{-2}$	$0.25 \cdot 10^{-2}$
Chirp (relative) [%/ μm]	0	0.5
norm. Emittance [mm mrad]		0.2
Bunch length [μm]	0.5	2
Undulator		
Undulator period [cm]		1.5
Undulator parameter		3.3
Taper [%/m]	0	5.3
FEL		
Radiation wavelength [nm]		135
Pierce parameter	$1.7 \cdot 10^{-2}$	$1.1 \cdot 10^{-2}$
Rayleigh length [m]		0.037
Cooperation length [μm]	3.7	1.4
Gain length [m]	0.41	0.17
Saturation length [m]	6.4	2.8
Saturation power [GW]	2.2	1.4

Table 3.3: Parameters of a lab-scale FEL estimated with the formalism of Xie [37] including the bunch length correction of Bajlekov [35] for the basic case and the decompressed case with a decompression factor $n = 4$.

mistaken for an FEL signal. The total power of spontaneous emission is given by the sum of coherent and incoherent power and can be written as

$$P(k) = P_1 (N_e + N_e(N_e - 1)f(k)) \approx N_e P_1 + N_e^2 P_1 f(k), \quad (3.21)$$

using the number of electrons in the bunch N_e , the power emitted by an individual electron P_1 , and the longitudinal form factor $f(k)$. The form factor depends on the wavenumber $k = k_l - k_u$ [76], k_l and k_u being the wavenumber of the radiation and the undulator, as

$$f(k) = \left| \int \lambda(z) \exp(ikz) dz \right|^2, \quad (3.22)$$

using the normalized current profile $\lambda(z)$, i.e. $\int \lambda(z) dz = 1$.

Since the figure of merit for a lab-scale FEL demonstration experiment is the power ratio $P_{\text{total}}/P_{\text{spont.}}$, it has to be ensured that the ratio of coherent to incoherent emitted power of the spontaneous emission given by

$$\frac{P_{\text{spont., coh.}}}{P_{\text{spont., incoh.}}} \approx N_e f(k), \quad (3.23)$$

is significantly smaller so that CSE cannot be mistaken for an FEL signal. Depending on the number of electrons and the current profile, however, this ratio can reach high numbers. Assuming a smooth Gaussian current profile the form factor is given by

$$f_{\text{Gaussian}}(k) = \exp(-k^2 \sigma_z^2), \quad (3.24)$$

using the wavenumber k as defined above and the rms length of the bunch σ_z . Even for an unstretched bunch with a length of $\sigma_z = 0.5 \mu\text{m}$ and setup parameters as in Table 3.2 the form factor is of the order of $f_{\text{Gaussian}} \approx \exp(-547) \ll 1/N_e$ and consequently coherent emission is negligible for any reasonable number of electrons. However, a smooth Gaussian is highly idealized and a bunch could have steeper edges better resembled by a parabolic or even flat-top distribution. For these cases the form factors are given by

$$f_{\text{parabola}}(k) = \left| \frac{3 \sin(kl/2)}{8 k^3 l^3} - \frac{3 \cos(kl/2)}{4 k^2 l^2} \right|^2, \quad (3.25)$$

$$f_{\text{flat-top}}(k) = \left| \frac{2}{k^2 l^2} (1 - \cos(kl)) \right|^2, \quad (3.26)$$

using the full length l in both cases. Assuming the same full width at half maximum as in the case of the Gaussian for all distributions the form factors become $f_{\text{parabola}} \approx 1.6 \cdot 10^{-7}$ and $f_{\text{flat-top}} \approx 2.8 \cdot 10^{-3}$. In the lab-scale case the electron number is approximately $N_e \approx 10^8$ and hence the power of the coherent spontaneous emission can reach the same order of magnitude as the FEL power and even exceed it by several orders of magnitude.

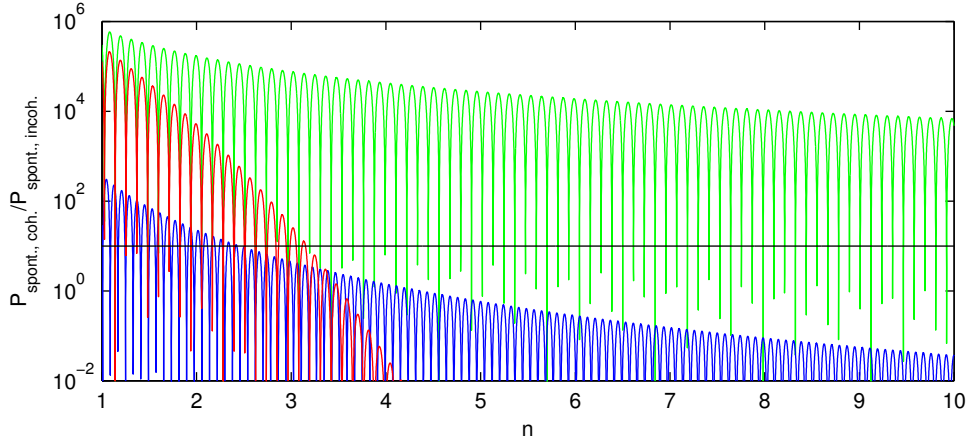


Figure 3.13: Power ratio of coherent to incoherent spontaneous emission as a function of the decompression factor for a flat-top distribution (green), a parabola shaped bunch (blue), and the convolution of flat-top bunch with a narrow Gaussian having a width of $2 \cdot 10^{-8} \mu\text{m}$ (red). All distributions have the same full width at half maximum as the originally proposed Gaussian bunch with an rms length of $\sigma_z = 0.5 \mu\text{m}$. The limit for the demonstration of FEL amplification of $P_{\text{total}}/P_{\text{spont.}} = 10$ is shown in black. A decompression by a factor of $n = 4$, as aimed at according to the previous optimization of the FEL performance, leads to a reduction of CSE below the critical detection level of the FEL signature.

Using the decompression approach the bunch length and therefore the form factor can be manipulated, allowing for a reduction of the coherent emission while at the same time increasing the FEL power. Figure 3.13 shows the ratio of coherent to incoherent spontaneous emission for three different bunch profiles: flat-top, parabola like, and smoothed flat-top. In all smooth cases the power ratio drops below the proposed FEL detection limit for a decompression factor of $n \geq 3$. Only in the extreme case of a sharp flat-top bunch a high power ratio is maintained for all discussed decompression factors $n \leq 10$.

For all cases discussed so far the basic bunch shape has been fixed while only varying its length. Assuming a Gaussian energy distribution in combination with the current profiles discussed above and a decompression in a dispersive section, e.g. a magnetic chicane, changes the situation. As soon as the bunch length is changed significantly in the chicane $R_{56}\sigma_\eta \geq l$, with R_{56} being the linear transport matrix element of the chicane linking longitudinal position and energy deviations (see Chaps. 5 and 7 for more details), and the bunch length l , the current profile converges to a Gaussian with a length of $\sigma_z \approx R_{56}\sigma_\eta$. This leads to an exponential drop of the coherently emitted power independent of the exact initial bunch shape.

The analytical scaling is confirmed by tracking individual electrons; however, the noise of a realistic electron distribution limits the minimum achievable power ratio to $N_e f(k) \approx 1$

for all discussed distributions. Since this level is an order of magnitude below the limit for an FEL signature, decompression can still provide a valuable tool to avoid the problem of mistaking a CSE signal for an FEL.

If necessary, further options to distinguish between a CSE and an FEL signal exist [77]. Since CSE only depends on the longitudinal form factor, the beam diameter can be varied without affecting the CSE power level. On the contrary the FEL gain length is proportional to $L_g \propto (\sigma_x \sigma_y)^{1/3}$, leading to a high sensitivity to any changes of the beam size. Furthermore, the taper of the undulator can be varied dominantly affecting the FEL performance (see Fig. 3.11) but not the power level of the spontaneous emission.

To sum up, coherent spontaneous emission can in general be mistaken for an FEL signal especially in scenarios with radiation wavelengths on the order of the bunch length as in the demonstration FEL concept. However, the decompression concept inherently suppresses CSE and provides several possibilities to distinguish it from an FEL signature.

3.4 TGU Concept

An alternative to the decompression concept in high energy spread cases is the transverse gradient undulator (TGU) suggested by Huang et al. [58]. The concept is based on an idea by Smith et al. [78] originally intended to reduce the sensitivity of FEL oscillators with respect to energy jitter. The goal of the scheme is again a reduction of the local energy spread at the cost of a loss of current density. In contrast to the decompression scheme the bunch is not dispersed in the longitudinal direction but in the transverse direction matching the wiggle plane of the electrons.

Using a dispersive section the beam can be sorted by energies in the transverse direction, leading to an increase of the bunch width of

$$n = \frac{\sigma_x}{\sigma_{x,0}} = \frac{\sqrt{\sigma_{x,0}^2 + R_{16}^2 \sigma_{\eta,0}^2}}{\sigma_{x,0}}, \quad (3.27)$$

with $\sigma_{x,0}$ being the initial bunch width, $\sigma_{\eta,0}$ the initial, relative energy spread, and the linear transport matrix element R_{16} linking the horizontal position and the energy deviation. The resulting transverse energy-position correlation is given by

$$\frac{d\eta}{dx}(n) = \frac{\sigma_{\eta,0}}{n\sigma_{x,0}}, \quad (3.28)$$

in analogy with the decompression concept. Also here the energy-position correlation can be compensated by an appropriate taper, although in this case in the transverse direction

$$\frac{dK}{dx} = \frac{2 + K_0^2}{K_0} \frac{d\eta}{dx}. \quad (3.29)$$

A noteworthy difference when compared to the decompression concept is the scaling of the taper with the energy. For the decompression case the taper required for a given relative chirp is proportional to $dK/ds \propto \gamma^{-2}$, whereas in the TGU case the matching taper dK/dx is energy independent. This significant difference is caused by the fact that in the TGU case electrons and photons have to be kept in resonance at the same longitudinal position. In the decompression case, however, the resonance has to be maintained as the photons slip through the bunch, significantly reducing the required taper depending on the slippage distance and therefore the energy.

The full cant angle between the undulator halves $2\Phi = \Delta y/\Delta x$ can be approximated using Elleaume's formula (2.3) yielding

$$\frac{dK}{dx} = 2\Phi \frac{\partial K_0}{\partial g} = 2\Phi K_0 \left(a_2 \frac{1}{\lambda_u} + 2a_3 \frac{g}{\lambda_u^2} \right). \quad (3.30)$$

The maximum taper supported by a given undulator is consequently limited by the maximum cant angle. A reasonable limit for the cant angle of an individual pole in a conventional undulator is $\Phi = 0.1$ rad [58].

The scaling of the gain length in the TGU concept can be derived in analogy to the decompression case. The ideal gain length scales as $L_{g,1D} \propto \rho^{-1} \propto (\sigma_x \sigma_y)^{1/3} \propto n^{1/3}$. The local energy spread decreases as $\Delta \propto n^{-2/3}$. Hence, in the one-dimensional model taking only energy spread into account the relation for the normalized gain length is the same as in the decompression case

$$\frac{L_g(n, \Delta)}{L_{g,1D}} = \left(1 + \frac{\Delta^2}{n^{4/3}} \right) n^{1/3}. \quad (3.31)$$

The ideal dispersion factor is therefore given by

$$n_{\text{opt}} = 3^{3/4} \Delta^{3/2}, \quad (3.32)$$

and is a function of the initial normalized, relative energy spread Δ . Using the normalized energy spread of the lab-scale scenario of $\Delta \approx 0.57$, consequently, allows no reduction of the gain length via transverse dispersion.

In analogy with the combined scaling in the decompression case, the energy spread based scaling can be extended to also include the bunch length correction. In the TGU concept, however, the bunch length remains constant and the bunch length scaling is only affected via the modified cooperation length $l_{\text{co}}(n, \Delta)$. The expression for the normalized gain length including energy spread and bunch length correction for the transverse dispersion reads

$$\frac{L_g(n, \Delta, \sigma_z)}{L_{g,1D}} = \left(1 + b_1 \exp \left(b_2 \left(\frac{\sigma_z}{l_{\text{co}}(n, \Delta)} \right)^{b_3} \right) \right) \left(1 + \frac{\Delta^2}{n^{4/3}} \right) n^{1/3}. \quad (3.33)$$

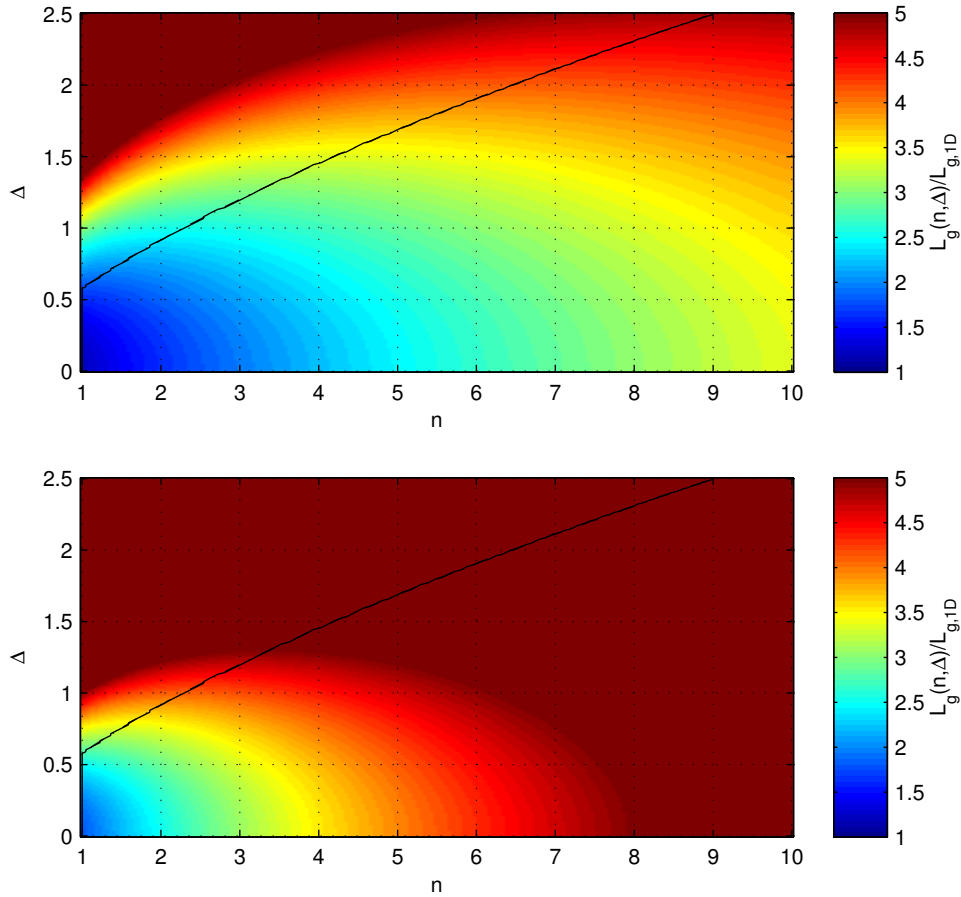


Figure 3.14: Normalized gain length as a function of the normalized energy spread Δ and the transverse dispersion factor n calculated with the combined scaling Eq. (3.33) for a normalized bunch length of $\sigma_z/l_{co,1D} = 3$ (top) and $\sigma_z/l_{co,1D} = 1$ (bottom). The black line indicates the ideal dispersion factor for a given initial energy spread. The comparison shows a significant increase of the gain length for short bunches; however, the ideal dispersion factor is nearly independent of the initial normalized bunch length.

Note the missing factor n in front of σ_z when compared to the scaling of the decompression scenario (3.19).

Figure 3.14 shows the normalized gain length as a function of the initial energy spread and the transverse dispersion factor for different initial ratios of bunch length to cooperation length. For long bunches the scaling is identical to the decompression case; however, for short bunches the gain length increases significantly also for dispersed cases. The ideal dispersion factor is still well estimated by the simple energy spread scaling and nearly independent of the initial normalized bunch length $\sigma_z/l_{co,1D}$. As in the case of the longitudinal decompression, a transverse dispersion is only of use for cases with a normalized energy spread of $\Delta > 0.6$, however, here this holds approximately independent of the initial bunch length. For the case of an initial energy spread of $\Delta = 1$ and a ratio of initial bunch length to ideal cooperation length of unity the gain length is minimized for a dispersion factor of $n \approx 2.3$ and results in a gain length drop of about 20%. For the lab-scale case also the combined scaling suggest no reduction of the gain length due to the too low initial energy spread.

The inclusion of further degrading effects changes the situation. As shown in Fig. 3.15 (top) the gain length is in general higher when further degrading effects are included, but a transverse dispersion allows to optimize the performance. This can be explained with Xie's scaling. In Fig. 3.15 (bottom) the degradation coefficients including the fit parameters are compared for the lab-scale case as a function of the transverse dispersion factor. The transverse dispersion can only approximately be included in Xie's scaling by setting $\sigma_x = \sigma_y = \sqrt{n}\sigma_{x,0}$ since a round beam is assumed in Xie's analytical model. As in the longitudinal decompression concept, the dominating correction factors are related to bunch length, energy spread, diffraction, and the combined impact of energy spread and diffraction. The impact of all other effects is at least four orders of magnitude smaller and thus negligible. In contrast to the longitudinal decompression, the impact of the bunch length is nearly independent of the transverse dispersion factor. Due to the approximate model assuming a round beam in the transverse dispersion case, the impact of diffraction on the FEL performance gets slightly reduced with increasing n . The effect is even more pronounced for the degradation factor measuring the combined effect of energy spread and diffraction on the gain length. It decreases by three orders of magnitude when varying n by one order of magnitude and is therefore even stronger influenced than the energy spread scaling. This reduction of the degradation factors characterizing energy spread and diffraction leads to the applicability of the TGU concept also for the here discussed scenario.

To further assess the use of the TGU concept for the here discussed parameters set aiming for a first lab-scale FEL demonstration experiment, the power ratio of total to spontaneously emitted power has been evaluated with GENESIS. For this purpose, GENESIS has been modified to support a linear dependence of the undulator parameter on the transverse position for routines calculating electron-radiation interaction. The

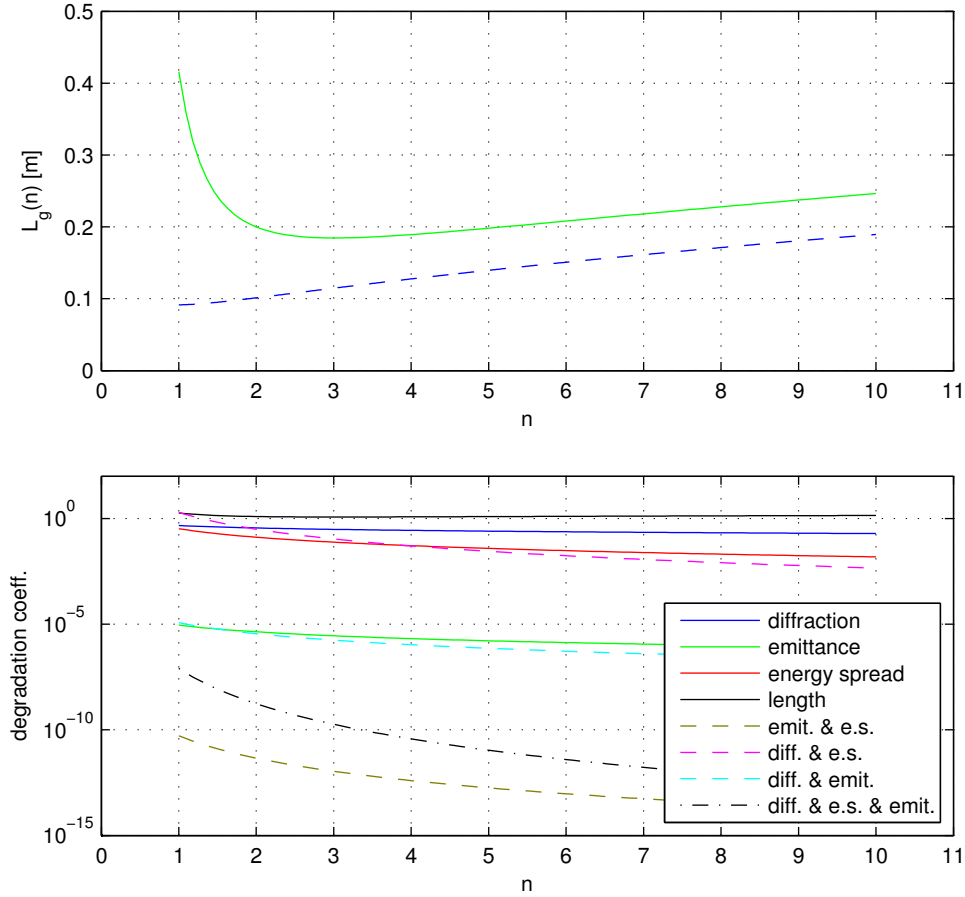


Figure 3.15: **Top:** Gain length of the demonstration FEL case as a function of the transverse dispersion factor estimated with the combined scaling (3.33) (dashed blue) and Xie's scaling including the bunch length correction (solid green). **Bottom:** Degradation coefficients of Xie's formula and bunch length correction including fit parameters, i.e. the diffraction coefficient corresponds to $\alpha_1 \eta_d^{\alpha_2}$ etc., as a function of the dispersion factor. Solid lines characterize individual contributions, whereas dashed lines refer to the combinations of two degrading effects. The most important degrading effects are energy spread, bunch length limitation, and diffraction. The combined coefficient of diffraction and energy spread overcomes both individual coefficients in the nondispersed case $n = 1$. All other correction factors are at least four orders of magnitude smaller. Transverse dispersion reduces all energy spread and diffraction related coefficients. The bunch length correction is nearly independent of the transverse dispersion factor.

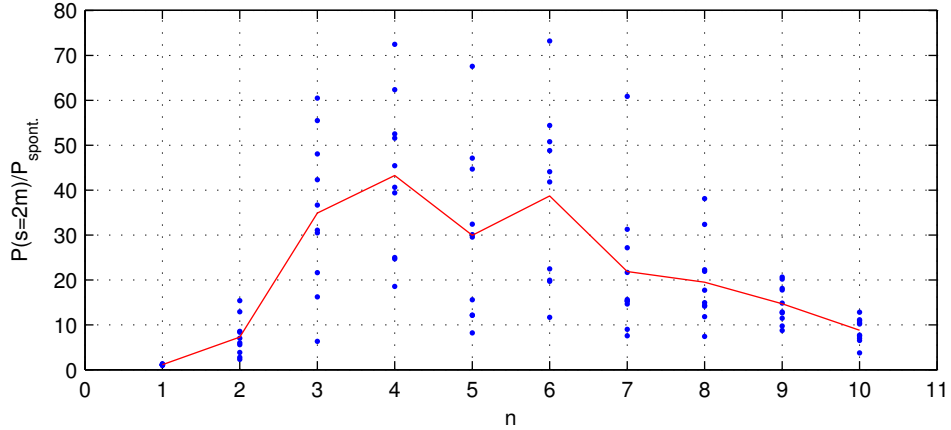


Figure 3.16: Ratio of power at the end of the undulator to spontaneous emission for the case of a transverse gradient undulator as a function of the transverse dispersion factor simulated with a modified version of GENESIS. Blue dots represent individual runs with different shot-noise seeds for the same general configuration. The solid red line is the mean value of the independent runs for each scenario. As in the longitudinal decompression scenario, an optimum dispersion factor of $n_{\text{opt}} \approx 4$ is found.

effect of the transverse gradient on the beam trajectory has been assumed to be compensated by a matching external dipole field. Figure 3.16 shows the power ratio as function of the transverse dispersion factor using a transverse gradient undulator with matching taper (see Eq. (3.30)). For transverse dispersion factors of $n = 3-9$ a ratio of $P(s = 2 \text{ m})/P_{\text{spont.}} > 10$ is obtained as required for the demonstration experiment. The ideal transverse dispersion factor is $n_{\text{opt}} \approx 4$ as in the case of longitudinal decompression. The highest power ratio reached in the TGU case, however, is only one fourth of the optimum in the longitudinal decompression case. This can be understood as a consequence of the still significant impact of the bunch length correction that cannot be compensated by the improved situation with respect to energy spread and diffraction.

A major limitation of the TGU concept is the maximum achievable cant angle of the undulator. Typically an upper limit of $\Phi = 0.1$ is regarded as reasonable [58]. This drastically limits the accessible taper and consequently the decompression parameter range. Figure 3.17 shows the power gain as a function of the transverse taper for a transverse dispersion factor of $n = 4$. Deviations from the ideal taper cause a fast reduction of the power growth. Figure 3.18 shows the required cant angle as a function of the decompression factor. Assuming the limit for the cant angle to hold, limits the decompression factors to $n \geq 20$ bringing the ideal parameter range $n = 3-9$ out of reach.

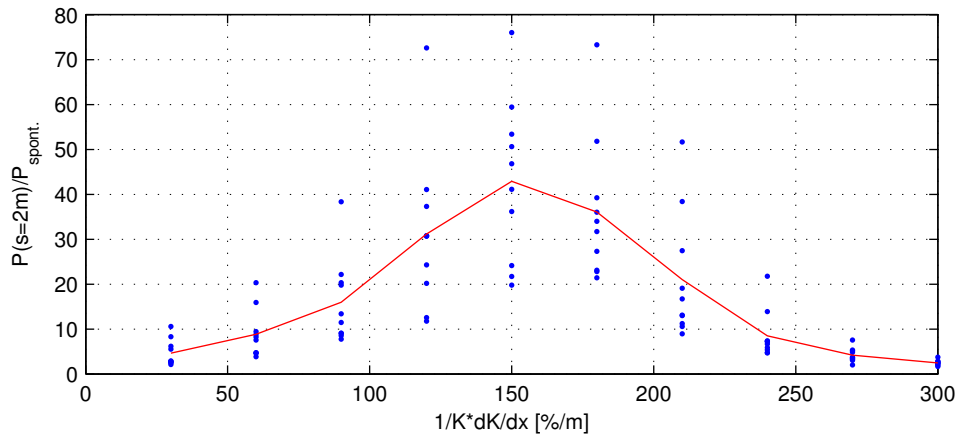


Figure 3.17: Power ratio at undulator exit as a function of the transverse taper for a transverse dispersion factor of $n = 4$. The dependence shows the high importance of the correct taper in order to mitigate the introduced transverse energy-position correlation.

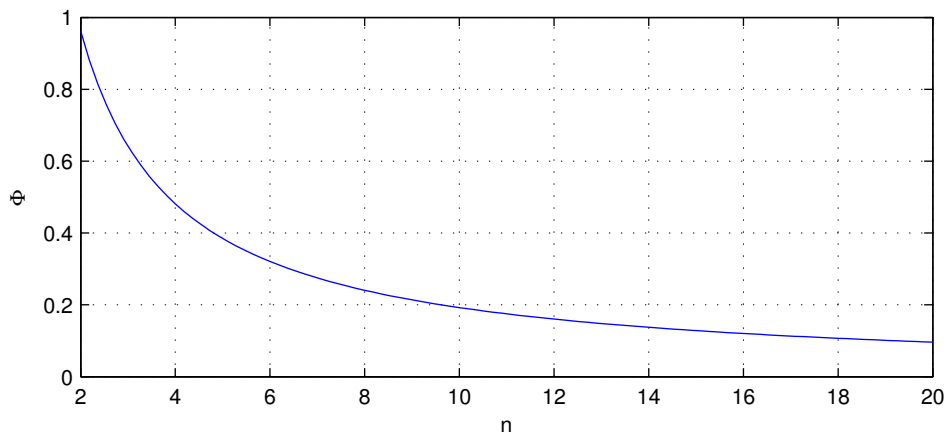


Figure 3.18: Cant angle of an individual pole required to create a transverse gradient matching the energy-position correlation introduced by a transverse dispersion by a factor of n based on Eqs. (3.27), (3.29), and (3.30), and the cryogenic undulator parameters $a_1 = 4.023$, $a_2 = -3.117$, and $a_3 = 2.012$. For the ideal dispersion factor $n_{\text{opt}} \approx 4$ a cant angle of $\Phi \approx 0.48$ would be required which is not feasible. Typically cant angles of $\Phi \leq 0.1$ are expected to be realistic [58] and would result in a dispersion factor range of $n \geq 20$.

3.5 Conclusion

In the sections above, one possible parameter set regarding the electrons and the undulator and two different setup concepts to allow for a first laser-plasma driven lab-scale FEL demonstration experiment with currently available electron beam parameters have been discussed. The design goal of the experiment is a first demonstration of gain, i.e. an output power at least one order of magnitude higher than in the case of spontaneous emission. Neither saturation nor a certain wavelength are required.

All electron parameters have been chosen in agreement with recent experiments at laser-plasma accelerators but have not yet been demonstrated in combination. The cornerstones of the parameter set are an intermediate energy of $\gamma = 600$ allowing for wavelengths in the UV range for typical undulator parameters and a rather high Pierce parameter, a low but already demonstrated energy spread of $\sigma_\eta = 1\%$, an ultra-low normalized emittance of $\epsilon_n = 0.2$ mm mrad recently measured, and a total bunch charge of $Q = 15$ pC routinely achieved in multiple experiments. Furthermore, a low bunch length of $\sigma_z = 0.5$ μm has been assumed, leading to high peak currents but also a significant impact of slippage effects.

The undulator design is based on recent achievements in the development of cryogenic undulators. To optimize the FEL performance, an intermediate period length of $\lambda_u = 15$ mm has been chosen in combination with a high undulator parameter of $K = 3.3$. This parameter combination is accessible with an undulator gap of $g = 3$ mm due to the cryogenic design, allowing for higher peak fields than in conventional hybrid undulators at a given gap. The undulator length has been limited to $L_u = 2$ m in the spirit of a lab-scale system.

This parameter set on its own does not allow for a first FEL demonstration since the spontaneous emission dominates over the FEL signal along the whole undulator. The FEL performance is subject to three major degrading effects: energy spread, slippage, and diffraction. Two concepts, longitudinal decompression and transverse dispersion, both trading a performance loss due to a current density reduction against a performance gain due to a local energy spread reduction have been compared.

In the longitudinal decompression concept the bunch is stretched in the longitudinal direction by a factor of n using a dispersive section like a magnetic chicane. This leads to a reduction of the local energy spread and the current proportional to n^{-1} . The introduced energy chirp can be compensated by a matching taper of the undulator. The loss of current density on the one side and the reduced local energy spread and longer interaction distance on the other side can be balanced, leading to an ideal decompression factor of $n_{\text{opt}} \approx 4$ and an increase of the output power by two orders of magnitude. For the correct estimate of the ideal decompression factor and the applicability of the decompression concept at all, it has been shown to be crucial to take the combined impact

of energy spread, bunch length, and diffraction into account. Individual scalings cannot explain the ideal decompression factor – they not even suggest an increase of the gain length under decompression. The taper required to compensate the relative energy chirp at the ideal decompression is $dK/(K_0 ds) \approx 5.3\%/m$, which limits the applicability of the concept to rather short undulators but is compatible with the suggested undulator for the demonstration experiment. The required taper drops with higher decompression factors $dK/ds \propto n^{-1}$ and the electron energy $dK/ds \propto \gamma^{-2}$ for a fixed relative energy chirp allowing for an extension of the applicability range.

The transverse gradient undulator concept, while following the same basic idea as the longitudinal decompression, features some noteworthy differences. The motivation is the same as in the case of longitudinal decompression: a reduction of the local energy spread proportional to n^{-1} is balanced against a reduction of the current density with the same proportionality. In high energy spread scenarios this concept allows to reduce the gain length. Due to the transverse dispersion, the beam width is increased further reducing diffractive losses, leading to an additional increase of the FEL performance. In contrast to the longitudinal decompression, however, slippage effects are only reduced due to the gain length reduction but not via changes of the bunch length. The transverse energy-position correlation introduced by the dispersion has to be compensated with a matching transverse taper to ensure resonance across the full bunch width. In opposition to the longitudinal decompression, photons and electrons have to be kept in resonance at the same longitudinal position within the bunch; therefore, the slope of the taper does not depend on the slippage of the radiation field with respect to the electrons. Consequently, the required taper can only be reduced by increasing the transverse decompression factor n . Since the typical cant angle of a pole is limited to $\Phi \leq 0.1$, this restricts the range of matching dispersion factors to $n > 20$ for the here discussed parameter set, leading to an FEL gain over the spontaneous background lower than the design goal of an order of magnitude. Due to these limitations, the transverse gradient undulator concept is not applicable to the parameter set of the lab-scale FEL demonstration experiment.

Due to the differences in the applicability of the two concepts, the longitudinal decompression concept is favored for the here discussed parameter range and will be used in all following discussions. So far, no degrading effects like the emission of coherent synchrotron radiation occurring during the decompression have been included. This will be addressed in detail in Chaps. 5 and 6.

4 FEL Tolerances

In the previous section a basic concept allowing for a first laser-plasma based FEL demonstration experiment using currently available electron beams from laser-wakefield accelerators has been discussed. While all basic parameters required for the electron beam as well as the undulator have already been demonstrated and can be seen as feasible, no statement about setup tolerances has been made so far.

Since the FEL bandwidth is characterized by the Pierce parameter, the errors of all parameters affecting the electron-radiation interaction can roughly be limited to this range, already indicating strict setup tolerances for all free-electron lasers. This limitation is of special importance for systems operating in the hard-X-ray range with typical Pierce parameters on the order of $\rho = 10^{-3}$ – 10^{-4} .

The parameter set for the the lab-scale FEL demonstration experiment has been chosen so that the Pierce parameter is maximized to increase the energy spread acceptance, resulting in $\rho \approx 10^{-2}$, leading to a relaxation of the basic requirements. Nevertheless, for a first demonstration experiment operating close to the detection threshold special care has to be taken to ensure the verifiability of an FEL amplification.

The setup tolerances can be grouped in three basic categories regarding the:

- **Undulator construction** in terms of random and systematic field variations.
- **Alignment** of the electron beam with respect to the undulator.
- **Optics mismatch**, resulting in a nonideal evolution of the beam envelope.

These types of errors will be addressed in the following, allowing to assess the feasibility of a first laser-plasma based free-electron laser demonstration experiment with respect to requirements on the construction of the individual components as well as the setup precision.

4.1 Tolerance Budget

In order to set the individual tolerances, the sensitivity of the FEL with respect to the discussed error source has to be determined. This is done by evaluating the power ratio $P(s = 2 \text{ m})/P_{\text{spont.}}$ as a function of each individual error parameter and fitting

the dependence by a Gaussian yielding the individual sensitivity σ_i . Assuming all error sources to be independent, the power ratio in the presence of all errors is given by the product of the individual dependencies

$$\frac{P(s = 2 \text{ m})}{P_{\text{spont.}}} = \frac{P_{\text{ref.}}(s = 2 \text{ m})}{P_{\text{spont.,ref.}}} \prod_i \exp\left(-\frac{x_i^2}{2\sigma_i^2}\right), \quad (4.1)$$

with the notation $*_{\text{ref.}}$ indicating the reference value neglecting all errors and the error sensitivities σ_i [79].

Restricting the drop of the power ratio to less than 40%, i.e. to stay within the one- σ -range, determines the tolerance budget. This requires the individual errors to be smaller than a fraction f_i of the individual sensitivity σ_i . The tolerances are therefore given by

$$t_i = f_i \sigma_i, \quad (4.2)$$

while the requirement $\sum_i f_i^2 = 1$ has to hold in order to stay within the one- σ -range. This requirement still allows to balance the coefficients f_i of the individual errors depending on their sensitivity and the practicability of the resulting requirements.

The error sources taken into account are:

- Undulator errors
 - Phase shake,
 - Beam wander,
 - Parabolic girder deformation,
 - Sinusoidal girder deformation,
 - Taper error,
- Alignment errors
 - Beam offset in x and y ,
 - Beam angle in x and y ,
- Optics mismatch in x and y .

Assigning all eleven errors the same weight results in the tolerances to be 30% of the individual sensitivity. Should further error sources be identified in the future the effect on the individual weight is minor since all errors are added in square. The weights can further be modified to balance the individual errors if necessary.

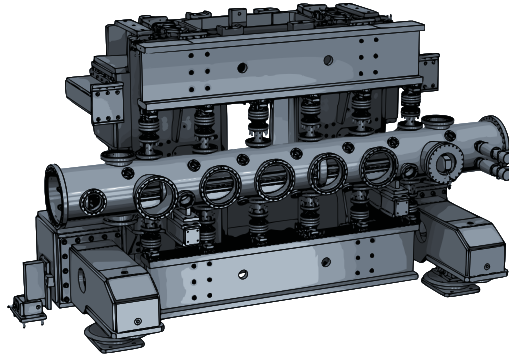


Figure 4.1: Support structure of the planned cryogenic undulator with a length of two meters. The actual undulator is located in the vacuum tube. Each of the undulator halves is mounted on six rods that are fed through the vacuum chamber. This allows to control the undulator gap and introduce a longitudinal taper but also causes a systematic deformation of the undulator. Undulator design courtesy of Helmholtz-Zentrum Berlin.

4.2 Sensitivities and Tolerances

All sensitivities and tolerances are characterized using time-dependent GENESIS simulations. Every error source is studied individually since the error sources are assumed to be independent. The preliminary tolerances are determined assuming equal weights for all errors.

4.2.1 Undulator

The heart of the free-electron laser is the undulator. Despite its simple description using a periodic magnetic field, it is a complex system with multiple error sources. In the case of the lab-scale demonstration experiment a cryogenic hybrid undulator with a variable gap is planned. The undulator will consist of 133 periods each being made up by two magnets and two poles per undulator half. The gap between the undulator halves is variable and allows to introduce a linear, longitudinal taper. This leads to various error sources ranging from mechanical construction tolerances of the support structure, over inhomogeneities of the heat flow, to errors of the magnetization direction of the magnets. Figure 4.1 shows the planned undulator support structure. The errors can be grouped into different categories: random magnet errors characterized by the resulting phase shake and beam wander [80], systematic errors caused by the girder deformation, and taper errors.

Phase Shake

The phase shake is a measure for the loss of the longitudinal synchronization between electrons and radiation. As discussed above (see Chap. 2) the position of the electrons with respect to the light wave is crucial for the FEL process since it determines the direction and amplitude of the electron energy change and conversely the energy transfer to or from the radiation field.

According to the resonance condition a photon slips by

$$z = \frac{\lambda_l}{2} = \frac{\lambda_u}{4\gamma^2} \left(1 + \frac{K^2}{2} \right), \quad (4.3)$$

with respect to the electrons per half undulator period. Assuming the field in each half-period to be a perfect half of a sine curve but allowing the amplitude to vary between half-periods results in a slippage error caused by the i -th half-period due to a change of the electron path length

$$\Delta z_i = \frac{\lambda_u}{4\gamma^2} \left(\frac{K_i^2}{2} - \frac{K_0^2}{2} \right). \quad (4.4)$$

Here K_i is the actual undulator parameter of the i -th half-period and K_0 is the ideal undulator parameter including the longitudinal taper. The resulting phase shift caused by the i -th half-period is then given by

$$\Delta \Psi_i = k_l \Delta z_i = k_l \frac{\lambda_u}{4\gamma^2} \left(\frac{K_i^2}{2} - \frac{K_0^2}{2} \right). \quad (4.5)$$

Summing up the individual phase shifts results in the phase offset at the n -th half-period

$$\Delta \Psi_n = \sum_{i=1}^n \Delta \Psi_i = k_l \frac{\lambda_u}{4\gamma^2} \sum_{i=1}^n \left(\frac{K_i^2}{2} - \frac{K_0^2}{2} \right). \quad (4.6)$$

The figure of merit for the FEL process is the rms phase error, the so-called rms phase shake or phase jitter, evaluated along the whole undulator [81]

$$\Psi = \sqrt{\frac{1}{2N_u} \sum_{n=1}^{2N_u} \Delta \Psi_n^2}, \quad (4.7)$$

with the number of undulator periods N_u .

Any realistic magnet error will always lead to a combination of phase shake and a transverse deflection of the beam. In order to study the isolated impact of the phase shake without any other degrading effects, a correlated field error has been used in the GENESIS simulations. Here neighboring half-periods are correlated in their strength so that no net deflection of the beam occurs (see Fig. 4.2). To cover a broad range of phase

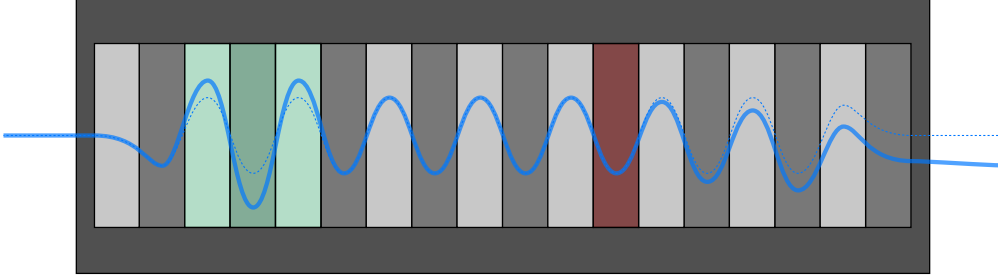


Figure 4.2: Sketch of the two basic types of undulator errors. The green half-periods have a correlated field error, resulting in a path length difference between ideal trajectory (dashed blue) and actual trajectory (solid blue) and hence a phase shake. The field error of the red half-period is not correlated with its neighbors and, therefore, results in a beam deflection, i.e. a beam wander.

errors, randomly generated undulator configurations with correlated relative rms field amplitude errors in the range $\sigma_K/K = 0\text{--}2.5\%$ have been scanned. Figure 4.3 shows the normalized power as a function of the phase shake. A Gaussian fit to the simulation results yields a sensitivity of $\sigma_\Psi = 1.02$ rad. The corresponding tolerance assuming equal weights for all error sources is $t_\Psi = 0.31$ rad. This criterion is on average met for an rms undulator strength error of $\sigma_K/K \approx 0.5\%$ and is comparable to the requirement found for the TESLA Test Facility FEL (TTF-FEL) [82].

The phase shake tolerance can be compared to the phase spread caused by the energy spread over one gain length [82]. The phase change of a detuned electron per gain length is given by

$$\Delta\Psi = \frac{d\Psi}{ds}L_g = 2k_u\eta L_g = \frac{4\pi}{\lambda_u}\eta L_g, \quad (4.8)$$

resulting in the energy spread induced rms phase spread of

$$\sigma_{\Psi_{\text{es}}} = \frac{4\pi}{\lambda_u}\sigma_\eta L_g. \quad (4.9)$$

For a gain length of $L_g \approx 17$ cm and a local energy spread of $\sigma_\eta = 0.25\%$ this results in a phase spread of $\sigma_{\Psi_{\text{es}}} \approx 0.36$ rad. When the undulator error based phase shake is reduced below this level, the gain reduction is dominated by the energy spread induced phase spread. Note, the usually used approximation for the energy spread based phase spread [82] $\sigma_{\Psi_{\text{es}}} = \sigma_\eta/(\rho\sqrt{3}) \approx 0.14$ rad is not applicable for the lab-scale FEL case since the significant impact of degrading effects on the FEL performance in terms of the gain length growth has to be taken into account.

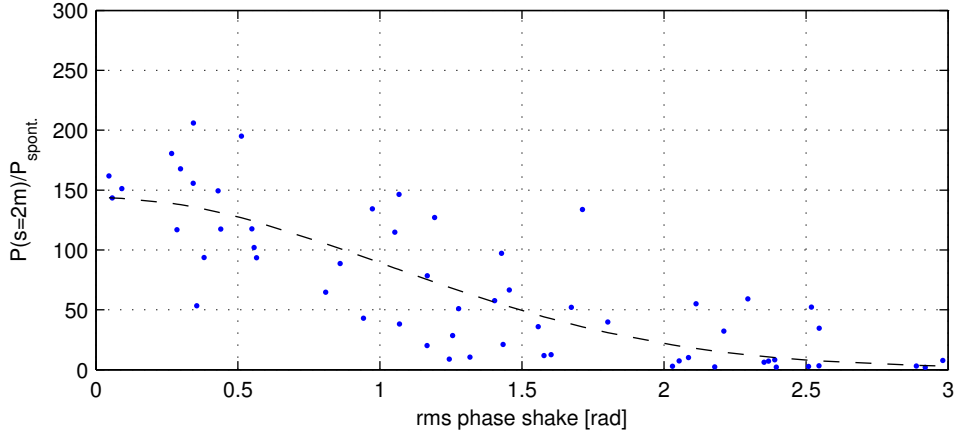


Figure 4.3: Normalized power as a function of the phase shake obtained with GENESIS. Each blue dot represents the mean normalized power for a given undulator configuration averaged over ten independent runs. All undulators have been generated assuming a correlated error, resulting in a pure phase shake without any beam wander. The dashed black line is the Gaussian fit measuring the sensitivity of the FEL process with respect to the phase shake. The found sensitivity is $\sigma_{\Psi} = 1.02$ rad.

The estimated energy spread induced phase shake is in good agreement with the tolerance limit for the field error based phase shake, confirming the simulation result. The required upper limit for the phase shake of $t_{\Psi} = 0.31$ rad is believed to be feasible for a cryogenic system [74]. This expectation is supported by studies regarding the construction tolerances [83].

Beam Wander

Besides a loss of longitudinal synchronization, the FEL performance can be degraded by a reduction of the transverse overlap of electron bunch and radiation field. This can be characterized by means of the acceptable beam wander.

In general the electron motion in a magnetic field is described by the Lorentz force

$$\gamma m \ddot{\mathbf{r}} = -e \dot{\mathbf{r}} \times \mathbf{B}. \quad (4.10)$$

Assuming the longitudinal velocity \dot{s} to be constant and the magnetic field to consist of a y -component only, allows to write the equation of motion for the x -component, i.e. the component describing the electron oscillation in the undulator, as a function of the longitudinal position

$$x''(s) = \frac{e}{\gamma m \dot{s}} B_y(s). \quad (4.11)$$

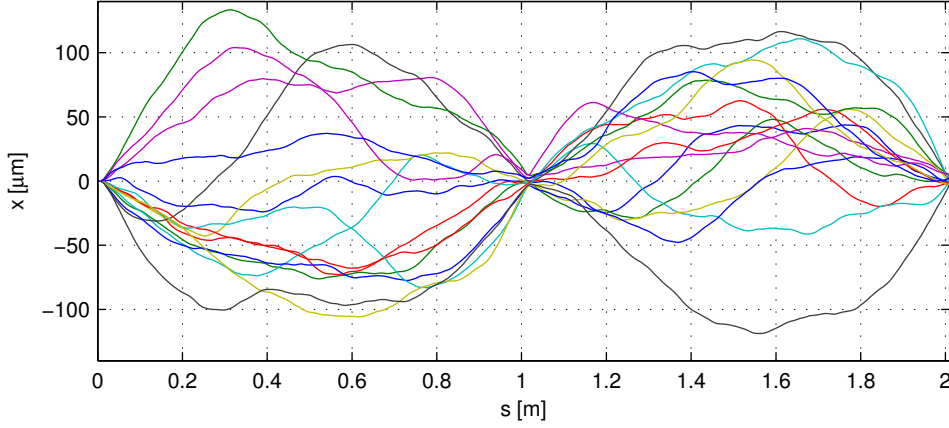


Figure 4.4: Period averaged bunch motion in the undulator based on random undulator configurations with $\sigma_K/K = 0.5\%$ and two steering correction at the undulator entrance and center minimizing the field integral at the undulator center and exit.

Integrating along the setup yields the slope at every position

$$x'(s) = \frac{e}{\gamma m \dot{s}} \int_0^s B_y(s_1) ds_1, \quad (4.12)$$

whereas a second integration yields the position

$$x(s) = \frac{e}{\gamma m \dot{s}} \int_0^s \int_0^{s_2} B_y(s_1) ds_1 ds_2. \quad (4.13)$$

Consequently, angle and offset of the electron trajectory are determined by the first and second field integral. For an ideal undulator the second field integral, i.e. the electron offset should vanish every half-period. Trajectory errors can therefore be linked to the field integrals allowing for a specification of the undulator quality and corresponding tolerance requirements.

The beam wander can be defined as the rms deviation of the electron trajectory from the ideal path [81]

$$x_{\text{bw}} = \sqrt{\frac{1}{2N_u} \sum_{n=1}^{2N_u} x_n^2}, \quad (4.14)$$

with x_n being the second field integral evaluated up to the n -th half-period.

The impact of the beam wander has been studied with GENESIS using an uncorrelated field error per half-period. The relative field error has been fixed to $\sigma_K/K = 0.5\%$ to ensure a minimal performance loss due to the phase shake. Each randomly generated undulator configuration has been modified assuming two steering corrections located

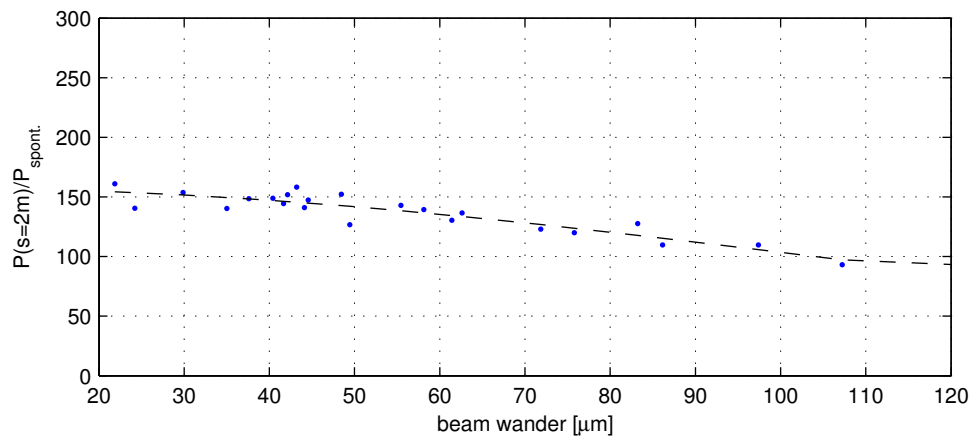


Figure 4.5: Normalized power as a function of the beam wander obtained with GENESIS. Each blue dot represents the mean normalized power for a given undulator configuration averaged over ten independent runs. For all undulator configurations the relative field error has been set to $\sigma_K/K = 0.5\%$ in order to minimize the impact of the phase error. Each undulator has been assumed to have two steering corrections at the undulator entrance and center yielding an vanishing beam offset at the undulator center and exit (see Fig. 4.4). The dashed black line is the Gaussian fit measuring the sensitivity of the FEL process with respect to the beam wander. The found sensitivity is $\sigma_{x_{\text{bw}}} = 109 \mu\text{m}$.

at the undulator entrance/center in order to ensure a vanishing second field integral at the undulator center/exit. The resulting bunch trajectories are shown in Fig. 4.4. This resembles an undulator with a minimum of field tuning, if necessary more steering corrections could be added to improve the performance.

Figure 4.5 shows the normalized FEL power as a function of the beam wander. The sensitivity based on a Gaussian fit is $\sigma_{x_{\text{bw}}} = 109 \mu\text{m}$, corresponding to a tolerance of $t_{x_{\text{bw}}} = 33 \mu\text{m}$. For the used electron parameters this is equivalent to a second field integral of 34 T mm^2 . This is comparable to the requirements on the undulator of the TTF-FEL [82] and is assumed to be challenging but feasible for a cryogenic undulator [74]. Despite the similarity in terms of the field integral requirement, there is a noteworthy difference. For the TTF-FEL the beam wander limit corresponds to $0.2\sigma_r$ with σ_r being the electron beam radius. In the case of the lab-scale demonstration experiment the beam size is on the order of $\sigma_x \approx 20 \mu\text{m}$ and the amplitude of the electron trajectory is $x_{\text{max}} \approx 13 \mu\text{m}$. Comparing these numbers to the beam wander tolerance limit of $t_{x_{\text{bw}}} = 33 \mu\text{m}$ shows that a rather large beam wander is acceptable. This can, *inter alia*, be understood as an effect of the very short Rayleigh length of only $s_R \approx 3.8 \text{ cm}$ in this case. This leads to a fast transverse expansion of the radiation field, leading to good overlap of radiation and electrons even in the case of significant trajectory fluctuations. This is in stark contrast to the situation at systems based on conventional linear accelerators like the TTF-FEL [82] and LCLS [40]. A further difference between the here discussed system and larger facilities is that in the case of a lab-scale system using a single 2-meter-long undulator no electron optics within the undulator are required. If optics are used within the undulator any beam offset gets amplified when traversing a quadrupole off-axis, consequently tightening the acceptable beam wander limits.

Girder Deformation

Besides random magnet errors leading to a phase shake and beam wander, systematic errors are expected. The undulator halves are mounted on steel rods (see Fig. 4.1) to ensure a minimum of heat flow between the cooled undulator and the rest of the support structure. This leads to a combination of a sinusoidal girder deformation with a period length of $\lambda_{\text{sine}} = 350 \text{ mm}$ and parabolic bending of the whole girder [84]. Both deformations result in a peak field variation along the undulator in addition to the required linear taper. The undulator parameter as function of the longitudinal position can be expressed as

$$K(s) = K_0 + \frac{dK}{ds} \left(s - \frac{L_u}{2} \right) + \Delta K_{\text{sine}} \sin \left(\frac{2\pi s}{\lambda_{\text{sine}}} \right) - \Delta K_{\text{par}} \left(s - \frac{L_u}{2} \right)^2, \quad (4.15)$$

using the undulator length L_u , the amplitude of the sine-like error ΔK_{sine} , and the amplitude of the parabola-like error ΔK_{par} . The effect of both error types has been

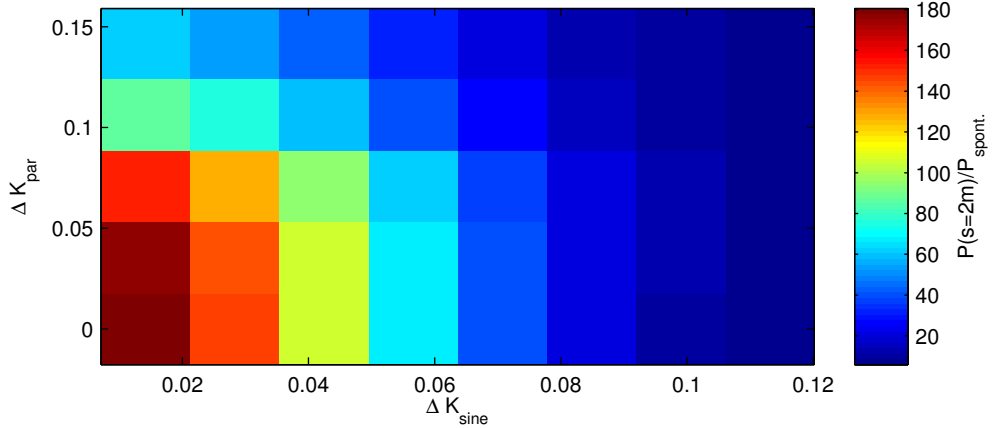


Figure 4.6: Normalized power as a function of the two systematic error amplitudes, the sine-like error and the parabola-like error caused by girder deformation. The effect of both errors on the FEL performance is in good approximation independent.

simulated with GENESIS independently as well as in combination. The effect of both errors on the FEL performance is uncorrelated and can be characterized individually. The simulation result is shown in Fig. 4.6. Both errors can be fitted by a Gaussian in order to characterize the sensitivities. The sensitivity with respect to the sine-like error is $\sigma_{\Delta K_{\text{sine}}} = 0.04$, leading to a tolerance of $t_{\Delta K_{\text{sine}}} = 0.012$. For the parabola-like error a sensitivity of $\sigma_{\Delta K_{\text{par}}} = 0.09$ is found, resulting in a sensitivity of $t_{\Delta K_{\text{par}}} = 0.027$. These tolerances can directly be related to gap variations using Elleaume's formula (2.3), leading to $\Delta g_{\Delta K_{\text{sine}}} = 24 \mu\text{m}$ and $\Delta g_{\Delta K_{\text{par}}} = 53 \mu\text{m}$. Since a precision on the sub-10- μm level is expected [84], this is acceptable.

Both error types affect the FEL in different ways. The sine-like error increases the bandwidth of the emitted radiation and the acceptable maximum is limited by the maximum bandwidth supported by the FEL process

$$\frac{\Delta K_{\text{sine}}}{K_0} = \frac{1 + \frac{K_0^2}{2}}{K_0^2} \frac{\Delta \lambda_l}{\lambda_l} < \frac{1 + \frac{K_0^2}{2}}{K_0^2} \rho. \quad (4.16)$$

This estimate leads to the requirement $\Delta K_{\text{sine}} < 0.02$ which is in good agreement with the simulation results.

The parabola-like error results in a change of the effective taper along the undulator. In the first undulator half the slope of the taper is increased, whereas it is decreased in the second half. A linear fit to one undulator half having a field variation matching the tolerance limits results in a deviation of the taper from the reference of $\Delta dK/(K ds) = 0.8\%/m$. This lies in the range of the taper sensitivity and tolerance and is therefore reasonable.

Taper

The undulator taper is crucial for an FEL concept relying on the decompression concept. Any deviation of the taper from the design value results in a nonideal cancellation of the energy chirp and, consequently, a reduction of the FEL performance. In Fig. 4.7 the result of a GENESIS scan is shown. The dependence of the normalized power on the taper is well described by a Gaussian. The sensitivity obtained is $\sigma_{dK/(Kds)} = 1.6\%/m$, leading to a tolerance of $t_{dK/(Kds)} = 0.48\%/m$. Since this tolerance requires a relative taper precision on the 10-%-level, it is regarded as feasible.

The taper limit can be motivated using the typical energy spread limit. Any taper deviation results in an only partial cancellation of the energy chirp and can therefore be expressed in terms of an effective energy chirp

$$\frac{d\eta}{dz} = \frac{K_0\gamma^2}{1 + \frac{K_0^2}{2}} \frac{dK}{ds}. \quad (4.17)$$

The remaining energy chirp can be converted to an effective energy spread by integrating over the cooperation length

$$\sigma_{\eta,ef} = \int_0^{l_{co}} \frac{d\eta}{dz} dz = \int_0^{\frac{\lambda_l}{\lambda_u} L_{g,3D}} \frac{d\eta}{dz} dz. \quad (4.18)$$

Using the tolerance limit as source of the effective taper and a cooperation length of $l_{co} = \lambda_l L_{g,3D}/\lambda_u = 1.5 \mu m$, based on a gain length of $L_{g,3D} \approx 17 \text{ cm}$, results in an effective, relative energy spread of $\sigma_{\eta,ef} \approx 0.44\%$ in good agreement with the energy spread limit of $\sigma_\eta < \rho/2 = 0.53\%$.

4.2.2 Alignment

Besides undulator construction related errors, also the alignment of the electron beam with respect to the undulator is crucial to ensure a minimum of performance loss. Any offset or angle of the bunch with respect to the undulator axis, e.g. caused by a source jitter, will lead to an oscillating motion in the field direction due to the focusing effect of the undulator, whereas it will cause a hyperbolic motion in the wiggle plane because of the transverse field dependence caused by the finite pole width (see Sect. 2.1). This is expressed by

$$x(s) = \Delta x \cosh(\kappa_x s) + \frac{\theta_{x,0}}{\kappa_x} \sinh(\kappa_x s), \quad (4.19)$$

$$y(s) = \Delta y \cos(\kappa_y s) + \frac{\theta_{y,0}}{\kappa_y} \sin(\kappa_y s), \quad (4.20)$$

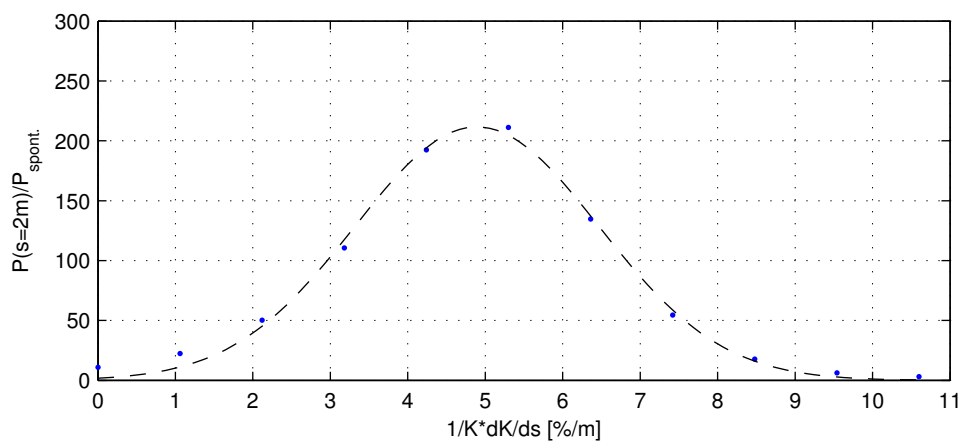


Figure 4.7: Normalized power as a function of the linear undulator taper obtained with GENESIS. Each blue dot represents the mean normalized power for a given undulator configuration averaged over ten independent runs. The dashed black line is the Gaussian fit measuring the sensitivity of the FEL process with respect to the taper. The found sensitivity is $\sigma_{dK/(Kds)} = 1.6\%/m$.

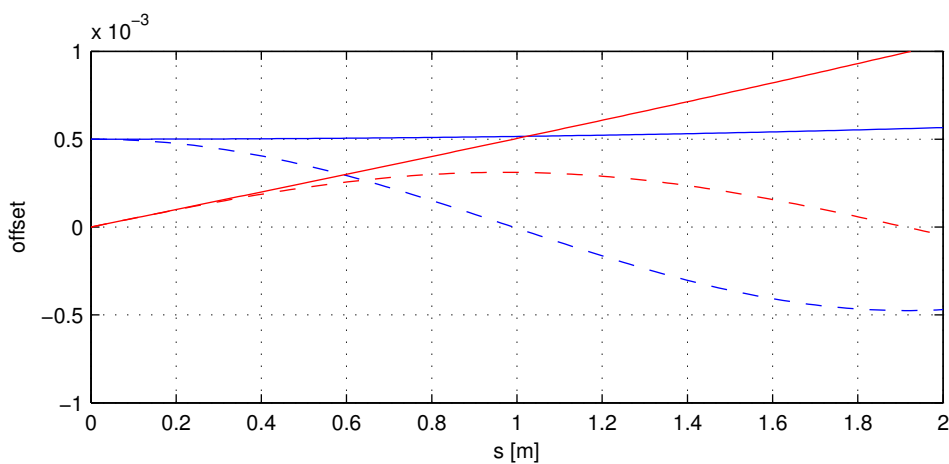


Figure 4.8: Period averaged trajectories for an initial offset (blue) $\Delta x = \Delta y = 500 \mu\text{m}$ or angle (red) $\theta_x = \theta_y = 500 \mu\text{rad}$ of the x -component (solid) and the y -component (dashed) based on Eqs. (4.19) and (4.20), and the parameter set of the demonstration experiment.

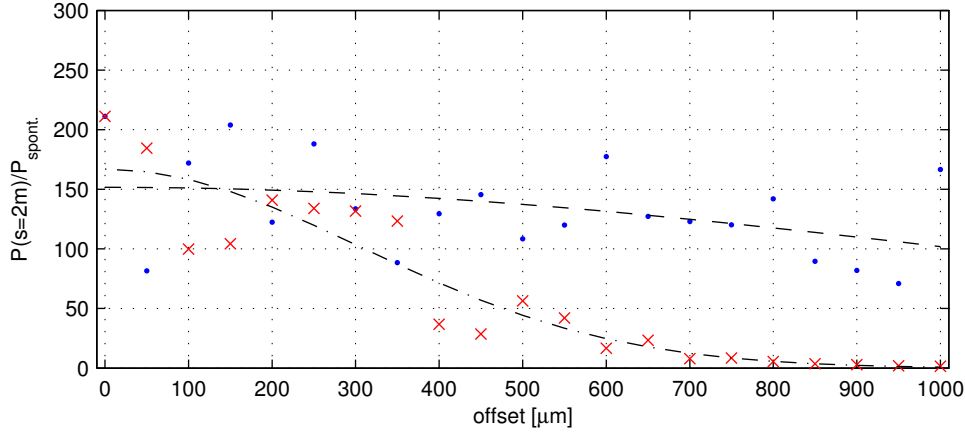


Figure 4.9: Normalized power as a function of the beam offset with respect to the undulator center for both components. Each blue dot/red cross represents the mean normalized power for a given x/y -offset averaged over ten independent runs. The dashed black line is the Gaussian fit measuring the sensitivity of the FEL process with respect to the x -offset, whereas the dash-dotted line corresponds to the fit to the y -offset-dependence. The found sensitivities are $\sigma_{\Delta x} = 1.1$ mm and $\sigma_{\Delta y} = 310$ μm .

using the initial beam positions and angles Δx , Δy , $\theta_{x,0}$, and $\theta_{y,0}$, as well as the spatial frequencies $\kappa_{x,y} = Kk_{x,y}/(\sqrt{2}\gamma)$.

For the lab-scale case the period length of the vertical motion is $\lambda_y \approx 3.8$ m, whereas the characteristic length of the horizontal, hyperbolic motion is $\lambda_x \approx 24$ m. Deviations in the field direction will therefore typically lead to a half, slow oscillation of the beam along the undulator, whereas errors in the horizontal component will result in a mainly straight motion dominated by the initial angle. Typical trajectories are depicted in Fig. 4.8.

Offsets

The offset sensitivity in both directions has been studied with GENESIS by varying the initial beam offset in the range $\Delta x = 0$ –1 mm. The scan results are shown in Fig. 4.9. Fitting the normalized power as a function of the offset with Gaussians in both cases results in the sensitivities $\sigma_{\Delta x} = 1.1$ mm and $\sigma_{\Delta y} = 310$ μm , corresponding to the tolerances $t_{\Delta x} = 332\mu\text{m}$ and $t_{\Delta y} = 93\mu\text{m}$.

The approximately factor of three difference between the tolerances can be understood as a consequence of the qualitatively different types of beam motion in both planes. A horizontal offset leads to a mainly straight trajectory parallel to the undulator axis, resulting in a shift of the central radiation wavelength to shorter wavelengths but having a minor impact on the FEL performance. Offsets in the vertical direction give rise to half

an oscillation around the undulator axis with extrema at the undulator entrance and in the vicinity of the undulator exit. The gain reduction can consequently be understood as a mix of:

- The resulting beam wander reducing the overlap of radiation and electrons. However, in this case the trajectory changes are not randomly distributed but follow a smooth curve, allowing the radiation field to partially adapt to the changes and reducing the impact on the FEL performance.
- A variation of the peak field traversed by the bunch changing the effective taper. The effective change of the taper, however, does not reach the tolerance limit.

Only the combination of the different effects can explain the found tolerance limit.

The tolerances are feasible in terms of the undulator alignment given a fixed reference axis since a sub-10- μm positioning precision can be reached. The resulting requirements on the optics and the source, however, are demanding, especially regarding the source jitter. More details are discussed in Sect. 7.2.

Angles

In contrast to the offset dependence the dependence of the normalized power on an initial angle is comparable for both dimensions. Figure 4.10 shows the result of the GENESIS runs. Both cases can be fitted by a Gaussian, leading to the sensitivities $\sigma_{\theta_x} = 600 \mu\text{rad}$ and $\sigma_{\theta_y} = 520 \mu\text{rad}$. The derived tolerances are $t_{\theta_x} = 181 \mu\text{rad}$ and $t_{\theta_y} = 157 \mu\text{rad}$. As in the offset analysis, the alignment constraints of the x -component are less strict than those of the y -component; however, the difference is smaller than expected with regard to the qualitative trajectory differences.

As in the case of the offset discussion, the trajectories resulting from the initial angles differ qualitatively. An initial angle in the vertical direction leads to an oscillatory motion, whereas a horizontal angle results in a linear motion. For the y -component the effect on the FEL performance can again be understood as a combination of reduced overlap of radiation and electrons and a change of the effective taper. In the case of the x -component the linear motion gives rise to an approximately quadratic drop of the magnetic peak field; however, the drop using the maximum allowed angle t_{θ_x} is on the order of 0.03% over the full undulator length and therefore well below the tolerance limit of the taper $t_{dK/(Kds)} = 0.48\%/m$. The mostly linear trajectory will also lead to negligible perturbations of the overlap of radiation field and electrons and can hence also not be seen as the source of the power drop.

The unexpected strict tolerance for the horizontal angle could be caused by approximations of the equations used in GENESIS, e.g. the use of the paraxial wave equation, and has been cross-checked using a different simulation approach suggested by S. Reiche [85].

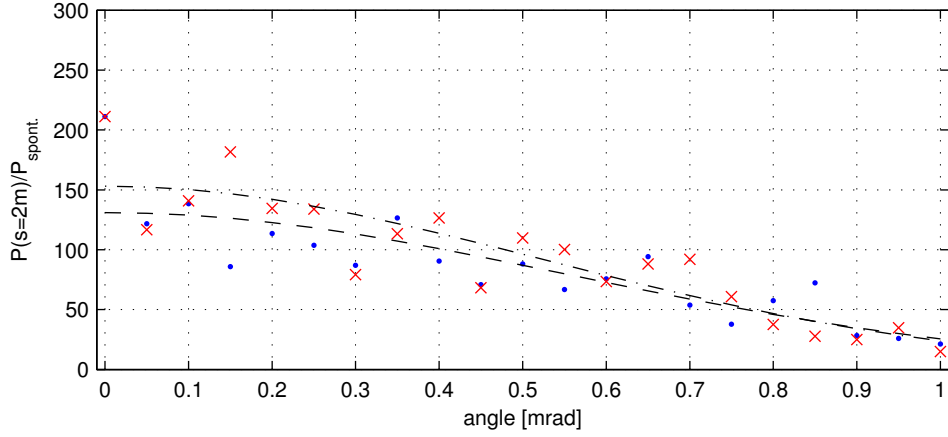


Figure 4.10: Normalized power as a function of the beam angle with respect to the undulator axis for both components. Each blue dot/red cross represents the mean normalized power for a given x/y -angle averaged over ten independent runs. The dashed black line is the Gaussian fit measuring the sensitivity of the FEL process with respect to the x -angle, whereas the dash-dotted line corresponds to the fit to the y -angle-dependence. The found sensitivities are $\sigma_{\theta_x} = 600 \mu\text{rad}$ and $\sigma_{\theta_y} = 520 \mu\text{rad}$.

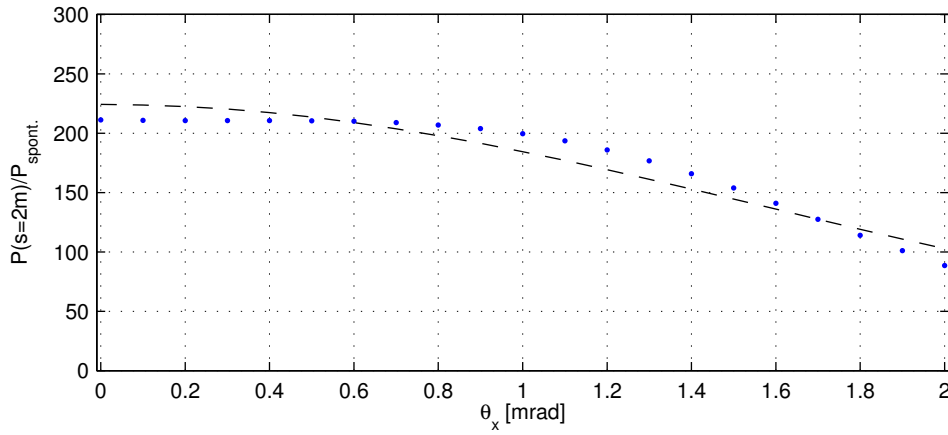


Figure 4.11: Normalized power as a function of the tilt angle of the undulator in x -direction with respect to the ideal beam trajectory. Due to the very weak defocusing effect of the undulator in the x -direction, this should be equivalent to an angle of the beam with respect to the undulator axis as shown in Fig. 4.10; however, the power dependence differs significantly. Each blue dot represents the mean normalized power for a given angle averaged over ten independent runs. The dashed black line is the Gaussian fit measuring the sensitivity of the FEL process with respect to the angle. The found sensitivity is $\sigma_{\theta_x} = 1.6 \text{ mrad}$.

The mostly linear electron motion can be modeled using a bunch propagating along the undulator axis combined with a linear shift of the undulator half-periods in the horizontal direction corresponding to the expected electron offset. The simulation result is shown in Fig. 4.11 and shows a completely different picture. The sensitivity of the power ratio with respect to the angle is drastically reduced, resulting in a sensitivity of $\sigma_{\theta_x} = 1.6$ mrad, leading to a tolerance of $t_{\theta_x} = 480 \mu\text{rad}$. Comparing these numbers to the case of angles in the y -direction yields a factor of three difference as in the case of the offset errors which is more plausible than the previous result given the different types of trajectories. The quadratic field evolution along the undulator half can be fitted with a straight line in the second half, resulting in an effective taper deviation of 0.15%/m when using the tolerance limit $t_{\theta_x} = 480 \mu\text{rad}$ and a taper deviation of 1.7%/m when using the sensitivity $\sigma_{\theta_x} = 1.6$ mrad. These effective taper changes are in the range of the determined taper sensitivity and tolerance and can, consequently, explain the major fraction of the performance loss.

The significant differences in the simulation results depending on the simulation approach indicate that all scenarios dealing with high angles of the electron beam with respect to the undulator axis should be considered with care. This includes simulations with initial offsets, angles, and beam wander. The alternative simulation approach by introducing undulator offsets instead of beam offsets can only be used when the period-averaged trajectory is approximately independent of the passed magnetic field. This limits the concept to the here discussed horizontal angles. In all other cases the electron path is significantly influenced by the position dependence of the magnetic field. The conventionally determined tolerances can in any case be seen as the most demanding requirement while the real situation could be more relaxed. Consequently, only the conventionally obtained results will be used for the tolerance limits.

4.2.3 Optics Mismatch

Besides undulator construction and alignment errors, the evolution of beam envelope has a significant effect on the FEL performance and has to be kept close to the ideal envelope. So far, the Twiss parameters have been designed to ensure an as small as possible average cross section along the undulator in order to maximize the Pierce parameter and, therefore, the energy spread acceptance as much as possible.

The sensitivity with respect to errors of the Twiss parameters of both planes has been evaluated using GENESIS runs. The results are shown in Figs. 4.12 and 4.13. The β -mismatch cannot directly be fitted by a Gaussian, but a good approximation is reached when using a base-10 logarithm of the β -function as parameter for the fit [79]. The found sensitivities and optima for both components are: $\beta_{x,\min} = 1.23$ m, $\beta_{x,\max} = 3.44$ m, $\beta_{x,0} = 2.04$ m and $\beta_{y,\min} = 0.23$ m, $\beta_{y,\max} = 2.00$ m, $\beta_{y,0} = 0.67$ m. The sensitivities

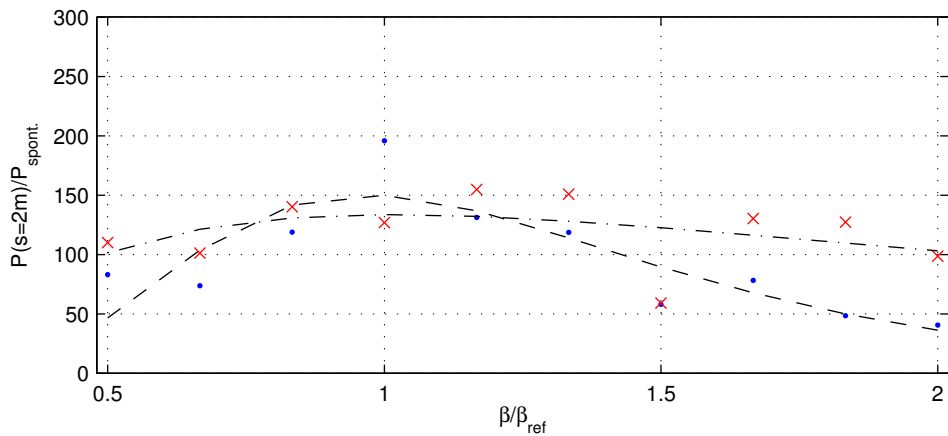


Figure 4.12: Normalized power as a function of the ratio $\beta_x/\beta_{x, \text{ref}}$ with $\beta_{x, \text{ref}} = 2.31\text{m}$ (blue dots) and $\beta_y/\beta_{y, \text{ref}}$ with $\beta_{y, \text{ref}} = 0.61\text{m}$ (red crosses). The Gaussian fits to $\log_{10}(\beta/\beta_{\text{ref}})$ measuring the sensitivity are given by the dashed (x -component) and dash-dotted black lines (y -component).

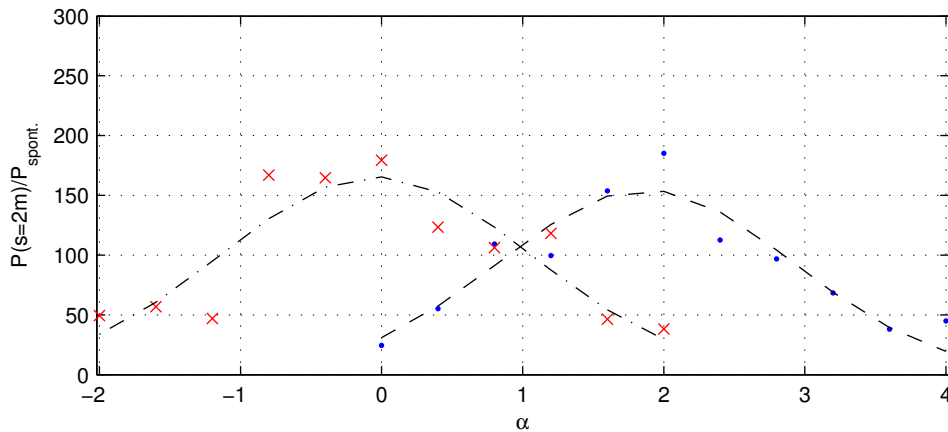


Figure 4.13: Normalized power as a function of the initial α -function. Each blue dot/red cross represents the mean normalized power for a given α_x/α_y averaged over ten independent runs. The dashed black line is the Gaussian fit measuring the sensitivity of the FEL process with respect to α_x whereas the dash-dotted line corresponds to the fit to the α_y -dependence. The found sensitivities are $\sigma_{\alpha_x} = 1.04$ and $\sigma_{\alpha_y} = 1.14$.

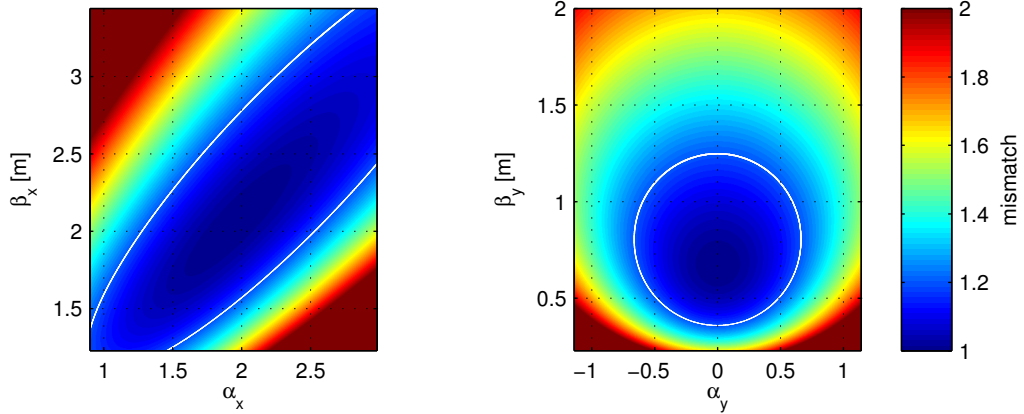


Figure 4.14: Mismatch for the x -component (left) and the y -component (right) as a function of the initial Twiss parameters at the undulator entrance. The white line indicates the tolerance limit in both cases. The different Twiss parameter dependencies are the direct result of the requirement for a converging beam in the x -direction and a beam waist in the y -direction.

and optima for the α -functions can be assessed by direct Gaussian fits, resulting in $\alpha_{x,0} = 1.94$, $\sigma_{\alpha_x} = 1.04$ and $\alpha_{y,0} = 0$, $\sigma_{\alpha_y} = 1.14$.

The found optima of the Twiss parameters are in good agreement with the initial design considerations aiming at a beam waist of the x -component at the undulator center and a matched beam size in the y -component utilizing the focusing of the undulator. The new optima will be used for the final design discussed in Chaps. 7 and 8.

In contrast to the other error sources, the effects of Twiss parameter errors of one dimension are not independent, i.e. starting with a too big but converging beam in the x -component is better than starting with the same beam size and a diverging beam. Consequently, not the individual errors but the specific combinations determine the FEL-performance. This can be expressed in terms of the deviation from the ideal beam shape measured by a deviation of the mismatch parameter [86] from unity

$$\Delta\zeta = \zeta - 1 = \frac{1}{2}(\beta\gamma_0 - 2\alpha\alpha_0 + \gamma\beta_0) - 1, \quad (4.21)$$

using the ideal Twiss parameters α_0 , β_0 , and γ_0 of the discussed component and the actual Twiss parameters α , β , and γ . Using the minimum or the maximum numbers for β_x and the sensitivity of α_x leads in both cases to a mismatch sensitivity of $\sigma_{\Delta\zeta_x} = 0.67$. For the y -component both combinations result in a sensitivity of $\sigma_{\Delta\zeta_y} = 0.65$. Converting to tolerances yields $t_{\Delta\zeta_x} \approx t_{\Delta\zeta_y} \approx 0.2$. This result shows that indeed deviations from the ideal beam shape of both components have the same effect on the FEL-performance since in any case the current density along the undulator gets reduced in the same way.

Error source	sensitivity	tolerance	dimension
Phase shake	1.02	0.31	rad
Beam wander	109	33	μm
Girder deformation (sine)	0.04	0.012	-
Girder deformation (parabola)	0.09	0.027	-
Taper	1.6	0.48	$\%/m$
Horizontal offset	1100	332	μm
Vertical offset	310	93	μm
Horizontal angle	600	181	μrad
Horizontal angle (based on undulator tilt)	1600	480	μrad
Vertical angle	520	157	μrad
Mismatch deviation (horizontal)	0.67	0.2	-
Mismatch deviation (vertical)	0.65	0.2	-

Table 4.1: Sensitivities and tolerances for the FEL demonstration experiment with respect to the most important error sources.

Figure 4.14 shows the mismatch of both components depending on the initial Twiss parameters.

Although the mismatch tolerances are comparable to conventional, linear accelerator based free-electron lasers [40, 41], they are challenging for the optics layout of laser-plasma based systems as well as the energy stability of the accelerator. More details regarding the resulting optics requirements are discussed in Sects. 7.2 and 7.4.

4.3 Conclusion

In this chapter, the tolerances for a laser-plasma based FEL demonstration experiment have been determined and discussed. A summary of the tolerances is shown in Table 4.1. The total error budget has been limited to the one- σ -range, consequently allowing a maximum reduction of the power ratio of 40%, assuming that the dependence of the output power on the error source can be modeled as a Gaussian for all discussed types of errors. All errors are assumed to be independent in order to set individual tolerance limits. The error sources taken into account are undulator errors, resulting from random magnet or pole errors as well as systematic errors due to the support structure, alignment errors of the electron beam with respect to the undulator, and optics errors, resulting in deviations of the electron beam from the ideal beam shape.

Despite the operation of the demonstration case in a challenging parameter range and far from saturation, the found tolerances for the undulator construction are comparable

to those of linear accelerator based free-electron lasers in many aspects [81,82], and even less demanding in some cases. The requirement on the phase shake is rather relaxed due to the broad energy spread that dominates phase errors for small undulator errors. In terms of the beam wander the found sensitivity is even significantly weaker than at large scale systems due to the high divergence of the radiation in this extreme parameter set, leading to good overlap of radiation and electrons even for trajectory errors on the order of the beam size. This is further relaxed due to the missing electron optics within the undulator in the lab-scale case, which would amplify beam offsets caused by magnet errors. All requirements are within the range of state-of-the-art cryogenic undulator concepts.

The alignment tolerances are in the 100- μm and 100- μrad range and hence acceptable in terms of the undulator alignment with respect to a fixed beam axis. The situation is more challenging regarding optics tolerances and source jitter. The tolerances found for the optics mismatch are similar to those of large scale system [40,41] and are therefore basically feasible; however, the extreme optics configurations required for laser-plasma based systems result in a challenge. More details regarding the consequences for optics and source requirements are discussed in Chap. 7.

In summary no show-stoppers have been found in the tolerance study, but the requirements are challenging in view of the full setup.

5 Bunch Decompression

A key element of the laser-plasma driven free-electron laser demonstration concept is the longitudinal bunch decompression. The goal of the decompression is to sort the bunch by energies, resulting in a reduction of the local energy spread, i.e. the energy spread of an infinitesimal longitudinal section of the bunch. This comes at the cost of a reduced peak current and an energy chirp.

The most efficient way to reach this effect is to use a dispersive beam transport section consisting of multiple magnets, leading to the desired path length differences due to the energy dependent deflection in the magnets. In general, a bunch decompression could be reached by simply using a long drift where the velocity differences of the particles will result in the position changes. This concept, referred to as velocity (de)bunching, however, is only of feasible at low energies since otherwise extremely long distances are needed.

A typical dispersive element used to manipulate the bunch length at large scale, linear accelerator based facilities is the so-called chicane [2, 6, 7, 40, 87]. A chicane is a series of dipoles leading to an energy dependent detour of the electron beam. Particles with the highest energy will take the shortest path through such a system, whereas the particles with the lowest energy will get deflected most, resulting in the longest path. At linear accelerator based systems this concept is used to decrease the bunch length by introducing an energy chirp prior to the passage through the chicane, leading to an increase of the peak current. The same magnet configuration can also be used to introduce an energy chirp when starting with an uncorrelated energy spread.

Since the particle motion in the chicane is energy dependent, any energy changes occurring inside the chicane will result in a perturbation of the particle trajectories and consequently lead to a degradation of the beam quality in terms of the emittance.

This chapter will address the basic concepts of a chicane based bunch (de)compressor, followed by a discussion of energy spread inducing effects and the resulting emittance growth mechanism.

5.1 (De)compression in Chicanes

Bunch length manipulations can in general be described independent of the specific setup. The individual setups have different advantages when degrading effects are included. These will be discussed in Sect. 5.3.

5.1.1 General

The coordinate system used within this chapter differs from the global coordinate system used in the FEL part. Since any beam transport system is designed to keep particles on a design orbit, it is customary in particle optics to use a coordinate system co-moving with a particle on the ideal orbit. Hence, all coordinates characterize deviations from this path*.

In this system the evolution of the particle offset with respect to the design position can be expressed using a matrix formalism characterizing the effect of a beam transport section on the particle coordinates. Using this formalism the energy dependence of the final, longitudinal particle position z_f can be expressed as

$$z_f = z_i + R_{56}\eta_i + T_{566}\eta_i^2 + \mathcal{O}(\eta_i^3), \quad (5.1)$$

using the initial, longitudinal particle position z_i , the initial, relative energy deviation η_i , the linear transport matrix element R_{56} , and the second order matrix element T_{566} . Elements higher than second order can usually be neglected.

The initial energy deviation for the here discussed cases can be seen as a combination of an energy deviation $\eta_{i,\text{loc}}$ caused by an uncorrelated energy spread and a contribution by an energy chirp $d\eta/dz$

$$\eta_i = \frac{d\eta}{dz}z_i + \eta_{i,\text{loc}}. \quad (5.2)$$

This resembles the basic energy distribution of a bunch as it is expected from laser-wakefield accelerators.

Using this initial energy distribution the final particle position can be obtained using the matrix formalism

$$z_f = \left(1 + R_{56}\frac{d\eta}{dz}\right)z_i + R_{56}\eta_{i,\text{loc}}. \quad (5.3)$$

The rms bunch length after this transformation is given by

$$\sigma_{z_f} = \sqrt{\left(1 + R_{56}\frac{d\eta}{dz}\right)^2 \sigma_{z_i}^2 + R_{56}^2 \sigma_{\eta_{i,\text{loc}}}^2}, \quad (5.4)$$

*For more details about the coordinate system and the basics of beam topics see Chap. 7.

using the initial rms bunch length σ_{z_i} and the initial, local, relative energy spread $\sigma_{\eta_{i,\text{loc}}}$. Three extreme cases can be distinguished:

- A completely uncorrelated initial, energy distribution, i.e. a vanishing initial energy chirp $d\eta/dz = 0$. Such a bunch will always be decompressed in a dispersive section.
- A pure positive chirp without any local energy spread $\sigma_{\eta_{i,\text{loc}}} = 0$. In a chicane this case leads to a decompression independent of the chicane strength in terms of its transport matrix element R_{56} .
- A negative chirp with a vanishing local energy spread. This is the case usually discussed in the context of bunch compression at linear accelerator based facilities. Here two sub-cases can be discussed:
 - $|R_{56}d\eta/dz| \leq 1$: the bunch will be compressed.
 - $|R_{56}d\eta/dz| > 1$: the bunch will be over compressed, resulting in a flipped chirp sign and possibly a longer bunch.

In any case the chicane strength has to be adjusted to control the desired final bunch length. The dependence of chicane strength R_{56} on the setup parameters like magnet strength and drift lengths is layout dependent.

5.1.2 C-Chicane

The probably most common chicane layout is the so-called C-chicane. A C-chicane consists of four magnets sending the beam on a C-shaped detour (see Fig. 5.1). Usually all bending magnets have the same length L_b , but the field strength and, therefore, the deflection angle ϕ_i can be chosen independently. Besides the simple symmetric layout this allows to build arbitrary, asymmetric chicane layouts; however, the common asymmetric layout consists of magnets with pairwise identical deflection angles $\phi_1 = \phi_2$ and $\phi_3 = \phi_4$, and different initial and final drift lengths $L_{12} \neq L_{34}$. In the special case of a symmetric layout all deflection angles as well as initial and final drift are identical. In terms of the basic (de)compression mechanism there is no advantage of asymmetric layouts with respect to the simple symmetric layout. The layout differences are only of use when taking degrading effects into account.

The chicane strength, i.e. the longitudinal dispersion R_{56} , can be determined by evaluating the energy dependence of the path length difference introduced by the chicane [88].

The path length difference with respect to a straight line introduced by the i -th bending magnet $\zeta_{b,i}$ for a particle with the reference energy is given by

$$\zeta_{b,i} = R\phi - L_b \approx \frac{L_b\phi^2}{6}, \quad (5.5)$$

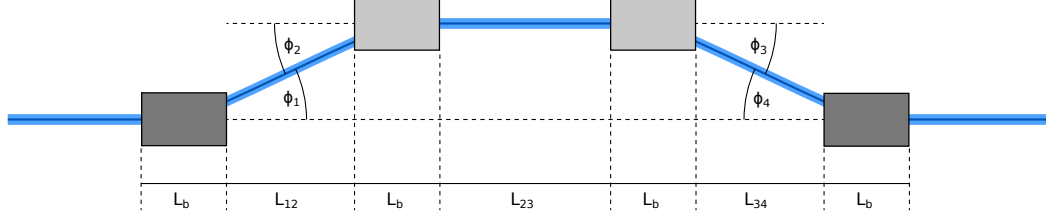


Figure 5.1: Schematic layout of a symmetric C-chicane. Typical asymmetric configurations can be obtained by shifting the central pair of magnets in the longitudinal direction.

using the radius of curvature of the trajectory within the magnet R , the deflection angle ϕ , and the magnet length L_b . Further path length differences $\zeta_{d,ij}$ between magnets i and j are caused by the drifts between the first two and the last two bending magnets

$$\zeta_{d,ij} = \frac{L_{ij}}{\cos \phi} - L_{ij} \approx \frac{L_{ij}\phi^2}{2}, \quad (5.6)$$

using the drift length L_{ij} and the deflection angle of the preceding magnet ϕ . The central drift L_{23} of all discussed C-chicane layouts is parallel to the reference beam path and does not contribute to any path length differences. The total path length difference with respect to the straight path without the chicane is given by the sum over all contributing elements

$$\zeta = \left(\frac{1}{3}L_b + \frac{1}{2}L_{12} \right) \phi_1^2 + \left(\frac{1}{3}L_b + \frac{1}{2}L_{34} \right) \phi_2^2. \quad (5.7)$$

Given the path length difference of a particle with the reference energy, the longitudinal dispersion can be evaluated by taking the energy dependence of the deflection angle for small energy deviations $\eta \ll 1$ into account. The energy deviation dependent deflection angle can be approximated by

$$\phi(\eta) \approx \frac{\phi_{\text{ref}}}{1 + \eta} \approx \phi_{\text{ref}}(1 - \eta + \eta^2), \quad (5.8)$$

using the ideal deflection angle ϕ_{ref} . With this approximation the path length difference taking energy deviations into account can be expressed as

$$\zeta \approx \left(\frac{1}{3}L_b + \frac{1}{2}L_{12} \right) \phi_1^2 (1 - \eta + \eta^2)^2 + \left(\frac{1}{3}L_b + \frac{1}{2}L_{34} \right) \phi_2^2 (1 - \eta + \eta^2)^2. \quad (5.9)$$

Consequently, the two lowest order dispersion contributions are well approximated by

$$R_{56} \approx \left(\frac{2}{3}L_b + L_{12}\right) \phi_1^2 + \left(\frac{2}{3}L_b + L_{34}\right) \phi_2^2, \quad (5.10)$$

$$T_{566} \approx -\left(L_b + \frac{3}{2}L_{12}\right) \phi_1^2 - \left(L_b + \frac{3}{2}L_{34}\right) \phi_2^2 = -\frac{3}{2}R_{56}. \quad (5.11)$$

Although the second order matrix element T_{566} is off the same order as the linear element R_{56} , its contribution can well be neglected for the cases discussed in this thesis.

Another interesting characteristic of a chicane is the transverse trajectory offset and the corresponding transverse dispersion. The transverse offset introduced by the i -th bending magnet is given by

$$\chi_{b,i} = L_b \tan\left(\frac{\phi}{2}\right) \approx L_b \left(\frac{\phi}{2} + \frac{1}{3}\left(\frac{\phi}{2}\right)^3\right), \quad (5.12)$$

including the angular dependence up to the third order. The offset change caused by the first or last drift within the chicane is

$$\chi_{d,ij} = L_{ij} \tan(\phi) \approx L_{ij} \left(\phi + \frac{\phi^3}{3}\right). \quad (5.13)$$

Summing up the individual contributions, the total offset at the chicane exit results in

$$\chi \approx 2L_b \left(\frac{\phi_1}{2} + \frac{1}{3}\left(\frac{\phi_1}{2}\right)^3\right) - L_{12} \left(\phi_1 - \frac{\phi_1^3}{3}\right) - 2L_b \left(\frac{\phi_2}{2} + \frac{1}{3}\left(\frac{\phi_2}{2}\right)^3\right) - L_{34} \left(\phi_2 + \frac{\phi_2^3}{3}\right). \quad (5.14)$$

Here again the assumption of a central drift parallel to the ideal beam path was used. In general, it is desired to have no final transverse offset of the beam in order to be independent of the chicane operation and strength. The offset relation $\chi = 0$ cannot exactly be solved for one of the angles due to the mixed dependence on $\tan(\phi)$ and $\tan(\phi/2)$. Assuming small angles, what is reasonable for most realistic cases, leads to the approximation

$$\phi_2 \approx \frac{L_b + L_{12}}{L_b + L_{34}} \phi_1, \quad (5.15)$$

linking the two deflection angles.

Including the lowest order energy dependence of the deflection angle yields the final offset at the chicane exit as a function of the energy deviation

$$\begin{aligned} \chi = & 2L_b \left(\frac{\phi_1}{2}(1-\eta) + \frac{1}{3}\left(\frac{\phi_1}{2}\right)^3(1-3\eta)\right) + L_{12} \left(\phi_1(1-\eta) + \frac{\phi_1^3}{3}(1-3\eta)\right) \\ & - 2L_b \left(\frac{\phi_2}{2}(1-\eta) + \frac{1}{3}\left(\frac{\phi_2}{2}\right)^3(1-3\eta)\right) - L_{34} \left(\phi_2(1-\eta) + \frac{\phi_2^3}{3}(1-3\eta)\right). \end{aligned} \quad (5.16)$$

The lowest order transverse dispersion is approximated by

$$R_{16} \approx \left(\left(\frac{L_b + L_{12}}{L_b + L_{34}} \right)^3 \left(\frac{L_b}{4} + L_{34} \right) - \left(\frac{L_b}{4} + L_{12} \right) \right) \phi_1^3. \quad (5.17)$$

This term only vanishes for symmetric layouts with $\phi_1 = \phi_2$, $L_{12} = L_{34}$. In the decompression scenario the induced transverse dispersion remains negligible for all reasonable chicane layouts. A typical parameter set for the decompression concept, yielding a bunch elongation by a factor of four in an asymmetric chicane, is $L_{12} = 7$ cm, $L_{34} = 27$ cm, $L_b = 7.5$ cm, and a deflection angle of $\phi_1 = 0.034$ rad, resulting in a transverse dispersion at the chicane exit of $R_{16} \approx -3$ μm . Combined with a bunch width on the order of tens of micrometers the transverse dispersion is negligible for all practical decompression cases discussed in this thesis and is also in good agreement with the tolerance limits.

Further interesting properties of a C-chicane are the transverse beam offset and the dispersion at the chicane center. A sufficient offsets allow to use the chicane to merge the electron beam with a photon beam when considering seeding schemes for an FEL. Furthermore, the dispersion at the chicane center is the key to the TGU concept discussed above, as well as the idea of energy filtering [16].

Based on the considerations above the beam offset at the chicane center is given by

$$\chi_{\text{center}} = 2L_b \tan\left(\frac{\phi_1}{2}\right) + L_{12} \tan(\phi_1) \approx (L_b + L_{12})\phi_1. \quad (5.18)$$

Taking the detuning dependence into account yields the linear dispersion

$$R_{16,\text{center}} \approx -(L_b + L_{12})\phi_1. \quad (5.19)$$

Using the typical numbers mentioned above yields an offset of $\chi_{\text{center}} \approx 5$ mm and a dispersion of $R_{16,\text{center}} \approx -5$ mm.

For the TGU concept applied to the demo FEL parameter set a dispersion of $|R_{16,\text{TGU}}| \geq 8$ mm is needed for a stretching factor of $n \geq 4$ and an assumed bunch radius of $\sigma_x = 20$ μm . Hence, a slightly longer drift or an increased deflection angle would be needed for the TGU concept; however, the orders of magnitude would remain comparable, allowing for a reasonable, compact setup.

In contrast, the discussed configuration does not allow for a reasonable energy filtering. Requiring a monochromatization to the level $\sigma_\eta \leq \rho/2$, i.e. $\sigma_\eta \leq 0.5\%$ in the lab-scale case, requires these energy ranges to be separated by at least $\Delta x = 6\sigma_x$. However, for the given setup the separation amounts to $\Delta x = R_{16,\text{center}}\Delta\gamma_{\text{max}}/\gamma \approx 25$ μm which is approximately the beam size and therefore a factor of six too small. A suited increase of the transverse dispersion at the chicane center would also result in an increase of the longitudinal dispersion at the chicane exit and hence result in an unwanted bunch prolongation even for the remaining energy range after monochromatization. A chicane layout

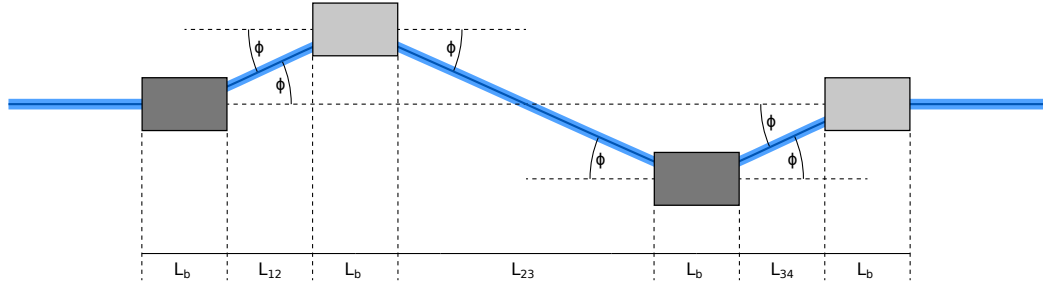


Figure 5.2: Schematic layout of a symmetric S-chicane. Typical asymmetric configurations can be obtained by shifting the central pair of magnets along the initial deflection direction.

for this purpose consequently has to be modified to be isochronous requiring additional quadrupoles within the chicane, significantly increasing the setup complexity. Furthermore, the increased dispersion also leads to an increase of degrading effects rendering this concept unfeasible [16].

In the further frame of this thesis the chicane will only be discussed in the context of bunch decompression.

5.1.3 S-Chicane

A common alternative to the C-chicane discussed above is the so-called S-chicane. The basic S-chicane configurations can be realized using either six or four magnets. In this thesis only setups consisting of four magnets with equal length will be discussed as shown in Fig. 5.2. This requires stronger deflections in the central magnets when compared to the outer ones but allows to consider configurations that can be built using the same magnets as in the C-chicane. As in the case of the C-chicane symmetric and asymmetric configurations will be considered. The asymmetric layout will be restricted to cases with identical deflection angles for all magnets, relying only on shifts of the central pair of magnets along the initial deflection direction.

In an S-chicane the length of the central drift L_{23} cannot be chosen arbitrarily anymore if a vanishing final beam offset is required. To reach a further on-axis propagation after the chicane, the central drift length has to be set to

$$L_{23} = L_{12} + L_{34} + 2L_b \frac{\tan \frac{\phi}{2}}{\tan \phi} \approx L_{12} + L_{34} + L_b. \quad (5.20)$$

The longitudinal dispersion can be derived evaluating the path length difference introduced by the chicane in analogy with the discussion above. Summing up the contributions of the individual components yields

$$\zeta = \left(\frac{7}{6}L_b + L_{12} + L_{34} \right) \phi^2, \quad (5.21)$$

using the deflection angle of the outer magnets ϕ . The path length contributions from central magnets, despite having the doubled deflection angle, are identical with those of the outer magnets. Including the energy dependence up to second order results in

$$\zeta = \left(\frac{7}{6}L_b + L_{12} + L_{34} \right) \phi^2 (1 - \eta + \eta^2)^2, \quad (5.22)$$

giving rise to the two lowest order longitudinal dispersion contributions

$$R_{56} \approx \left(\frac{7}{3}L_b + 2L_{12} + 2L_{34} \right) \phi^2, \quad (5.23)$$

$$T_{566} \approx - \left(\frac{7}{2}L_b + 3L_{12} + 3L_{34} \right) \phi^2 = -\frac{3}{2}R_{56}. \quad (5.24)$$

The relation between the first and second order dispersion found for the C-chicane is retained for the case of the S-chicane. The basic scaling does not show any significant differences when compared to the C-chicane. Both layouts result in comparable setup lengths when using magnets with a comparable deflection angle. The advantage of the modified layout only becomes clear when degrading effects are taken into account (see Sect. 5.3 and Chap. 6).

As for the C-chicane, the transverse offset and dispersion at the chicane exit can be evaluated

$$\chi \approx -\frac{L_b \phi^3}{4} + \frac{L_b \phi_0^2 \phi}{4}. \quad (5.25)$$

Here ϕ_0 is the angle used for the design determining the length of the central drift L_{23} , and ϕ is the actual angle depending on the setup and beam properties. As long as the chicane is operated with the design parameters, i.e. $\phi = \phi_0$, no net deflection occurs; however, any scan of the longitudinal dispersion by means of the deflection angle will result in an additional beam offset. A typical parameter set for the decompression scenario using an S-chicane is $L_{12} = L_{34} = 15$ cm, $L_b = 7.5$ cm, and $\phi_0 = 0.016$ rad. Reducing the actual deflection angle of this configuration to $\phi = \phi_0/2$ induces an offset of $\chi \approx 30$ nm, whereas an increase of the deflection angle to $\phi = 2\phi_0$ leads to an offset of $\chi \approx -0.5$ μm . For both cases the effect is negligible and does not result in any conflict with the desired setup tolerances discussed in Chap. 4 (see Table 4.1).

The transverse dispersion at the chicane exit is given by

$$R_{16} \approx \frac{3L_b \phi^3}{4} - \frac{L_b \phi_0^2 \phi}{4}. \quad (5.26)$$

In contrast to the C-chicane, the transverse dispersion never vanishes for an S-chicane. Using the same setup parameters as above and an increased deflection angle of $\phi = 2\phi_0$ results in a transverse dispersion of $R_{16} \approx 17 \mu\text{m}$ which is approximately a factor of five higher than in the C-chicane but still negligible for all discussed cases.

Both chicane layouts, the C-chicane as well as the S-chicane, are suited for the decompression concept. The required setup parameters and the resulting setup lengths are comparable and suited for a lab-scale system. The final beam offsets and residual dispersion are negligible for all practical cases. The differences and advantages of the individual layouts emerge when taking energy spread induced emittance growth into account and are discussed below.

5.2 Energy Spread Generation

So far, the effects of different chicane layouts on the electron bunch have only been discussed in terms of the introduced dispersion and offsets. The electron energy distribution has been assumed to be constant. However, an electron bunch propagating through the chicane is a source of strong electromagnetic fields, causing the build-up of an energy modulation during the pass through the chicane.

Any energy change of an electron occurring within the chicane will result in additional changes of the trajectory due to the dispersive character of the chicane. Effects to be considered are:

- The emission of **synchrotron radiation**
- Direct electron-electron interaction via **space-charge** forces
- Indirect electron-electron interaction via **wall wakefields**

In this section the characteristics and basic scalings of the different effects are discussed. The emittance growth caused by the energy modulations will be the subject of the next section.

5.2.1 Synchrotron Radiation

The most prominent degrading effect, discussed in the context of most bunch (de)compressors, is the emission of synchrotron radiation. This effect cannot be avoided in any magnetic structure.

To understand the basic effects it sufficient to study the process in an individual magnet independent of the complete setup layout. The radiation spectrum emitted by a single electron moving in an arc of a circle is given by [23]

$$\frac{dP_1}{d\omega} = \frac{P_1}{\omega_c} S\left(\frac{\omega}{\omega_c}\right), \quad (5.27)$$

using the total power emitted by an electron P_1 , the critical frequency defined as $\omega_c = 3c\gamma^3/(2R)$, and the spectral power density $S(\omega/\omega_c)$. The total power emitted by a single electron reads

$$P_1 = \frac{1}{6\pi\epsilon_0} \frac{e^2 c \gamma^4}{R^2}, \quad (5.28)$$

using the bending radius R , and the spectral power density is given by

$$S\left(\frac{\omega}{\omega_c}\right) = \frac{9\sqrt{3}}{8\pi} \frac{\omega}{\omega_c} \int_{\omega/\omega_c}^{\infty} K_{5/3}(x) dx, \quad (5.29)$$

using the modified Bessel function $K_{5/3}$. Depending on the bunch length and shape the low frequency part of the spectrum can get amplified coherently. Assuming a Gaussian bunch profile with an rms length σ_z the spectrum including coherent amplification reads

$$\frac{dP}{d\omega} = \frac{dP_1}{d\omega} \left(N_e + N_e(N_e - 1) \exp\left(-\left(\frac{\sigma_z \omega}{c}\right)^2\right) \right), \quad (5.30)$$

using the number of electrons in the bunch N_e . Coherent amplification is relevant for all kinds of (de)compression systems operating with short electron bunches. For laser-plasma based systems using bunches of a few micrometers or less, i.e. about an order of magnitude shorter than the shortest bunch at linear accelerator based systems like LCLS [89], this is of special importance. The synchrotron spectrum with and without coherent amplification for a bunch with the parameters of the lab-scale FEL case is shown in Fig. 5.3.

If the emission is completely incoherent the total emitted power is given by

$$P_{ic} = \frac{1}{6\pi\epsilon_0} \frac{e^2 c \gamma^4}{R^2} N_e, \quad (5.31)$$

whereas in the case of fully coherent emission the power scales according to

$$P_{fc} = \frac{1}{6\pi\epsilon_0} \frac{e^2 c \gamma^4}{R^2} N_e^2. \quad (5.32)$$

In the case of the lab-scale FEL demonstration experiment using a total charge of $Q = 15$ pC, corresponding to approximately 10^8 electrons, this is a significant difference.

For the here discussed scenario, and most other systems, none of the two extreme cases is a good approximation since neither full coherence nor total incoherence can be reached.

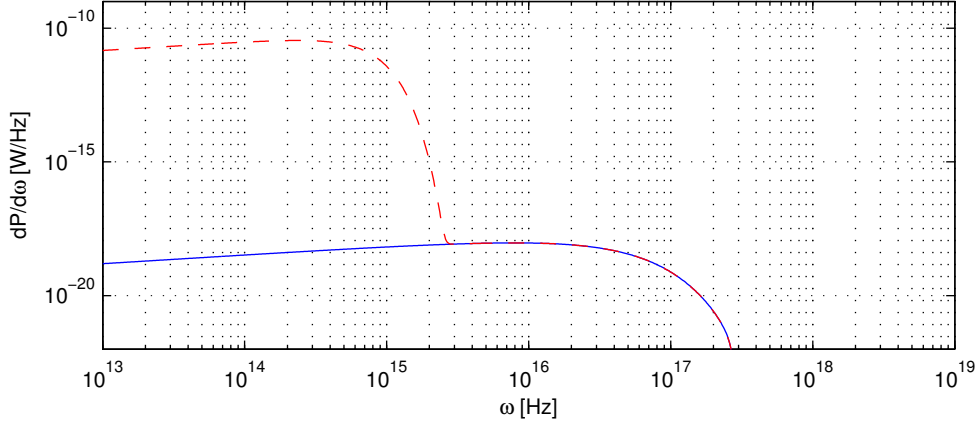


Figure 5.3: Synchrotron spectrum of a bunch with a total charge of $Q = 15$ pC and normalized energy $\gamma = 600$ moving on a circle with radius $R = 3.5$ m. The solid blue line shows the incoherent spectrum based on Eqs. (5.28) and (5.29), whereas the dashed red line shows the coherent amplification assuming a Gaussian bunch with length $\sigma_z = 0.5$ μm based on Eq. (5.30).

The total emitted power, however, is dominated by the coherent fraction of the spectrum with the amount of coherent emission depending on the bunch length. It can be approximated by the partially coherent power [90, 91]

$$P_{\text{pc}} \approx \frac{3^{1/6} \Gamma(2/3)^2}{8\pi^2 \epsilon_0} \frac{e^2 c}{R^{2/3} \sigma_z^{4/3}} N_e^2, \quad (5.33)$$

using the gamma function Γ . For a fixed radius of curvature the emitted power is, consequently, independent of the electron energy. Any increase of the energy for a given radius leads to an increase of the critical frequency and results in an extension of the emitted spectrum into the high frequency range which is incoherent and usually negligible.

If the radiation emission would only result in a uniform energy loss of the electrons, the effect would be relatively easy to handle since the downstream sections of the setup could be adapted to the reduced energy, e.g. by reducing the field strength in the following magnets. The actual situation, however, is more complex. Radiation emitted by one part of the bunch can propagate forward through the rest of the bunch and interact with other electrons modulating their energy. The analytical description of this effects is usually restricted to one-dimensional cases, i.e. cases fulfilling the criterion [91]

$$\frac{\sigma_r}{\sigma_z} \ll \left(\frac{R}{\sigma_z} \right)^{1/3}, \quad (5.34)$$

with $\sigma_r = \sigma_x = \sigma_y$ being the bunch radius. If this requirement is fulfilled, the bunch can be approximated by a normalized line-charge distribution $\lambda(z)$ with $\int \lambda(z) dz = 1$.

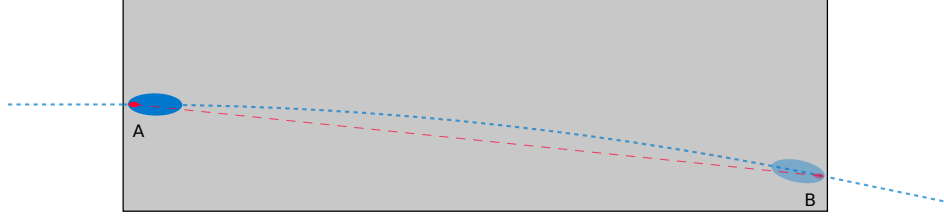


Figure 5.4: Interaction of bunch head and tail due to emission of CSR in a bending magnet. A photon emitted by the bunch tail at point A (red dot) can overtake a fraction of the bunch (blue) during the passage through the magnet and interact with electrons at the bunch head at point B . This leads to the build-up of an energy modulation within the bunch.

Assuming an electron of the bunch to emit a photon at point A on its way through a bending magnet, the photon can overtake electrons located ahead due to the path length difference of the electron bunch moving on the arc of a circle and the emitted radiation propagating on a straight line. Finally, it can interact with another electron at point B as shown in Fig. 5.4. The distance between these two electrons is given by the path length difference, i.e. the slippage distance,

$$\Delta z \approx \text{arc}(AB) - |AB| = R\phi - 2R \sin\left(\frac{\phi}{2}\right) \approx \frac{R\phi^3}{24}. \quad (5.35)$$

All electrons of a bunch of length σ_z can interact if the path length through the magnet is longer than the overtaking distance $l_{\text{ov}} = \text{arc}(AB) \approx (24\sigma_z R^2)^{1/3}$. For a typical decompression setup with an initial bunch length of $\sigma_z = 0.5 \mu\text{m}$ and radius of curvature of $R = 3.5 \text{ m}$ the overtaking length amounts to $l_{\text{ov}} \approx 3.5 \text{ cm}$. When using a typical magnet length of $L_b = 7.5 \text{ cm}$, consequently, all electrons of the bunch are located within the interaction distance.

The rate of energy change for electrons in the bunch can be expressed as [90]

$$\frac{dE(z)}{cdt} = -\frac{N_e e^2}{3^{1/3} 2\pi\epsilon_0 R^{2/3}} \left(\frac{\lambda(z - \Delta z) - \lambda(z - 4\Delta z)}{\Delta z^{1/3}} + \int_{z-\Delta z}^z \frac{1}{(z-z')^{1/3}} \frac{d\lambda(z')}{dz'} dz' \right), \quad (5.36)$$

using the slippage distance Δz as defined above and the normalized, one-dimensional current profile $\lambda(z)$. The first summand is an entrance transient that drops to zero for sufficiently long magnets. The second summand usually dominates the rate of energy

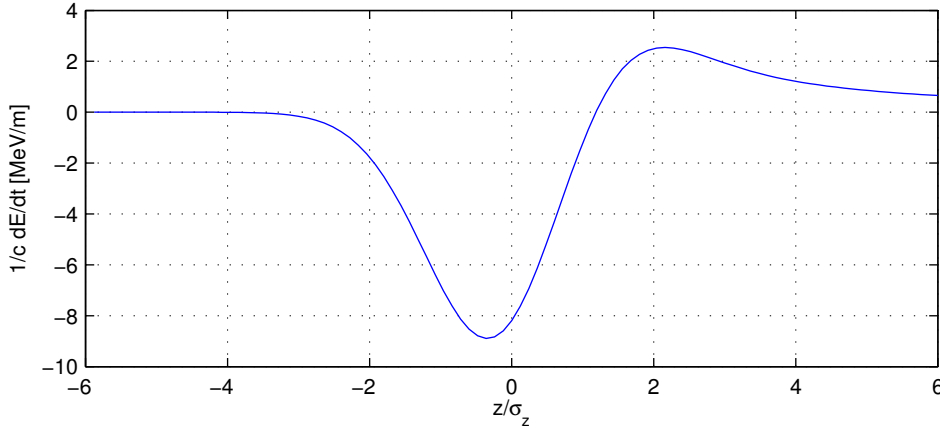


Figure 5.5: Rate of energy change due to CSR as a function of the longitudinal position within the bunch obtained with the steady state version of Eq. (5.36). A typical bunch with a length of $\sigma_z = 0.5 \mu\text{m}$, a bunch charge of $Q = 15 \text{ pC}$, and a normalized energy of $\gamma = 600$ has been assumed to traverse a magnet with a deflection angle of $\Phi = 0.0212 \text{ rad}$ equivalent to a radius of curvature of $R = 3.5 \text{ m}$. Electrons at the bunch tail and center lose energy, whereas electrons at the bunch head gain energy.

change. The limits of the integral indicate that only electron within the slippage distance Δz can interact. For long magnets, i.e. $\Delta z \rightarrow \infty$, all electrons within the bunch can interact and the rate of energy change converges to a steady state. The dominant effect is the build-up of an energy chirp along the bunch. Electrons at the head gain energy, whereas electrons at the tail lose energy, resulting in an energy chirp. On average this can be characterized by a reduction of the mean energy and an additional energy spread.

Using the electron parameters of the lab-scale case, i.e. a Gaussian bunch with a length of $\sigma_z = 0.5 \mu\text{m}$, containing a charge of $Q = 15 \text{ pC}$, and an average energy of $\gamma = 600$, in combination with a magnet length of $L_b = 7.5 \text{ cm}$ with a deflection angle of $\Phi = 0.0212 \text{ rad}$ equivalent to a bending radius of $R = 3.5 \text{ m}$ the integrated, relative energy spread induced during the propagation through a single magnet in the steady-state model is $\sigma_{\eta, \text{CSR}} = 8.6 \cdot 10^{-4}$. The corresponding CSR wake based on the steady state model is shown in Fig. 5.5. Although the additional energy spread, which is mainly an energy chirp, is well below the energy spread of the electron bunch and therefore negligible in its impact on the FEL performance, it can have a significant influence on the beam emittance due to the chromaticity of the chicane as will be discussed in Sect. 5.3.

5.2.2 Space-Charge

An effect usually neglected in the design of bunch compressors at linear accelerator based facilities is space-charge. For laser-plasma accelerator based systems, however,

space-charge effects can become intense [38, 39] due to the unique combination of high peak currents and intermediate electron energies.

In the context of bunch decompression the most important effect caused by space-charge forces is an energy modulation along the bunch as in the case of CSR. In an intuitive picture the process can be understood as the bunch tail being decelerated by the electrons ahead, whereas the bunch head gets accelerated by the trailing electrons. The on-axis energy change for a cylindrically symmetric beam can be expressed as [38]

$$\frac{dE(z)}{cdt} = \frac{e^2 N_e}{2\pi^2 \epsilon_0 \gamma^2 \sigma_z^2} \Lambda(z), \quad (5.37)$$

using the helper function

$$\Lambda(z) = \frac{1}{\sigma_z} \int_{-\infty}^z \Lambda'(\tau) d\tau, \quad (5.38)$$

with

$$\Lambda'(z) = \int \exp\left(-\frac{i\bar{k}z}{\sigma_z}\right) \exp\left(\frac{\bar{k}^2 b^2}{4}\right) \Gamma\left(0, \frac{\bar{k}^2 b^2}{4}\right) \frac{\bar{k}^2}{4} f(k) d\bar{k}, \quad (5.39)$$

using $\bar{k} = k\sigma_z$, with k being the wave number, $b = \sigma_r/(\gamma\sigma_z)$, the upper incomplete gamma function Γ not to be confused with the gamma function used in the CSR discussion above, and the longitudinal form factor of the bunch $f(k) = \int \lambda(z) \exp(ikz) dz$ based on the longitudinal beam profile $\lambda(z)$.

For the demonstration parameter set assuming a Gaussian bunch with the parameters as above and a radius of $\sigma_r \approx 20 \mu\text{m}$, the resulting energy modulation caused by space-charge can be estimated, and is shown in Fig. 5.6. As in the case of CSR the energy modulation is dominated by a longitudinal chirp. The energy spread introduced within a typical magnet assuming a fixed bunch length and a magnet length of $L_b = 7.5 \text{ cm}$ is $\sigma_{\eta, \text{SC}} = 3.7 \cdot 10^{-4}$. This is on the same order as the CSR induced energy spread and, therefore, of importance for the here discussed case.

5.2.3 Wall Wakefields

Besides the direct interaction of the electrons via radiation and electrostatic fields, another way of interaction exists. The electric field of the bunch can be scattered at surfaces in the vicinity of the electron trajectory and act back on the bunch again causing an energy modulation. This effect only becomes important for bunches propagating in narrow beam tubes since otherwise the field amplitude at the surface becomes negligible.

Laser-plasma based systems are often designed as fully in-vacuum setups where all structures like the undulator, focusing optics, and additional components like a chicane are placed within the vacuum chamber. For those cases wall wakefields are usually negligible since no surfaces like beam tubes in the direct vicinity of the electron bunch are required.

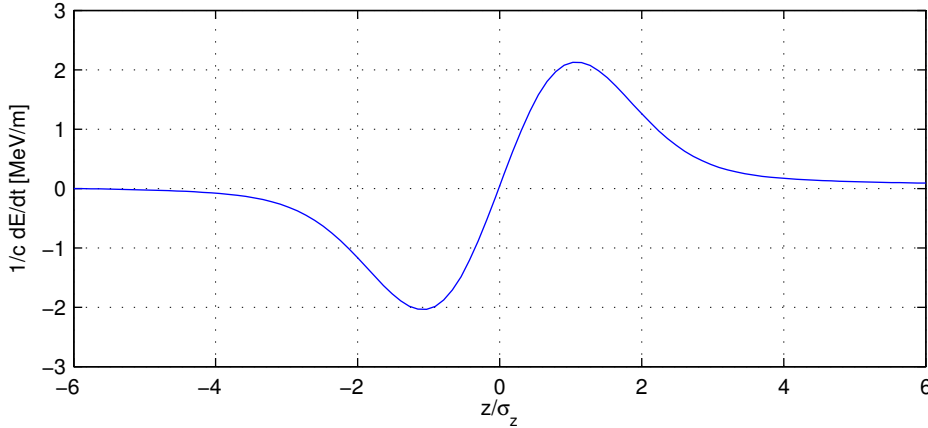


Figure 5.6: Space-charge induced rate of energy change as a function of the longitudinal position within the bunch based on Eq. (5.37). A typical bunch with a length of $\sigma_z = 0.5 \mu\text{m}$, a bunch charge of $Q = 15 \text{ pC}$, and a normalized energy of $\gamma = 600$ was assumed. The rate of energy change is of the same order of magnitude as in the case of CSR.

However, depending on the vacuum and spatial requirements larger structures like the chicane might have to be placed outside of the vacuum, therefore, requiring the use of a beam tube. The gap of the dipoles used for a typical chicane in the here discussed decompression scenarios is on the order of 1 cm and would require a beam tube with a radius of $r \approx 5 \text{ mm}$. Under these conditions wall wakefields can also become important for laser-plasma based systems.

Resistive Wall Wakefields

A class of wakefields that can never be avoided during the propagation through a conducting beam pipe are the resistive wall wakefields. The most typical case is the effect occurring during the propagation through a round beam tube. In this case the wakefield is characterized by the conductivity and radius of the beam tube as well as the peak current of the electron beam.

The on-axis wakefield of a single electron moving in a round beam tube is given by [92]

$$w_z(z)[\text{V/m}] = -\frac{4e}{\pi\epsilon_0 r^2} \left(\frac{\exp\left(-\frac{z}{z_0}\right)}{3} \cos\left(\frac{\sqrt{3}z}{z_0}\right) - \frac{\sqrt{2}}{\pi} \int_0^\infty \frac{x^2 \exp\left(-\frac{x^2 z}{z_0}\right)}{x^6 + 8} dx \right), \quad (5.40)$$

using the radius of the beam tube r , the distance behind the test particle causing the wakefield z , the characteristic length $z_0 = (2r^2\epsilon_0 c/\sigma)^{1/3}$ with the conductivity of the beam tube σ .

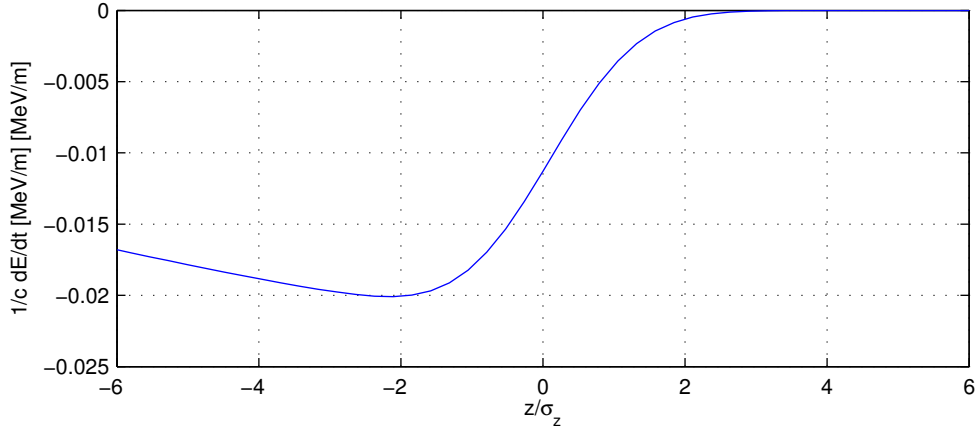


Figure 5.7: Rate of energy change due to a resistive wall wakefield caused by a bunch with a length of $\sigma_z = 0.5 \mu\text{m}$ and a bunch charge of $Q = 15 \text{ pC}$ propagating through a round copper beam pipe with conductivity $\sigma = 58.1 \cdot 10^6 \text{ A}/(\text{V m})$ and a radius of $r = 5 \text{ mm}$. Due to the short bunch length, the major effect is the build-up of a linear energy chirp.

The wakefield of the whole electron bunch is obtained by convolution of the single electron wake with the longitudinal beam profile

$$W_z(z)[\text{V/m}] = \int_0^\infty w_z(z)N(z - z')dz'. \quad (5.41)$$

Here the beam profile is normalized to $\int N(z)dz = N_e$. The so-obtained wakefield is a longitudinal electric field modulating the electron energy depending on the internal bunch coordinate z .

The situation is special for typical laser plasma-based bunches with a length of less than $\sigma_z \leq 1 \mu\text{m}$. They are shorter than the characteristic length of the wakefield z_0 , leading to the build-up of a mostly linear energy chirp along the bunch. Regarding the FEL performance this chirp can be compensated in the undulator by adapting the taper.

Using the electron parameters of the demonstration case and assuming a bunch to pass a copper beam tube with radius $r = 5 \text{ mm}$, i.e. matching the gap of the bending magnets, the conductivity $\sigma = 58.1 \cdot 10^6 \text{ A}/(\text{Vm})$, and the length of a magnet of $L_b = 7.5 \text{ cm}$ results in an additional, projected energy spread of $\sigma_{\eta,\text{res}} = 1.5 \cdot 10^{-6}$. This is two orders of magnitude smaller than the previously discussed energy spreads due to synchrotron radiation and space-charge, and is hence negligible regarding the beam propagation through the chicane.

Geometric Wall Wakefields

Another class of wakefields are the geometric wall wakefields caused by sudden changes of the beam tube geometry. Analytical solutions for this kind of problem exist for very simple cases only, in general numerical algorithms are needed.

One simple but often encountered case is a so-called step transition (see Fig.5.8), e.g. occurring at the transition between vacuum tubes of different size. An effect on the beam is only found for a step-out transition, i.e. when moving from a narrow to a wide tube [93]. The effect on the beam can be characterized by either the longitudinal impedance [93,94]

$$Z_{\parallel} = \frac{Z_0}{\pi} \ln \left(\frac{r_2}{r_1} \right), \quad (5.42)$$

with the radii fulfilling $r_2 > r_1$, or the corresponding longitudinal single particle wake obtained via an inverse Fourier transform

$$w_{\parallel}(z)[V/C] = Z_{\parallel} c \delta(z) = \frac{Z_0 c}{\pi} \ln \left(\frac{r_2}{r_1} \right) \delta(z). \quad (5.43)$$

In both cases Z_0 is the impedance of free space. The resulting energy change is obtained by convolution of the single particle wake with the longitudinal charge distribution

$$W_{\parallel}(z)[V] = \int_{-\infty}^z Q(z') w_{\parallel}(z - z') dz' = Z_{\parallel} c Q(z). \quad (5.44)$$

Here the longitudinal charge distribution is normalized according to $\int Q(z) dz = N_e e$.

Using the typical demonstration case bunch and a step out transition from $r_1 = 5$ mm to $r_2 = 10$ mm, as it could occur in the chicane after leaving a magnet and switching to a wider beam tube on a drift, results in an additional, projected energy spread of $\sigma_{\eta, \text{step}} = 2.7 \cdot 10^{-4}$. This is on the same order of magnitude as CSR and space-charge based effects and, therefore, has to be taken into account if the beam tube diameter changes within the chicane.

A second, similar case that can be described analytically is a tapered transition between two round beam tubes. Here the analytical model is restricted to small tapering angles, i.e. cases fulfilling the condition $|r'(s)| \ll 1$ with r' being the derivative of the beam radius with respect to the longitudinal position. The longitudinal impedance for this type of transition is given by [94,95]

$$Z_{\parallel} = -\frac{i\omega Z_0}{4\pi c} \int_{-\infty}^{\infty} (r'(s))^2 ds. \quad (5.45)$$

Assuming a linear taper over the length L from radius r_1 to r_2 yields the single particle wake

$$w_{\parallel}(z)[V/C] = \frac{Z_0 c}{4\pi} \frac{(r_2 - r_1)^2}{L} \delta'(z). \quad (5.46)$$

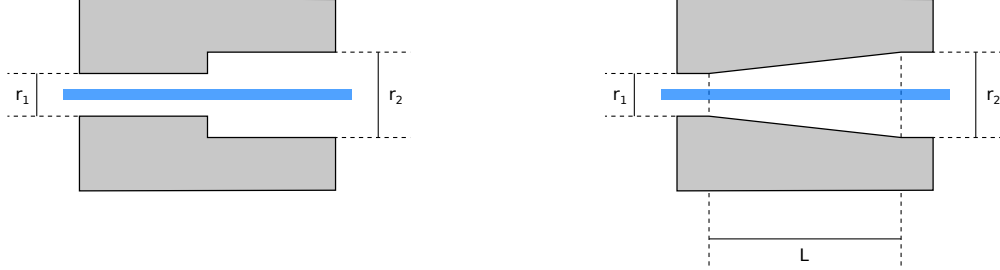


Figure 5.8: The two typical types of transitions occurring in beam tubes, resulting in geometric wall wakefields, a step transition (left) and a tapered transition (right).

The total energy change due to the whole bunch obtained via convolution reads

$$W_{\parallel}(z)[\text{V}] = \int_{-\infty}^z Q(z')w_{\parallel}(z-z')dz' = \frac{Z_0c}{4\pi} \frac{(r_2 - r_1)^2}{L} Q'(z). \quad (5.47)$$

In contrast to the step-out transition the tapered transition depends on the derivative of the longitudinal charge distribution.

Considering the same scenario as in the step transition but with a linear taper over a length of $L = 1$ m results in an additional energy spread of $\sigma_{\eta, \text{taper}} = 7.7 \cdot 10^{-3}$, which is even larger than in the case of the step transition. This is caused by the dependence of the energy change on the derivative of the longitudinal charge distribution combined with the ultra-short bunches. In this case a tapered transition is, consequently, not of advantage when compared to a step transition and should be considered with care. The introduced energy spread exceeds that of all previously discussed effects.

In summary, sources of both types of geometric wakefields should be avoided if possible since the short bunches cause significant energy changes when traversing such structures spoiling the emittance as discussed in the next section.

5.3 Emittance Growth

The major problem of any bunch (de)compression system is the induced emittance growth. Since up to now all X-ray FELs are emittance limited (see Sect. 2.4.4), any emittance growth in a bunch (de)compressor is critical for the operation of the whole system.

5.3.1 Basic Mechanism

The emittance growth mechanism in a chicane can be explained with a simple model. During the passage through the chicane, every electron is subject to various sources of energy changes, as discussed in the section above. Due to the dispersive properties of the chicane, any energy change will affect the electron trajectory in the subsequent magnets and alter the final particle position and angle.

Reducing this continuous process to a single kick model with each energy changes occurring at the end of a magnet or following drift, the final particle coordinate can be expressed as

$$x_f = x_{f,0} + \sum_i \Delta x_i(\eta_i), \quad (5.48)$$

$$x'_f = x'_{f,0} + \sum_i \Delta x'_i(\eta_i), \quad (5.49)$$

using the ideal, final particle position $x_{f,0}$ and angle $x'_{f,0}$ as well as the energy change induced offsets $\Delta x_i^{(l)}(\eta_i)$. In the single kick model the energy change $\eta_i = \Delta\gamma_i/\gamma$ occurs at the end of the i -th magnet or drift. Consequently, it will have no influence on the particles angle or transverse position up to the magnet $i + 1$ as shown in Fig. 5.9. The energy change induced offsets and angles can be written as

$$\Delta x_i(\eta_i) = R_{16}^i \eta_i, \quad (5.50)$$

$$\Delta x'_i(\eta_i) = R_{26}^i \eta_i. \quad (5.51)$$

Here R_{16}^i and R_{26}^i are the transport matrix elements from the i -th magnet to the end of the chicane.

Using the definition of the emittance

$$\epsilon_x = \sqrt{\text{Var}(x_f) \text{Var}(x'_f) - \text{Cov}^2(x_f, x'_f)}, \quad (5.52)$$

this allows to estimate the impact of a certain chicane configuration on the final emittance. The variance terms in the single kick model can be expressed as

$$\text{Var}(x_f) = \text{Var}(x_{f,0}) + \sum_i \text{Var}(\Delta x_i) + 2 \sum_i \text{Cov}(x_{f,0}, \Delta x_i) + 2 \sum_i \sum_{j>i} \text{Cov}(\Delta x_i, \Delta x_j), \quad (5.53)$$

$$\text{Var}(x'_f) = \text{Var}(x'_{f,0}) + \sum_i \text{Var}(\Delta x'_i) + 2 \sum_i \text{Cov}(x'_{f,0}, \Delta x'_i) + 2 \sum_i \sum_{j>i} \text{Cov}(\Delta x'_i, \Delta x'_j), \quad (5.54)$$

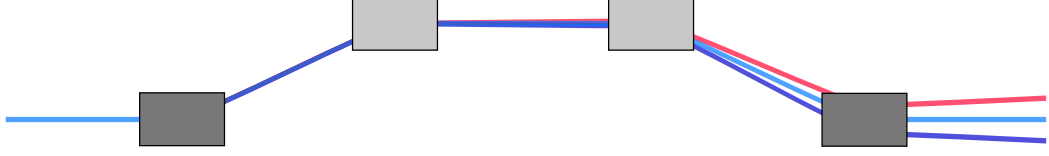


Figure 5.9: Schematic of the emittance growth mechanism. The electron bunch is subject to energy changes during its whole propagation. Due to energy changes occurring in the chicane the deflections of the magnets before and after the energy change do not cancel anymore. Here an energy modulation occurring at the exit of the first magnet has been assumed. Up to the second magnet no effect on the trajectories is found. Starting from the second magnet on the beam widens due to the energy dependent deflections.

whereas the covariance can be expanded into

$$\text{Cov}(x_f, x'_f) = \text{Cov}(x_{f,0}, x'_{f,0}) + \sum_i \text{Cov}(x_{f,0}, \Delta x'_i) + \sum_i \sum_j \text{Cov}(\Delta x_i, \Delta x'_j). \quad (5.55)$$

The offset dependent terms can further be written as

$$\text{Var}(x_{f,0}) = \sigma_{x_{f,0}}^2 = \beta_x \epsilon_{x,0}, \quad (5.56)$$

$$\text{Var}(\Delta x_i) = \sigma_{x_i}^2 = (R_{16}^i)^2 \sigma_{\eta_i}^2, \quad (5.57)$$

$$\text{Cov}(x_{f,0}, \Delta x_i) = R_{16}^i \text{Cov}(x_{f,0}, \eta_i), \quad (5.58)$$

$$\text{Cov}(\Delta x_i, \Delta x_j) = R_{16}^i R_{16}^j \text{Cov}(\eta_i, \eta_j), \quad (5.59)$$

as well as the relations for the angles

$$\text{Var}(x'_{f,0}) = \sigma_{x'_{f,0}}^2 = \gamma_x \epsilon_{x,0}, \quad (5.60)$$

$$\text{Var}(\Delta x'_i) = \sigma_{x'_i}^2 = (R_{26}^i)^2 \sigma_{\eta_i}^2, \quad (5.61)$$

$$\text{Cov}(x'_{f,0}, \Delta x'_i) = R_{26}^i \text{Cov}(x'_{f,0}, \eta_i), \quad (5.62)$$

$$\text{Cov}(\Delta x'_i, \Delta x'_j) = R_{26}^i R_{26}^j \text{Cov}(\eta_i, \eta_j). \quad (5.63)$$

The covariance terms including offsets and angles can be simplified using

$$\text{Cov}(x_{f,0}, x'_{f,0}) = -\alpha_x \epsilon_{x,0}, \quad (5.64)$$

$$\text{Cov}(x_{f,0}, \Delta x'_i) = R_{26}^i \text{Cov}(x_{f,0}, \eta_i), \quad (5.65)$$

$$\text{Cov}(\Delta x_i, \Delta x'_j) = R_{16}^i R_{26}^j \text{Cov}(\eta_i, \eta_j). \quad (5.66)$$

Using these relations, all contributions can be related to the ideal Twiss parameters α_x , β_x , and γ_x at the chicane exit, the ideal final emittance $\epsilon_{x,0}$, the linear transport matrix elements, and covariances of either the ideal positions/angles and the individual energy changes or of two energy changes. The covariances between two different energy changes can in general not be obtained analytically.

Neglecting higher order contributions of the induced energy spread $\mathcal{O}(\sigma_\eta^4)$ and any covariances involving energy changes allows for a simple emittance estimate

$$\epsilon_x \approx \sqrt{\epsilon_{x,0}^2 + \epsilon_{x,0} \sum_i \frac{\sigma_{\eta_i}^2}{\beta_x} \left((R_{16}^i)^2 + (\beta_x R_{26}^i + \alpha_x R_{16}^i)^2 \right)}, \quad (5.67)$$

using the energy spread created at the i -th magnet or drift σ_{η_i} . This scaling has also been suggested by Di Mitri et al. [96] but further simplified, taking only the effect of a single magnet and CSR based energy changes into account. In the more general scaling above the energy spreads can be caused by a mix of all previously discussed effects. These different sources of energy changes are again correlated. For the two most important effects that cannot be neglected for any decompression system, coherent synchrotron radiation and space-charge, the combined energy spread can be approximated by

$$\sigma_{\eta_i} = \sqrt{\sigma_{\eta_i, \text{CSR}}^2 + \sigma_{\eta_i, \text{SC}}^2 + 1.22 \sigma_{\eta_i, \text{CSR}} \sigma_{\eta_i, \text{SC}}}, \quad (5.68)$$

using the covariance of CSR and space-charge induced energy spread $\text{Cov}(\sigma_{\eta_i, \text{CSR}}, \sigma_{\eta_i, \text{SC}}) \approx 0.61$, which has been obtained with the analytical models above (Eqs. (5.36) and (5.37)).

Since all effects leading to energy changes are bunch length dependent, an important point to be taken into account when estimating the energy changes induced in the chicane is the projected bunch length [97]

$$\sigma_{z, \text{proj.}} = \sqrt{\sigma_z^2 + R_{51}^2 \sigma_{x,w}^2 + (R_{52} - R_{51}s)^2 \sigma_{x',w}^2 + R_{56}^2 \sigma_\eta^2}, \quad (5.69)$$

using the initial bunch length σ_z , the bunch size and divergence at the waist $\sigma_{x,w}$ and $\sigma_{x',w}$, the initial, relative energy spread σ_η , the linear transport matrix elements R_{51} , R_{52} and R_{56} from the chicane entrance, and the distance between entrance and waist s . This is crucial due to the significant bunch length dependence of all energy spread inducing effects and the pancake-like shape of laser-plasma based bunches that leads to significant changes of the projected bunch length during the deflection in a magnet even when monoenergetic bunches are considered [98].

5.3.2 C-Chicane

Besides the energy changes, also the rest of the emittance growth mechanism depends on the linear transport matrix elements and consequently the specific chicane geometry. For a C-chicane the matrix elements characterizing the dependence of the horizontal offset on the energy deviation are

$$R_{16}^1 = \phi_1 \left(\frac{5}{2} L_b + L_{23} + L_{34} \right) + \phi_2 (L_b + L_{34}), \quad (5.70)$$

$$R_{16}^2 = \phi_2 (L_b + L_{34}), \quad (5.71)$$

$$R_{16}^3 = -\phi_2 \frac{L_b}{2}, \quad (5.72)$$

$$R_{16}^4 = 0. \quad (5.73)$$

The matrix elements linking the horizontal angle and the energy deviations are given by

$$R_{26}^1 = \phi_1, \quad (5.74)$$

$$R_{26}^2 = 0, \quad (5.75)$$

$$R_{26}^3 = -\phi_2, \quad (5.76)$$

$$R_{26}^4 = 0. \quad (5.77)$$

In both sets the fourth element vanishes since in the single kick model the last energy change occurs at the end of the fourth magnet, resulting in all transport matrix elements to be zero.

The resulting final particle offsets and angles are

$$\Delta x = \phi_1 \left(\frac{5}{2} L_b + L_{23} + L_{34} \right) \eta_1 + \phi_2 \left((L_b + L_{34}) \eta_1 + (L_b + L_{34}) \eta_2 - \frac{L_b}{2} \eta_3 \right), \quad (5.78)$$

$$\Delta x' = \phi_1 \eta_1 - \phi_2 \eta_3. \quad (5.79)$$

In general, the offset contributions can only cancel each other in the case of alternating signs of the energy changes η_i since R_{16}^1 and R_{16}^2 have the same sign and R_{16}^3 is significantly smaller and usually negligible. For the case of decreasing energy change amplitudes of the same sign along the setup $|\eta_1| > |\eta_2| > |\eta_3|$, which approximately holds for a decompression scenario due to the lengthening of the bunch, a compensation of the offset contributions is not possible. The situation is different for a compression system where the absolute energy changes rise along the chicane due to the shortening of the bunch. There a partial cancellation of the individual contributions is possible. The angular contributions cannot cancel in a symmetric chicane $\phi_1 = \phi_2$ due to the increasing/decreasing energy changes along the chicane. In an asymmetric configuration with $\phi_1 > \phi_2$ operating as a bunch compressor the increasing energy changes due to the shortening of the bunch and the lower deflection angle can result in a cancellation of the contributions from the first and third magnet.

5.3.3 S-Chicane

The matrix elements characterizing the energy dependence of horizontal offsets and angles in the case of the S-chicane differ significantly from their counterparts of the C-chicane. The energy dependence of the offsets is given by

$$R_{16}^1 = \phi \left(\frac{9}{2}L_b + 2L_{12} + 2L_{34} \right), \quad (5.80)$$

$$R_{16}^2 = -\phi \left(\frac{5}{2}L_b + 2L_{34} \right), \quad (5.81)$$

$$R_{16}^3 = \phi \frac{L_b}{2}, \quad (5.82)$$

$$R_{16}^4 = 0. \quad (5.83)$$

The dependence of the horizontal angle on the energy deviations reads

$$R_{26}^1 = \phi, \quad (5.84)$$

$$R_{26}^2 = -\phi, \quad (5.85)$$

$$R_{26}^3 = \phi, \quad (5.86)$$

$$R_{26}^4 = 0. \quad (5.87)$$

Again the last transport matrix elements vanish.

The final particle offsets and angles are

$$\Delta x = \phi \left(\left(\frac{9}{2}L_b + 2L_{12} + 2L_{34} \right) \eta_1 - \left(\frac{5}{2}L_b + 2L_{34} \right) \eta_2 + \frac{L_b}{2} \eta_3 \right), \quad (5.88)$$

$$\Delta x' = \phi (\eta_1 - \eta_2 + \eta_3). \quad (5.89)$$

In contrast to the case of the C-chicane, a (partial) cancellation of the individual offset contributions is also possible in the case of nonalternating signs of the energy changes η_i . In a symmetric S-chicane, i.e. $L_{12} = L_{34}$, assuming energy changes of the same sign and similar amplitude after the first and second magnet $\eta_1 \approx \eta_2$ allows the contribution from the second magnet to compensate approximately 50% of the offset introduced by the first magnet $R_{16}^1 \eta_1 + R_{16}^2 \eta_2 \approx 0.5 R_{16}^1 \eta_1$. This ratio can even be improved by switching to an asymmetric layout and shortening of the initial drift L_{12} . A further difference when compared to the C-chicane is the doubled deflection angle of the central magnets in a four-magnet S-chicane. This increases the energy changes η_2 and η_3 for a given bunch length and facilitates the possibility to reach a configuration with $\eta_1 \approx \eta_2$ despite the increased bunch length in the second magnet and the corresponding reduction of energy changes. This idealized cancellation might not fully be reached in real life systems; however, it already indicates the advantage of the S-chicane. How the chicane layouts can be optimized in order to minimize the emittance growth will be discussed in the next chapter.

5.4 Compression vs. Decompression

Emittance growth plays a major role for bunch compressors, as they are used at conventional linear accelerator based free-electron lasers, as well as bunch decompressors, as planned for laser-plasma accelerator based systems. Although the underlying physics is the same, the two scenarios differ significantly.

The most obvious difference between the two kinds of systems is the evolution of the bunch length. In bunch compressors the bunch length reduces along the setup, resulting in more intense effects, like the emission of synchrotron radiation, at the end of the chicane. In these system the minimum achievable bunch length and the resulting bunch degradation due to emittance growth can be balanced, i.e. the emittance growth can be reduced at the cost of a lower peak current after compression. On the contrary, decompression systems start with the shortest bunch, resulting in the most intense effects, occurring in the first chicane sections, to be unavoidable. This difference becomes important when using merit functions to optimize the setup performance. For linear accelerator based systems usually only the effects occurring in the last magnet are considered [96]. When optimizing a decompressor, the situation not only changes to the first magnet dominating, but also the second and third magnet cannot be neglected anymore in an optimization. Moreover, the optimization has not only to be carried out in terms of minimizing the appropriate transport matrix elements linking energy, position, and angle; also the layout dependence of the energy spread causing effects has to be taken into account (see Chap. 6). Furthermore, the two cases not only differ in where the shortest bunch length is reached in the setup but also in the minimum bunch length itself. The shortest, compressed bunch at linear accelerator based facilities is usually at least one order of magnitude longer than the longest bunch in a laser-plasma accelerator based system using decompression [17, 69, 89, 96].

A further difference is given by the difference in typical energies in combination with the bunch length. Both types of systems usually operate in the partially coherent regime of synchrotron radiation. Linear accelerator based facilities can, due to their higher energies, however, operate in parameter ranges where the incoherent fraction of the spectrum contributes significantly to the total energy changes [99]. In contrast, laser-plasma accelerator based systems for first FEL demonstration experiments will operate at energies at least one order of magnitude below those of linear accelerator based free-electron lasers, and will be dominated by the coherent synchrotron radiation. This difference is even intensified by the bunch length difference.

The situation changes when considering space-charge effects. These can usually be neglected in bunch compressors at linear accelerator facilities. In the case of a compressor located in the vicinity of the electron gun the long initial bunch length suppresses these effects despite the moderate energy. Further downstream the accelerator these effects get

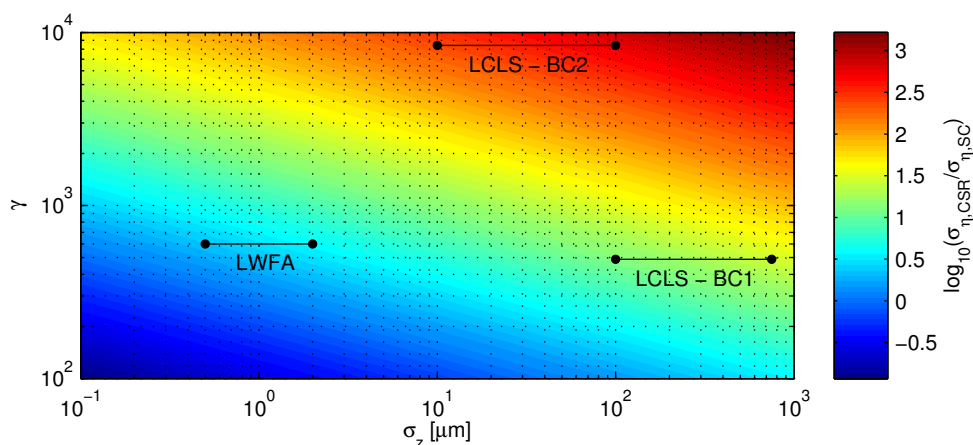


Figure 5.10: Comparison of energy spread caused by CSR and space-charge in a bending magnet as a function of the bunch length and energy based on Eqs. (5.36) and (5.37). The magnet has been assumed to have a field typical for the here discussed cases of $B \approx 0.3$ T. The markers indicate the parameter ranges for the here discussed laser-plasma based case (LWFA) and for LCLS in the two compressors BC1 and BC2 [89].

mitigated due to the high energies on the multi-GeV-level, although the bunch length reduces. A typical laser-plasma based free-electron laser demonstration will use moderate energies of a few hundred MeV in combination with bunches at least one order of magnitude shorter than the shortest bunch at linear accelerator based facilities, resulting in space-charge effects to become important for the setup design. Comparing the energy spread caused by coherent synchrotron radiation to the space-charge induced contribution as a function of bunch length and energy as shown in Fig. 5.10 indicates that linear and laser-plasma accelerator driven systems differ drastically. Laser-plasma accelerators produce bunches on the order of one micrometer and operate in the energy range $\gamma = 10^2$ – 10^3 . Linear accelerators, however, start with bunch lengths on the order of millimeters before a first bunch compression and comparable energies, and end up at the 10- μm -range after the last compression but with energies on the order of $\gamma = 10^4$. Consequently, laser-plasma accelerators are in a range where CSR and space-charge induced energy spread are of the same order of magnitude, whereas for linear accelerators CSR clearly dominates during the whole acceleration and compression process.

Besides the bunch length, a further difference of importance is the initial energy distribution. The initial electron bunches at linear accelerator based systems are well approximated by a vanishing local energy spread and a linear energy chirp introduced by off-crest acceleration just before the compression stage. Due to this correlation, longitudinal slices of the electron bunch do not get mixed during the compression. Hence, all electrons of a slice are subject to the same energy changes and no additional, local energy spread builds up. Therefore, the slice emittance is conserved as long as higher order effects as well as

the projected length of a slice can be neglected [97]. Only the projected emittance of the bunch grows due to the different energy changes along the bunch. This growth can be minimized by using compensating effects of layouts like an S-chicane or combinations of C-chicanes [97, 100]. Laser-plasma based accelerators are, up to now, not capable of producing bunches with energy spreads as low as it is possible with linear accelerators. Depending on the injection mechanism the projected energy spread is a mix of an energy chirp and an uncorrelated energy spread. So far no exact phase space information are available and a completely uncorrelated energy spread has to be assumed as a worst case. This uncorrelated spread results in significant longitudinal position changes during the decompression and a mixing of the initial longitudinal slices. Consequently, not only the projected but also the slice emittance grows significantly. Furthermore, the use of layouts like the S-chicane gets reduced.

Due to these differences, the well established optimization concepts developed for bunch compressors cannot directly be transferred to decompression systems. The merit functions for the design have to be adapted and the different concepts have to be re-evaluated (see Chap. 6).

5.5 Conclusion

In this chapter, the basics of longitudinal phase space manipulation using chicane have been introduced.

The most important parameter in the context of a (de)compression system is the longitudinal dispersion R_{56} which measures the energy dependence of the path length and therefore the chromatic effect of a chicane on the bunch length. The same effect can be reached using different layouts like symmetric and asymmetric C- and S-chicanes.

The differences and advantages of the different layouts emerge when degrading effects are taken into account. The most important issue is the emittance growth induced by energy changes occurring during the pass through the chicane.

The two strongest sources of energy changes in a decompression system as it is discussed here are coherent synchrotron radiation and space-charge. This is in stark contrast to compression systems used at linear accelerator based facilities which can usually neglect any space-charge effects. Further sources of energy changes are resistive and geometric wall wakefields that become important if beam tubes are used. Since they can reach and even exceed the other effects, they should be avoided by using an in-vacuum setup.

The differences of a compression and decompression system regarding the typical parameter sets as well as the evolution of the bunch in the chicane require a re-evaluation of optimization concepts in order to minimize the emittance growth discussed in the next chapter.

6 Decompressor Optimization

For the planned demonstration experiment of a laser-plasma accelerator based free-electron laser a bunch decompression is required. The bunch has to be stretched by a factor of four in order to obtain an optimum balance between local energy spread, slippage and peak current (see Sect. 3.3).

During the bunch decompression the ultra-low emittance has to be preserved as far as possible to ensure the highest possible current density in the undulator. The expected rise of the energy spread due to effects like synchrotron radiation is negligible in terms of the FEL performance since it is about one order of magnitude below the initial energy spread and is not considered as an optimization goal.

In addition to the preservation of the beam quality, a compact setup layout is required to be suited for a lab-scale system. All discussed layouts will consist of four magnets based on an already existing chicane.

All optimizations rely on 3D simulations of the bunch propagation through the chicane since the analytical model above can only give rough performance estimates due to the used simplifications.

6.1 Simulation

For the setup optimization the well tested code CSRTRACK [101, 102] has been used. It allows to use different simulation concepts ranging from a simple 1D algorithm to a fully 3D model including the full field evolution and particle interaction.

The 1D model is based on the analytical CSR formula discussed above (see Eq. (5.36)). Here only the longitudinal current profile of the bunch is taken into account. Using the analytical 1D formalism the longitudinal field is obtained and the particle energies are changed accordingly. The advantage of this approach is the low simulation effort that only depends linearly on the particle number $\mathcal{O}(N)$. Due to its high speed, this approach is well suited for parameter scans. The problem in the context of the here discussed cases is twofold: First, the bunches studied do not strictly fulfill the 1D criterion [91]. In these cases the 1D model is assumed to give an upper limit for the emittance growth [79] but is not reliable anymore. Second, space-charge effects are neglected. Since the analytical

discussion above showed that this effect is on the same order of magnitude as coherent synchrotron radiation, it will lead to significant deviations from the actual situation.

Besides the 1D model, different 3D models are supported by CSRTRACK. In all models all particles are treated as three-dimensional sub-bunches. The fields of all these sub-bunches get calculated based on their trajectory taking retardation effects into account. For all cases in this thesis the “Pseudo Green’s Function Approach” has been used [101]. It provides a good compromise between the exact point to point interaction and the 1D model. The numerical effort is of the order $\mathcal{O}(N^2)$ and, consequently, significantly larger than in the 1D model limiting the size of parameter scans.

In all simulations 4k macro particles were used. The initial distribution consisted of 20 longitudinal slices each containing 200 particles with an appropriate weighting to model the Gaussian current profile. Convergence tests with up to 16k macro particles did not yield any significant changes. The transverse coordinates as well as the momentum were represented by Gaussian distributions cut off at the three- σ -range. The sub-bunch dimensions were set to $\sigma_{\text{long}} = 0.3 \mu\text{m}$ and $\sigma_{\text{rad}} = 5.0 \mu\text{m}$. Tests with larger sub-bunches resulted in an artificial smoothing of the current profile distorting the results. The use of self-scaling sub-bunches showed no significant effect and was therefore discarded. In general these simulation parameters are in good agreement with the results of [103].

The electron parameters are those of the decompression setup (see Table 3.3). All simulations start at the chicane entrance and neglect any chromatic effects of an upstream focusing system to allow for a discussion independent of a specific optics layout. Furthermore, any degrading effects caused by the setup geometry like wall wakefields are neglected in the spirit of an in-vacuum system and in order to be as general as possible.

6.2 Twiss Optimization

One optimization possibility is the adjustment of the Twiss parameters at the chicane entrance [97, 104, 105] characterizing the beam in the transverse phase space. Any change of the initial Twiss parameters also changes the shape and orientation of the final phase space ellipse at the chicane exit.

In the single kick model (see Sect. 5.3) each energy change leads to an additional particle offset and angle at the chicane exit characterized by the amount of energy change and the linear transport matrix elements according to Eqs. (5.50) and (5.51). In the transverse phase space this translates into a shift of all particles along the direction

$$\theta_{\text{CSR}}^i = \tan^{-1} \left(\frac{R_{26}^i}{R_{16}^i} \right), \quad (6.1)$$

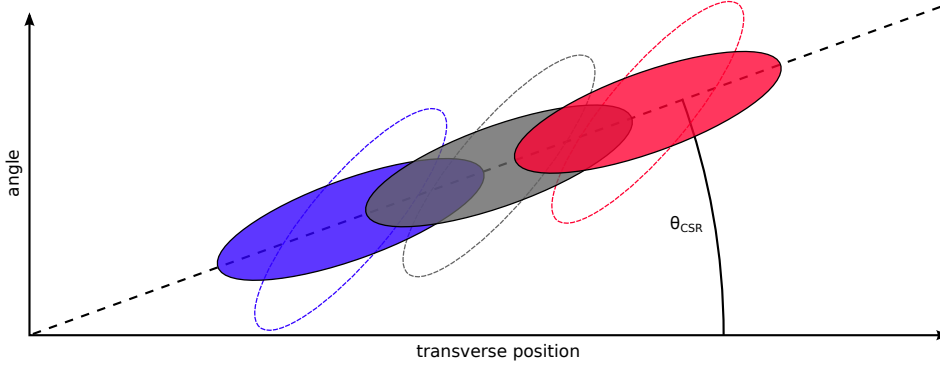


Figure 6.1: Sketch of the transverse phase space of a bunch at the chicane exit. Two longitudinal slices (blue and red) have been displaced along the direction θ_{CSR} with respect to the reference slice (grey) due to an energy modulation occurring at one position in the chicane. Both shifts in the transverse phase space were caused by the same absolute energy change but opposite signs. For an optimized orientation of the phase space ellipse (solid) the emittance growth is minimized. Other orientations (dashed) result in a reduction of the overlap of the individual ellipses and therefore result in a larger emittance growth [105].

with the amplitude of the shift given by

$$a_{\text{CSR}} = \sqrt{(R_{16}^i)^2 + (R_{26}^i)^2} \eta_i. \quad (6.2)$$

If only a single energy change is considered, all longitudinal slices, defined at the time of the energy kick, get shifted along the same direction but with different amplitudes. The emittance growth in this case depends on the shape and orientation of the ideal, final phase space ellipse, given by the Twiss parameters, with respect to the shift direction θ_{CSR}^i . The effect is illustrated in Fig. 6.1.

In general the transverse ideal phase space coordinates can be characterized by

$$x(\Psi) = \sqrt{\epsilon\beta} \cos(\Psi), \quad (6.3)$$

$$x'(\Psi) = -\sqrt{\frac{\epsilon}{\beta}} (\alpha \cos(\Psi) + \sin(\Psi)), \quad (6.4)$$

using the particle phase Ψ . For $\alpha \neq 0$ the semi axes of the so described ellipses do not coincide with the coordinate axes. The particle phase matching the semi-major axis is

$$\Psi_{\text{maj}} = \tan^{-1} \left(\frac{-\beta^2 - \alpha^2 + 1 + \sqrt{(\beta^2 + \alpha^2)^2 - 2\beta^2 + 2\alpha^2 + 1}}{2\alpha} \right). \quad (6.5)$$

Hence, the orientation of the semi-major axis is

$$\begin{aligned}\theta_{\text{maj}} &= \tan^{-1} \left(\frac{x'(\Psi_{\text{maj}})}{x(\Psi_{\text{maj}})} \right) \\ &= -\tan^{-1} \left(\frac{-\beta^2 + \alpha^2 + 1 + \sqrt{(\beta^2 + \alpha^2)^2 - 2\beta^2 + 2\alpha^2 + 1}}{2\alpha\beta} \right).\end{aligned}\quad (6.6)$$

For a single kick and a given energy change of the particles the emittance growth can consequently be minimized by aligning the semi-major axis of the phase space ellipse with the kick direction $\theta_{\text{maj}} = \theta_{\text{CSR}}^i$ and maximizing the length of the semi-major axis $r_{\text{maj}} = \sqrt{x^2(\Psi_{\text{maj}}) + x'^2(\Psi_{\text{maj}})}$. In this case the total phase space volume occupied after the shift of the longitudinal slices gets minimized.

This ideal optimization, however, is only feasible in the case of a single kick dominating the phase space evolution. In the decompression scenario all contributions from the first three magnets have to be taken into account; furthermore, the broad uncorrelated energy spread causes a mixing of the longitudinal slices over time significantly restricting this idealized optimization concept.

The use of the optics optimization has been tested with CSRtrack for a reference chicane layout, a symmetric C-chicane with a magnet length of $L_b = 7.5$ cm and a drift length of approximately $L_{12} = L_{34} \approx 17$ cm. Figure 6.2 shows the projected and slice emittance growth as a function of the Twiss parameters at the chicane entrance. The projected emittance growth varies from $\sim 35\%$ up to $\sim 80\%$ and is minimized for small, initial β -functions in combination with low, positive values of α . The slice emittance growth of the central slice defined at the chicane exit varies from $\sim 15\%$ up to $\sim 85\%$. Besides the difference in absolute numbers also a qualitative difference of the dependence of the emittance growth on the Twiss parameters is found.

The scaling difference can be explained as follows: Electrons of the final central slice at the chicane exit are distributed over the full bunch length at the chicane entrance (see Fig. 6.3). Therefore, these electrons sample the full CSR and space-charge fields during their pass through the first magnet and drift. This leads to energy changes with a high variance, causing a significant contribution to the emittance growth according to Eq. (5.67). In the subsequent magnets downstream the chicane the bunch has already been decompressed, resulting in the electrons of the final central slice to be distributed over a shorter longitudinal fraction of the bunch and a general reduction of the degrading effects. The electrons consequently only sample a small fraction of these weaker fields, resulting in smaller energy changes with a lower variance. The resulting contributions to the emittance growth reduce along the chicane. Accordingly, the slice emittance growth is dominated by the initial energy changes occurring in the first magnet and drift. The projected emittance growth, however, is a combined effect of all energy changes occurring within the chicane. Hence, the optimum Twiss parameter region minimizing the projected

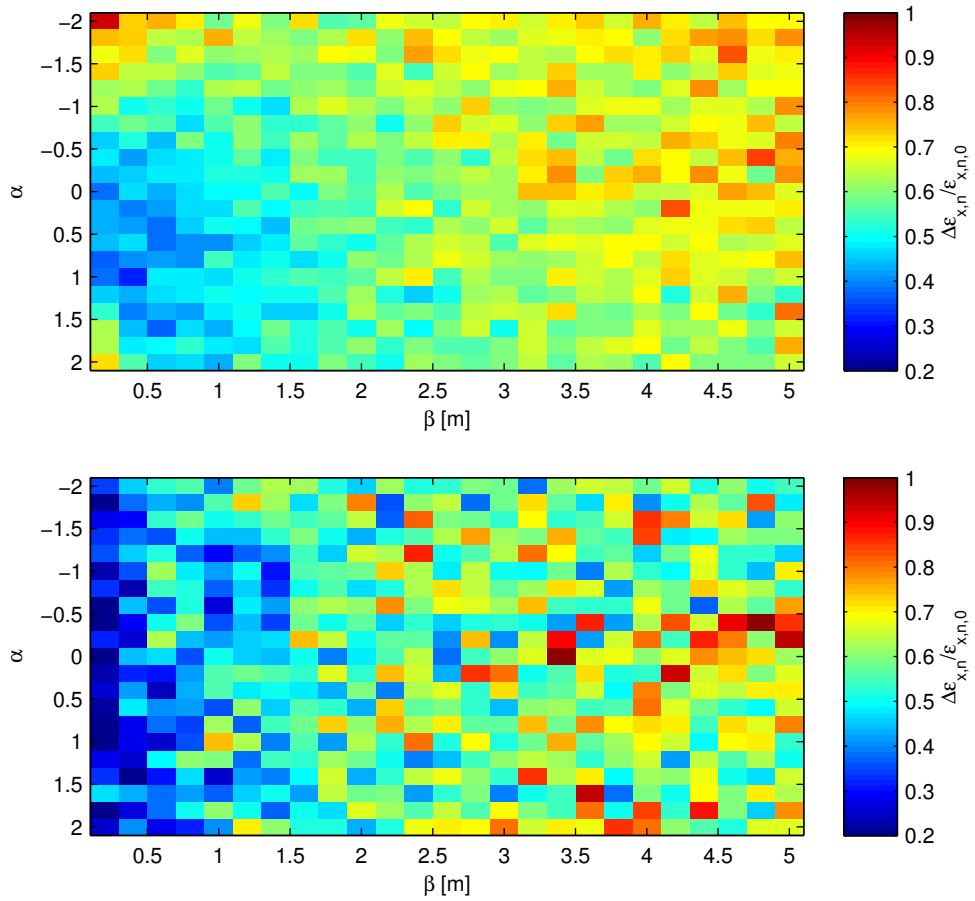


Figure 6.2: Relative growth of the normalized, projected emittance (top) and the normalized emittance of the central slice (bottom) as a function of the Twiss parameters at the chicane entrance obtained with CSRTRACK.

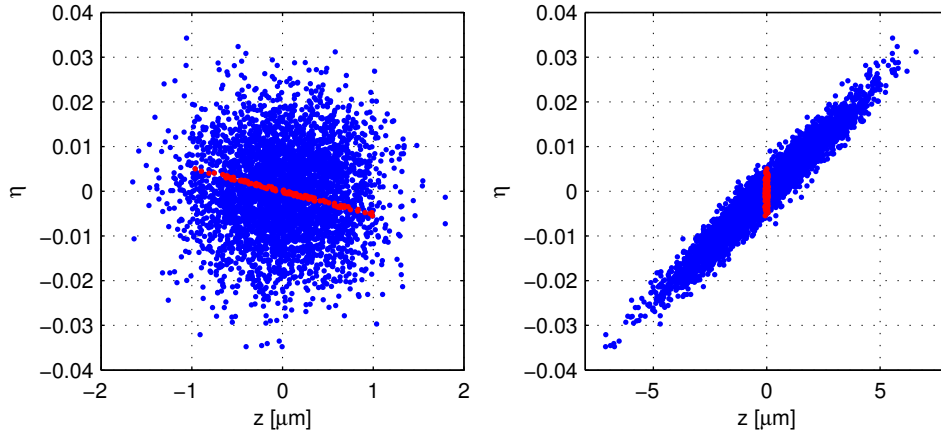


Figure 6.3: Longitudinal phase space at the chicane entrance (left) and exit (right). The red dots indicate particles located in a final central slice. At the entrance these electrons are distributed along the whole bunch and are, therefore, subject to a broad range of energy changes.

emittance growth is narrowed down when compared to the region minimizing the slice emittance growth.

The scaling difference can also be understood in terms of the alignment of the phase space ellipses semi-major axis θ_{maj} with respect to the directions of the CSR kicks θ_{CSR}^i . For the case of the slice emittance a broad range of Twiss parameter combinations (small β and arbitrary α), resulting in the same orientation of the final phase space ellipse, is favored. This orientation matches, or is close to, the direction of the first CSR kick $\theta_{\text{maj}} = \theta_{\text{CSR}}^1 \approx 57^\circ$. Furthermore, this Twiss parameter range maximizes the semi-major axis length at the chicane exit. This combination of matching orientation and long semi-major axis results in a low emittance growth. The ellipse orientation and the semi-major axis length for this case are shown in Fig. 6.4. In contrast, the projected emittance is subject to all CSR kicks $\theta_{\text{CSR}}^{1-3}$. Orienting the major-semi axis along the first CSR kick direction and maximizing its length conflicts with the kick directions of the subsequent magnets. These additional kicks can, in the worst case, lead to a shift perpendicular to the ellipse orientation and significantly increase the emittance. This effect becomes more pronounced if the semi-major axis of the phase space ellipse is much longer than the semi-minor axis $r_{\text{maj}} \gg r_{\text{min}}$. Only a small range of Twiss parameters minimizes the combined effect of the different kicks.

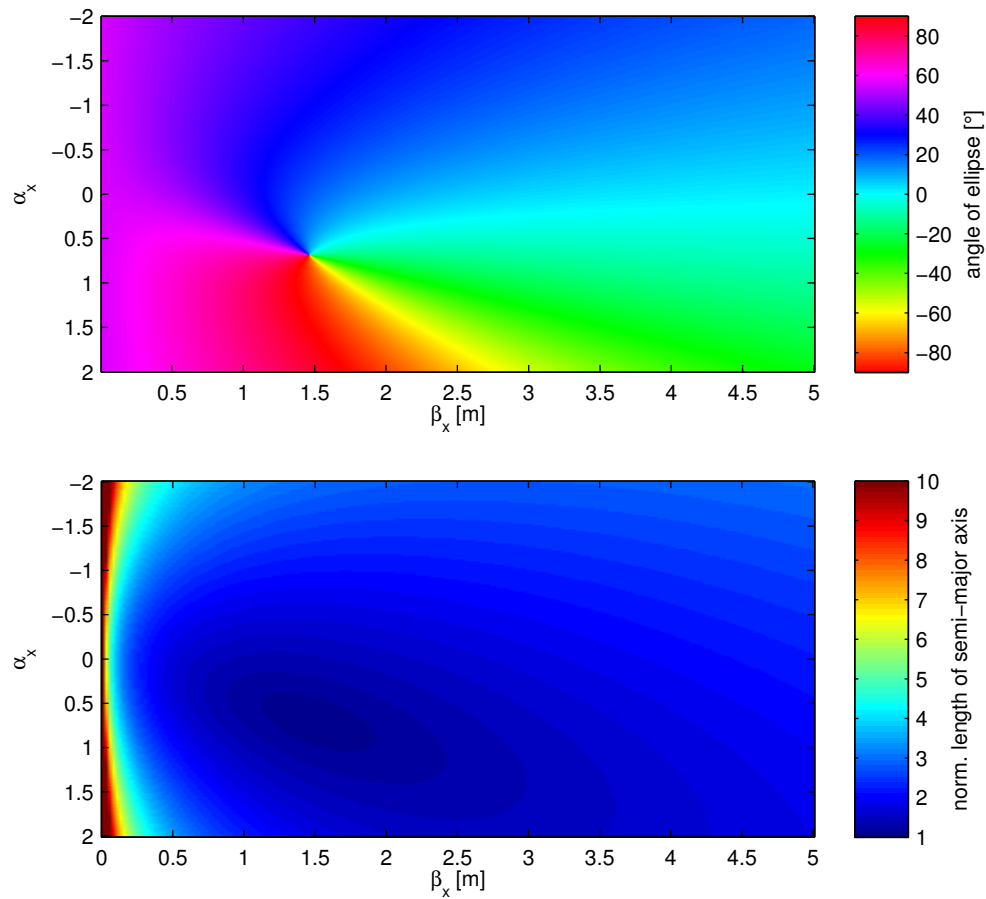


Figure 6.4: Orientation of the phase space ellipse (top) and length of the semi-major axis normalized to its minimum (bottom) as a function of the initial Twiss parameters for a C-chicane with $L_{12} = L_{34} \approx 17$ cm, $L_{23} = 5$ cm, and $L_b = 7.5$ cm and a bunch according to the FEL demonstration parameter set.

6.3 Layout Optimization

Besides the Twiss parameter optimization for a given setup, also the general chicane layout can be varied for a given R_{56} . This allows to modify the linear transport matrix elements R_{16}^i and R_{26}^i contributing to the emittance growth as well as the induced energy spreads σ_{η_i} . For the decompression concept symmetric and asymmetric C- and S-chicane configurations are discussed. For all cases the longitudinal dispersion is fixed to $R_{56} = 193 \mu\text{m}$. For each layout the Twiss parameters have been optimized individually in the ranges $\alpha \in [0, 3]$ and $\beta \in [0.2 \text{ m}, 3 \text{ m}]$ which are feasible for realistic setups and cover the vicinity of the optimum found in the Twiss parameter optimization.

6.3.1 C-Chicane

The simplest layout is the symmetric C-chicane. The parameters that have been varied are the outer two drift lengths $L_{12} = L_{34}$ as well as the length of the bending magnets L_b . In order to ensure a constant final bunch decompression, the magnet strength has been adjusted for each case. The central drift has been fixed to $L_{23} = 5 \text{ cm}$ which is the minimum distance for an already existing magnet set due to the housing and coil size. This drift does not have any effect on the longitudinal dispersion and only elongates the setup; therefore, it should be kept as short as possible in any layout. Across all simulations the total simulated distance has been fixed to 2.65 m by adding a drift after the last magnet to ensure comparable results independent of the chicane length.

Figure 6.5 shows the projected emittance growth as a function of the setup parameters L_{12} and L_b obtained with CSRTRACK using the 3D and the 1D model. For each chicane configuration the Twiss parameters have been scanned and optimized individually*. Both scans not only show a significant difference in the absolute numbers but also in the qualitative features. The 1D model only including CSR effects favors setups consisting of long magnets and drifts. This reflects the typical optimization approach used at linear accelerator based facilities, leading to a reduction of CSR emission and the associated energy spread by only using as weak as possible bending magnets although the transport matrix elements R_{16}^i and R_{26}^i get increased. This is in stark contrast to the optimization concept suggested by the simulations using the 3D model. Here the emittance growth is minimized for moderate drift lengths $L_{12} \approx 20 \text{ cm}$ and short bending magnets. The reason for the different dependencies is the inclusion of space-charge effects in the 3D simulations. The space-charge induced energy spread grows proportional to the traversed path length. Therefore, the setup configuration resulting in a minimum emittance growth is a compromise of minimizing CSR effects by using weak magnets and long drifts and minimizing space-charge effects by reducing the overall setup length. Both scalings can

*This is the reason for the limited plot resolution since each data-point in the figures represent a whole Twiss parameter scan.

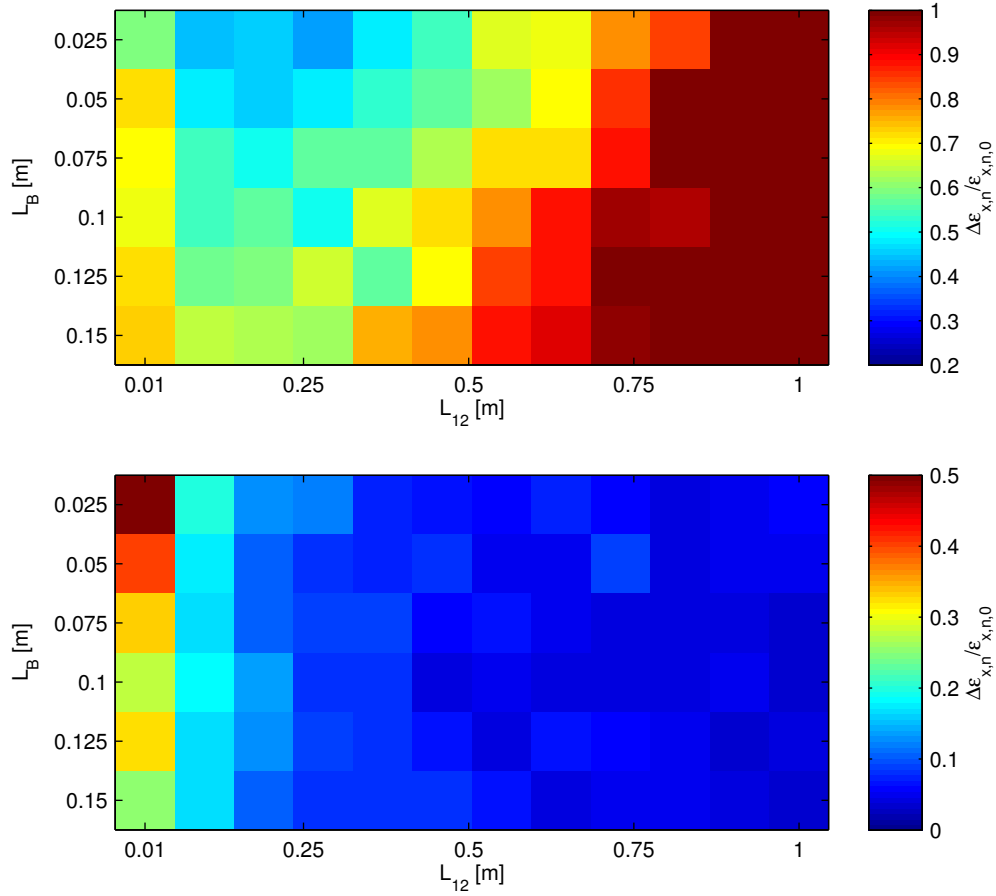


Figure 6.5: Relative growth of the normalized, projected emittance in a symmetric C-chicane as a function of the setup parameters at the chicane entrance obtained with CSRTRACK using the 3D model (top) and the 1D model (bottom). For each configuration the Twiss parameters have been optimized individually, consequently limiting the number of reasonably accessible data-points in terms of the computation time. The qualitative and absolute differences are dominantly caused by the inclusion of space-charge effects in the 3D model. This leads to a higher emittance growth for longer setups in the 3D model despite the reduction of CSR that leads to a lower emittance growth in the 1D model.

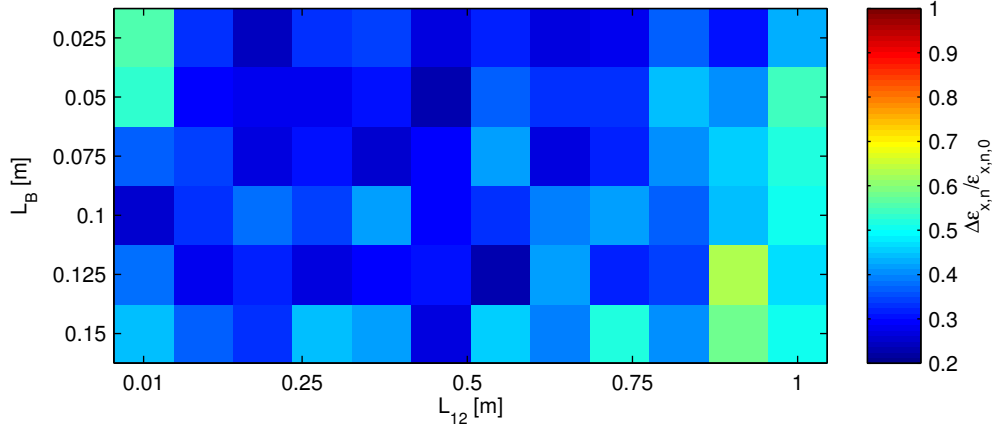


Figure 6.6: Relative growth of the normalized slice emittance in a symmetric C-chicane as a function of the setup parameters at the chicane entrance obtained with CSRTRACK using the 3D model. Despite the increased noise the result confirms the optimization concept suggested by the scaling of the projected emittance shown in Fig. 6.5 (top).

be qualitatively confirmed by using the analytical model (5.67) and either including or neglecting space-charge effects. The optimized configuration in the 3D model results in an emittance growth of $\sim 40\%$. The optimization concept also holds for the slice emittance as is shown in Fig. 6.6.

The emittance growth can be further minimized by using an asymmetric layout via shifting the central two magnets by L_{off} towards the chicane entrance or exit. At bunch compressors located at linear accelerator based facilities usually the final drift L_{34} is increased at the same time leading to a decrease of the field strength and deflection angle of the last two magnets ϕ_2 . This allows to reduce the emission of CSR when the bunch is shortest [106]. Transferring this concept to a CSR dominated bunch decompressor starting with the shortest bunch length would consequently require to elongate the initial drift L_{12} since this reduces the deflection angle ϕ_1 , leading to a reduction of the largest transport matrix element R_{16}^1 as well as the CSR induced energy contributions of the first two magnets $\sigma_{\eta_{1,\text{CSR}}}$ and $\sigma_{\eta_{2,\text{CSR}}}$.

The concept has been tested using a reference setup with $L_b = 7.5$ cm and $L_{12} = L_{34} \approx 17$ cm in the symmetric case. The offset of the central dipole pair with respect to the chicane center L_{off} has been scanned with negative offsets corresponding to a shift of the magnets towards the chicane entrance. The expected CSR dominated behavior is, if at all, confirmed by the 1D model based simulation. As shown in Fig. 6.7 the 3D model indicates a reduction of the emittance growth for negative offsets, i.e. a shortened initial drift and elongated final drift. The optimum is reached for an offset of $L_{\text{off}} \approx -10$ cm reducing the emittance growth to $\sim 30\%$. The reason for this scaling is given by the

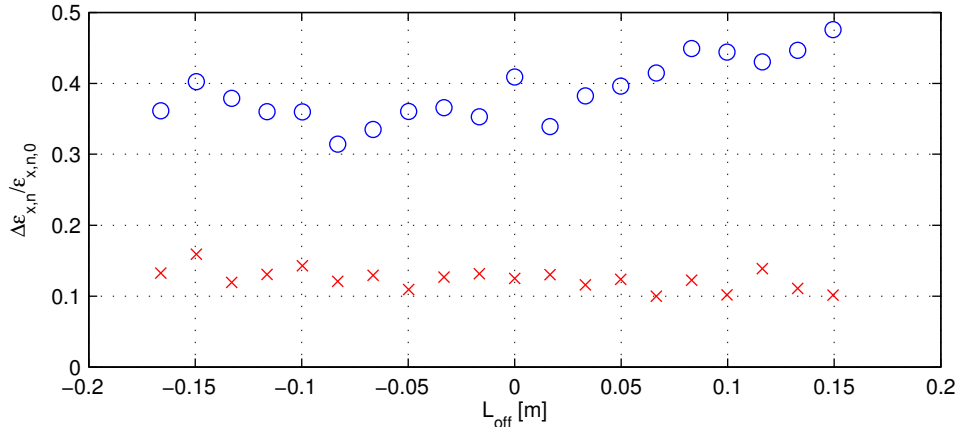


Figure 6.7: Relative growth of the normalized, projected emittance in an asymmetric C-chicane as a function of the longitudinal offset of the central magnets based on the 3D model (blue circles) and the 1D model (red crosses).

space-charge induced energy spread. Due to the bunch length dependence of the space-charge effect, an early bunch decompression is favorable. A reduction of the initial drift beyond $L_{\text{off}} \approx -10$ cm results in a slight increase of the emittance growth compared to the optimum. Here CSR dominates over space-charge again due to the rise of the deflection angle ϕ_1 .

6.3.2 S-Chicane

A promising alternative to the C-chicane is a four-magnet S-chicane. As discussed in Sect. 5.3.3, an advantage of the S-chicane is the possibility of a partial cancellation of offset contributions from the first two magnets due to opposite signs of the transport matrix elements R_{16}^1 and R_{16}^2 . As a first test symmetric configurations have been simulated by varying the outer two drifts $L_{12} = L_{34}$ and the length of the bending magnets L_b . In contrast to the scans of the C-chicane the length of the central drift has to be adapted too and is always set to $L_{23} = L_{12} + L_{34} + 2L_b \tan(\phi/2) / \tan(\phi)$ in order to ensure a vanishing bunch offset at the chicane exit. The total longitudinal dispersion of the chicane has been kept constant by adjusting the magnet strength for each configuration. The total simulation distance has been fixed to 2.33 m.

Figure 6.8 shows the scan result obtained with CSRTRACK. The projected emittance has been evaluated as a function of the setup parameters L_{12} and L_b using the 1D and 3D model. The scan range for the drift length L_{12} has been reduced when compared to the C-chicane to ensure a comparable total setup length when correctly scaling the central drift L_{23} . For each setup layout the Twiss parameters have been optimized in order to

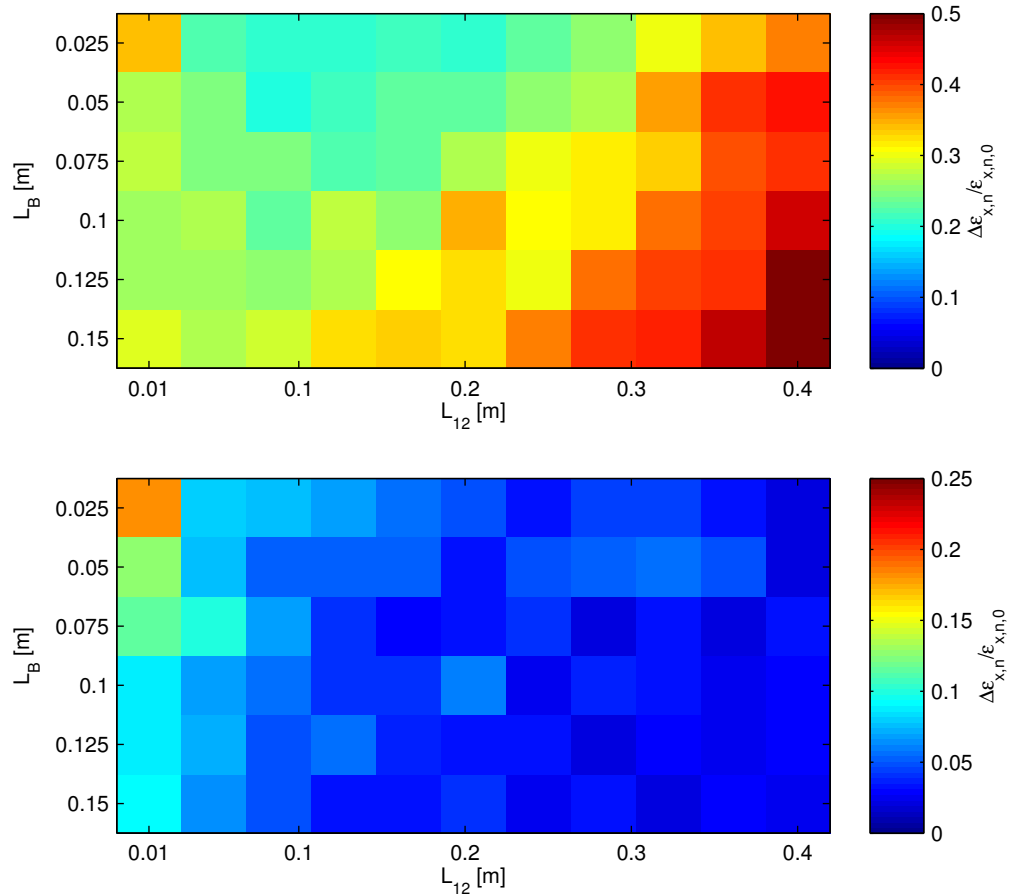


Figure 6.8: Relative growth of the normalized, projected emittance in a symmetric S-chicane as a function of the setup parameters at the chicane entrance obtained with CSRTRACK using the 3D model (top) and the 1D model (bottom). As in the case of the C-chicane, the qualitative and absolute differences are dominantly caused by the inclusion of space-charge effects in the 3D model. Compared to the C-chicane the emittance growth is reduced by 50% on average.

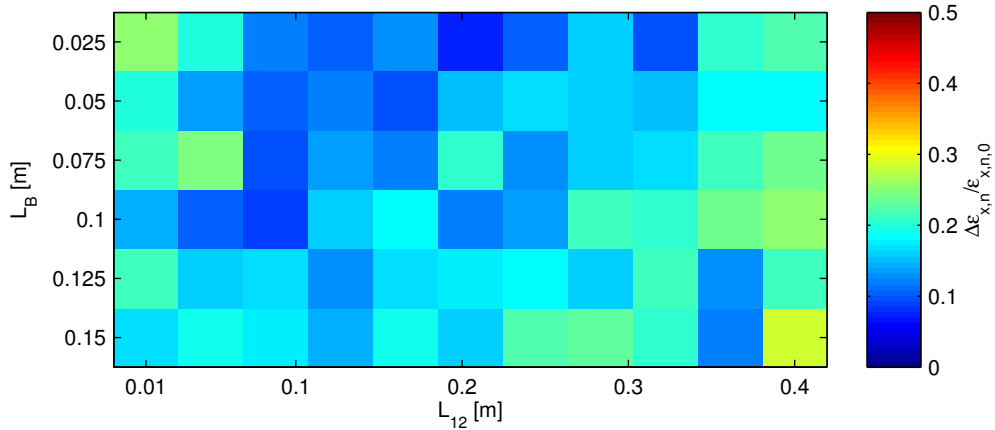


Figure 6.9: Relative growth of the normalized, slice emittance in a symmetric S-chicane as a function of the setup parameters at the chicane entrance obtained with CSRTRACK using the 3D model. The scan confirms the optimization strategy found for the projected emittance growth.

ensure a minimum emittance growth. Both models show a similar result as in the case of the C-chicane scan; however, the emittance growth has been reduced by approximately 50%. This can be understood as an effect of the opposing signs of the transport matrix elements and the resulting CSR kicks. Still, the 1D model suggests to increase drift and magnet lengths in order to reduce the CSR emission. The 3D model, taking space-charge into account, indicates that space-charge and CSR effects have to be balanced, resulting in a minimum emittance growth of $\sim 20\%$ for intermediate drift lengths of $L_{12} \approx 14$ cm and as short as possible magnets. The optimization also holds for the slice emittance as indicated by Fig. 6.9.

As in the case of the C-chicane, the emittance growth can be further reduced by using an asymmetric layout. As discussed in Sect. 5.1.3, the asymmetric layout variations of the S-chicane in this thesis are restricted to shifts of the central two magnets along the initial direction of deflection ϕ . All shifts are characterized by the introduced longitudinal offset L_{off} as in the case of the C-chicane. As reference a symmetric layout with a magnet length of $L_b = 7.5$ cm and drift lengths $L_{12} = L_{34} = 14$ cm has been chosen. The scan result obtained with CSRTRACK is shown in Fig. 6.10. The 1D model does not show any significant offset dependence of the emittance growth. The 3D model, however, shows a similar result as in the case of the C-chicane. Moderate longitudinal shifts of the central magnets towards the chicane entrance are favored. A minimum is found for $L_{\text{off}} \approx -10$ cm, resulting in an emittance growth of $\sim 15\%$. The effect can again be understood as a result of reducing the space-charge induced energy spread by an early decompression and is further supported by the better cancelation of the offset contributions $R_{16}^1 \eta_1$ and $R_{16}^2 \eta_2$.

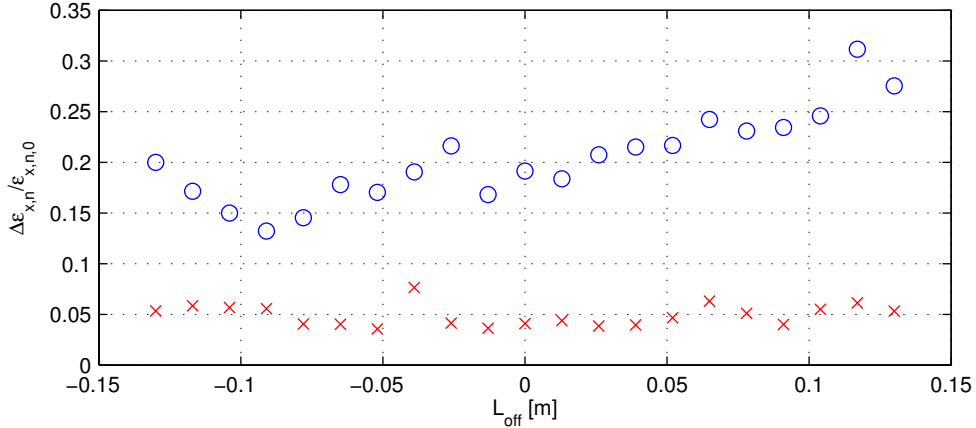


Figure 6.10: Relative growth of the normalized, projected emittance in an asymmetric S-chicane as a function of the longitudinal offset of the central magnets based on the 3D model (blue circles) and the 1D model (red crosses).

6.3.3 Influence of an Energy Chirp

So far, all discussed cases were based on a completely uncorrelated energy spread which can be seen as a worst case scenario. According to laser-wakefield acceleration theory an energy chirp is to be expected contributing to the projected energy spread. The structure of the energy-position correlation will depend on the acceleration parameters, e.g. the amplitude of the accelerating field and whether dephasing is reached or not. As a more realistic scenario bunches with a projected energy spread as above made up by a smaller local energy spread $\sigma_{\eta,\text{loc}}$ and a linear energy chirp $d\eta/dz$ can be assumed.

In general, for a fixed projected energy spread, a linear energy chirp is of advantage in two ways: First, the energy-position correlation reduces the mixing of longitudinal slices and in the case of a pure chirp eliminates the mixing completely. This lowers the slice emittance growth and increases correlations between energy changes η_i caused in different sections of the chicane, allowing for a mutual cancellation of individual CSR kicks as in an S-chicane. Second, for a given chicane configuration and projected energy spread a positive chirp will lead to a faster decompression with the bunch length given by

$$\sigma_z(s) = \sqrt{(1 + R_{56}(s)d\eta/dz)^2 \sigma_z^2 + R_{56}^2(s)\sigma_{\eta,\text{loc}}^2}, \quad (6.7)$$

using the initial local energy spread $\sigma_{\eta,\text{loc}}$ and the initial bunch length σ_z . Furthermore, the final bunch length will be increased. This reduces the energy changes caused by CSR and space-charge, leading to a reduction of the projected and slice emittance growth. If the chicane is modified to ensure the same final bunch length as in the case of a completely

uncorrelated energy spread, i.e. the R_{56} gets reduced, also the emission of CSR will be reduced, again lowering the resulting emittance growth.

All setups discussed above have also been tested for the case of a bunch having the same projected energy spread as before, i.e. $\sigma_\eta = 1\%$, but this time made up by the combination of a local energy spread of $\sigma_{\eta,\text{loc}} = 0.5\%$ [53] and a linear energy chirp of $d\eta/dz = 1.73 \cdot 10^4 \text{ m}^{-1}$. In the setup scan of the symmetric C- and S-chicane all qualitative features are retained, but the average projected emittance growth is reduced by 29% in the case of the C-chicane and by 33% in the case of the S-chicane when compared to the results obtained with a completely uncorrelated energy spread. The higher performance improvement of the S-chicane is based on the increased correlations, allowing for a better mutual compensation of CSR as well as space-charge kicks caused in the first and second magnet. The optimization concept in general does not depend on the initial chirp and a positive linear chirp always reduces the emittance growth.

The influence of the chirp becomes more pronounced in the case of asymmetric chicane configurations (see Fig. 6.11). The asymmetry scan of the C-chicane shows an average reduction of the emittance growth by 35% with a weak offset dependence. The effect becomes stronger in the case of the asymmetric S-chicane, resulting in average reduction of the projected emittance growth by 44% with a strong offset dependence in favor of negative offsets. This is again a result of the increased correlations between energy changes occurring in the first and second magnet and the mutual compensation of offsets (see Sect. 5.3.3). The minimum emittance growth achievable with an asymmetric S-chicane gets reduced to approximately 5%.

6.4 Scalability

An interesting question regarding the decompression concept is its scalability towards combinations of higher initial energy spreads and bunch charges, which are believed to be easier accessible [107]. Keeping the chicane strength in terms of R_{56} unmodified the decompression factor is given by

$$n = \frac{\sigma_{z,f}}{\sigma_{z,i}} \approx \frac{R_{56}\sigma_{\eta_i}}{\sigma_{z,i}}, \quad (6.8)$$

using the initial and final bunch length $\sigma_{z,i}$ and $\sigma_{z,f}$, and the initial relative energy spread σ_{η_i} . This results in a final local energy spread of

$$\sigma_{\eta_{\text{sl},f}} = \frac{\sigma_{\eta_i}}{n} \approx \frac{\sigma_{z,i}}{R_{56}}, \quad (6.9)$$

and a final peak current of

$$I_{\text{peak},f} = \frac{I_{\text{peak},i}}{n} \approx \frac{I_{\text{peak},i}\sigma_{z,i}}{R_{56}\sigma_{\eta_i}}. \quad (6.10)$$

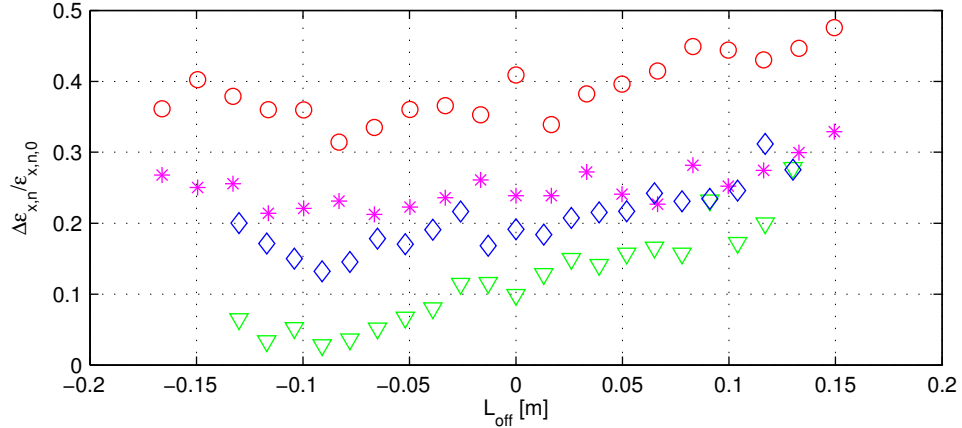


Figure 6.11: Relative growth of the normalized, projected emittance in an asymmetric S-chicane and C-chicane as a function of the longitudinal offset of the central magnet pair obtained with the 3D model. The marker represent: red circles: C-chicane, no chirp; magenta stars: C-chicane, chirp; blue diamonds: S-chicane, no chirp; green triangles: S-chicane, chirp.

Both, the final local energy spread $\sigma_{\eta_{sl},f}$ and the final peak current $I_{\text{peak},f}$ are independent of the initial energy spread and current, as long as the ratio of initial peak current and energy spread $I_{\text{peak},i}/\sigma_{\eta_i}$ is constant. Under this condition the only difference affecting the FEL performance is the final bunch length $\sigma_{z,f}$, which will be increased for higher initial energy spreads and improve the performance in slippage limited cases. This scaling of the decompression concept is, however, limited by the rising emittance growth caused by the increased CSR and space-charge effects when operating with higher initial peak currents.

A scan of the initial bunch charge for a fixed ratio of peak current to energy spread has been performed with the reference C-chicane layout in combination with a Twiss parameter optimization for each case. The result is shown in Fig. 6.12. A linear rise of the emittance growth as a function of the bunch charge is found for the projected as well as the slice emittance. This is caused by the linear dependence of the energy change caused by CSR and space-charge on the bunch charge. However, also the change of the decompression rate due to the different energy spreads has an effect on the system performance. For higher energy spreads the difference between the bunch length in the first and the later magnets increases. Therefore, the impact of the effects occurring in the first magnet and drift relative to the rest of the chicane rises, leading to a change of the ideal Twiss parameters favoring smaller initial values of α and β . This has to be considered in the optics design.

Any change of the horizontal slice emittance affects the FEL performance via the change

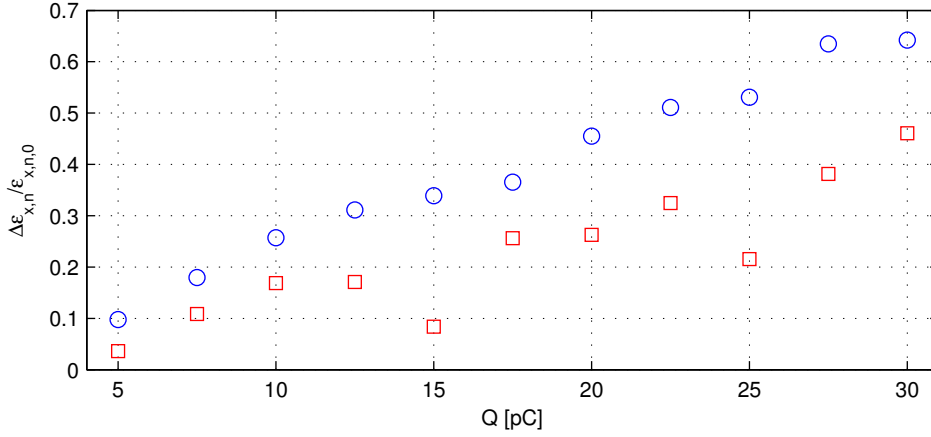


Figure 6.12: Relative growth of the normalized, projected (blue circles) and slice (red squares) emittance as a function of the bunch charge for a fixed ratio of charge to energy spread at the chicane entrance corresponding to $Q = 15$ pC and $\sigma_\eta = 1\%$. Projected and slice emittance both grow approximately linearly as suggested by Eq. (5.67).

of the horizontal beam size*. The power gain length depends on the beam size as

$$L_g \propto (\sigma_x \sigma_y)^{1/3}. \quad (6.11)$$

Expressing the horizontal beam size as a function of the emittance yields

$$\sigma_x = \sqrt{\epsilon_x \beta_x}, \quad (6.12)$$

and shows that any change of the horizontal emittance by a factor m affects the gain length according to

$$L_g \propto m^{1/6}. \quad (6.13)$$

The final FEL power reduction as a function of the longitudinal position s and the scaling factor of the emittance m is then given by

$$\frac{P(s, m)}{P_{\text{ref.}}(s)} = \exp\left(-\frac{s}{L_{g,3D}} \left(1 - m^{-1/6}\right)\right). \quad (6.14)$$

Doubling the horizontal slice emittance $m = 2$ in the demonstration case relying on decompression with a total undulator length of $s = 2$ m and a gain length of $L_{g,3D} \approx 17$ cm results in a power reduction of approximately 72%. This scaling has been confirmed with GENESIS as shown in Fig. 6.13. Furthermore, any change of the emittance in the chicane is accompanied by a change of the Twiss parameters, resulting in a mismatch at the undulator entrance that reduces the FEL performance if it is not compensated by adapting the optics. This is discussed in the context of the start-to-end simulation in Chap. 8.

*In general, also the effective energy spread due to emittance has to be taken into account (see Sect. 2.4.4); however, for the here discussed parameters this effect is negligible.

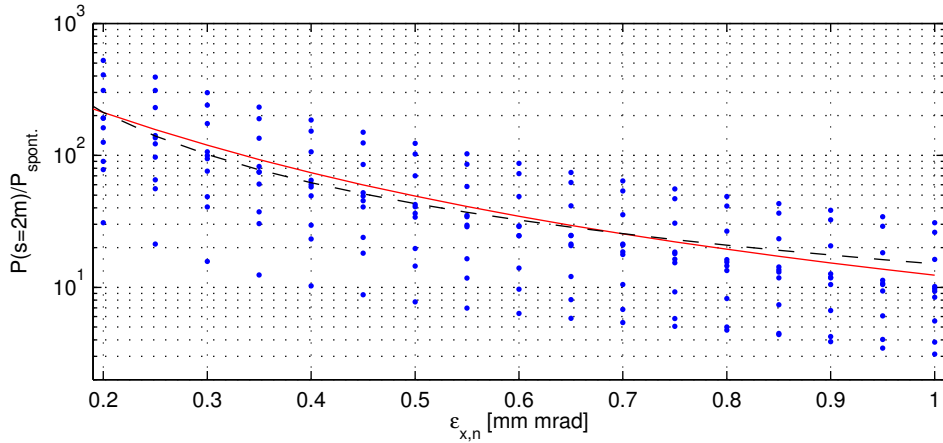


Figure 6.13: Normalized power as a function of the normalized emittance obtained with GENESIS. For each emittance 10 independent runs have been performed (blue dots), their average is indicated by the solid red line. The analytical model (6.14) is shown as the dash-dotted black line and holds very well although it neglects any 3D effects.

6.5 Conclusion

The emittance growth in the chicane can be minimized in different ways. For a given chicane layout it depends on the Twiss parameters of the beam. They describe the size and orientation of the phase space ellipse. Orienting the phase space ellipse at the chicane exit so that it coincides with the dominant CSR-kick direction minimizes the emittance growth. This works best for the case of the slice emittance growth which is dominated by the first magnet and the corresponding CSR-kick. The projected emittance growth, however, is affected by all magnets and therefore the optimum Twiss parameter region is narrowed down. In general a converging beam is favored for the slice as well as the projected emittance.

In addition to the Twiss parameters also the chicane layout in terms of magnet and drift lengths and the resulting required magnetic fields can be optimized. At large scale facilities the optimization concept can usually be reduced to the idea of decreasing CSR effects by using as weak as possible bending magnets and long drifts. This does not hold for the here discussed scenario due to the non-negligible impact of space-charge induced energy modulations. Hence, an optimized setup is a compromise between using weak bending magnets in order to minimize CSR effects and using a short setup to minimize the impact of space-charge. The chicane lengths on the order of one meter resulting from this compromise fortunately are in the spirit of a lab-scale system and can be used in upcoming setups. Comparing C- and S-chicanes shows that for comparable chicane lengths the emittance growth in an S-chicane is reduced by 50% when compared to a C-chicane.

Both types of chicanes can be modified to asymmetric configurations. At linear accelerator based facilities using bunch compression, the idea is to reduce the strength of the final bending magnets and elongate the last drift to reduce CSR emission where the bunch is shortest. For a decompressor the inverse concept could be expected due to the short initial bunch length; however, 3D simulations show that stronger magnets and short drifts in the first chicane half are favored. This is again the result of space-charge effects that can be reduced by decompressing the bunch as soon as possible. The best setup, resulting in the lowest emittance growth, is an asymmetric S-chicane causing a relative, projected emittance growth of less than 20%.

If an initial chirp is assumed in combination with the same projected energy spread, the emittance growth gets reduced for all cases. This is based on the faster decompression of the bunch in the case of a chirp, resulting in lower CSR and space-charge effects and the reduced position changes within the bunch, allowing for a better cancellation of individual CSR-kicks. This can especially be exploited in asymmetric S-chicanes, making a relative projected emittance growth as low as approximately 5% possible.

Extending the decompression concept to cases with higher bunch charges and broader energy spreads for a fixed ratio of charge to energy spread is ultimately limited by the emittance growth. Doubling the charge and energy spread in a simple symmetric C-chicane nearly doubles the resulting emittance growth. The full effect can only be assessed in a start-to-end simulation also taking the chromatic effects of the optics into account and is discussed in Chap. 8.

7 Electron Optics

This chapter addresses the last missing piece of the demonstration FEL puzzle – the transverse electron optics.

The beam optics are a crucial part of every accelerator needed to control the transverse and longitudinal beam dynamics. In the frame of this thesis they have, so far, only been used in terms of the chicane manipulating the longitudinal phase space. How the desired transverse dynamics assumed in the previous discussion can be achieved will be discussed here.

First, the basics of electron optics theory are reviewed followed by an overview over the most important error sources. Then the concept of chromatic focus matching is introduced as a countermeasure for chromatic effects. Finally, an optics concept for the demonstration FEL case is presented and discussed.

7.1 Electron Optics Theory

In this section the basics of beam optics, including the typical magnets, the transport matrix formalism, and the Twiss parameters, are reviewed. They are the basis for the later considerations and are based on the book by Wille [21] and the course by Rossbach [108].

7.1.1 Coordinate System

For the description of the particle motion in an arbitrary beam transport system one could use the laboratory system. However, if one considers circular or other curved transport sections and is interested in describing the beam shape and small deviations from a reference path the laboratory system is not suited. It is therefore customary in beam optics to use a coordinate system co-moving with a reference particle. In this thesis the following naming convention is used: The z -component of the coordinate system points in the instantaneous direction of flight of the reference particle, x is the horizontal, and y the vertical offset with respect to the reference particle. The reference particle is characterized by $\{0, 0, 0\}$ for all times, and its path is called the orbit. All

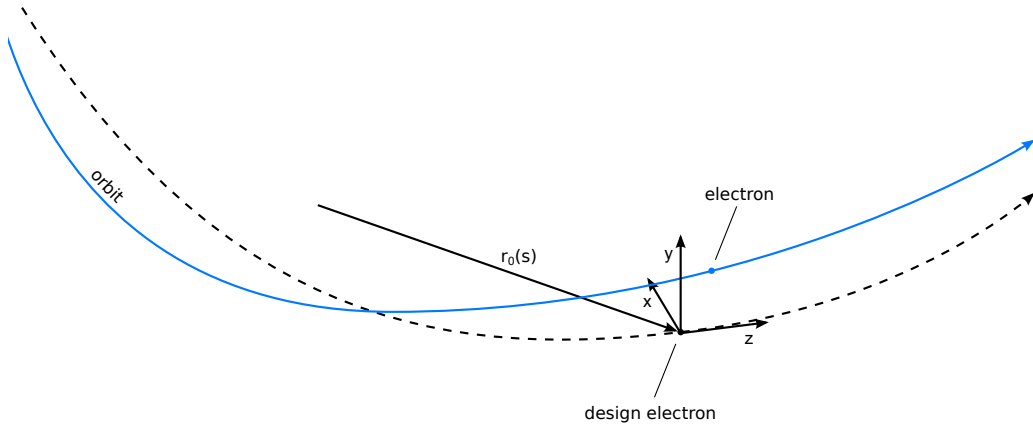


Figure 7.1: Coordinate system relative to the reference path as it is customary in beam optics.

other particles can be described by the triple $\{x(\tilde{s}), y(\tilde{s}), z(\tilde{s})\}$ with \tilde{s} measuring the path length along the orbit. A sketch of the coordinate system is shown in Fig. 7.1.

7.1.2 Magnets

In general arbitrary magnetic fields can be used to manipulate the beam shape and direction; however, any magnetic field can be expanded in a Taylor series in the vicinity of the orbit. The lowest orders of this expansion are the dipole, the quadrupole, and the sextupole. These magnets have distinct effects on the beam and can be built as “separated-function” magnets providing, a field corresponding to one of the aforementioned orders of the expansion, or as “combined-function” magnets combining multiple orders. The later type is dominantly found at older facilities whereas modern systems usually rely on “separated-function” magnets [108]. A sketch of the three basic magnets is shown in Fig. 7.2. Although combined function magnets exist, they will not be considered in the further discussion.

The probably most well known magnet is the dipole. It is used to steer the beam and is consequently an essential component for circular structures like synchrotrons but is also the key component of undulators and chicanes. An idealized dipole has a constant magnetic field B_y^* and is typically characterized by either the inverse radius of curvature $1/R$ of an electron moving in its field

$$\frac{1}{R} = \frac{eB}{p} \approx 0.2998 \frac{B[\text{T}]}{W[\text{GeV}]}, \quad (7.1)$$

*All dipoles will be assumed to have a purely vertical field in this thesis as it is customary in beam optics. This is sufficient for most real life setups, but the derived equations can also be extended to more complex configurations.

using the electrons momentum p and its energy W , or the corresponding deflection angle Φ for a given dipole length L_B

$$\Phi = \frac{L_B}{R} \approx 0.2998 \frac{B[\text{T}]L_B[\text{m}]}{W[\text{GeV}]}.$$
 (7.2)

Both ways of describing a dipole explicitly characterize its influence on an electron trajectory and therefore provide a direct insight in the resulting setup geometry.

The next higher order of the magnetic field series is the quadrupole. In general quadrupoles are used to focus a beam, i.e. to control the transverse beam shape*. The field of an ideal quadrupole is given by [21]

$$B_x = gy,$$
 (7.3)

$$B_y = gx,$$
 (7.4)

using the field gradient g . One important characteristic of a quadrupole is that its effect on both transverse planes is decoupled. A significant difference when compared to focusing lenses in light optics is that a quadrupole always focuses one plane but defocuses the other. Consequently, multiple quadrupoles rotated with respect to each other around the beam axis by 90° are needed to focus a beam[†]. In analogy to the inverse radius of curvature characterizing the dipole strength, the quadrupole strength can be characterized by

$$k = \frac{eg}{p} \approx 0.2998 \frac{g[\text{T/m}]}{W[\text{GeV}]},$$
 (7.5)

again characterizing the effective strength of the magnet for a given electron energy. By convention the sign of k is chosen to be negative if the quadrupole is focusing in the horizontal plane, and positive if the quadrupole is defocusing. Using the strength of the quadrupole k and its length l , its focal length is given by

$$f = \frac{1}{kl}.$$
 (7.6)

The next higher order of magnet type is the sextupole. It can be used for the correction of chromatic effects in dispersive sections [21, 109]. The field of a sextupole is nonlinear

$$B_x = g'xy,$$
 (7.7)

$$B_y = \frac{1}{2}g'(x^2 - y^2),$$
 (7.8)

and results in a coupling of both planes in contrast to the previous two types of magnets. The strength of the sextupole can be characterized in analogy to the previous two cases

$$m = \frac{eg'}{p} \approx 0.2998 \frac{g'[\text{T/m}^2]}{W[\text{GeV}]}.$$
 (7.9)

*More specialized use cases, like dispersion control, exist (see e.g. [109]).

[†]“Don’t rotate quadrupoles unless you know what you are doing!” [108]

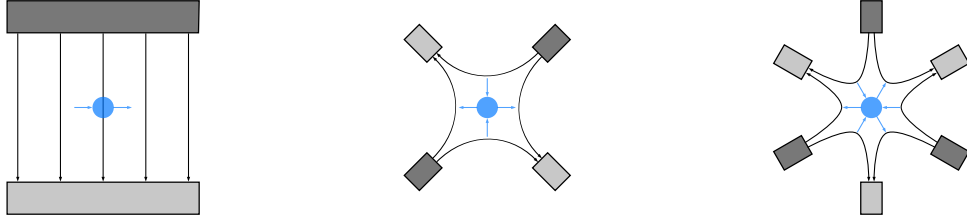


Figure 7.2: Sketches of the most common types of magnets used in beam optics: dipole, quadrupole, and sextupole (left to right). Black arrows indicate the field lines, blue arrows the force acting on an electron bunch moving into the projection plane.

In this thesis all discussions will be restricted to linear beam optics where horizontal and vertical motion are decoupled; therefore higher order magnets like sextupoles are excluded*.

7.1.3 Equations of Motion

When considering the description of the particle motion in beam optics, the most important information regard the transverse particle positions with respect to the orbit.

Assuming deviations from the design orbit to be much smaller than the radius of curvature, i.e., $x \ll R$ and $y \ll R$, purely transverse magnetic fields $\mathbf{B} = (B_x, B_y, 0)$, and allowing only small deviations from the reference momentum, i.e., $\Delta p/p \ll 1$ leads to two second-order differential equations describing the particle motion with respect to the orbit [21, 108]

$$x''(\tilde{s}) - \left(k(\tilde{s}) - \frac{1}{R^2(\tilde{s})} \right) x(\tilde{s}) = \frac{1}{R(\tilde{s})} \frac{\Delta p}{p}, \quad (7.10)$$

$$y''(\tilde{s}) + k(\tilde{s})y(\tilde{s}) = 0. \quad (7.11)$$

Neglecting energy deviations both differential equations are of the same type and can be written as

$$x''(\tilde{s}) - \tilde{k}(\tilde{s})x(\tilde{s}) = 0, \quad (7.12)$$

*The use for chromatic correction purposes in the chicane has been evaluated and discarded since the introduced perturbations of the beam exceeded the effect of the chromatic correction.

with $\tilde{k}(\tilde{s}) = k(\tilde{s}) - 1/R^2(\tilde{s})$. Assuming \tilde{k} to be constant along the section under consideration, i.e. within an idealized magnet or drift, yields the solution

$$x(\tilde{s}) = x_0 \cosh\left(\sqrt{\tilde{k}}\tilde{s}\right) + \frac{x'_0}{\sqrt{\tilde{k}}} \sinh\left(\sqrt{\tilde{k}}\tilde{s}\right), \quad (7.13)$$

$$x'(\tilde{s}) = x_0 \sqrt{\tilde{k}} \sinh\left(\sqrt{\tilde{k}}\tilde{s}\right) + x'_0 \cosh\left(\sqrt{\tilde{k}}\tilde{s}\right), \quad (7.14)$$

with the initial position x_0 and the initial angle x'_0 . This solution allows to express the effect of each section of a beam line with a constant \tilde{k} and length \tilde{s} , i.e. each element or drift, by a matrix.

The matrix formalism can be extended to include both transverse components as well as the longitudinal offset and the energy deviation. A particle is then characterized by (x, x', y, y', z, η) . All transport matrices then have the form

$$\mathbf{R} = \begin{pmatrix} R_{11} & R_{12} & 0 & 0 & 0 & R_{16} \\ R_{21} & R_{22} & 0 & 0 & 0 & R_{26} \\ 0 & 0 & R_{33} & R_{34} & 0 & 0 \\ 0 & 0 & R_{43} & R_{44} & 0 & 0 \\ R_{51} & R_{52} & 0 & 0 & 1 & R_{56} \\ 0 & 0 & 0 & 0 & 0 & 1 \end{pmatrix}. \quad (7.15)$$

The matrix elements for a drift, dipole, and quadrupole are given in Table 7.1. This formalism can be extended to include higher order effects. The transformation of a particle in the extended formalism reads

$$r_i = R_{ij}r_{0,j} + T_{ijk}r_{0,j}r_{0,k} + \dots \quad (7.16)$$

This formalism is implemented in most beam optics codes and can also be used for analytical discussions. A disadvantage of the formalism is that all particles have to be treated individually and it gives no insight into the evolution of the beam envelope.

The envelope evolution can be determined by solving the differential equation (7.12) only considering drifts and quadrupoles [21]

$$x''(\tilde{s}) - k(\tilde{s})x(\tilde{s}) = 0. \quad (7.17)$$

This differential equation of Hill's type is solved by

$$x(\tilde{s}) = \sqrt{\epsilon} \sqrt{\beta(\tilde{s})} \cos(\Psi(\tilde{s}) + \Phi), \quad (7.18)$$

$$x'(\tilde{s}) = -\frac{\sqrt{\epsilon}}{\sqrt{\beta(\tilde{s})}} (\alpha(\tilde{s}) \cos(\Psi(\tilde{s}) + \Phi) + \sin(\Psi(\tilde{s}) + \Phi)), \quad (7.19)$$

using the Twiss parameters [66], i.e. the setup dependent β -function $\beta(\tilde{s})$ and the α -function $\alpha(\tilde{s}) = -\beta'(\tilde{s})/2$, the beam emittance ϵ , the electron phase $\Psi(\tilde{s})$ and the initial

	drift	dipole	quadrupole (focusing)
R_{11}	1	$\cos\left(\frac{\tilde{s}}{R}\right)$	$\cos\left(\sqrt{ k }\tilde{s}\right)$
R_{12}	\tilde{s}	$R \cos\left(\frac{\tilde{s}}{R}\right)$	$\frac{1}{\sqrt{ k }} \cos\left(\sqrt{ k }\tilde{s}\right)$
R_{16}	0	$R\left(1 - \cos\left(\frac{\tilde{s}}{R}\right)\right)$	0
R_{21}	0	$-\frac{1}{R} \sin\left(\frac{\tilde{s}}{R}\right)$	$-\sqrt{ k } \sin\left(\sqrt{ k }\tilde{s}\right)$
R_{22}	1	$\cos\left(\frac{\tilde{s}}{R}\right)$	$\cos\left(\sqrt{ k }\tilde{s}\right)$
R_{26}	0	$\sin\left(\frac{\tilde{s}}{R}\right)$	0
R_{33}	1	1	$\cosh(\sqrt{ k }\tilde{s})$
R_{34}	\tilde{s}	\tilde{s}	$\frac{1}{\sqrt{k}} \sinh\left(\sqrt{ k }\tilde{s}\right)$
R_{43}	0	0	$\sqrt{k} \sinh\left(\sqrt{ k }\tilde{s}\right)$
R_{44}	1	1	$\cosh\left(\sqrt{ k }\tilde{s}\right)$
R_{51}	0	$-\sin\left(\frac{\tilde{s}}{R}\right)$	0
R_{52}	0	$R\left(\cos\left(\frac{\tilde{s}}{R}\right) - 1\right)$	0
R_{56}	$\frac{\tilde{s}}{\gamma^2}$	$\frac{\tilde{s}}{\gamma^2} - \tilde{s} + R \sin\left(\frac{\tilde{s}}{R}\right)$	$\frac{\tilde{s}}{\gamma^2}$

Table 7.1: Elements of the linear transport matrix \mathbf{R} for drift, dipole, and focusing quadrupole [110].

phase offset Φ . Combining both functions and introducing the third Twiss parameter $\gamma(\tilde{s}) = (1 + \alpha^2(\tilde{s}))/\beta(\tilde{s})$ yields

$$\gamma(\tilde{s})x^2(\tilde{s}) + 2\alpha(\tilde{s})x(\tilde{s})x'(\tilde{s}) + \beta(\tilde{s})x'^2(\tilde{s}) = \epsilon. \quad (7.20)$$

This equation describes an arbitrarily oriented ellipse in the x - x' plane with area $A = \pi\epsilon$ (see Fig. 7.3). Consequently, the emittance is a measure for the phase space volume occupied by the electrons and is a conserved quantity as long as acceleration and degrading effects are neglected. The resulting beam size and divergence are given by

$$\sigma_x(\tilde{s}) = \sqrt{\beta(\tilde{s})\epsilon}, \quad (7.21)$$

$$\sigma_{x'}(\tilde{s}) = \sqrt{\gamma(\tilde{s})\epsilon}. \quad (7.22)$$

For a given emittance it is hence sufficient to characterize the evolution of the Twiss parameters along the setup to completely describe the beam.

The transport matrix formalism used above for the propagation of individual particles can be adapted to the propagation of the Twiss parameters [21]. The transport matrix linking initial and final Twiss parameters of the horizontal component for an arbitrary

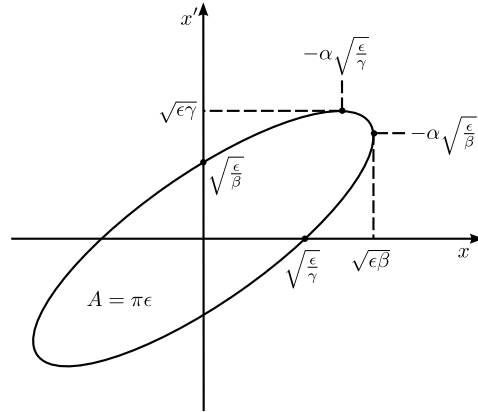


Figure 7.3: Phase space ellipse and Twiss parameters characterizing the shape and orientation according to Eq. (7.20). The area of the ellipse is proportional to the emittance.

beam transport system is given by

$$\begin{pmatrix} \beta_f \\ \alpha_f \\ \gamma_f \end{pmatrix} = \begin{pmatrix} R_{11}^2 & -2R_{11}R_{12} & R_{12}^2 \\ -R_{11}R_{21} & R_{12}R_{21} + R_{11}R_{22} & -R_{12}R_{22} \\ R_{21}^2 & -2R_{21}R_{22} & R_{22}^2 \end{pmatrix} \begin{pmatrix} \beta_i \\ \alpha_i \\ \gamma_i \end{pmatrix}, \quad (7.23)$$

using the transport matrix elements R_{ij} of the particle transport matrix. Using this formalism the evolution of the beam envelope along an arbitrary system can be determined.

7.2 Error Sources

The formalism above, intended for the description of the ideal particle propagation, can be used to characterize the basic error sources of a beam transport system. The following considerations are based on the demonstration FEL concept but can be applied to any other system.

The estimated errors already indicate the order of magnitude that can be expected; however, the exact dependence of the induced beam degradation on the errors of the beam transport system depends on the specific layout of the focusing system and the resulting interplay of the different quadrupoles and is discussed in Sect. 7.4.

7.2.1 Transverse Quadrupole Offsets

Any transverse offset of a quadrupole will result in an effective dipole field, causing a deflection of the electron beam. It is given by

$$B_{x,\text{eff}} = g\Delta y, \quad (7.24)$$

$$B_{y,\text{eff}} = g\Delta x, \quad (7.25)$$

using the gradient of the quadrupole g and the transverse offsets Δx and Δy . The resulting deflection can be approximated by

$$\phi_{x/y} \approx \frac{leB_{x/y,\text{eff}}}{p}, \quad (7.26)$$

with l being the quadrupole length, and p the particle momentum. Assuming typical parameters for miniature permanent magnet quadrupoles [111] like $g = 500$ T/m, $l = 1.5$ cm, a normalized beam energy of $\gamma = 600$, and a positioning accuracy of $\Delta x = \Delta y = 1$ μm achievable with commercially available linear stages (e.g. [112]) results in a deflection angle $\phi_{x/y} \approx 7.3$ μrad . Combined with a typical propagation distance from the optics to the undulator entrance on the order of 1 m this results in an offset on the order of 10 μm which is within the tolerance limits of the FEL (see Table 4.1).

The effect of a transverse offset of the full focusing system (or the source) can be estimated as follows: In general the transport matrix describing the beam transport from the accelerator to the undulator entrance in terms of the transverse coordinates is given by

$$\begin{pmatrix} x_f \\ x'_f \end{pmatrix} = \begin{pmatrix} R_{11} & R_{12} \\ R_{21} & R_{22} \end{pmatrix} \begin{pmatrix} x_i \\ x'_i \end{pmatrix}, \quad (7.27)$$

using the transverse position and angle at the accelerator exit x_i and x'_i . Requiring the optics to be imaging, i.e. $R_{12} = 0$, which approximately holds for the beam transport from the accelerator to the undulator, the matrix can be expressed as [108]

$$\begin{pmatrix} x_f \\ x'_f \end{pmatrix} = \begin{pmatrix} m & 0 \\ r & \frac{1}{m} \end{pmatrix} \begin{pmatrix} x_i \\ x'_i \end{pmatrix}, \quad (7.28)$$

with m being the magnification and r the overall refractive power of the optics system. For the here discussed laser-plasma accelerator based experiment, the source size is on the order of a micrometer; however, the beam size at the undulator entrance has to be an order of magnitude larger in order to ensure a minimum beam diameter along the undulator (see Sect. 3.2.3). This requires a magnification of $m \approx 10$. This large magnification will also amplify any offset of the source or the whole focusing system by the same factor. With the offset tolerance being on the order of 100 μm this results in acceptable source or focusing system offsets of $\Delta x \approx \Delta y < 10$ μm . In terms of the optics

positioning this is feasible; however, regarding the source stability this can be seen as a challenge.

This issue is of importance for all laser-plasma based systems. Due to the injection and acceleration mechanism, typical laser-plasma based electron beams are characterized by a small source size and a high divergence [113, 114]. This leads to the requirement of focusing systems with high magnification and refractive power when trying to ensure a small average beam size over several meters like in an undulator. A possibility to reduce the divergence and increase the beam size is the use of a density downramp at the accelerator exit. In general the matched beam size during acceleration is given by $\sigma_{x,m} = \sqrt{\epsilon_x/k_\beta}$, with the betatron wave number in the blow-out regime $k_\beta = k_p/\sqrt{2\gamma}$ [115], using the plasma wavenumber k_p . Due to the scaling of the plasma wave number with the electron density $k_p \propto \sqrt{n_e}$ the beam size is proportional to $\sigma_{x,m} \propto n_e^{-1/4}$. A properly designed density downramp, i.e. a downramp with a roll-off scale comparable to or greater than the betatron wavelength λ_β , allows to increase the beam size while keeping the emittance constant, leading to a reduction of the divergence at the same time [114]. The feasibility of this concept still has to be tested.

7.2.2 Focusing Strength Errors

Focusing strength errors of a quadrupole can have different reasons: A deviation of the field gradient or quadrupole length from the design parameters due to manufacturing and measurement limitations, and deviations of the electron energy from the design energy.

The matrix of a quadrupole in the thin lens approximation including the dependence on focusing strength errors can be written as [108]

$$\mathbf{M}_q = \begin{pmatrix} 1 & 0 \\ -kl(1-\delta) & 1 \end{pmatrix}, \quad (7.29)$$

using the quadrupole strength k , its length l , and the focusing strength deviation $\delta = \Delta\gamma/\gamma = -\Delta l/l = -\Delta k/k$.

The transport matrix linking initial and final Twiss parameters for a quadrupole in the thin lens approximation including focusing strength errors is given by

$$\begin{pmatrix} \beta_f(\delta) \\ \alpha_f(\delta) \\ \gamma_f(\delta) \end{pmatrix} = \begin{pmatrix} 1 & 0 & 0 \\ kl(1-\delta) & 1 & 0 \\ (kl)^2(1-\delta)^2 & 2kl(1-\delta) & 1 \end{pmatrix} \begin{pmatrix} \beta_i \\ \alpha_i \\ \gamma_i \end{pmatrix}. \quad (7.30)$$

The final Twiss parameter as a function of the initial Twiss parameters and the focusing

strength error are

$$\beta_f(\delta) = \beta_f(0) = \beta_i, \quad (7.31)$$

$$\alpha_f(\delta) = \alpha_f(0) - kl\delta\beta_i = kl\beta_i + \alpha_i - kl\delta\beta_i, \quad (7.32)$$

$$\gamma_f(\delta) = \gamma_f(0) - 2k^2l^2\delta\beta_i + k^2l^2\delta^2\beta_i - 2kl\delta\alpha_i. \quad (7.33)$$

This allows to calculate the mismatch parameter [86] after the pass through the quadrupole

$$\begin{aligned} \zeta &= \frac{1}{2} (\beta_f(\delta)\gamma_f(0) - 2\alpha_f(\delta)\alpha_f(0) + \gamma_f(\delta)\beta_f(0)) \\ &= 1 + \frac{1}{2}k^2l^2\delta^2\beta_i^2. \end{aligned} \quad (7.34)$$

In order to stay below a given mismatch, the error δ has to fulfill the requirement

$$\delta < \frac{\sqrt{2(\zeta - 1)}}{|k|l\beta_i}. \quad (7.35)$$

Assuming parameters typical for a laser plasma based setup $\beta_i = 20$ m, $l = 1.5$ cm, and $k = 490$ m⁻² in combination with a tolerance limit of the mismatch parameter of $\zeta < 1.2$ results in the requirement $\delta < 0.4\%$. Such strict requirements have also been found for a triplet lattice considered for the beam transport at LCLS, resulting, in combination with other reasons, in the rejection of this optics layout [116]*. Based on these results, focusing strength errors can be seen as a challenge regarding the optics setup and the acceptable energy jitter of the source.

7.2.3 Longitudinal Offsets

Longitudinal offsets of quadrupoles in a focusing system have a similar effect as focusing strength errors, a beam mismatch is introduced. The transport matrix linking initial and final Twiss parameters for a drift including a length error is given by

$$\begin{pmatrix} \beta_f(\Delta\tilde{s}) \\ \alpha_f(\Delta\tilde{s}) \\ \gamma_f(\Delta\tilde{s}) \end{pmatrix} = \begin{pmatrix} 1 & -2(\tilde{s} + \Delta\tilde{s}) & (\tilde{s} + \Delta\tilde{s})^2 \\ 0 & 1 & -(\tilde{s} + \Delta\tilde{s}) \\ 0 & 0 & 1 \end{pmatrix} \begin{pmatrix} \beta_i \\ \alpha_i \\ \gamma_i \end{pmatrix}. \quad (7.36)$$

The final Twiss parameter as a function of the initial Twiss parameters and the drift length error are

$$\beta_f(\Delta\tilde{s}) = \beta_f(0) - 2\alpha_i\Delta\tilde{s} + 2\gamma_f(0)\tilde{s}\Delta\tilde{s} + \gamma_f(0)\Delta\tilde{s}^2, \quad (7.37)$$

$$\alpha_f(\Delta\tilde{s}) = \alpha_f(0) - \gamma_i\Delta\tilde{s}, \quad (7.38)$$

$$\gamma_f(\Delta\tilde{s}) = \gamma_f(0) = \gamma_i. \quad (7.39)$$

*The summary was short: "The triplet lattice for the LCLS undulator is a clear prescription for failure." [116]

Using the relation $\alpha_f(0) = \alpha_i - \gamma_i \tilde{s}$, the resulting mismatch at the end of the drift as a function of the drift length error reads

$$\begin{aligned}\zeta &= \frac{1}{2} (\beta_f(\Delta\tilde{s})\gamma_f(0) - 2\alpha_f(\Delta\tilde{s})\alpha_f(0) + \gamma_f(\Delta\tilde{s})\beta_f(0)) \\ &= 1 + \frac{1}{2}\gamma_i^2\Delta\tilde{s}^2.\end{aligned}\quad (7.40)$$

To fulfill the mismatch requirements of the demonstration FEL scenario the relation

$$|\Delta\tilde{s}| < \frac{\sqrt{2(\zeta - 1)}}{\gamma_i}, \quad (7.41)$$

has to hold. Considering the first drift between the exit of the laser-plasma accelerator and the first quadrupole, the beam can be seen to start at a waist yielding $\gamma_i = 1/\beta_i$. Assuming $\beta_i \approx 2 \cdot 10^{-3}$ m which is typical for the here discussed system and $\zeta = 1.2$, based on the tolerance study in Chap. 4 (see Table 4.1), yields an acceptable length precision requirement of $\Delta\tilde{s} < 1$ mm, which is rather easy to fulfill. The same holds for the drift between the focusing system and the undulator where the situation is even more relaxed due to the larger β -function. The requirements tighten within a focusing system. In a quadrupole triplet consisting of miniature permanent magnet quadrupoles the γ -function can reach values on the order of $\gamma_i \sim 10^4$ m⁻¹, resulting in a precision requirement on the order of $\Delta\tilde{s} < 100$ μ m. These requirements are feasible.

7.2.4 Roll errors

A further error source are roll errors of quadrupoles around the beam axis. Any deviation from the ideal quadrupole orientation, that allows only $\Delta\Phi = \pi/2$ steps between focusing and defocusing quadrupoles, leads to a coupling of the otherwise independent components x and y and an emittance growth. In a quadrupole with a roll error the vertical field component B_y is not only a function of the horizontal position but also depends on the vertical position and vice versa. Consequently, the effect not only depends on the roll error but also on the beam sizes.

The relative emittance growth of both components $\Delta\epsilon = \Delta\epsilon_x = \Delta\epsilon_y$ in a thin lens with a roll error can be estimated by [116]

$$\frac{\Delta\epsilon}{\epsilon} \approx 2\Phi^2 k^2 l^2 \beta_x \beta_y. \quad (7.42)$$

Given an acceptable limit for the emittance growth, the roll error has to fulfill

$$|\Phi| < \frac{\sqrt{\Delta\epsilon/\epsilon}}{|k|l\sqrt{2\beta_x\beta_y}}. \quad (7.43)$$

Assuming parameters typical for a focusing system used at a laser-plasma accelerator $\beta_{x,\max} \approx \beta_{y,\max} \approx 20$ m, $l = 1.5$ cm, and $k = 490$ m⁻² and allowing an emittance growth of 10% results in a roll tolerance of $\Phi < 1.5$ mrad. This is challenging but feasible for linear accelerator as well as laser-plasma accelerator based setups [116, 117].

7.2.5 Chromatic Emittance Growth

Besides errors arising due to fabrication or positioning errors, also the intrinsic properties of magnet based beam optics have to be considered. The effect of a magnet on the beam always depends on the energy. This dependence is exploited in the decompression concept using the path length differences in a chicane; however, it also leads to chromatic focusing errors. Due to the broad energy spreads typical for laser-plasma accelerator based systems, this has been regarded as a challenge [118].

Using the matrix formalism, the particle coordinates as a function of the energy deviation after passing a quadrupole in the thin lens approximation are given by

$$\begin{pmatrix} x_f(\eta) \\ x'_f(\eta) \end{pmatrix} = \begin{pmatrix} 1 & 0 \\ -kl(1-\eta) & 1 \end{pmatrix} \begin{pmatrix} x_i \\ x'_i \end{pmatrix}. \quad (7.44)$$

Using the definition of the emittance

$$\epsilon_{x,f} = \sqrt{\text{Var}(x_f) \text{Var}(x'_f) - \text{Cov}^2(x_f, x'_f)}, \quad (7.45)$$

and assuming the initial transverse particle position and energy deviation to be uncorrelated, i.e. $\langle x_i^2 \eta \rangle = \langle x_i^2 \rangle \langle \eta \rangle = 0$ as well as $\langle x_i^2 \eta^2 \rangle = \sigma_{x,i}^2 \sigma_\eta^2$, which is fulfilled for the initial particle distribution only, one obtains the emittance after passing through a quadrupole [119]

$$\begin{aligned} \epsilon_{x,f} &= \epsilon_{x,i} \sqrt{1 + \left(\frac{kl\sigma_{x,i}^2 \sigma_\eta}{\epsilon_{x,i}} \right)^2} \\ &= \epsilon_{x,i} \sqrt{1 + (kl\beta_{x,i} \sigma_\eta)^2}. \end{aligned} \quad (7.46)$$

Assuming $\beta_{x,i} = 20$ m, $l = 1.5$ cm, $k = 490$ m⁻², and a relative energy spread of $\sigma_\eta = 1\%$ results in an increase of the emittance by 78%. The effect can be partially compensated by the optics located further downstream the beamline but will not be negligible in any case due to the broad energy spread and high gradient quadrupoles typically used in a laser-plasma accelerator based experiment.

7.2.6 Conclusion

The basic error sources discussed in this section (transverse and longitudinal offsets, focusing strength errors, and roll errors) already indicate challenging requirements on the focusing system for a laser-plasma accelerator based system, but all errors are within a feasible range and no show-stoppers have been found. The exact requirements depend on the specific layout of the focusing system and are assessed in Sect. 7.4.2.

A rough estimate already suggested that chromatic effects can be severe for the considered parameter set. A possible compensation scheme is discussed in the following section.

7.3 Chromatic Focus Matching

In a setup using the decompression concept the effect of the projected chromatic emittance growth on the FEL performance can be reduced by chromatic focus matching. This concept has independently been suggested by Loulergue et al. [120].

Due to the decompression and the resulting sorting of the bunch by energies, the total chromatic effect can be separated in a chromatic growth of the slice emittance and a mismatch of the Twiss parameters of each slice. The chromatic growth of the slice emittance depending on the slice energy spread cannot be avoided; however, the mismatch caused by the mean energy offset of each slice can be controlled and optimized. Since after the decompression the bunch is sorted by energies, the chromaticity of the focusing system can be used to create a moving focus within the bunch synchronized with the slippage of a radiation pulse. This continuously minimizes the beam size in the interaction region and boosts the FEL performance. The situation is illustrated in Fig. 7.4.

7.3.1 Matching Goal

The slippage of a power spike within the bunch during exponential amplification is given by (see Sect. 2.3.4)

$$\Delta z = \frac{1}{3} \frac{\lambda_l}{\lambda_u} \Delta s, \quad (7.47)$$

with Δs being the longitudinal distance covered by the bunch in the setup. A longitudinal distance travelled by the bunch corresponds to a slippage distance of the radiation pulse within the bunch. Due to the chirp induced by the decompression, this is equivalent to a change of the detuning at the position of the pulse

$$\Delta \eta = \frac{d\eta}{dz} \Delta z = \frac{d\eta}{dz} \frac{1}{3} \frac{\lambda_l}{\lambda_u} \Delta s, \quad (7.48)$$

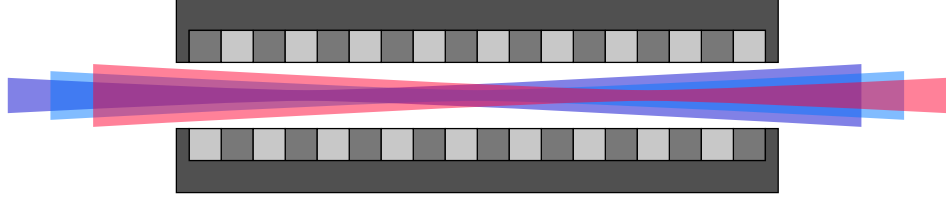


Figure 7.4: Energy dependent focus in the undulator. The chromaticity of the focusing system can be matched so that the energy dependent focus always coincides with the position of the radiation pulse that slips through the chirped electron bunch. The lowest energy (purple) corresponding to the bunch tail is focused first generating the initial radiation pulse. The radiation pulse slips through the bunch and interacts with the higher energies (blue and red) each having the highest current density in the particular interaction region.

with $d\eta/dz$ being the relative energy chirp. To increase the FEL gain, the chromaticity of the focusing system can be used to ensure a minimum beam cross section at the position of the power spike, i.e. for the corresponding mean energy. The required dependence of the focus position on the energy is characterized by

$$\frac{ds}{d\eta} = \frac{3\lambda_u}{\lambda_l} \left(\frac{d\eta}{dz} \right)^{-1}. \quad (7.49)$$

Consequently, the ideal focus position as a function of the energy reads

$$s_{\text{focus}}(\eta) = s_{\text{focus},0} + \frac{ds}{d\eta}\eta, \quad (7.50)$$

using the ideal focus position of the resonance energy $s_{\text{focus},0}$.

The effect of a planar undulator with a field in the y -direction on the beam envelope evolution in the x -direction is usually negligible and it can be approximated by a drift. The resulting energy dependent focus position of the horizontal component with respect to the undulator entrance is given by

$$s_{\text{focus},x}(\eta) = \frac{\alpha_x(\eta)}{\gamma_x(\eta)}, \quad (7.51)$$

with $\alpha_x(\eta)$ and $\gamma_x(\eta)$ being the horizontal Twiss parameters at the undulator entrance. The appropriate energy dependence can therefore be achieved by requiring the Twiss

parameters at the undulator entrance to fulfill

$$\frac{\alpha_x(\eta)}{\gamma_x(\eta)} = \frac{\alpha_{x,0}}{\gamma_{x,0}} + \frac{3\lambda_u}{\lambda_l} \left(\frac{d\eta}{dz} \right)^{-1} \eta, \quad (7.52)$$

with the ideal focus position in the undulator given by $s_{\text{focus},x,0} = \alpha_{x,0}/\gamma_{x,0}$ using the Twiss parameters obtained in the tolerance study in Chap. 4 (see Table 4.1). Since the focal length of a quadrupole can be approximated by $f = 1/(k(\eta)l) \approx (1 + \eta)/(kl)$, the requirement can be fulfilled by a suited optics design.

For the y -component, i.e. the direction of the magnetic field, the focusing effect of the undulator is in general not negligible. The effect of the undulator on the beam can be described using the transport matrix based on Eq. (2.12)

$$\mathbf{M}_{\text{und}} = \begin{pmatrix} \cos(\kappa_y s) & \frac{1}{\kappa_y} \sin(\kappa_y s) \\ -\kappa_y \sin(\kappa_y s) & \cos(\kappa_y s) \end{pmatrix}. \quad (7.53)$$

The evolution of the vertical Twiss parameters in the undulator is consequently given by

$$\begin{pmatrix} \beta_f(\eta) \\ \alpha_f(\eta) \\ \gamma_f(\eta) \end{pmatrix} = \mathbf{M}_{\text{und, Twiss}} \begin{pmatrix} \beta_i(\eta) \\ \alpha_i(\eta) \\ \gamma_i(\eta) \end{pmatrix}, \quad (7.54)$$

using the transport matrix for the Twiss parameters

$$\mathbf{M}_{\text{und, Twiss}} = \begin{pmatrix} \cos^2(\kappa_y s) & -\frac{2}{\kappa_y} \sin(\kappa_y s) \cos(\kappa_y s) & \frac{1}{\kappa_y^2} \sin^2(\kappa_y s) \\ \kappa_y \sin(\kappa_y s) \cos(\kappa_y s) & -\sin^2(\kappa_y s) + \cos^2(\kappa_y s) & -\frac{1}{\kappa_y} \sin(\kappa_y s) \cos(\kappa_y s) \\ \kappa_y^2 \sin^2(\kappa_y s) & 2\kappa_y \sin(\kappa_y s) \cos(\kappa_y s) & \cos^2(\kappa_y s) \end{pmatrix}. \quad (7.55)$$

By requiring the vertical component to have a waist at the beginning of the undulator $\alpha_{f,y}(s_{\text{focus},y} = 0) = 0$ and solving for the position, one obtains the focus position with respect to the undulator entrance as a function of the initial, energy dependent Twiss parameters

$$s_{\text{focus},y}(\eta) = \frac{1}{\kappa_y} \left(n\pi/2 - \tan^{-1} \left(\frac{\sqrt{4\alpha_y^2(\eta)\kappa_y^2 + (\beta_y(\eta)\kappa_y^2 - \gamma_y(\eta))^2 - \beta_y(\eta)\kappa_y^2 + \gamma_y(\eta)}}{2\alpha_y(\eta)\kappa_y} \right) \right), \quad (7.56)$$

with $n = 1, 3, 5, \dots$. This relation is in general not compatible with the desired linear dependence of the focus position on the energy deviation. However, with increasing energies the focusing effect of the undulator drops due to the proportionality $\kappa_y \propto \gamma^{-1}$.

When the scale of the slow oscillation caused by the undulator reaches the order of the undulator length, i.e. $\kappa_y^{-1} > L_u/2$, the focus motion can be approximated by

$$s_{\text{focus},y}(\eta) \approx \frac{\alpha_y(\eta)}{\gamma_y(\eta)}, \quad (7.57)$$

resembling the motion on a drift. In this limit the focus motion can be matched.

In the limiting case of a very low energy and, therefore, strong focusing of the undulator, i.e. $\kappa_y^{-1} \ll L_u/2$, the beam propagation becomes independent of the initial divergence, i.e. independent of γ_i , and only depends on the initial beam size and the correlations within the beam. In this case the focus position is given by

$$s_{\text{focus},y}(\eta) = \frac{1}{\kappa_y} \left(n\pi/2 - \tan^{-1} \left(\frac{\sqrt{4\alpha_y^2(\eta)\kappa_y^2 + \beta_y^2(\eta)\kappa_y^4} - \beta_y(\eta)\kappa_y^2}{2\alpha_y(\eta)\kappa_y} \right) \right), \quad (7.58)$$

and cannot be synchronized with the radiation slippage. In order to reach a minimum beam size along the undulator for this case, the energy dependence of the β -function should be minimized, and the β -function of the reference energy should be matched to the undulator focusing so that a constant beam size is ensured. This results in an as large as possible part of the bunch to have the constant, matched beam size along the undulator.

7.3.2 Matching Concept

If chromatic focus matching is possible for a component, e.g. the horizontal one, it can be reached as follows: The beam transport from the accelerator exit to the focus position of the reference energy $s_{\text{focus},0}$ can be expressed as a combination of drifts and quadrupoles. The corresponding chromatic transport matrix can be approximated by

$$\mathbf{M}(\eta) = \begin{pmatrix} R_{11} + T_{116}\eta & R_{12} + T_{126}\eta \\ R_{21} + T_{216}\eta & R_{22} + T_{226}\eta \end{pmatrix}, \quad (7.59)$$

using the energy independent transport matrix elements R_{ij} and the energy related, higher order terms T_{ij6} with $i, j \in \{1, 2\}$. Assuming the initial Twiss parameters at the accelerator exit to be energy independent results in an energy dependent evolution of the Twiss parameters according to

$$\begin{pmatrix} \beta_f(\eta) \\ \alpha_f(\eta) \\ \gamma_f(\eta) \end{pmatrix} = \mathbf{M}_{\text{Twiss}}(\eta) \begin{pmatrix} \beta_i \\ \alpha_i \\ \gamma_i \end{pmatrix}, \quad (7.60)$$

using the transport matrix for the Twiss parameters

$$\mathbf{M}_{\text{Twiss}}(\eta) = \begin{pmatrix} M_{11}^2(\eta) & -2M_{11}(\eta)M_{12}(\eta) & M_{12}^2(\eta) \\ -M_{11}(\eta)M_{21}(\eta) & M_{12}(\eta)M_{21}(\eta) + M_{11}(\eta)M_{22}(\eta) & -M_{12}(\eta)M_{22}(\eta) \\ M_{21}^2(\eta) & -2M_{21}(\eta)M_{22}(\eta) & M_{22}^2(\eta) \end{pmatrix}. \quad (7.61)$$

Provided that the beam transport starts at a waist $\alpha_i = 0$, and requiring a focus for the reference energy at the target $\alpha_f(0) = 0$, e.g. the undulator center, yields the Twiss parameter relations

$$\begin{aligned}\alpha_f(\eta) = & - (R_{11}T_{216}\eta + R_{21}T_{116}\eta + T_{116}T_{216}\eta^2)\beta_i \\ & - (R_{12}T_{226}\eta + R_{22}T_{126}\eta + T_{126}T_{226}\eta^2)\gamma_i,\end{aligned}\quad (7.62)$$

and

$$\begin{aligned}\gamma_f(\eta) = & \gamma_f(0) + (2R_{21}T_{216}\eta + T_{216}^2\eta^2)\beta_i \\ & + (2R_{22}T_{226}\eta + T_{226}^2\eta^2)\gamma_i,\end{aligned}\quad (7.63)$$

using $\gamma_f(0) = R_{21}^2\beta_i + R_{22}^2\gamma_i$. Particles without an energy offset clearly fulfill the criterion $\alpha_f(0) = 0$, i.e. they end at a beam waist and have a divergence measured by $\gamma_f(0)$. Any detuned electrons will either be diverging $\alpha_f(\eta) < 0$, or converging $\alpha_f(\eta) > 0$ at this position.

To reach a focus for the detuned energy η , requires an additional drift relative to the focus position of the reference energy, i.e. $0 = \alpha_{\text{focus}} = \alpha_f(\eta) - \gamma_f(\eta)\Delta s$. The required additional drift length is given by

$$\Delta s(\eta) = \frac{-(R_{11}T_{216}\eta + R_{21}T_{116}\eta + T_{116}T_{216}\eta^2)\beta_i - (R_{12}T_{226}\eta + R_{22}T_{126}\eta + T_{126}T_{226}\eta^2)\gamma_i}{\gamma_f(0) + (2R_{21}T_{216}\eta + T_{216}^2\eta^2)\beta_i + (2R_{22}T_{226}\eta + T_{226}^2\eta^2)\gamma_i}.\quad (7.64)$$

Linearizing the relation with respect to η yields

$$\Delta s(\eta) \approx \frac{-(R_{11}T_{216} + R_{21}T_{116})\beta_i - (R_{12}T_{226} + R_{22}T_{126})\gamma_i}{R_{21}^2\beta_i + R_{22}^2\gamma_i}\eta.\quad (7.65)$$

Since typical laser-plasma based systems have a very small source size, i.e. a small initial β -function $\beta \approx 10^{-3}$ m, the initial divergence is high $\gamma_i = 1/\beta_i \approx 10^3$ m⁻¹ and the γ_i -dependent terms dominate*

$$\Delta s(\eta) \approx -\frac{R_{12}T_{226} + R_{22}T_{126}}{R_{22}^2}\eta.\quad (7.66)$$

In order to obtain chromatic matching the beam transport has to fulfill the condition

$$-\frac{R_{12}T_{226} + R_{22}T_{126}}{R_{22}^2} = \frac{3\lambda_u}{\lambda_l} \left(\frac{d\eta}{dz} \right)^{-1},\quad (7.67)$$

which can be ensured by a suited optics design. In order to control the Twiss parameters of the reference energy of both components at the undulator entrance, as well as the focus

*The differences of the matrix elements are negligible when compared to the differences of the Twiss parameters $\gamma_i/\beta_i \approx 10^6$.

motion, sufficient degrees of freedom in the optics system have to be ensured. This can only fully be achieved by using at least two triplets or doublets of quadrupoles for the focusing system as suggested by [120]. A single focusing system, either doublet or triplet, however, can still provide an approximate matching due to the intrinsic chromaticity (see Chap. 8).

In the case of a non-negligible, vertical focusing strength of the undulator, the energy dependence of the vertical beam size should be minimized, in order to ensure a matched beam size for a wide energy range. The β -function after the propagation through the beam transport system is given by

$$\begin{aligned}\beta_f(\eta) = \beta_f(0) &+ (2R_{33}T_{336}\eta + T_{336}^2\eta^2)\beta_i \\ &+ (2R_{34}T_{346}\eta + T_{346}^2\eta^2)\gamma_i,\end{aligned}\quad (7.68)$$

using $\beta_f(0) = R_{33}^2\beta_i + R_{34}^2\gamma_i$. Consequently, to ensure a minimal energy dependence, the matrix elements T_{336} and T_{346} have to be minimized. If this is to be achieved in combination with the horizontal matching, sufficient degrees of freedom in the beam transport system have to be ensured. A good approximation can, however, be achieved with a simple triplet as demonstrated in Chap. 8.

7.3.3 Performance Estimate

The effect of chromatic matching in detail can only be determined by time-dependent 3D simulations taking radiation slippage and the beam envelope evolution into account. However, a rough analytical estimate of the effect is possible. As a reference an idealized, achromatic system with a minimized, average β -function along the undulator can be considered (see Sect. 3.2.3). The average β -function is given by

$$\bar{\beta} = \beta_0 - \alpha_0 L_u + \frac{1}{3}\gamma_0 L_u^2, \quad (7.69)$$

using the undulator length L_u . It is minimized by the Twiss parameters at the undulator entrance $\beta_0 = \sqrt{4/3}L_u$, $\alpha_0 = \sqrt{3}$, and $\gamma_0 = 2\sqrt{3}/L_u$, resulting in an average β -function of $\bar{\beta} = L_u/\sqrt{3}$. The minimum beam size reached at the undulator center is $\beta_{\min} = L_u/(2\sqrt{3}) = \bar{\beta}/2$.

For the case of the achromatic system, i.e. no chromatic matching, the beam size can be approximated by using the average β -function along the undulator for both components. In this case the gain length is proportional to

$$L_{g,3D} \propto \left(\sqrt{\bar{\beta}_x \bar{\beta}_y} \right)^{1/3}. \quad (7.70)$$

If perfect chromatic matching of both components is achieved, the electron beam size at the radiation pulse position is always minimized and the gain length scales as

$$L_{g,3D,\text{matched}} \propto \left(\sqrt{\beta_{x,\text{min}}\beta_{y,\text{min}}} \right)^{1/3}. \quad (7.71)$$

The power ratio of these two cases is therefore given by

$$\frac{P_{\text{matched}}(s)}{P(s)} = \exp\left(\frac{s}{L_{g,3D}} \left(2^{1/3} - 1\right)\right). \quad (7.72)$$

As an extreme case an operation close to saturation can be assumed. Setting $s = 20L_{g,3D}$ results in a power boost by a factor of ~ 180 . The effect can be even greater, if other degrading effects are considered whose impact can be reduced by the increased current density. However, the accompanying chromatic slice emittance growth has also been neglected which will lead to a performance reduction.

If chromatic matching can only be achieved for one component, e.g. due to a strong focusing effect of the undulator, the scaling becomes

$$\frac{P_{\text{matched}}(s)}{P(s)} = \exp\left(\frac{s}{L_{g,3D}} \left(2^{1/6} - 1\right)\right), \quad (7.73)$$

since only one β -function differs. Assuming an undulator length of $s = 2$ m, a reference gain length of $L_{g,3D} = 17$ cm and chromatic matching of one component, which resembles the situation of the demonstration case, results in a power increase by a factor of four due to chromatic matching.

The energy dependence of the focus position of the horizontal component $ds_{\text{focus},x}/d\eta$ has been scanned with GENESIS by artificially generating bunches with the suited energy dependent Twiss parameters. The result is shown in Fig. 7.5. The power is increased by approximately 26% at the optimum when compared to the case with no energy dependence of the focus position $ds_{\text{focus},x}/d\eta = 0$ m. The effect is weaker than in the analytical estimate which can be explained by the chromatic slice emittance growth that was neglected in the analytical scaling and the short bunch length (see below). The maximum of the Gaussian fit is located at $ds_{\text{focus},x}/d\eta \approx 89$ m which is slightly higher than the analytically estimated optimum of $ds_{\text{focus},x}/d\eta \approx 67$ m. This can be understood as an effect of the short bunch length that affects the slippage dependent focus optimization. A higher value of the energy dependence of the focus position $ds_{\text{focus},x}/d\eta$ is equivalent to a focus staying longer in the vicinity of the bunch center*.

Assuming the bunch center to be focused at the undulator center, a bunch of $\sigma_z = 2$ μm , and an focus-energy-dependence of $ds_{\text{focus},x}/d\eta \approx 67$ m, results in the bunch part located at $z = 3$ μm to be focused at the undulator exit. Consequently, the focus leaves the

*This might seem contradicting but is explained by the relation $z_{\text{focus}} \propto \eta_{\text{focus}} \propto (ds_{\text{focus}}/d\eta)^{-1}\Delta s$. An example is shown in Fig. 8.7.

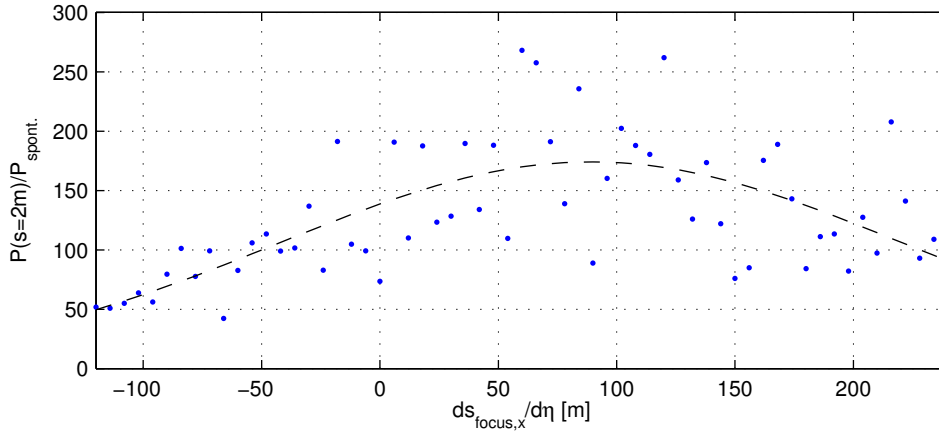


Figure 7.5: Normalized power at the undulator exit as a function of the energy dependence of the focus position of the horizontal component. The vertical component has been assumed to be energy independent. Each blue dot has been averaged over ten GENESIS runs, the dashed black line is a Gaussian fit to the simulation data.

central one- σ -range. Using $ds_{\text{focus},x}/d\eta \approx 89$ m results in a focus of the bunch fraction at $z = 2.2 \mu\text{m}$ at the undulator exit. Here the focus nearly stays within the central one- σ -range, resulting in a better performance due to the minimized beam size of the bunch part containing most of the charge and despite the worse synchronization with the slippage of an ideal radiation pulse. This indicates that chromatic focus matching is only fully usable in cases that are not slippage limited.

7.3.4 Conclusion

In this section the concept of chromatic focus matching has been discussed and tested. The basic idea is to synchronize the movement of the focus through the bunch caused by the chromaticity of the focusing system with the slippage of the FEL radiation pulse in a chirped electron bunch.

For the here discussed parameter set the chromatic focus matching has a non-negligible effect on the FEL performance and should be taken into account in the optics design. However, the full potential, when compared to the idealized case of no energy dependence of the focus position, cannot be tapped. Limiting factors are the strong focusing of the undulator allowing only the horizontal component to be matched and the short bunch length limiting the usable interaction range of photons and electrons due to slippage. The short bunch length even causes a higher focus-energy-dependence $ds_{\text{focus},x}/d\eta$ to be of advantage when compared to the analytical estimate based on the idea of synchronizing

focus position and radiation pulse slippage. More details regarding the interplay of the different effects are discussed in Chap. 8.

Comparing the two FEL demonstration concepts discussed in Chap. 3 it is worth to note that chromatic focus matching can only be combined with the longitudinal decompression concept but not the TGU concept relying on transverse dispersion. In a TGU system chromatic effects will not only spoil the FEL performance via the envelope variations and corresponding current density changes, but the beam size evolution along the undulator can also result in an increase of the effective, local energy spread at a given transverse position.

7.4 Layout Concept

The beam transport layout discussed in this thesis is designed with the spatial limitations of the upcoming facility Centre for Advanced Laser Applications (CALA) in mind, where a first lab-scale FEL demonstration experiment is planned. The full beamline will be 16 meters long, which might seem long for a lab-scale system; however, this includes the focusing of the laser, the gas target for the electron acceleration, the beam transport, the undulator, as well as electron and radiation diagnostics. The suggested layout will take these boundary conditions into account, but it can be adapted to other facilities as well.

7.4.1 General Concept

The requirements on the beam transport system for a first demonstration experiment can be characterized as follows:

- **Mismatch free** – The setup has to be designed such that the desired Twiss parameters at the undulator entrance $\beta_{x,0}$, $\beta_{y,0}$, $\alpha_{x,0}$, and $\alpha_{y,0}$, obtained in the tolerance study (see Table 4.1), are reached. This defines the minimum number of needed quadrupoles in order to provide sufficient degrees of freedom.
- **Simplicity** – It should be as simple as possible in order to minimize the degrading effects caused by the optics. Therefore, a minimum of components with reasonable parametrization should be used. This is of high importance due to the tight limits for errors of the focusing systems expected based on the estimates above (see Sect. 7.2).
- **Compactness** – Due to the spatial limitations of most laser facilities and in the spirit of a lab-scale system, the setup length should be kept short. For the beamline layout in CALA a beam transport section on the order of ~ 2 m is planned.

Strictly following these principles rules out the use of multiple focusing positions in the setup, e.g. two doublets or triplets, as they would be needed to match an electron beam to the chicane as well as the undulator, or in order to achieve perfect chromatic focus matching. These more complex layouts double the number of optical elements and, consequently, the error sources and lead to approximately twice as long setups.

Restricting the setup to a single focusing station results in two options: If all quadrupole strengths in terms of the k parameters, as well as all drift lengths can be freely chosen, a mismatch free setup can be achieved by a quadrupole doublet. The next better solution, allowing for more degrees of freedom, is the quadrupole triplet. In the case of a triplet also an adaption to changes of the mean energy for a fixed setup length is possible which is of advantage given the limited source stability expected for a first demonstration experiment.

If only a single focusing position is considered, the setup parametrization and dimensions can roughly be estimated by discussing a single lens only. The evolution of the Twiss parameters from the accelerator to the quadrupole is given by

$$\beta_{\text{quad, in}} = \beta_{\text{acc}} + \frac{s_1^2}{\beta_{\text{acc}}}, \quad (7.74)$$

$$\alpha_{\text{quad, in}} = -\frac{s_1}{\beta_{\text{acc}}}, \quad (7.75)$$

$$\gamma_{\text{quad, in}} = \frac{1}{\beta_{\text{acc}}}, \quad (7.76)$$

with the drift length between accelerator and quadrupole s_1 and assuming a beam waist at the accelerator exit, i.e. $\alpha_{\text{acc}} = 0$. Conversely, the parameters at the quadrupole exit are defined by the requirements at the undulator

$$\beta_{\text{quad, out}} = \beta_{\text{und}} + \frac{s_2^2}{\beta_{\text{und}}}, \quad (7.77)$$

$$\alpha_{\text{quad, out}} = \frac{s_2}{\beta_{\text{und}}}, \quad (7.78)$$

$$\gamma_{\text{quad, out}} = \frac{1}{\beta_{\text{und}}}. \quad (7.79)$$

Here again a beam waist at the undulator has been assumed, i.e. $\alpha_{\text{und}} = 0$. This assumption either holds at the undulator entrance, if a matching of the beam to the undulator focusing is desired, or at the undulator center for the case of a minimized average beam size along the undulator. Using the thin lens approximation, these sets of equations are linked by

$$\beta_{\text{quad, out}} = \beta_{\text{quad, in}}, \quad (7.80)$$

$$\alpha_{\text{quad, out}} = kl\beta_{\text{quad, out}} + \alpha_{\text{quad, in}}, \quad (7.81)$$

$$\gamma_{\text{quad, out}} = k^2l^2\beta_{\text{quad, in}} + 2kl\beta_{\text{quad, in}} + \gamma_{\text{quad, in}}, \quad (7.82)$$

using the quadrupole strength k and its length l .

In this simple model the length of the second drift is a function of the first drift length and the Twiss parameters at the undulator as well as the accelerator

$$s_2 = \sqrt{\beta_{\text{und}} \left(\beta_{\text{acc}} - \beta_{\text{und}} + \frac{s_1^2}{\beta_{\text{acc}}} \right)}. \quad (7.83)$$

The focusing strength of the quadrupole is given by

$$kl = \frac{s_2}{\beta_{\text{und}} \left(\beta_{\text{acc}} + \frac{s_1^2}{\beta_{\text{acc}}} \right)} + \frac{s_1}{\beta_{\text{acc}} \left(\beta_{\text{acc}} + \frac{s_1^2}{\beta_{\text{acc}}} \right)}. \quad (7.84)$$

Requiring a beam transport length of $s_1 + s_2$ on the order of 2 m results in $s_1 \approx 0.11$ m, $s_2 = 1.89$ m and an integrated quadrupole strength of $kl = 9.5 \text{ m}^{-1}$. This can be achieved by a quadrupole with a length of $l = 2$ cm, and a gradient of $g \approx 480 \text{ T/m}$.

Since a doublet or triplet is needed to achieve focusing in both planes, the relations above can only be used for a rough estimate, but they already indicate that high gradient quadrupoles [111, 117] are needed in order to build a setup in the spirit of a lab-scale system. Within limits quadrupole length and gradient can be traded off against each other; however, for low gradients ultimately longer setups are needed and the average beam size in the beam transport rises. Any increase of the beam size for a fixed integrated quadrupole strength kl will, however, tighten the precision requirements of the optics in terms of rotation and focusing strength errors. Therefore, the use of high gradient quadrupoles is strongly recommended.

7.4.2 Single Triplet Layout

Based on the estimates above a beam transport relying on a single triplet consisting of high gradient permanent magnet miniature quadrupoles (PMQ) has been designed. The layout and β -functions along the setup are shown in Fig. 7.6, with the setup parameters shown in Table 7.2. All quadrupoles have been assumed to have a gradient of $g = 480 \text{ T/m}$ and be available with length increments of millimeters. Furthermore, micrometer precision for the quadrupole placement has been assumed. Since up to now no free tuning of the gradient is available for the PMQs, matching of the optics has been achieved by varying quadrupole lengths and positions.

Basic Performance

The basic setup performance has been evaluated for the reference energy of $\gamma = 600$ neglecting all degrading effects. The Twiss parameters of a monoenergetic bunch obtained at the undulator entrance are $\beta_x = 2.39$, $\alpha_x = 2.41$, and $\beta_y = 0.67$, $\alpha_y = 0.01$.

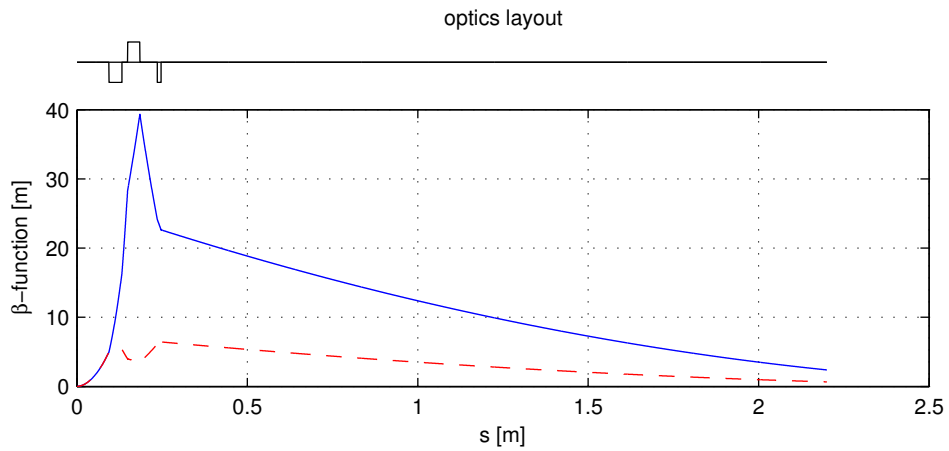


Figure 7.6: Evolution of β -functions of horizontal (solid blue) and vertical (dashed red) component as a function of the position in the setup between accelerator exit and undulator entrance obtained for the reference energy. The quadrupole configuration is indicated by the black line above.

name	length [mm]	k [m^{-2}]
quadrupoles		
Q1	38	469.342
Q2	36	-469.342
Q3	11	469.342
drifts		
L1	93.877	-
L2	16.710	-
L3	51.293	-
L4	1953.12	-

Table 7.2: Parameters of the matched beam transport system using a single triplet consisting of high gradient PMQs. The setup and resulting evolution of the β -functions are shown in Fig. 7.6.

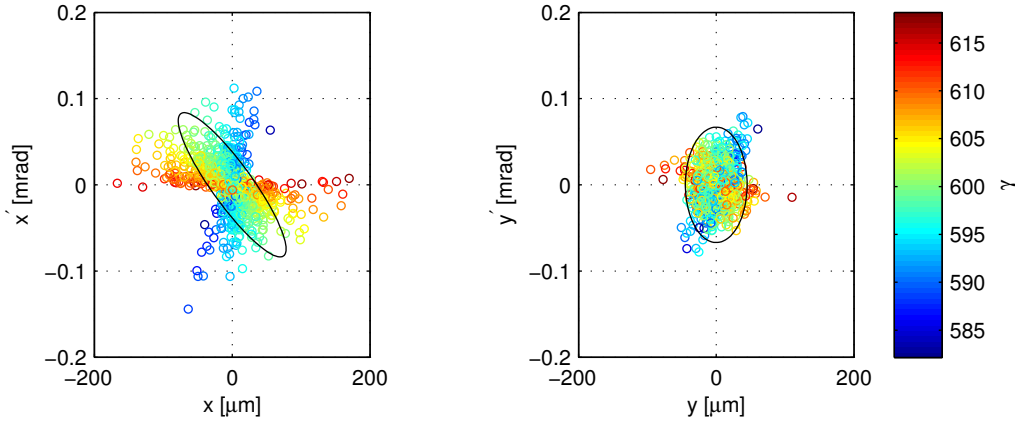


Figure 7.7: Transverse phase spaces at the undulator entrance obtained with ELEGANT taking chromatic effects of the optics into account. The black ellipses indicate the the three- σ -range of the ideal phase space ellipses.

Comparing these parameters with the design parameters obtained in the tolerance study of the FEL (see Chap. 4) results in a deviation of the mismatch parameters from unity of $\Delta\zeta_x = 2 \cdot 10^{-2}$ and $\Delta\zeta_y = 5 \cdot 10^{-5}$. Since the induced mismatch is at least one order of magnitude below the tolerance limit of $t_{\Delta\zeta_x} = t_{\Delta\zeta_y} = 0.2$ in both cases, the setup can be seen as mismatch free. Consequently, it fulfills the first two design requirements above, it is mismatch free and simple. Given a total length of only 2.2 m it also fulfills the requirement of compactness.

The situation changes with the inclusion of energy spread. Based on the parameters of the demonstration experiment (see Table 3.3) a relative energy spread of 1% has been assumed. Due to the chromaticity of the optics, a significant chromatic emittance growth is found. The impact differs significantly between the x - and y -component. The vertical emittance increases by $\Delta\epsilon_y/\epsilon_y = 28\%$, whereas the horizontal emittance grows by $\Delta\epsilon_x/\epsilon_x = 260\%$. The effect can clearly be seen in the transverse phase space diagrams shown in Fig. 7.7. The chief cause of this difference is the interplay of the individual quadrupoles and the resulting differences in the transverse beam sizes. The maximum vertical beam size is characterized by $\beta_{y,\max} \approx 6$ m, whereas the horizontal component reaches $\beta_{x,\max} \approx 39$ m. For any system not relying on the decompression concept this chromatic emittance growth can be seen as a show stopper.

As discussed above, degrading chromatic effects can be reduced by chromatic focus matching when using the decompression concept (for details see discussion of chromatic focus matching in Sect. 7.3 and the full beam transport analysis in Sect. 8.1). As already indicated by the low vertical emittance growth, also the energy dependence of the vertical beam size at the undulator entrance is weak, a 1% energy deviation increases the

beam size by approximately 40%. Consequently, the vertical beam size is close to the matched beam size of the undulator for a wide energy range. Since the vertical beam size within the undulator is mainly given by the beam size at the undulator entrance and is only weakly dependent on the initial divergence due to the moderate energy (see Sect. 7.3), the low energy dependence of the initial beam size results in low vertical beam size variations within the undulator, allowing for a high current density independent of the energy.

The energy dependence of the horizontal focus position is $ds_{\text{focus},x}/d\eta \approx 123$ m which is approximately two times higher than ideal for the demonstration experiment (see Eq. (7.49)); however, it is still within reasonable limits according to GENESIS simulations (see Fig. 7.5) and will only result in a power loss of less than 10% when compared to the optimum. Given the limited degrees of freedom of the optics layout this is considered well suited.

Error Tolerances

For the simple triplet fulfilling the design requirements the basic error tolerances regarding the:

- **Transverse positioning** accuracy of the quadrupoles,
- **Roll error** of each quadrupole around the beam axis,
- **Longitudinal positioning** accuracy of the quadrupoles,
- **Focusing strength** accuracy requirements of the quadrupoles,

have been evaluated in order to assess the feasibility of the setup. Here perfect hard-edge magnets without higher order magnetic moments and other degrading effects have been assumed.

The **transverse lens positioning** error is limited by the maximum acceptable beam offset at the undulator (see Table 4.1). In addition to lens positioning errors with respect to the undulator, any source jitter will contribute to the final beam offset at the undulator entrance. Assigning the same weight to the source jitter and the transverse lens positioning accuracy leads to the requirements $\sigma_{\Delta x} < 5 \mu\text{m}$ and $\sigma_{\Delta y} < 2 \mu\text{m}$ for all quadrupoles (see Fig. 7.8 (left)). As can be seen, the vertical direction with the stricter tolerance requirement coincides with the less sensitive plane of the optics. A basic control of the sensitivity for a quadrupole triplet is given by the sequence of (horizontally) focusing (F) and defocusing (D) lenses. For this setup the D-F-D sequence resulted in the desired lower sensitivity of the vertical plane.

In addition to a beam offset, any transverse positioning error will also result in an additional beam angle with respect to the undulator axis. The resulting requirements on

the positioning accuracy are, however, more relaxed than those given by the beam offset and do therefore not limit the lens positioning requirements.

An advantage of the here proposed compact setup is the use of a single focusing triplet. This allows to pre-align all quadrupoles in the setup with respect to each other prior to the implementation in the beamline. Assuming a perfect internal alignment of the triplet, the acceptable offset error of the whole triplet is given by $\sigma_{\Delta x, \text{full}} < 23 \mu\text{m}$ and $\sigma_{\Delta y, \text{full}} < 3 \mu\text{m}$. If an internal alignment error of $\sigma_{\Delta x, \text{int}} = \sigma_{\Delta y, \text{int}} = 1 \mu\text{m}$ can be achieved, the tolerance requirement for the full triplet drops to $\sigma_{\Delta x, \text{full}} < 21 \mu\text{m}$ and $\sigma_{\Delta y, \text{full}} < 3 \mu\text{m}$. Since the pre-alignment significantly reduces the precision required for the positioning of the lenses with respect to the undulator, this approach should be considered. In general the transverse alignment requirements are challenging and up to an order of magnitude stricter than those of LCLS [40] but still within the feasible range regarding positioning control with commercially available linear stages (e.g. [112]).

One alignment concept used at large scale facilities, like synchrotrons and linear accelerators, is beam based alignment (BBA). This concept usually relies on the tunability of the quadrupole strength of electromagnet based quadrupoles. By varying the quadrupole strength and analyzing the effect on the beam trajectory, e.g. via beam position monitors (BPMs), the position of the quadrupole can be optimized until the effect of a strength variation on the trajectory is minimized. The fixed strength of the here used PMQs requires a slightly different concept. While the basic BBA concept above can be used with all magnets in place, here the magnets have to be inserted into the beam path individually what is not compatible with the idea of an internal pre-alignment of the triplet. Comparing the reference beam trajectory, i.e. without any magnets, and the trajectory perturbed by a quadrupole allows to minimize the final beam offset from the reference trajectory and hence the PMQ offset. Assuming a few meter distance between the quadrupole and the detection position also requires μm -scale precision for the beam position measurement which is feasible with state-of-the-art cavity BPMs [121]; however, any beam position jitter caused by the source will complicate the alignment and reduce the achievable accuracy. An internal pre-alignment of the triplet could be achieved by means of the pulsed-wire-method [122] or variations of it like the vibrating-wire-method [123]. In any case the optics alignment can be seen as a challenge.

Assuming equal weights for the transverse triplet and source position/angle tolerances for the given setup regarding the resulting beam offsets and angles at the undulator entrance results in the source position tolerance given by $\sigma_{\Delta x, \text{source}} < 23 \mu\text{m}$ and $\sigma_{\Delta y, \text{source}} < 4 \mu\text{m}$, limited by the x -angle and y -offset at the undulator entrance, as well as the angle tolerances $\sigma_{\theta_x, \text{source}} < 2 \text{ mrad}$ and $\sigma_{\theta_y, \text{source}} < 3 \text{ mrad}$, both limited by the angle at the undulator entrance. As discussed in Sect. 7.2.1, the high sensitivity with respect to initial offsets is a direct consequence of the required magnification of the optical system. Since the optics layout is imaging, the restrictions on the initial angles are relaxed. While the requirements on the angles at the source are feasible given a typical pointing stability

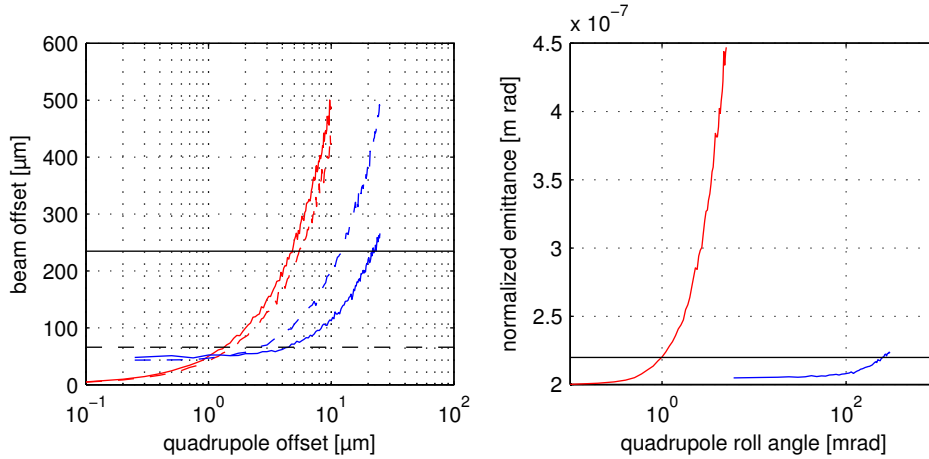


Figure 7.8: **Left:** Beam offset (rms) in the horizontal (solid) and vertical (dashed) direction at the undulator entrance as a function of the rms quadrupole offset assuming no internal alignment of the triplet (red) and an internal alignment precision of 1 μm (blue). The black lines indicate the tolerance limits. **Right:** Average normalized emittance as a function of the rms quadrupole roll angle. The red line indicates the case with no internal pre-alignment, whereas the blue curve assumes an internal alignment precision of 0.5 mrad. The black line represents the tolerance limit.

on the order of 1 mrad [124], the offset tolerances at the source are very challenging assuming a position jitter on the order of the laser waist size and a typical laser waist size at the gas target on the order of tens of micrometers [125].

Roll errors of the quadrupoles around the beam axis result in an emittance growth as well as a Twiss parameter mismatch. Limiting the emittance growth to 10% results in a rotation error limit of $\sigma_{\Phi} < 1$ mrad for each quadrupole (see Fig. 7.8 (right)). Using the mismatch limit of the FEL tolerance study and taking into account that rotation as well as focusing strength errors and longitudinal lens offsets contribute to the final mismatch independently leads to the rotation error requirement $\sigma_{\Phi} < 3$ mrad which would be accompanied by an emittance growth of 50%. This is not acceptable since it exceeds the emittance growth caused by other degrading effects like CSR and chromatic focusing, consequently the stricter limit above has to be used.

A perfect internal pre-alignment of the quadrupole triplet reduces the roll tolerance of the full assembly to $\sigma_{\Phi, \text{full}} < 280$ mrad limited by the emittance growth. Assuming an internal alignment precision of $\sigma_{\Phi, \text{int}} = 0.5$ mrad results in a tolerance for the full triplet of $\sigma_{\Phi, \text{full}} < 250$ mrad. Comparing the tolerances for the individual roll error and the full, pre-aligned triplet shows that the limiting factor is the alignment of the quadrupoles with respect to each other and not relative to the undulator. Since a pre-alignment significantly reduces the required roll precision of the whole triplet with respect to the undulator when compared to the individual alignment, it should be preferred. The

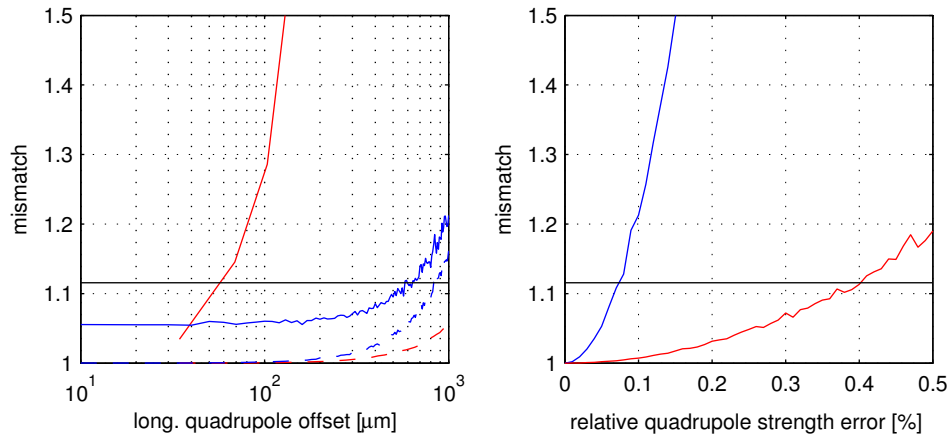


Figure 7.9: **Left:** Average mismatch of the horizontal (solid) and vertical (dashed) component as a function to the rms longitudinal quadrupole offset error. The red lines assume no internal alignment of the triplet, the blue lines show the case of an internal alignment precision of $20 \mu\text{m}$. The solid black line is the tolerance limit of both components. **Right:** Average mismatch as a function of the relative rms quadrupole focusing strength error for the horizontal component (blue) and the vertical component (red). The solid black line is the tolerance limit of both components.

internal alignment is assumed to be feasible using Hall probe measurements [126].

Like the transverse offset tolerances also the roll error limits for the individual quadrupoles are stricter than those found at linear accelerator based facilities, e.g. LCLS. There only a roll tolerance of 10 mrad [40, 116] is required. From this point of view, the required tolerance can be seen as a challenge for the quadrupole alignment in a lab-scale setup. However, the unique advantage of the compact setup allowing for a pre-alignment of all quadrupoles with respect to each other relaxes the situation.

An issue linked to any mismatch discussion is the problem of the mismatch characterization. The well established method of a quadrupole scan in order to determine the Twiss parameters and the emittance is hindered by the energy spread [119]. Although the method can be extended to include the energy dependence [63], a precise characterization of the Twiss parameters and therefore the possibility to diagnose a mismatch caused by alignment errors is limited.

In addition to the roll error, also **longitudinal positioning errors** of the quadrupoles cause a Twiss parameter mismatch. The error is limited by the mismatch of the x -component due to the significantly larger beam size of this component in the quadrupoles and the resulting larger effects of quadrupole errors on the beam. In order to fulfill the mismatch criterion, the longitudinal positioning accuracy has to fulfill $\sigma_{\Delta_s} < 34 \mu\text{m}$ (see Fig. 7.9 (left)).

Assuming a perfect internal alignment results in a longitudinal positioning requirement of the full triplet of $\sigma_{\Delta s, \text{full}} < 820 \mu\text{m}$. Setting the internal alignment precision to $\sigma_{\Delta s, \text{int}} = 10 \mu\text{m}$ reduces the alignment tolerance of the full triplet to $\sigma_{\Delta s, \text{full}} < 580 \mu\text{m}$. Assuming micrometer precision for linear stages, these requirements can well be met with already existing equipment.

The last error source contributing to a Twiss parameter mismatch is the **focusing strength error** of quadrupoles. The relative focusing strength error limit is given by $\sigma_{kl}/(kl) < 7 \cdot 10^{-4}$ (see Fig. 7.9 (right)) with k being the quadrupole strength and l the length. Translating this to a gradient error and the related error of the aperture again leads to a micrometer precision but this time regarding the radial position of the quadrupole magnet segments. As in the case of longitudinal positioning errors, the focusing strength error is limited by the x -component due to the larger beam size. Again this requirement is about one order of magnitude stricter than that required for a linear accelerator based system like LCLS [40, 116]. Although high precision measurement and tuning concepts for PMQs have already been developed [117], these still have to be further improved in order to reach the precision required for a first lab-scale FEL demonstration experiment.

Besides the electron optics related errors, the source stability in terms of the energy jitter has to be improved by two orders of magnitude when compared to state-of-the-art experiments [124] since energy deviations are equivalent to focusing strength errors of the quadrupoles. This is a major challenge on the path to a first laser-plasma based free-electron laser and cannot be mitigated by adapting the optics if chromatic focus matching is used because in this case the energy dependence of the focusing system is a desired property.

Error source	scope	tolerance	dimension
Horizontal offset	quad., pre-align.: none	5	μm
	triplet, pre-align.: ideal	32	μm
	triplet, pre-align.: $1 \mu\text{m}$	22	μm
Vertical offset	quad., pre-align.: none	2	μm
	triplet, pre-align.: ideal	3	μm
	triplet, pre-align.: $1 \mu\text{m}$	3	μm
Roll error	quad., pre-align.: none	1	mrad
	triplet, pre-align.: ideal	280	mrad
	triplet, pre-align.: 0.5 mrad	250	mrad
Longitudinal offset	quad., pre-align.: none	34	μm
	triplet, pre-align.: ideal	820	μm
	triplet, pre-align.: $20 \mu\text{m}$	580	μm
Relative strength error	quad.	0.07	%

Table 7.3: Tolerance requirements for the individual quadrupoles and the full triplet (see scope column) based on the FEL tolerances (see Table 4.1).

7.5 Conclusion

For the planned FEL demonstration experiment not only the characteristics of the accelerator and the resulting optimization concept plays an important role, but also the layout of the electron optics has to be considered carefully.

Various effects make designing a suited optics configuration a challenge. Closely related to the decompression concept minimizing the energy spread induced performance loss is the chromatic emittance growth caused by the optics. This effect cannot be avoided since an achromatic focusing with quadrupole lenses is not possible [127]. In combination with the decompression concept, however, it is possible to exploit this effect. To lowest order, the chromatic focusing of the quadrupoles causes a linear dependence of the focus position on the energy. This moving focus can be synchronized with the photon pulse slipping through the electron bunch maximizing the current density in the interaction region. By employing this concept, chromatic effects of the focusing system can be mitigated.

Besides the chromatic properties also the precision requirements for the focusing system play an important role (see Table 7.3). An as simple and compact as possible focusing system consisting of a permanent magnet quadrupole triplet has been designed. It fulfills all basic requirements derived from the demonstration FEL concept. The required alignment precision for this setup is up to one order of magnitude stricter than at linear accelerator based sources like LCLS. The strict requirements are in many cases a direct

result of the required magnification of the optics system and are therefore typical for laser-plasma accelerator based sources.

A major challenge is given by the requirement on the precision of the focusing strength. Here the extremely high gradients and small apertures of the PMQs result in a major challenge.

An interesting characteristic of the required positioning tolerances is that the requirements on the alignment of the quadrupoles with respect to each other are significantly stricter than those found for the alignment of the whole triplet with respect to the undulator. Here the compactness of the setup can be exploited by pre-aligning the whole triplet with additional diagnostics or even at other facilities and benefitting from the less strict requirements when it comes to the positioning of the triplet within the beamline.

A crucial criterion for the satisfiability of the – basically feasible – precision requirements are reliable and precise beam diagnostics. These are hindered by the extreme beam parameters like the energy spread and source fluctuations typical for laser-wakefield accelerator based systems.

Besides the tolerances of the optics, also the precision requirements on the accelerator which are linked to the optics design are very challenging. Here the magnification of the optical system amplifies any offsets, resulting in very strict limits for the position jitter of the accelerator. Since the position jitter is dominantly determined by the pointing of the laser driving the acceleration, with typical focus position fluctuations on the order of the waist size, this limit is a critical issue for all laser-plasma accelerator based FELs. Furthermore, the energy jitter has to be reduced by two orders of magnitude when compared to the state-of-the-art, down to an unprecedented level for this type of accelerator, clearly pushing the limits of this accelerator technology.

8 Start-to-End Simulation

In the previous chapters the individual components needed for a first laser-plasma accelerator based FEL demonstration experiment and their design concepts have been discussed individually. To test the applicability of the individual concepts and evaluate the interplay of the different effects, a complete start-to-end simulation of the setup is required which is presented in this chapter.

The layout sketch of the simulated setup is shown in Fig. 8.1. The simulations do not include the laser-wakefield acceleration itself since particle-in-cell simulations used to model laser-wakefield acceleration and real life experiments show significant deviations in the bunch charge – one of the most critical parameters regarding the FEL as well as all degrading effects – up to now [128]. The electron parameters used are the same as in the discussion of the general FEL concept (see Table 3.3). For the simulation of the electron optics and the chicane ELEGANT [129] has been used. Although ELEGANT only supports a 1D CSR model, it allows to combine it with a 1D space-charge model, resulting in a good approximation of the most important effects that have been identified in the previous chapters*. The electron distributions obtained with ELEGANT have been imported into GENESIS allowing to maintain all details of the phase space distribution built up during the beam transport. The setup parameters are shown in Table 8.1.

8.1 Beam Transport

The beam transport consisting off the focusing optics and the chicane is based on the concepts and optimizations discussed in Chaps. 6 and 7. The choice of a single focusing quadrupole triplet for the optics does not allow to use the ideal Twiss parameters required for minimizing the emittance growth in the chicane since this would require a beam waist within the chicane for most chicane configurations which is not compatible with the Twiss parameters and the corresponding tolerances required at the undulator entrance. The Twiss optimization for the chicane is also limited for more complex optics due to the chromaticity of the optics and can only be achieved for one energy.

*For a more precise simulation ELEGANT and CSRTRACK could be combined; however, the high particle number ($N > 10^5$) required for an import of the final phase space into the FEL simulation GENESIS leads to a drastic increase of the required computation time making any numerical optimization and parameter scan unfeasible.

name	value	dimension
drifts		
L_1 length	93.469	mm
L_2 length	16.934	mm
L_3 length	52.017	mm
L_4 length	25.000	mm
L_{12} length	50.000	mm
L_{23} length	355.000	mm
L_{34} length	230.000	mm
L_5 length	992.580	mm
quadrupoles		
Q_1 length	38	mm
Q_2 length	36	mm
Q_3 length	11	mm
all gradients	478.729	T/m
dipoles		
all lengths	75	mm
D_1 deflection angle	0.0162	rad
D_2 deflection angle	-0.0325	rad
D_3 deflection angle	0.0325	rad
D_4 deflection angle	-0.0162	rad
undulator		
length	2	m
mean undulator parameter	3.3	-
linear taper	5.3	%/m
period length	15	mm
horizontal wavenumber k_x	66.7	m^{-1}
vertical wavenumber k_y	424.2	m^{-1}

Table 8.1: Setup parameters used for the start-to-end simulation. All elements are consecutively numbered. Drifts in the chicane are identified by a double index. The electron parameters are identical with those shown in Table 3.3.

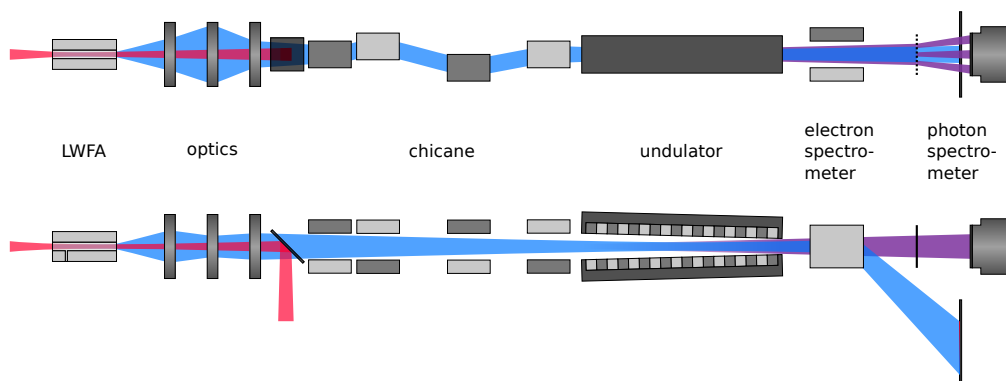


Figure 8.1: Sketch of the conceptual design of the setup shown from the top (top) and side (bottom). The electrons (blue) are produced and accelerated by a high-power infrared laser beam (red) which is focused into a hydrogen gas target. A quadrupole triplet is used to focus the electron beam. After the optics an asymmetric S-chicane decompresses the bunch reducing the slice energy spread in order to optimize the FEL performance. The undulator produces an intense VUV beam (purple) and is longitudinally tapered to compensate for the energy chirp introduced by the decompression. Finally electrons and photons are characterized by the corresponding spectrometers.

The position of the chicane has been chosen so that the drift length before the chicane is as short as possible, i.e. only limited by geometric constraints like the coil size of the dipole magnets. This allows to minimize space-charge effects, e.g. the build-up of a longitudinal energy chirp (see Sect. 5.2.2 and [38, 39]), which would otherwise directly degrade the FEL performance as well as increase the emittance growth [98]. Due to the placement of the chicane in the vicinity of the optics, the space-charge induced energy changes are an order of magnitude below the energy spread (see Fig. 8.2). Moving the chicane closer to the undulator, however, would increase the energy changes by a factor of four proportional to the drift between accelerator exit and chicane entrance. This would bring the energy deviations to a level on the order of the energy spread, resulting in significant changes of the decompression characteristics and a degradation of the resulting FEL performance.

In the previous chapter the optics layout has been designed so that the horizontal and vertical mismatch were minimized for the reference energy. The combination of the original optics with the chicane, however, leads to emittance changes and consequently also alterations of the Twiss parameters. This results in a non-negligible mismatch for the reference energy at the undulator entrance. The effect has to be taken into account for the quadrupole positioning. A comparison of the mismatch parameters as a function of the longitudinal, bunch internal coordinate for both optics layouts is shown in Fig. 8.3.

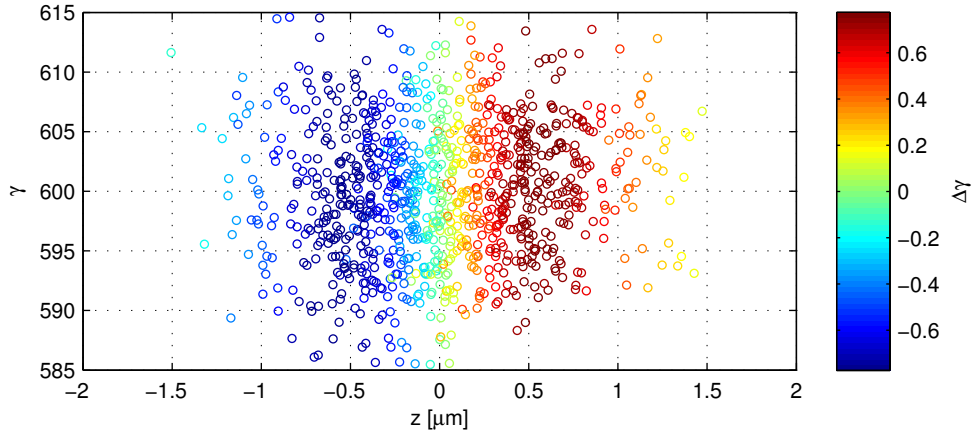


Figure 8.2: Longitudinal phase space at the chicane entrance. The color code indicates the energy changes with respect to the initial distribution at the accelerator exit caused by space-charge. The energy changes are an order of magnitude smaller than the energy spread. However, a placement of the chicane further downstream, close to the undulator entrance, would increase the changes by a factor of four, proportional to the change of the upstream drifts, resulting in an effect on the order of the energy spread. This would significantly alter the decompression characteristics and reduce the FEL performance.

The rise of the mismatch when moving from the center towards the head or tail of the bunch is a direct result of the chromatic focusing combined with the decompression. Due to the decompression in the chicane, the energy dependence of the Twiss parameters and therefore the mismatch is converted to a dependence on the longitudinal position.

The significant difference between the dependence of the horizontal and vertical mismatch on the longitudinal position is directly linked to the difference in the emittance growth of both components found for the original optics setup (see Sect. 7.4.2). The link is given by the orientations of the phase space ellipses of the different energies shown in Fig. 8.4. The chromatic focusing results in an energy dependence of the phase space ellipse orientation. Since each energy corresponds to a certain longitudinal position within the bunch after the decompression, the phase space ellipse orientation is directly linked to the longitudinal position. The orientation of the phase space ellipse defines the corresponding Twiss parameters and consequently the local mismatch. In terms of the emittance the combination of different ellipse orientations results in a larger populated area in the phase space corresponding to an emittance growth. Chromatic effects are therefore directly linked to the local mismatch as well as the emittance. The significant difference between horizontal and vertical plane shown in Fig. 8.3 is hence also found in Fig. 8.4 and the corresponding difference in the emittance growth.

The difference between the two planes is also noticeable when comparing the slice emit-

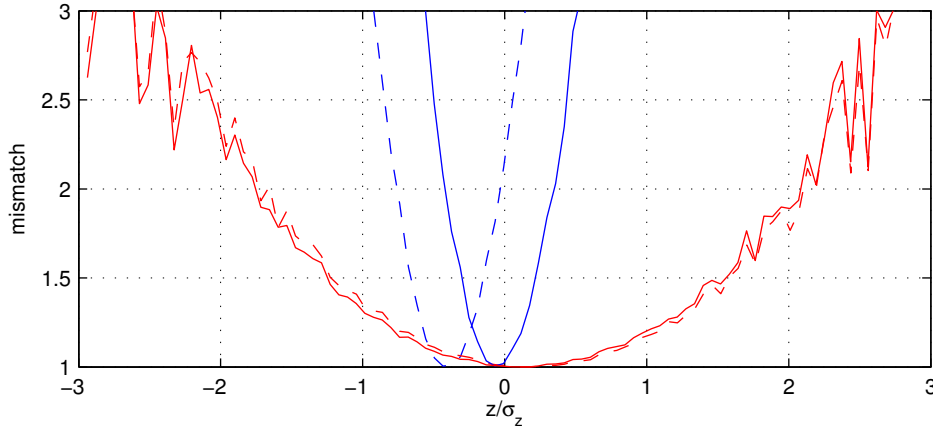


Figure 8.3: Mismatch parameter at the undulator entrance for x -component (blue) and y -component (red) as a function of the longitudinal position within the electron bunch. The dashed lines show the mismatch when using the initially designed optics (see Sect. 7.4.2) in combination with the chicane. Although the optics have originally been designed such that a minimum of the mismatch is reached for the reference energy, i.e. at the bunch center, the minimum of the mismatch curve of the x -component is shifted towards the bunch tail. This shift is caused by the emittance growth and the corresponding changes of the Twiss parameters in the chicane. The effect on the y -component is negligible. A correction is possible by adapting the quadrupole positions (solid lines).

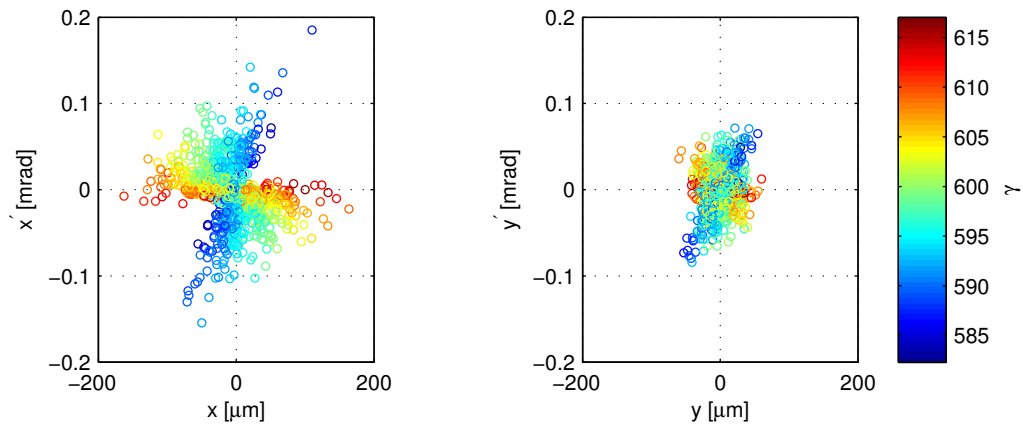


Figure 8.4: Transverse phase spaces of the x -component (left) and y -component (right) at the undulator entrance. The color code represents the particle energy. The different orientations of the phase space ellipses corresponding to the different energies resulting in the chromatic emittance growth are very pronounced for the x -component. This is also directly linked to the slice mismatch shown in Fig. 8.3.

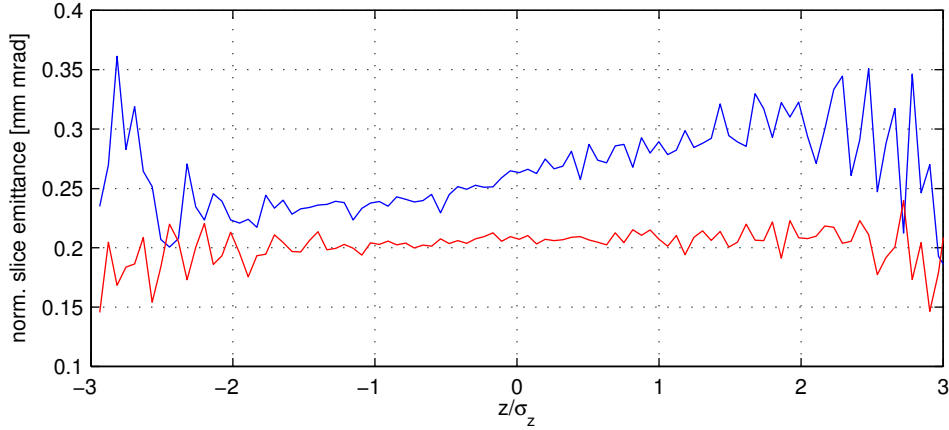


Figure 8.5: Normalized emittance of x -component (blue) and y -component (red) as a function of the longitudinal position within the electron bunch evaluated at the undulator entrance. The fluctuations at the bunch head and tail are caused by the low particle number in these regions and the resulting statistics. The emittance growth of the y -component is negligible as already indicated by the low mismatch along the bunch (see Fig. 8.3).

tances shown in Fig. 8.5. When it comes to the chromatic slice emittance growth the energy range to be taken into account is given by the slice energy spread which is only $\sigma_\eta = 0.25\%$ after the decompression. This reduction of the energy range and the corresponding phase space area results in the low, average slice emittance of the horizontal component of $\epsilon_{x,n,\text{slice}} = 0.26$ mm mrad, in contrast to the projected emittance of the whole bunch $\epsilon_{x,n} = 0.88$ mm mrad. The slice emittance growth of the vertical component is negligible, which is a direct result of the smaller differences between the phase space ellipse orientations above. The position dependence of the slice emittance within the bunch is caused by the different phase space ellipse orientations in the chicane and the resulting differences in the emittance growth (see Chap. 6).

The emittance has so far only been discussed in the context of chromatic effects, but it is also affected by coherent synchrotron radiation and space-charge in the chicane (see Chap. 5). The chicane layout has been chosen to be asymmetric, as suggested by the optimization concept discussed in Chap. 6, in order to minimize the emittance growth. Simulations without CSR and space-charge result in a pure chromatic emittance growth yielding $\epsilon_{n,x} = 0.74$ mm mrad. The inclusion of space-charge and CSR leads to a further emittance growth, resulting in the final horizontal emittance of $\epsilon_{n,x} = 0.88$ mm mrad. Compared to the chromatic effects the emittance growth within the chicane is minor and only contributes approximately 20% to the total emittance growth. This shows another advantage of the chosen layout: both mostly independent* sources of significant

*The different phase space ellipse orientations caused by the chromatic focusing have an effect on the

emittance growth (chromatic focusing and energy changes in the chicane) dominantly affect the same plane, whereas the emittance of the other plane is conserved. This leads to a minimum of the total emittance growth and therefore a maximum of the achievable current density in the undulator.

The final bunch geometry at the undulator entrance affected by chromatic focusing, CSR, as well as space-charge is shown in Fig. 8.6. The effect of the chromatic focusing and the decompression can clearly be seen. In the longitudinal direction the bunch is sorted by energies. The horizontal plane has a beam waist for energies slightly below the reference energy $\gamma_{\text{waist}} \approx 592$. Lower energies are already diverging, whereas higher energies are still converging. This directly represents the position dependent mismatch shown in Fig. 8.3. During the propagation through the undulator the beam waist will slip forward through the bunch and result in the chromatic focus matching discussed above (see Sect. 7.3). Consequently, the large mismatch values found at the bunch head and tail are no issue as long as the mismatch of the reference energy is minimized and the focus motion is within reasonable limits (see Fig. 7.5). In the vertical plane only a very small dependence of the beam size on the longitudinal position is found, as already indicated by the less pronounced position dependence of the mismatch. The reference energy reaches a waist at the undulator entrance with bunch head and tail being slightly larger. Due to the moderate mean energy, these slight beam size deviations allow for a nearly constant beam size within the undulator for all energies, i.e. all longitudinal slices of the bunch (see Sect. 7.3), independent of the divergence.

8.2 Undulator – FEL

The undulator is the same as in the discussion of the decompression concept (see Sect. 3.3). The final figure of merit for the FEL demonstration experiment is an output radiation power exceeding the spontaneous power by at least one order of magnitude. To achieve this goal using the decompression concept, the undulator has to be tapered in order to compensate for the energy chirp introduced by the chicane, and the current density has to be kept as high as possible.

As stated above, the optics design ensures a well suited bunch shape allowing for a reasonable chromatic focus matching and an overall minimized beam size along the undulator. Figure 8.7 shows the evolution of the beam size in both planes as a function of the bunch internal coordinate and the position within the undulator. The focus motion of the x -component resembles an approximately linear motion as desired, although the slope does not perfectly match the ideal curve. The energy dependence of the horizontal focus position is $ds_{\text{focus},x}/d\eta \approx 104$ m. This exceeds the analytical ideal focus motion

emittance growth of the different energy ranges in the chicane causing differences in the contributions to the final slice emittance but can be seen as independent regarding the projected emittance growth.

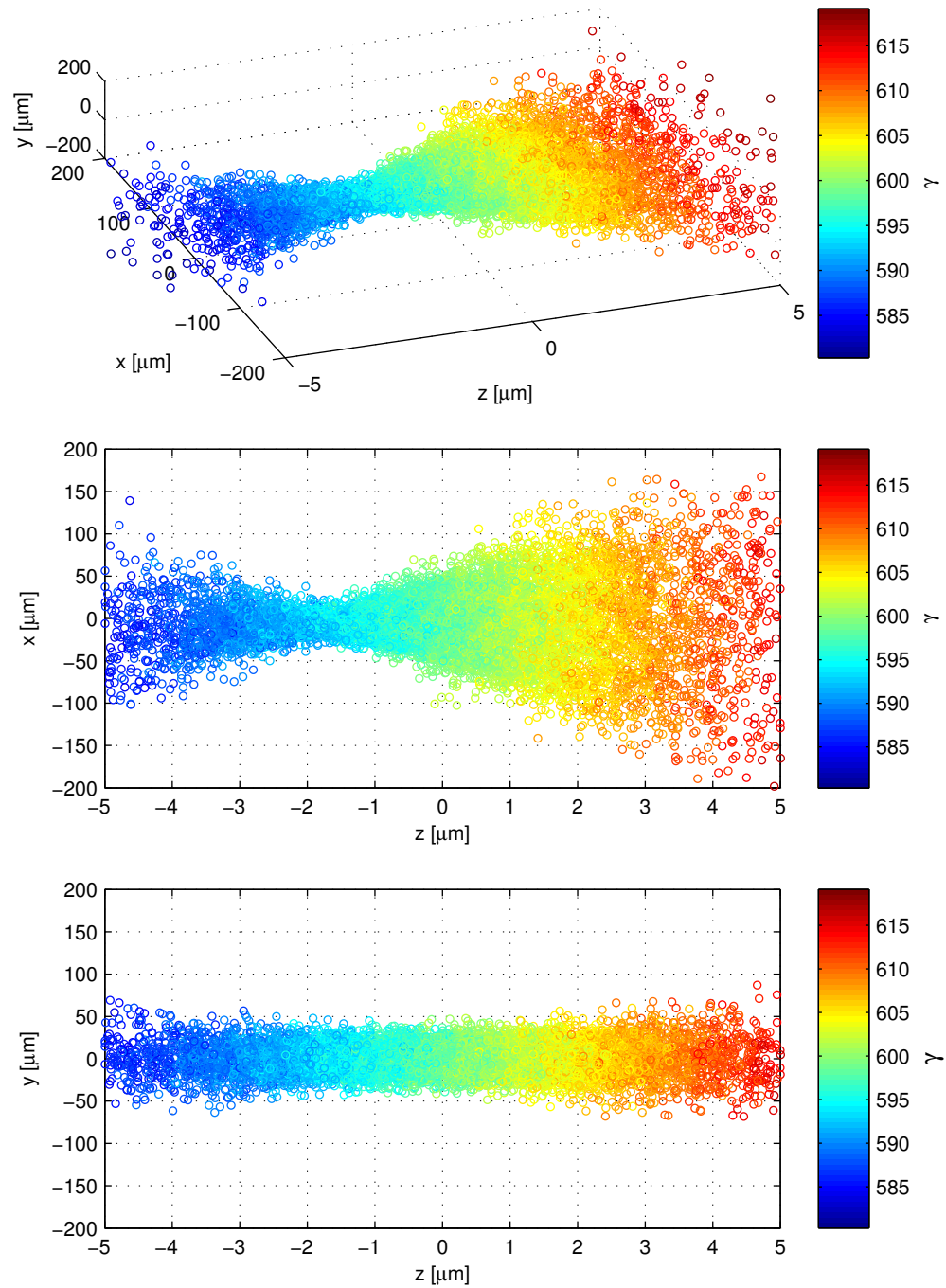


Figure 8.6: Electron distribution at the undulator entrance. The top view (center) shows the significant energy dependence of the beam size in the x -direction in contrast to the dependence of the y -component on the energy (bottom).

characterized by $ds_{\text{focus},x}/d\eta \approx 67$ m (see Eq. (7.49)) and the optimum according to GENESIS simulations at $ds_{\text{focus},x}/d\eta \approx 89$ m. Despite the deviation the reduction of the FEL performance is minor according to the GENESIS scan (see Fig. 7.5).

The evolution of the radiation power in the undulator normalized to the spontaneous emission within 100% bandwidth is shown in Fig. 8.8. A clear exponential growth along the undulator is achieved with a final, average amplification over the spontaneous emission of $P(s = 2 \text{ m})/P_{\text{spont.}} = 57$, fulfilling the design goal. The mean gain length is $L_g = 20$ cm. When compared to the FEL design concept discussed in Chap. 3 the amplification is reduced by a factor of about three with the chief cause being the slice emittance growth. According to Eq. (6.14) a power reduction by a factor of two can be expected due to the emittance growth itself. Since this equation was only based on the ideal FEL theory, the further degradations, e.g. caused by the increased sensitivity to energy spread due to the reduced current density, are not included and can explain the remaining fraction of the power loss. While the gain reduction is significant, it should be noted that this simulation takes all important degrading effects occurring during the beam transport into account, including chromatic emittance growth, the space-charge induced energy chirp, and emittance growth caused by the decompression. The decompression concept can therefore be seen as feasible despite the challenges caused by the usage of the extreme bunches produced by laser-wakefield accelerators.

On average an FEL pulse reaches a peak power of $P_{\text{peak}} = 1.1$ MW with an average rms pulse duration of $\sigma_t = 4.2$ fs. The spectral power peak is not located at the design wavelength of $\lambda_l = 135$ nm but is shifted towards longer wavelengths and is on average found at 147 nm (see Fig.8.9 (left)). This spectral shift is explained by the tapered undulator and the short bunch. Due to the short bunch, the radiation pulse is mainly built up by the leading edge of the electron bunch where the maximum microbunching is found. This region of the bunch amplifies radiation produced by trailing electrons which has a longer wavelength due to the lower electron energies at the tail of the bunch. This mechanism also explains the asymmetric pulse shape shown in Fig. 8.9 (right). The average bandwidth is $\sigma_\omega = 5 \cdot 10^{14}$ Hz which is larger than expected from the analytical model (Eq. (6.14)) $\sigma_{\omega,\text{analytical}} = 1.9 \cdot 10^{14}$ Hz. This difference is a result of the chirped electron bunch which results in a broadening of the emitted spectrum.

The coherence time of the FEL pulse (based on Eq. (2.48) using the parameters obtained with the simulations) is $t_{\text{co},3D} \approx 6.5$ fs. Combined with the short bunch duration of $t_{\text{bunch}} \approx 6.7$ fs this results in an average number of modes of $M = 1.0$. Evaluating the pulse energy distribution shown in Fig. 8.10 (see Eq. (2.50)) suggests a nearly exponential distribution, confirming the low number of modes. A fit of the gamma distribution yields $M = 1.2$ in good agreement with the estimate above. This characteristic feature of the FEL could be used as one of the indicators for a working FEL process in a first FEL demonstration experiment.

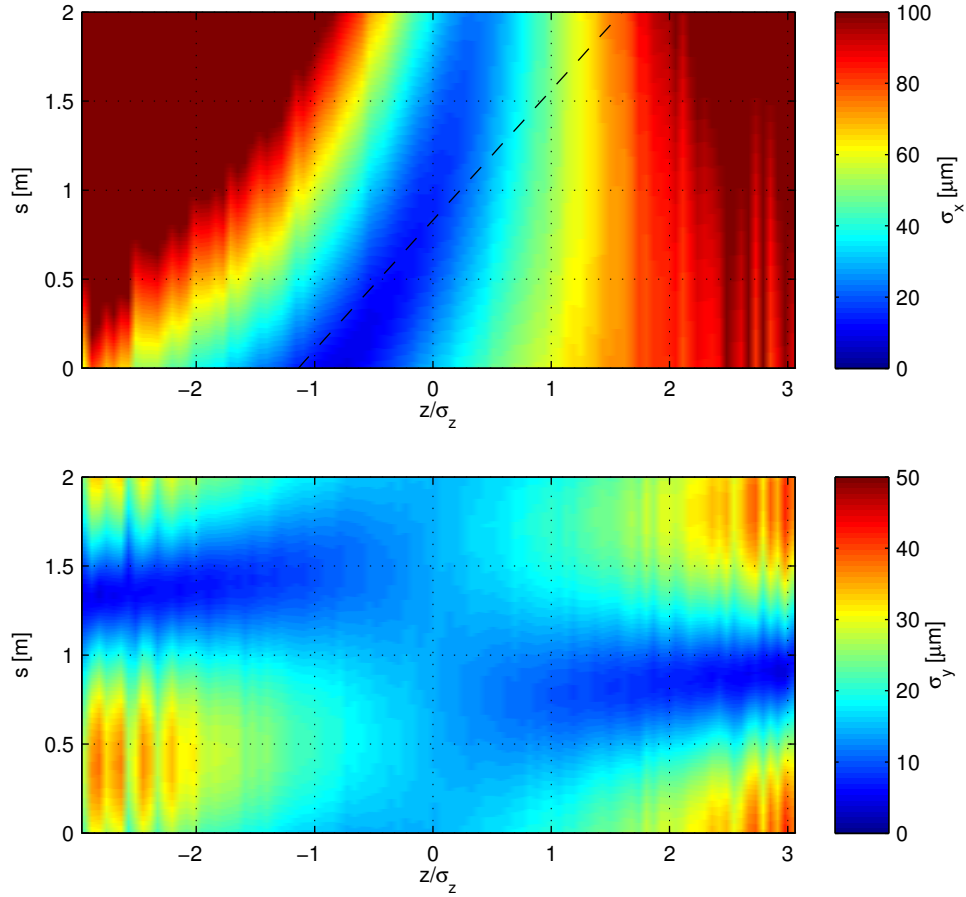


Figure 8.7: Beam size in x -direction (top) and y -direction (bottom) as a function of the longitudinal position within the bunch and the longitudinal position along the undulator. Note the different scales. For the x -component an approximately linear focus motion is achieved as desired for the chromatic focus matching (see Sect. 7.3). The ideal focus position of the horizontal component according to Eq. (7.49) is indicated by the dashed black line. The vertical beam size is well matched to the focusing of the undulator over the central section of the bunch, allowing for a small, constant beam size along the undulator.

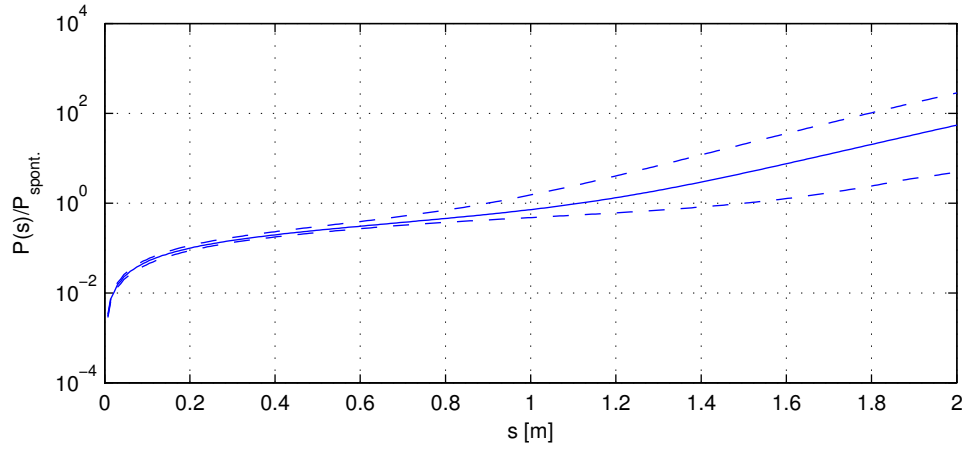


Figure 8.8: Normalized average pulse power as a function of the longitudinal position within the undulator. The solid line is averaged over 100 independent GENESIS runs. The dashed lines indicate the best and worst case. All runs result in an exponential power growth with an average gain length of $L_g \approx 20$ cm.

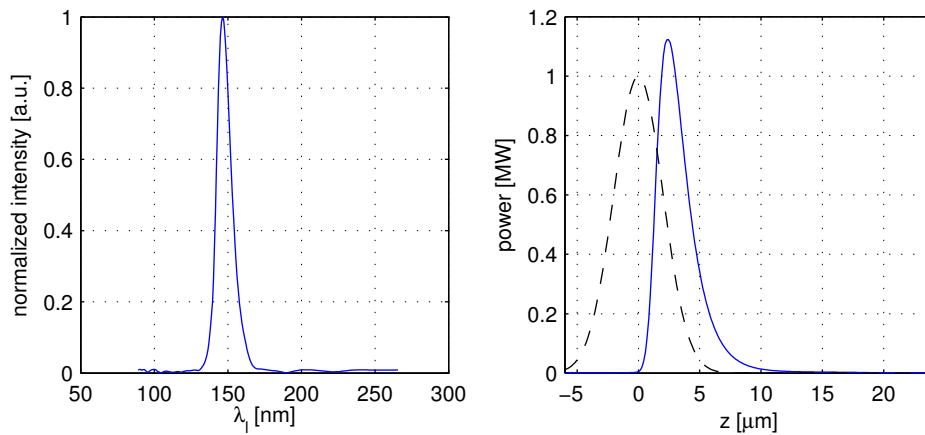


Figure 8.9: Spectrum of an FEL pulse (left) and time structure (right) at the end of the undulator. The pulse has a bandwidth of $\sigma_\omega = 4.5 \cdot 10^{14}$ Hz and is peaked at 146 nm in contrast to the design wavelength of $\lambda_l = 135$ nm. This shift of the wavelength can be explained by the taper. The time structure shows a significant shift of the radiation pulse (solid blue) with respect to the electron bunch (dashed black) which is only shown for reference purposes and is not to scale. The pulse duration is $\sigma_t = 4.2$ fs.

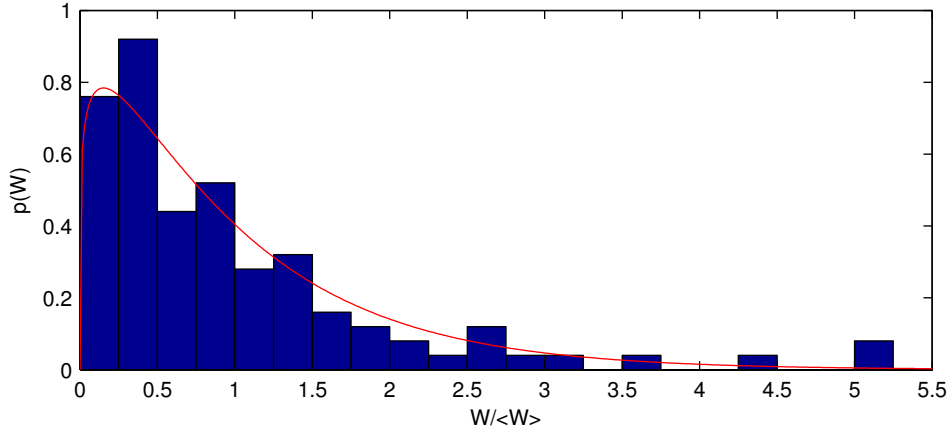


Figure 8.10: Pulse energy distribution as a function of the normalized pulse energy using the individual pulse energy W and the average over 100 independent runs $\langle W \rangle$ (blue bars). The red curve represents the fit of the gamma distribution (see Eq. (2.50)) to the simulation data. The obtained number of modes is $M = 1.2$.

A further point, besides the general setup performance, that can only be addressed in start-to-end simulations is the scalability of the decompression concept towards higher/lower bunch charges and energy spreads. Combinations of higher charges and energy spreads are assumed to be easier accessible in upcoming experiments [107]. For a fixed ratio of energy spread to charge the FEL performance in an ideal decompression setup would remain unaltered. Given a fixed chicane strength R_{56} , an increase of the initial energy spread by a factor n results in a scaling of the final bunch length by the same factor. If the initial bunch charge is also scaled by the same factor the final slice energy spread and peak current remain unchanged, resulting in the same FEL performance. For slippage limited cases the increasing bunch length could even be beneficial (see Sect. 2.4.6). For any real setup this scaling, however, results in an increase of CSR and space-charge effects due to the increased peak current in the chicane, leading to an increase of the projected and slice emittance (see Chap. 5). The interplay of the different effects and the resulting FEL performance can only be evaluated in the start-to-end simulation. Figure 8.11 shows the result of a charge and energy spread scan for a fixed ratio of initial energy spread to bunch charge σ_η/Q . The reference case is given by $\sigma_\eta = 1\%$ and $Q = 15$ pC, and the setup has been the same for all runs. Lower charge and energy spread combinations are favorable down to approximately $Q = 10$ pC. Here the drop of CSR and space-charge effects due to the lower charge can be exploited. Below this range the final bunch length gets so short that the FEL performance gets degraded due to slippage effects. Increasing charge and energy spread results in a drop of the FEL performance due to the rise of the slice emittance as shown in Fig. 8.12. Due to the emittance changes, also the Twiss parameters at the undulator entrance get modified depending on the initial charge. This

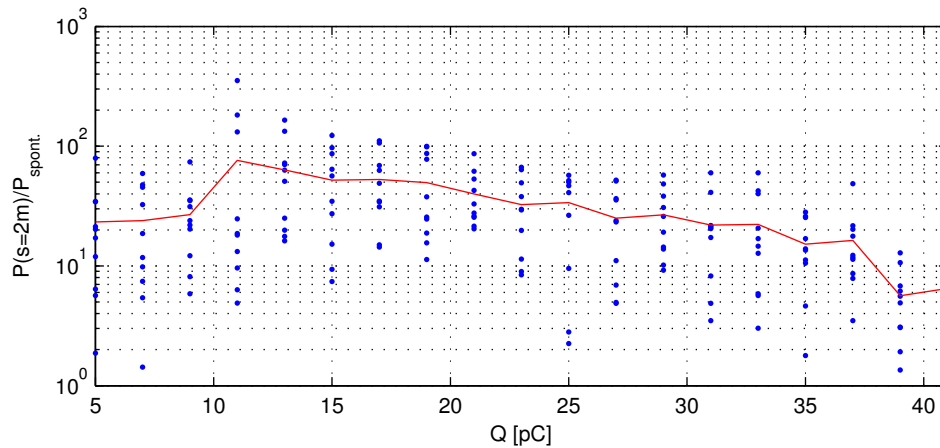


Figure 8.11: Normalized power as a function of the initial bunch charge for a fixed ratio of bunch charge and energy spread σ_η/Q . The reference case is given by $\sigma_\eta = 1\%$ and $Q = 15$ pC. Individual runs are represented by blue dots, the red line indicates the average for each case. All cases are equivalent as long as degrading effects are neglected, but CSR and space-charge during the beam transport limit the acceptable charge and energy spread range (see Fig. 8.12).

results in a mismatch at the undulator entrance further reducing the FEL performance. In summary, the scan shows that the decompression concept is applicable for the charge range $Q = 5\text{--}35$ pC for a fixed ratio of charge to energy spread. Consequently, the initial energy spread can be doubled bringing the demonstration concept closer to the performance of state-of-the-art laser-wakefield accelerators.

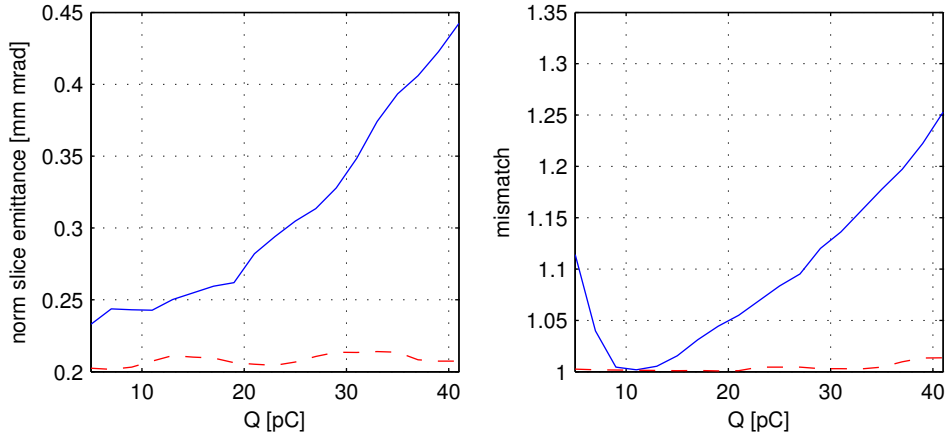


Figure 8.12: Normalized emittance (left) and mismatch (right) of the central slice at the undulator entrance as a function of the initial bunch charge for a fixed ratio of bunch charge and energy spread σ_η/Q . The x -component (solid blue) is the limiting factor when compared to the y -component (dashed red) in both cases.

8.3 Conclusion

The combination of all individual concepts and optimizations discussed in the previous chapters by means of a start-to-end simulation allowed to assess the interplay of the various components and effects which was impossible in the individual discussions. The feasibility of a laser-plasma accelerator driven demonstration experiment has been successfully demonstrated.

The start-to-end simulation shows that the electron optics have to be readjusted when compared to the initial optics design in order to ensure a minimum mismatch at the undulator entrance. Here the emittance growth and resulting Twiss parameter changes caused by the chicane have to be taken into account. The adjustment has been shown to be possible by a simple repositioning of the quadrupole lenses which makes this a reasonable concept of operation for a first demonstration experiment. A major challenge in this context is given by the requirement of precise phase space information to be able to identify and correct an occurring mismatch. These setup corrections are, however, not applicable to shot-to-shot fluctuations, resulting in the requirement of a stable source and precise charge measurements.

Due to the decompression, the chromatic slice emittance growth could be reduced from $\Delta\epsilon_x/\epsilon_x = 260\%$ down to $\Delta\epsilon_x/\epsilon_x \approx 35\%$. For the vertical components the slice emittance growth even dropped from $\Delta\epsilon_y/\epsilon_y = 28\%$ to $\Delta\epsilon_y/\epsilon_y = 1\%$. The decompression translates the remainder of the chromatic effect into a mismatch depending on the internal, longitudinal position within the bunch. For the x -component this position dependent

mismatch finally results in the desired chromatic focus matching within the undulator. The vertical beam size is only weakly energy dependent and allows for a nearly matched beamsize for all energies.

The chicane was positioned as close to the focusing system as possible to minimize the space-charge induced energy chirp by an early decompression. Although the simple triplet layout and the chromatic effects did not allow for an optimization of the Twiss parameters in the asymmetric S-chicane, the contribution of the chicane to the total emittance growth was only 20% and therefore regarded as acceptable.

The moderate emittance growth and the chromatic focus matching allowed to reach a ratio of FEL power to spontaneous emission of $P(s = 2 \text{ m})/P_{\text{spont.}} = 57 > 10$, clearly fulfilling the design goal even with the inclusion of all important degrading effects. This shows that the decompression concept is indeed feasible.

The FEL simulations showed that ultra-short pulses $\sigma_t = 4.2 \text{ fs}$ with a peak power of $P_{\text{peak}} = 1.1 \text{ MW}$ are already possible with a first demonstration experiment. The broad bandwidth $\sigma_\omega = 5 \cdot 10^{14} \text{ Hz}$ even allows for a compression down to 1 fs when a Fourier limited pulse is assumed.

The start-to-end simulation allowed to assess the scalability of the decompression concept to higher and lower charges for a fixed ratio of energy spread to charge. Towards low charges the decompression concept is ultimately limited by slippage effects and the ultra-short electron bunch. Higher charges, which are assumed to be easier to realize in upcoming experiments, result in an increase of the emittance growth due to CSR and space-charge. This makes the decompression concept studied in this thesis applicable for the charge range $Q = 5\text{--}35 \text{ pC}$ and the corresponding initial energy spreads $\sigma_\eta = 0.33\%\text{--}2.33\%$.

On the whole, the start-to-end simulation has shown that the decompression concept is not only feasible from an FEL physics point of view but also when the full beam transport is included. Moreover, it is capable of delivering ultra-short high-power UV pulses which could already be used for first applications.

9 Conclusion and Outlook

In the previous chapters the different challenges of a laser-plasma accelerator driven FEL demonstration experiment have been identified and addressed, and new setup optimization concepts have been studied.

The first and probably most prominent issue of a laser-plasma accelerator driven system is the gain reduction due to the broad energy spread typical for bunches produced by state-of-the-art laser-wakefield accelerators. For the envisioned parameter set the FEL performance can be increased by multiple orders of magnitude using the decompression concept. Here the local energy spread is reduced at the cost of a reduced peak current via sorting the bunch by energies using a magnetic chicane. Balancing both effects allows to boost the FEL performance. In addition to the reduction of energy spread this concept also minimizes the impact of slippage issues caused by the rather long radiation wavelength (~ 100 nm) which is nearly on the order of the initial bunch length of only 500 nm. The requirements on the taper of the undulator, needed to compensate the energy chirp induced by the decompression, are challenging but feasible for the here considered 2-meter-long undulator. For longer undulators the required taper cannot be sustained.

The alternative optimization concept using transverse dispersion of the electrons, also lowering the local energy spread, has been ruled out for two reasons: First of all, this scheme does not reduce the impact of slippage effects. Second, the transverse field gradients of the undulator, needed to compensate the transverse energy-position correlations at the ideal dispersion range, are not feasible for conventional undulator designs. Advantages of the setup, given a suited parameter range, are, however, a higher saturation power and no sensitivity regarding energy jitter*.

For the chosen concept the general precision requirements on the setup and especially the undulator have been studied. They are of high importance for a first demonstration experiment since even in the design case it will operate close to the detection limit. In general the found requirements are comparable to, or less strict than, those of large scale systems like the TTF-FEL or LCLS. The strong diffraction actually limiting the FEL performance even becomes an advantage when it comes to the undulator errors which cause a beam wander. The requirements on the undulator construction ranging from random magnet errors to systematic errors due to girder deformation are all within reach

*This only refers to the FEL process itself and not the inevitable performance degradation due to the chromaticity of the beam transport.

of state-of-the-art cryogenic undulator design. A cryogenic undulator adhering to the design criteria of the decompression concept and the tolerance study is currently under construction and will be commissioned in 2015. The results of field measurements are still pending, but first tests of a prototype are promising [130].

Besides the basic concept and its tolerances, the actual decompression mechanism has been studied and optimized. The limiting factor of the decompression is the induced emittance growth that can spoil the beam quality and make it unusable for an FEL.

In the demonstration scenario two effects causing energy changes in the chicane and therefore leading to emittance growth have to be considered: coherent synchrotron radiation and space-charge. The impact of space-charge is owed to the moderate energies and the ultra-short bunch length. Due to the build-up of the space-charge induced energy modulation, the typical optimization concept used at linear accelerator based facilities of using long setups with weak magnets becomes unusable and a compromise is needed. The resulting setups have a chicane length on the order of one meter and rely on short and strong magnets. A fully optimized setup, i.e. an asymmetric S-chicane, allows for an emittance growth of less than 10% which is regarded as acceptable. Care has to be taken when extending the concept to higher bunch charges since this will lead to an inevitable rise of the emittance growth that cannot be mitigated by adapting the chicane layout and will ultimately prevent the FEL process at all.

Even more care has to be taken if the decompression setup is not built as a fully in-vacuum system but uses a narrow beam tube. In this case also resistive and geometric wall wakefields have to be taken into account. Their effects can even exceed those of synchrotron radiation and space-charge. Usually tapered sections are used to minimize effects of beam tube transitions on the bunch; however, since the wall wakefield of a tapered transition depends on the derivative of the beam profile, the effect of short bunches becomes even more intense. Depending on the beamline layout this should be considered with great care and the use of beam tubes should be avoided.

A chicane consisting of 7.25-cm-long magnets providing a maximum field of about 0.6 T is being commissioned and will be used for first phase space manipulation and characterization tests. It provides a 1-cm-gap and can be used as an in-vacuum device but could also be operated with a reasonably sized beam tube if necessary and if the geometric and resistive wall wakefields can be kept at bay.

The last missing component of the big picture, the electron optics, have also been addressed. Besides their general need for the control of the beam size, they are closely connected to two points discussed earlier, the energy spread and the setup tolerances.

Since the focusing strength of the quadrupoles is energy dependent, the broad energy spread results in a chromatic emittance growth. If no energy-position correlation exists

within the bunch, this effects can spoil the FEL performance drastically. In the decompression concept, however, this effect can even be exploited by chromatic focus matching. The electron optics can be designed such that the chromatic focus slips through the bunch at the same rate as the light pulse, resulting in a continuous maximization of the current density in the interaction region.

In addition to the energy spread related optimization, beam alignment tolerances have to be considered for the electron optics design. The small source size of the laser-wakefield accelerator requires a beam magnification of an order of magnitude in order to ensure a minimum average beam size during the propagation through the undulator. This high magnification factor also amplifies offset errors caused by either the optics or the source itself, resulting in tight alignment tolerances of the optics and the source. The absolute tolerances are further tightened due to the high gradients and small apertures. The resulting requirements are challenging in terms of the optics and beam diagnostics as well as the source stability but are feasible in terms of the available positioning precision. Similar optics have already been successfully used in various experiments [13,63,131] and precise characterization methods exist [117]; however, a demonstration of the required measurement and alignment precision is still pending.

The requirements on the source stability regarding position and energy jitter are the major points to be addressed in the future development. Here improvements of about one order of magnitude are required to ensure a reliable FEL demonstration.

In a nutshell, the current status of a first laser-plasma accelerator driven FEL demonstration experiment based on this thesis is:

- The **decompression concept** for the improvement of the FEL performance balancing energy spread, bunch length, and peak current, in the case of a broad energy spread and slippage limited bunches, has been characterized and optimized. It can be adapted to any set of initial conditions.
- An optimized **chicane layout** for bunch decompression reaching the design goal of the decompression concept and taking the characteristics of laser-plasma accelerator based bunches into account has been designed. The setup is a compromise of minimizing CSR as well as space-charge effects and the resulting setup dimensions are in the spirit of a compact, lab-scale system.
- **Chromatic focus matching** mitigating the chromatic effects of a quadrupole based focusing system has been proposed. This concept can be used at any setup relying on the decompression concept.
- The **setup tolerances** have been determined and assessed. They are feasible in terms of the undulator design but challenging regarding the optics alignment and the source stability.

- The combination of all assumed **electron beam** parameters has still to be demonstrated and further improvements of the source stability are required.
- The **electron optics** characterization, fiducialization, and alignment has to be enhanced.

This work lays down the path to be followed for a first laser-plasma accelerator based lab-scale free-electron laser demonstration experiment. Still several challenges have to be met, but a first fifth-generation light source is within grasp.

Bibliography

- [1] F. R. Elder, A. M. Gurewitsch, R. V. Langmuir, and H. C. Pollock. Radiation from Electrons in a Synchrotron. *Phys. Rev.*, 71:829, 1947.
- [2] W. Ackermann, G. Asova, V. Ayvazyan, A. Azima, N. Baboi, et al. Operation of a free-electron laser from the extreme ultraviolet to the water window. *Nature Photonics*, 1:336, 2007.
- [3] E. Allaria, R. Appio, L. Badano, W. A. Barletta, S. Bassanese, et al. Highly coherent and stable pulses from the FERMI seeded free-electron laser in the extreme ultraviolet. *Nature Photonics*, 6:699, 2012.
- [4] P. Emma, R. Akre, J. Arthur, R. Bionta, C. Bostedt, et al. First lasing and operation of angstrom-wavelength free-electron laser. *Nature Photonics*, 4:641, 2010.
- [5] T. Ishikawa, H. Aoyagi, T. Asaka, Y. Asano, N. Azumi, et al. A compact X-ray free-electron laser emitting in the sub-angstrom region. *Nature Photonics*, 6:540, 2012.
- [6] M. Altarelli, R. Brinkmann, M. Chergui, W. Decking, B. Dobson, et al. XFEL: The European X-Ray Free-Electron Laser : Technical design report. Technical report, Deutsches Elektronen-Synchrotron (DESY), Hamburg, 2006.
- [7] H. H. Braun, R. Ganter, B. Patterson, R. Abela, A. Adelman, et al. SwissFEL-Conceptual design report. Technical report, 2010.
- [8] T. Tajima and J. M. Dawson. Laser electron accelerator. *Phys. Rev. Lett.*, 43(4):267–270, 1979.
- [9] J. Faure, Y. Glinec, A. Pukhov, S. Kiselev, S. Gordienko, et al. A laser–plasma accelerator producing monoenergetic electron beams. *Nature*, 431:541, 2004.
- [10] C. G. R. Geddes, C. Toth, J. van Tilborg, E. Esarey, C. B. Schroeder, et al. High-quality electron beams from a laser wakefield accelerator using plasma-channel guiding. *Nature*, 431:538, 2004.
- [11] S. P. D. Mangles, C. D. Murphy, Z. Najmudin, A. G. R. Thomas, J. L. Collier, et al. Monoenergetic beams of relativistic electrons from intense laser–plasma interactions. *Nature*, 431:535, 2004.

- [12] F. Grüner, S. Becker, U Schramm, T Eichner, M. Fuchs, et al. Design considerations for table-top, laser-based VUV and X-ray free electron lasers. *Appl. Phys. B*, 86:431, 2007.
- [13] M. Fuchs, R. Weingartner, A. Popp, Zs. Major, S. Becker, et al. Laser-driven soft-X-ray undulator source. *Nature Phys.*, 5:826, 2009.
- [14] A. R. Maier. *Generation and Characterization of Few-Fs X-Ray Pulses*. PhD thesis, University of Hamburg, 2013.
- [15] A. R. Maier. Design Considerations for a First Table-Top SASE FEL Proof-of-Concept Experiment. Master's thesis, Ludwig-Maximilians-Universität, 2009.
- [16] T. Seggebrock. Concepts for a laser-driven fel demonstration by tailored electron bunches. Master's thesis, Ludwig-Maximilians-Universität, 2010.
- [17] A. R. Maier, A. Meseck, S. Reiche, C. B. Schroeder, T. Seggebrock, et al. Demonstration Scheme for a Laser-Plasma-Driven Free-Electron Laser. *Phys. Rev. X*, 2(3):031019, 2012.
- [18] Z. Huang and K.-J. Kim. Review of x-ray free-electron laser theory. *Phys. Rev. ST Accel. Beams*, 10:034801, 2007.
- [19] P. Schmüser, M. Dohlus, and J. Rossbach. *Ultraviolet and Soft X-Ray Free-Electron Lasers*, volume 229 of *Springer Tracts in Modern Physics*. Springer, 2008.
- [20] S. Reiche. *Numerical studies for a single pass high gain free-electron laser*. PhD thesis, University of Hamburg, 1999.
- [21] K. Wille. *Physik der Teilchenbeschleuniger und Synchrotronstrahlungsquellen*. B. G. Teubner, 1996.
- [22] E. L. Saldin, E. A. Schneidmiller, and M. V. Yurkov. *The Physics of Free Electron Lasers*. Springer, Berlin, 2000.
- [23] J. A. Clarke. *The Science and Technology of Undulators and Wigglers*, volume 4 of *Oxford Series on Synchrotron Radiation*. Oxford University Press, 2004.
- [24] A. Bacci, C. Maroli, V. Petrillo, A. R. Rossi, L. Serafini, et al. Compact X-ray free-electron laser based on an optical undulator. *Nucl. Instrum. Methods Phys. Res. Sect. A*, 587:388, 2008.
- [25] R. Bonifacio, N. Piovela, M. M. Cola, and L. Volpe. Experimental requirements for X-ray compact free electron lasers with a laser wiggler. *Nucl. Instrum. Methods Phys. Res. Sect. A*, 577:745, 2007.
- [26] E. T. Scharlemann. Wiggle plane focusing in linear wigglers. *J. Appl. Phys.*, 58:2154, 1985.

-
- [27] P. Elleaume, J. Chavanne, and B. Faatz. Design considerations for a 1Å SASE undulator. *Nucl. Instrum. Methods Phys. Res. Sect. A*, 455:503, 2000.
- [28] J. Mun, Y. U. Jeong, N. A. Vinokurov, K. Lee, K.-H. Jang, et al. Variable-period permanent-magnet helical undulator. *Phys. Rev. ST Accel. Beams*, 17(8):080701, 2014.
- [29] K. J. Kim. Angular distribution of undulator power for an arbitrary deflection parameter K. *Nucl. Instrum. Methods Phys. Res. Sect. A*, 246:67–70, 1986.
- [30] C. Penman and B W J McNeil. Simulation of input electron noise in the free-electron laser. *Opt. Commun.*, 90:82–84, 1992.
- [31] R. Bonifacio, C. Pellegrini, and L. M. Narducci. Collective instabilities and high-gain regime in a free electron laser. *Opt. Commun.*, 50:373, 1984.
- [32] R. Bonifacio, L. De Salvo, P. Pierini, N. Piovella, and C. Pellegrini. Spectrum, Temporal structure, and fluctuations in a High-Gain Free-Electron Laser Starting from Noise. *Phys. Rev. Lett.*, 73:70, 1994.
- [33] E. L. Saldin, E. A. Schneidmiller, and M. V. Yurkov. Statistical properties of radiation from VUV and X-ray free electron laser. *Opt. Commun.*, 148:383, 1998.
- [34] R. Bonifacio, C. Maroli, and N. Piovella. Slippage and superradiance in the high-gain FEL: Linear theory. *Opt. Commun.*, 68:369, 1988.
- [35] S. Bajlekov. *Towards a Free-Electron Laser Driven by Electrons from a Laser-Wakefield Accelerator: Simulations and Bunch Diagnostics*. PhD thesis, University of Oxford, 2011.
- [36] S. Reiche. GENESIS 1.3: a fully 3D time-dependent FEL simulation code. *Nucl. Instrum. Methods Phys. Res. Sect. A*, 429:243, 1999.
- [37] M. Xie. Exact and variational solutions of 3D eigenmodes in high gain FELs. *Nucl. Instrum. Methods Phys. Res. Sect. A*, 445:59–66, 2000.
- [38] F. Grüner, C. B. Schroeder, A. R. Maier, S. Becker, and J. M. Mikhailova. Space-charge effects in ultrahigh current electron bunches generated by laser-plasma accelerators. *Phys. Rev. ST Accel. Beams*, 12:020701, 2009.
- [39] G. Geloni, E. L. Saldin, E. A. Schneidmiller, and M. V. Yurkov. Longitudinal wake field for an electron beam accelerated through an ultrahigh field gradient. *Nucl. Instrum. Methods Phys. Res. Sect. A*, 578:34, 2007.
- [40] J. Arthur et al. Linac Coherent Light Source (LCLS) Conceptual Design Report. Technical report, Stanford Linear Accelerator Center (SLAC), 2002.

- [41] M. Pedrozzi. SwissFEL injector conceptual design report. Accelerator test facility for SwissFEL. Technical report, Paul Scherrer Institut, 2010.
- [42] E. Esarey, C. B. Schroeder, and W. P. Leemans. Physics of laser-driven plasma-based electron accelerators. *Rev. Mod. Phys.*, 81(3):1229–1285, 2009.
- [43] D. P. Umstadter, J. K. Kim, and E. Dodd. Laser Injection of Ultrashort Electron Pulses into Wakefield Plasma Waves. *Phys. Rev. Lett.*, 76:2073, 1996.
- [44] J. Faure, C. Rechatin, A. Norlin, A. Lifschitz, Y. Glinec, et al. Controlled injection and acceleration of electrons in plasma wakefields by colliding laser pulses. *Nature*, 444(7120):737–739, 2006.
- [45] A. Pak, K. A. Marsh, S. F. Martins, W. Lu, W. B. Mori, et al. Injection and Trapping of Tunnel-Ionized Electrons into Laser-Produced Wakes. *Phys. Rev. Lett.*, 104:025003, 2010.
- [46] C. McGuffey, A. G. R. Thomas, W. Schumaker, T. Matsuoka, V. Chvykov, et al. Ionization Induced Trapping in a Laser Wakefield Accelerator. *Phys. Rev. Lett.*, 104:025004, 2010.
- [47] C. E. Clayton, J. E. Ralph, F. Albert, R. A. Fonseca, S. H. Glenzer, et al. Self-guided laser wakefield acceleration beyond 1 gev using ionization-induced injection. *Phys. Rev. Lett.*, 105(10):105003, 2010.
- [48] K. Schmid, A. Buck, C. M. S. Sears, J. M. Mikhailova, R. Tautz, et al. Density-transition based electron injector for laser driven wakefield accelerators. *Phys. Rev. ST Accel. Beams*, 13:091301, 2010.
- [49] A. Buck, J. Wenz, J. Xu, K. Khrennikov, K. Schmid, et al. Shock-Front Injector for High-Quality Laser-Plasma Acceleration. *Phys. Rev. Lett.*, 110:185006, 2013.
- [50] A. Pukhov and J. Meyer-ter Vehn. Laser wake field acceleration: the highly non-linear broken-wave regime. *Applied Physics B: Lasers and Optics*, 74:355, 2002.
- [51] W. P. Leemans, A. J. Gonsalves, H. S. Mao, K. Nakamura, C. Benedetti, et al. Multi-GeV Electron Beams from Capillary-Discharge-Guided Subpetawatt Laser Pulses in the Self-Trapping Regime. *Phys. Rev. Lett.*, 113:245002, 2014.
- [52] S. M. Wiggins, R. C. Issac, G. H. Welsh, E. Brunetti, R. P. Shanks, et al. High quality electron beams from a laser wakefield accelerator. *Plasma Phys. Controlled Fusion*, 52(12):124032, 2010.
- [53] C. Lin, J. van Tilborg, K. Nakamura, A. Gonsalves, N. Matlis, et al. Long-Range Persistence of Femtosecond Modulations on Laser-Plasma-Accelerated Electron Beams. *Phys. Rev. Lett.*, 108:094801, 2012.

-
- [54] G. R. Plateau, C. G. R. Geddes, D. B. Thorn, M. Chen, C. Benedetti, et al. Low-Emittance Electron Bunches from a Laser-Plasma Accelerator Measured using Single-Shot X-Ray Spectroscopy. *Phys. Rev. Lett.*, 109:064802, 2012.
- [55] A. Buck, M. Nicolai, K. Schmid, C. M. S. Sears, A. Sävert, et al. Real-time observation of laser-driven electron acceleration. *Nature Phys.*, 7:543, 2011.
- [56] O. Lundh, J. Lim, C. Rechatin, L. Ammoura, A. Ben-Ismaïl, et al. Few femtosecond, few kiloampere electron bunch produced by a laser-plasma accelerator. *Nature Phys.*, 7:219, 2011.
- [57] M. E. Couprie, C. Benabderrahmane, L. Cassinari, J. Daillant, C. Herbeaux, et al. Progress of the LUNEX5 Project. In *Proc. FEL Conf.*, page 502, 2013.
- [58] Z. Huang, Y. Ding, and C. B. Schroeder. Compact X-ray Free-Electron Laser from a Laser-Plasma Accelerator Using a Transverse-Gradient Undulator. *Phys. Rev. Lett.*, 109:204801, 2012.
- [59] M. Heigoldt, S. I. Bajlekov, A. Popp, K. Khrennikov, J. Wenz, et al. Temporal evolution of longitudinal bunch profile in a laser wakefield accelerator. *arXiv.org*, 1406.6653, 2014.
- [60] S. Karsch, J. Osterhoff, A. Popp, T. P. Rowlands-Rees, Zs. Major, et al. GeV-scale electron acceleration in a gas-filled capillary discharge waveguide. *New J. Phys.*, 9:415, 2007.
- [61] W. P. Leemans, B. Nagler, A. J. Gonsalves, C. Toth, K. Nakamura, et al. GeV electron beams from a centimetre-scale accelerator. *Nature Phys.*, 2:696, 2006.
- [62] K. Nakamura, B. Nagler, Cs. Tóth, C. G. R. Geddes, C. B. Schroeder, et al. GeV electron beams from a centimeter-scale channel guided laser wakefield accelerator. *Phys. Plasmas*, 14:056708, 2007.
- [63] R. Weingartner, S. Raith, A. Popp, S. Chou, J. Wenz, et al. Ultralow emittance electron beams from a laser-wakefield accelerator. *Phys. Rev. ST Accel. Beams*, 15:111302, 2012.
- [64] Johannes Bahrtdt, H J Backer, M Dirsatt, W Frentrup, Andreas Gaupp, et al. Cryogenic Design of a PrFeB-based Undulator. In *Proc. Int. Part. Accel. Conf.*, page 3111, June 2010.
- [65] J. Bahrtdt. Pushing the limits of short period permanent magnet undulators. In *Proc. FEL Conf.*, page 435, 2011.
- [66] E. D. Courant and H. S. Snyder. Theory of the Alternating-Gradient Synchrotron. *Ann. Phys.*, 3:1, 1958.

- [67] J. Andruszkow, B. Aune, V. Ayvazyan, N. Baboi, R. Bakker, et al. First Observation of Self-Amplified Spontaneous Emission in a Free-Electron Laser at 109 nm Wavelength. *Phys. Rev. Lett.*, 85, 2000.
- [68] D. Xiang. Overview of Phase Space Manipulations of Relativistic Electron Beams. *SLAC-PUB-15196*, 2012.
- [69] T. Seggebrock, A. R. Maier, I. Dornmair, and F. Grüner. Bunch decompression for laser-plasma driven free-electron laser demonstration schemes. *Phys. Rev. ST Accel. Beams*, 16:070703, 2013.
- [70] E. L. Saldin, E. A. Schneidmiller, and M. V. Yurkov. Self-amplified spontaneous emission FEL with energy-chirped electron beam and its application for generation of attosecond x-ray pulses. *Phys. Rev. ST Accel. Beams*, 9(5):050702, 2006.
- [71] M. Dohlus. private communication. 2010.
- [72] S. I. Bajlekov, S. M. Hooker, and R. Bartolini. Simulating sub-wavelength temporal effects in a seeded FEL driven by laser-accelerated electrons. In *Proc. FEL Conf.* Liverpool, UK, 2009.
- [73] C. Maroli, V. Petrillo, and M. Ferrario. One-dimensional free-electron laser equations without the slowly varying envelope approximation. *Phys. Rev. ST Accel. Beams*, 14:070703, 2011.
- [74] J. Bahrdt. private communication. 2012.
- [75] A. Doria, R. Bartolini, J. Feinstein, G. P. Gallerano, and R. H. Pantell. Coherent emission and gain from a bunched electron beam. *IEEE J. Quantum Electron.*, 29(5):1428–1436, 1993.
- [76] D. A. Jaroszynski, R. J. Bakker, A. F. G. van der Meer, D. Oepts, and P. W. van Amersfoort. Coherent startup of an infrared free-electron laser. *Phys. Rev. Lett.*, 71:3798–3801, 1993.
- [77] R. Prazeres, J. M. Ortega, F. Glotin, and D. A. Jaroszynski. Observation of coherent and self-amplified spontaneous emission with the CLIO free-electron laser. *Nucl. Instrum. Methods Phys. Res. Sect. A*, 407:474, 1998.
- [78] T. I. Smith, J. M. J. Madey, L. R. Elias, and D. A. G. Deacon. Reducing the sensitivity of a free-electron laser to electron energy. *J. Appl. Phys.*, 50:4580, 1979.
- [79] S. Reiche. private communication. 2012.
- [80] B. L. Bobbs, G. Rakowsky, and P. Kennedy. In search of a meaningful field-error specification for wigglers. *Nucl. Instrum. Methods Phys. Res. Sect. A*, 296:574–578, 1990.

-
- [81] B. Faatz, J. Pflüger, and P. Pierini. Dependence of the VUV-FEL performance at the TESLA Test Facility on magnetic field errors. *Nucl. Instrum. Methods Phys. Res. Sect. A*, 375:441, 1996.
- [82] B. Faatz, J. Pflüger, and Y. M. Nikitina. Study of the Undulator Specification for the VUV-FEL at the TESLA Test Facility. *Nucl. Instrum. Methods Phys. Res. Sect. A*, 393:380, 1997.
- [83] F. Holy. private communication. 2011.
- [84] J. Bahrtdt. private communication. 2013.
- [85] S. Reiche. private communication. 2014.
- [86] M. Sands. A beta mismatch parameter. *SLAC-AP-85*, pages 1–21, 1991.
- [87] C. J. Bocchetta, A. Abrami, E. Allaria, I. Andrian, D. Bacescu, et al. FERMI@Elettra Conceptual Design Report. Technical report, 2007.
- [88] I. S. Ko. Beam dynamics newsletter no. 38, 2005.
- [89] R. Akre, A. Brachmann, F. J. Decker, Y. Ding, D. Dowell, et al. Commissioning of the LCLS Linac and Bunch Compressors. *SLAC-PUB-13373*, 2008.
- [90] E. L. Saldin, E. A. Schneidmiller, and M. V. Yurkov. On the coherent radiation of an electron bunch moving in an arc of a circle. *Nucl. Instrum. Methods Phys. Res. Sect. A*, 398:373, 1997.
- [91] Y. Derbenev, J. Rossbach, and E. L. Saldin. Microbunch radiative tail-head interaction. *TESLA FEL-Report 1995-05*, 1995.
- [92] K. L. F. Bane. The short range resistive wall wakefields. *SLAC/AP-87*, 1991.
- [93] I. Zagorodnov. Some Recipes for Wakefield Calculations - Fast Analytical Estimations and Scaling. 2013.
- [94] G. V. Stupakov, K. L. F. Bane, and I. Zagorodnov. Impedance scaling for small angle transitions. *Phys. Rev. ST Accel. Beams*, 14:014402, 2011.
- [95] K. Yokoya. Impedance of slowly tapered structures. *CERN SL/90-88 (AP)*, 1990.
- [96] S. Di Mitri and M. Cornacchia. Merit functions for the linac optics design for colliders and light sources. *Nucl. Instrum. Methods Phys. Res. Sect. A*, 735:60, 2014.
- [97] M. Dohlus and T. Limberg. Impact of Optics on CSR-Related Emittance Growth in Bunch Compressor Chicanes. In *Proc. Part. Accel. Conf.*, 2005.
- [98] S. Rauch. private communication. 2014.

- [99] F. Stulle, A. Adelman, and M. Pedrozzi. Designing a bunch compressor chicane for a multi-TeV linear collider. *Phys. Rev. ST Accel. Beams*, 10:031001, 2007.
- [100] F. Stulle. *A bunch compressor for small emittances and high peak currents at the VUV Free-Electron Laser*. PhD thesis, University of Hamburg, Hamburg, 2004.
- [101] M. Dohlus and T. Limberg. CSRtrack: Faster Calculation of 3D CSR effects. In *Proc. FEL Conf.*, Trieste, 2004.
- [102] M. Dohlus. Modelling of Space Charge and CSR Effects in Bunch Compression Systems. In *Proc. Europ. Part. Accel. Conf.*, 2006.
- [103] A. Ashmore, R. Bartolini, and N. Delerue. Numerical analysis of space charge effects in electron bunches at laser-driven plasma accelerators. *Cent. Eur. J. Phys.*, 9:980, 2011.
- [104] M. Dohlus, A. Kabel, and T. Limberg. Optimal beam optics in the TTF-FEL bunch compression sections: Minimizing the emittance growth. In *Proc. Part. Accel. Conf.*, volume 3, pages 1650–1652, 1999.
- [105] M. Shimada, K. Yokoya, T. Suwada, and A. Enomoto. Lattice and beam optics design for suppression of CSR-induced emittance growth at the KEK-ERL test facility. *Nucl. Instrum. Methods Phys. Res. Sect. A*, 575:315, 2007.
- [106] M. Borland. A highly flexible bunch compressor for the aps leu1 fel. In *Proc. Int. Linac Conf.*, page 863, 2000.
- [107] S. Karsch. private communication. 2013.
- [108] J. Rossbach and P. Schmüser. Basic course on accelerator optics.
- [109] R. J. England, J. B. Rosenzweig, G. Andonian, P. Musumeci, G. Travish, et al. Sextupole correction of the longitudinal transport of relativistic beams in dispersionless translating sections. *Phys. Rev. ST Accel. Beams*, 8:12801, 2005.
- [110] R. J. England. *Longitudinal Shaping of Relativistic Bunches of Electrons Generated by an RF Photoinjector*. PhD thesis, University of California, 2007.
- [111] T. Eichner, F. Grüner, S. Becker, M. Fuchs, D. Habs, et al. Miniature magnetic devices for laser-based, table-top free-electron lasers. *Phys. Rev. ST Accel. Beams*, 10:82401, 2007.
- [112] Owis. Product information: Limes 80 high-precision linear stage, Feb. 2015.
- [113] P. Antici, A. Bacci, C. Benedetti, E. Chiadroni, M. Ferrario, et al. Laser-driven electron beamlines generated by coupling laser-plasma sources with conventional transport systems. *J. Appl. Phys.*, 112:044902, 2012.

-
- [114] C. M. S. Sears, A. Buck, K. Schmid, J. M. Mikhailova, F. Krausz, et al. Emittance and divergence of laser wakefield accelerated electrons. *Phys. Rev. ST Accel. Beams*, 13:092803, 2010.
- [115] E. Esarey, B. Shadwick, P. Catravas, and W. P. Leemans. Synchrotron radiation from electron beams in plasma-focusing channels. *Phys. Rev. E*, 65:056505, 2002.
- [116] P. Emma and H.-D. Nuhn. Quadrupole magnet error sensitivities for FODO-cell and triplet lattices in the LCLS undulator. *LCLS-TN-00-5*, 2000.
- [117] S. Becker, M. Bussmann, S. Raith, M. Fuchs, R. Weingartner, et al. Characterization and tuning of ultrahigh gradient permanent magnet quadrupoles. *Phys. Rev. ST Accel. Beams*, 12(10):102801, 2009.
- [118] R. Brinkmann. Accelerators and photons. trends, challenges, opportunities. EuroNNAc Workshop, CERN, 2011.
- [119] A. Mostacci, M. Bellaveglia, E. Chiadroni, A. Cianchi, M. Ferrario, et al. Chromatic effects in quadrupole scan emittance measurements. *Phys. Rev. ST Accel. Beams*, 15:082802, 2012.
- [120] A. Loulergue, M. Labat, C. Evain, C. Benabderrahmane, V. Malka, et al. Beam manipulation for compact laser wakefield accelerator based free-electron lasers. *New J. Phys.*, 17:1–10, 2015.
- [121] M. Stadler, R. Baldinger, R. Ditter, B. Keil, R. Kramert, et al. Beam test results of undulator cavity bpm electronics for the european XFEL. In *Proc. Int. Beam. Inst. Conf.*, page TUPA27, 2012.
- [122] R. W. Warren. Limitations on the use of the pulsed-wire field measuring technique. *Nucl. Instrum. Methods Phys. Res. Sect. A*, 272:257, 1988.
- [123] Z. Wolf. A vibrating wire system for quadrupole fiducialization. *LCLS-TN-05-11*, 2005.
- [124] S. M. Hooker. Developments in laser-driven plasma accelerators. *Nature Photonics*, 7:775, 2013.
- [125] J. Osterhoff. *Stable, ultra-relativistic electron beams by laser-wakefield acceleration*. PhD thesis, Ludwig-Maximilians-Universität, Munich, 2009.
- [126] S. Raith. private communication. 2014.
- [127] E. D. Courant. Impossibility of achromatic focusing with magnetic quadrupoles and solenoids. *Part. Accel.*, 2:117, 1971.
- [128] M. Gilljohann. private communication. 2014.

- [129] M. Borland. Elegant: A flexible SDDS-compliant code for accelerator simulation. Technical report, Advanced Photon Source LS-287, 2000.
- [130] F. Holy, A. R. Maier, B. Zeitler, R. Weingartner, S. Raith, et al. First spectral measurements of a cryogenic high-field short-period undulator. *Phys. Rev. ST Accel. Beams*, 17:050704, 2014.
- [131] R. Weingartner, M. Fuchs, A. Popp, S. Raith, S. Becker, et al. Imaging laser-wakefield-accelerated electrons using miniature magnetic quadrupole lenses. *Phys. Rev. ST Accel. Beams*, 14, 2011.

Publications

- S. Karsch, J. Wenz, K. Khrennikov, M. Heigoldt, A. Popp, A. Buck, J. Xu, L. Veisz, S.-W. Chou, A. Maier, N. Kajumba, **T. Seggebrock**, F. Grüner, A. Guggenmos, U. Kleineberg, S. Schleede, M. Bech, P. Thibault, and F. Pfeiffer: *X-ray Generation by Relativistic Laser-Accelerated Electrons*, CLEO: Applications and Technology. Optical Society of America, JTh3L.5, (2014)
- **T. Seggebrock**, I. Dornmair, T. Tajima, G. Mourou, F. Grüner: *The Pulse Intensity-Duration Conjecture: Evidence from Free-Electron Lasers*, Progress of Theoretical and Experimental Physics, 013A02 (2014)
- **T. Seggebrock**, A. R. Maier, I. Dornmair, and F. Grüner: *Bunch decompression for laser-plasma driven free-electron laser demonstration schemes*, Phys. Rev. ST Accel. Beams 16, 070703 (2013)
- A. R. Maier, **T. Seggebrock**, and F. Grüner: *Conceptual Design Report for a Laser-Plasma Driven Free-Electron Laser*, (2013)
- A. R. Maier, A. Meseck, S. Reiche, C. B. Schroeder, **T. Seggebrock**, and F. Grüner: *Demonstration scheme for a laser-plasma driven free-electron laser*, Phys. Rev. X 2, 031019 (2012)
- M. Günther, P. Thirolf, **T. Seggebrock**, and D. Habs: *Seeded quantum FEL at 478 keV*, DPG-Verhandlung Mainz 2012 – Anwendungen kernphysikalischer Methoden
- R. Weingartner, M. Fuchs, A. Popp, S. Raith, S. Becker, S. Chou, M. Heigoldt, K. Khrennikov, J. Wenz, **T. Seggebrock**, B. Zeitler, Zs. Major, J. Osterhoff, F. Krausz, S. Karsch, and F. Grüner: *Imaging laser-wakefield-accelerated electrons using miniature magnetic quadrupole lenses*, Phys. Rev. ST Accel. Beams 14, 052801 (2011)

Acknowledgements

The work presented here has only been made possible thanks to the support of several people. I would like to thank all colleagues who supported this work and hope nobody has been forgotten:

Prof. Dr. Florian Grüner

Florian made it possible for me to graduate in his group despite his move to Hamburg. Thank you for this opportunity and your confidence in my work.

Dr. Nathaniel Kajumba

Natty, our former postdoc, was a great help regarding all aspects ranging from scientific discussions to organizational matters. We endured countless CALA meetings together.

Dr. Andreas Maier

Andi was the first person to tell me about the crazy project of a lab-scale (at that time even table-top) free-electron laser. Thank you for all the interesting and fruitful discussions.

Dr. Sven Reiche

As the developer of GENESIS, Sven is *the* person to ask when it comes to FEL simulations. Thank you for all the support and discussions, and your help regarding the peculiarities and hidden parameters of GENESIS.

Dr. Martin Dohlus

Martin provided the 1D FEL code used in this thesis and is one of the developers of CSRTRACK. Thank you for these great tools and your support.

Priv.-Doz. Dr. Atoosa Meseck

Ati has been a great help in setting up and understanding GENESIS as well as CSRTRACK simulations.

Dr. Johannes Bahrtdt and Dr. Andreas Gaupp

Johannes and Andreas were the driving force behind the undulator development which is the heart to the concept discussed in this thesis. They have been a great source of information regarding undulator design and the feasibility of the proposed undulator configuration.

Prof. Dr. Jörg Schreiber

Jörg kindly agreed to review this thesis and has always been available for helpful discussions about research and also organizational matters.

Prof. Dr. Friedhelm Bell

Friedhelm provided lots of feedback and triggered several interesting discussions.

Prof. Dr. Toshiki Tajima

It was an honor to work with the inventor of laser-wakefield acceleration during his time here in Munich. Thank you for this great opportunity.

Florian Holy

Flo² was my local source of information for all questions regarding undulators and undulator radiation. Thank you for all the great discussions.

Sebastian Raith

Sebastian was the person to ask when it came to discussions about beam optics. In case you missed a soccer game in the recent decade and would like to know anything about the game – ask Sebastian.

Stephanie Rauch

Stephanie was a great support in understanding the peculiarities of bunch decompression and emittance growth. Thank you for your great work, the fruitful discussions, and all your feedback regarding this thesis.

Irene Dornmair

Despite her move to Hamburg Irene has been a great source of information and feedback in the recent years. Thank you very much.

The FEL-Team

The whole team in Munich and Hamburg (Ben, Moritz, Andreas, Jessica, Niels, Chris, Jakob, ...) has been an invaluable source of information, help, and feedback. Thank you to all of you.

The MAP-Team

The MAP-team members, especially Katharina Adler and Dr. Martin Groß, always were very helpful when it came to organizational and funding matters. Thank you for your support.

Isy

Thank you for your continuous support during the whole time and the many discussions! It was also very helpful to have someone to talk to who has a feeling for design and presentation style.

My parents

Thank you for your continuous encouragement and making all this possible!